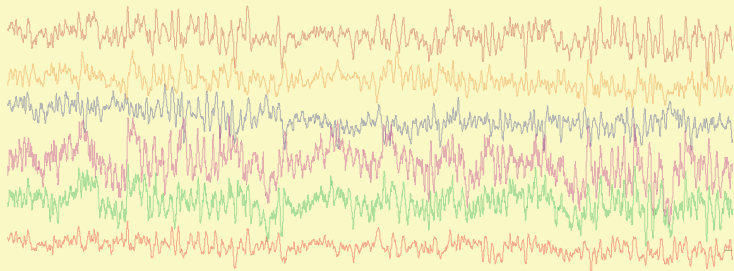
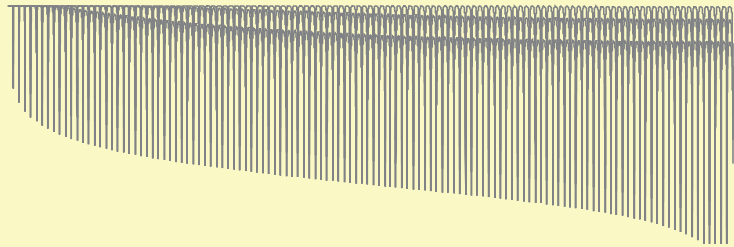


Design and Evaluation of Filtering Methods for Gradient Artefact Suppression in EEG Recordings during Co-registered EEG-fMRI



José Leonardo Ferreira

Design and evaluation of filtering methods for gradient artefact suppression in EEG recordings during co-registered EEG-fMRI

PROEFSCHRIFT

ter verkrijging van de graad van doctor aan de Technische Universiteit Eindhoven, op gezag van de rector magnificus prof.dr.ir. F.P.T. Baaijens, voor een commissie aangewezen door het College voor Promoties, in het openbaar te verdedigen op dinsdag 21 januari 2020 om 16:00 uur

door

José Leonardo Ferreira

geboren te Diamantina, Brazilië

Dit proefschrift is goedgekeurd door de promotoren en de samenstelling van de promotiecommissie is als volgt:

voorzitter:	prof.dr.ir. A.B. Smolders
1 ^e promotor:	prof.dr. R.M. Aarts
copromotor(en):	dr. Y. Wu dr.ir. R.M.H. Besseling (Demcon Advanced Mechatronics)
leden:	prof.dr. R. van Ee (RUN) prof.dr.ir. R.N.J. Veldhuis (UT) prof.dr. J.B.A.M. Arends prof.dr.ir. M. Mischi

Het onderzoek of ontwerp dat in dit proefschrift wordt beschreven is uitgevoerd in overeenstemming met de TU/e Gedragscode Wetenschapsbeoefening.

Design and evaluation of filtering methods for gradient artefact suppression in EEG recordings during co-registered EEG-fMRI

José Leonardo Ferreira

Design and evaluation of filtering methods for gradient artefact suppression in EEG recordings during co-registered EEG-fMRI / by José Leonardo Ferreira – Eindhoven: Eindhoven University of Technology, 2020.

A catalogue record is available from the Eindhoven University of Technology Library
ISBN: 978-90-386-4968-9.

The research presented in this thesis was financially supported by Erasmus Mundus – EBW II project and by CNPq – Science without Borders program

Cover Design: José Leonardo Ferreira and Otniel Ribeiro
Reproduction: Eindhoven University of Technology.

Copyright © 2020, José Leonardo Ferreira

All rights reserved. Copyright of the individual chapters belongs to the publisher of the journal listed at the beginning of each respective chapter. No part of this publication may be reproduced, stored in a retrieval system, or transmitted, in any form or by any means, electronic, mechanical, photocopying, recording or otherwise, without the prior written permission from the copyright owner.

To my beloved parents

Summary

Co-registered EEG-fMRI, i.e. the simultaneous acquisition of electroencephalography (EEG) and functional magnetic resonance imaging (fMRI), has emerged as a multimodal technique in the 1990s. It is considered an essential research tool in basic and cognitive neuroscience, as co-registered EEG-fMRI combines the high temporal resolution offered by EEG and the high spatial resolution offered by fMRI. Hence, it allows high spatiotemporal measurements of brain activity beyond the capabilities of each individual technique. In the past decades, co-registered EEG-fMRI has been applied in numerous neuroscientific and neurophysiological studies, e.g. epilepsy, cognitive measures of memory performance and learning capabilities, and neuropsychiatric disorders studies like depression and post-traumatic stress disorder.

Despite its promise for high spatiotemporal brain imaging, co-registered EEG-fMRI is still deemed a challenging technique. This is because of the artefacts caused by the magnetic fields of the MRI scanner that severely compromise the quality of the EEG recordings, as described in Chapter 2 of this thesis. Most significantly, magnetic field gradients and RF pulses used in MRI pulse sequences induce an interference voltage, the so-called gradient or imaging acquisition artefact, in the electrical potential recorded in the scalp electrodes (i.e. scalp potential).

Several correction approaches have been proposed to suppress the gradient artefact from the scalp potential recordings and, consequently, improve the quality of the corrected EEG signal. Most of the gradient artefact correction methods, including the often-used average artefact subtraction (AAS) and the fMRI artefact slice template removal (FASTR) methods, are based on comb-filtering. As discussed in Chapter 3, a common shortcoming of these approaches is that the residual artefacts after correction still corrupt neuronal EEG bands higher than 80 Hz. These residual artefacts are mainly a result of the broadening of the spectral lines due to micro-movements of the subject within the MRI scanner. As the frequency range above 80 Hz features the EEG gamma band and high-frequency oscillations (HFOs), some studies into memory and attention processes, ERPs, and fast ripples in the onset of epileptic seizures and others involving HFOs can be compromised or even not be performed. To access EEG high-

frequency and ultra-high-frequency oscillations, correction approaches currently have to be combined with customised MRI sequences that are not widely available to all investigators.

In Chapter 4, we describe the design of a novel comb-filtering approach, the optimised moving-average (OMA) filter, which we combine with other filtering approaches in a novel gradient artefact correction methodology. We propose the use of the finite impulse response (FIR) moving-average filter as well as the exponential average filter within an iterative filtering-based method to improve the gradient artefact correction and its correction-related residuals in the high-frequency bands (Chapters 5 and 6). Additionally, we devised a novel filtering approach based upon the difference between consecutive samples of the digital signal to construct a non-linear low-pass filter specifically targeting residual artefacts (Chapter 7).

A second challenge in EEG-fMRI co-registration is the design of objective measures to evaluate artefact removal and signal preservation. In this thesis, we propose a novel and simple evaluation approach to assess this (Chapter 3). As most of the gradient artefact correction evaluation strategies proposed in the literature do not take into account the assessment of preservation of the EEG signal after performing the gradient artefact correction, our novel approach can help future researches to compare different correction strategies and evaluate which strategy is most suitable for their application.

In Chapters 5 and 6, we demonstrate that our proposed gradient artefact correction methodology offers a better balance for the trade-off between artefact attenuation and preservation of the EEG signal than the AAS and FASTR methods. Our methodology is especially useful in the higher-frequency EEG bandwidth usually contaminated by residual artefacts. Preliminary visual inspection performed by a trained EEG expert indicated that epileptiform activity can be successfully identified in the resulting artefact-corrected EEG, and is comparable to the epileptiform activity identified in artefact-corrected EEG after using the FASTR method. Moreover, the proposed methodology was shown to be more robust to alterations of the artefact waveform caused by head movements (Chapters 6 and 8). In conclusion, we therefore believe that this methodology is a promising tool to obtain gradient artefact-corrected EEG of a higher quality in scenarios in which abrupt head movements cannot be prevented like in epileptic patients, as discussed in Chapter 9. In addition, we envisage that the novel gradient artefact correction evaluation procedure adopted in this thesis can potentially be used for performance evaluation of artefact correction methods in general.

List of abbreviations

AAS – Average artefact subtraction

ADC – Analogue-to-digital converter

AEP – Auditory evoked potential

Ag-AgCl – Silver-silver chloride

ANC – Adaptive noise cancelling

AP – Action potential

BCG – Ballistocardiogram or pulse artefact

BOLD – Blood oxygen level dependence effect

CBF – Cerebral blood flow

CBV – Cerebral blood volume

CMRO₂ – Cerebral metabolic rate of oxygen consumption

CNS – Central nervous system

CSF – Cerebro-Spinal Fluid

CT – Computerised tomography

DC – Direct current

DMS – Difference model subtraction

DT – Delay time

ECG – Electrocardiogram/electrocardiography

ECoG – Electrocorticography

EEG – Electroencephalogram/electroencephalography

EEG-fMRI – Co-registered or simultaneous acquisition of EEG and fMRI data

EIT – Electrical impedance tomography

EMG – Electromyogram/electromyography

EOG – Electrooculogram

EP – Evoked potential

EPI – Echo-planar imaging sequence

EPSP – Excitatory post-synaptic potential

ERP – Event-related potential

FASTR – FMRI artefact slice template removal

FID – Free induction decay

FIR – Finite impulse response

fMRI – Functional magnetic resonance imaging

FT – Fourier Transform

fTCD – Functional transcranial doppler sonography

H – Hydrogen

HFO – High-frequency oscillations

HP – High-pass filter

HSN – Highly selective notch filtering

IAR – Imaging artefact reduction

ICA – Independent component analysis

IFD – Iterative filtering decomposition

IFT – Inverse Fourier transform

IMF – Intrinsic mode function

IPSP – Inhibitory post-synaptic potential

LP – Low-pass filter

MEG – Magnetoencephalography

mGLM – Moving general linear model

MR – Magnetic resonance

MRI – Magnetic resonance imaging

MSE – Mean squared error

NMR – Nuclear magnetic resonance

-
- OBS** – Optimal basis set
- OEA** – Optimised exponential average
- OLS** – Ordinary least-squares
- OMA** – Optimised moving-average filtering
- PA** – Pulse artefact
- PCA** – Principal component analysis
- PET** – Positron emission tomography
- PSP** – Post-synaptic potential
- PTSD** – Post-traumatic stress disorder
- RF** – Radiofrequency
- RMS** – Root mean square
- SNR** – Signal-to-noise ratio
- SPRLIO** – Spiral k-space filling sequence
- SSD** – Signal slope adaption
- SVD** – Singular value decomposition
- TE** – Echo time
- TR** – Volume repetition time
- TR-slice** – Slice repetition time
- VEP** – Visual evoked potential
- WHO** – World Health Organization

Contents

Summary	vii
List of abbreviations	ix
Contents	xiii
1 Introduction	1
1.1 Outline, objectives, and contributions of this work	3
1.1.1 Overview of EEG, fMRI, co-registered EEG-fMRI, and artefacts during co-registered EEG-fMRI	3
1.1.2 Evaluation of the artefact attenuation and EEG signal preservation during gradient artefact correction	4
1.1.3 Design of novel filtering techniques for suppression of the gradient artefact and other applications	4
1.1.4 Concluding remarks and directions for future work	7
2 EEG, fMRI, Co-Registered EEG-fMRI, and the Problem of Artefacts during Co-Registration of EEG and fMRI data	9
2.1 Electrical activity of the brain: the EEG signal	9
2.1.1 The origin of the EEG signal	9
2.1.2 Main features of the EEG signal	14
2.1.3 EEG signal for identification of brain states and abnormalities, and other applications	20
2.2 Functional magnetic resonance imaging – fMRI	22
2.2.1 The basis of MRI physics: the nuclear magnetic resonance (NMR)	23
2.2.2 Magnetic resonance image reconstruction	26
2.2.3 Physiological background of fMRI	30
2.2.4 Use of fMRI for research and clinical purposes	32
2.3 Co-registered EEG-fMRI	33
2.4 The quality of the EEG and fMRI signal during co-registered EEG-fMRI: the problem of artefacts	35
2.4.1 The gradient artefact	36
2.4.2 The pulse artefact	40
2.4.3 The movement artefact	41
2.4.4 Artefacts in the MR image due to the EEG system	46
3 Gradient Artefact Suppression and Correction Evaluation	49
3.1 Abstract	49
3.2 Introduction	50
3.3 Overview of the existing methods for gradient artefact correction	55
3.3.1 Artefact attenuation at the source	55

3.3.2 Model of the actual situation in post-processing solutions	56
3.3.3 Usual approximation considered by the existing methods to correct the gradient artefact.....	57
3.3.4 Subtraction in time-domain-based methods.....	58
3.3.5 Filtering in frequency-domain-based methods (Fourier filtering)	62
3.4 Overview of the existing approaches for pulse artefact correction	64
3.4.1 The pulse artefact (PA) subtraction correction method and its variants	64
3.4.2 Other solutions for pulse artefact correction.....	66
3.4.3 Remaining challenges on suppression of the pulse artefact.....	67
3.5 Overview and critical analysis of the existing approaches for evaluation of gradient artefact correction methods	68
3.5.1 Measurement of the artefact reduction.....	68
3.5.2 Measurement of the EEG signal preservation.....	71
3.5.3 Use of phantoms and simulated data.....	77
3.6 Methodology for evaluation of gradient artefact correction methods proposed for the current thesis.....	79
3.6.1 Assessment of the artefact reduction.....	80
3.6.2 Measurement of EEG signal preservation.....	81
3.6.3 Visual inspection by a trained EEG expert	82
3.7 Concluding remarks.....	83
4 Enhancement of the Comb-filtering Selectivity using Iterative Moving-Average for Periodic Waveform and Harmonic Elimination	85
4.1 Abstract.....	85
4.2 Introduction	86
4.3 Methods	90
4.3.1 Design of a novel comb-filtering approach for elimination of periodic waveforms.....	91
4.3.2 Iterative application of time-domain averaging	93
4.3.3 Using the proposed method to design a novel notch filtering approach	93
4.4 Results	95
4.4.1 Frequency characteristics of the novel comb-filtering approach	95
4.4.2. Iterative application of time-domain averaging	96
4.4.3 Notch filter characteristics obtained by iterative moving-average.....	99
4.5 Further comparative analyses and discussion.....	99
4.6 Conclusions	103
5 Gradient Artefact Correction and Evaluation of the EEG Recorded Simultaneously with fMRI Data using Optimised Moving-Average.....	105
5.1 Abstract.....	105
5.2 Introduction	106
5.3 Methods	110
5.3.1 EEG and fMRI data.....	110
5.3.2 Proposed methodology for gradient artefact correction.....	112
5.3.3 Peak detection and TR-slice estimation	112
5.3.4 Optimised moving-average filtering (OMA)	112
5.4 Evaluation of the gradient artefact correction and comparative analysis.....	118

5.4.1 Assessment of the artefact attenuation.....	119
5.4.2 Evaluation of the EEG preservation	119
5.4.3 Comparative analysis.....	120
5.5 Results	121
5.6 Discussion	130
5.7 Conclusions	134
6 Evaluating the Relative Efficacy and Clinical Usefulness of the Gradient Artefact Correction using Iterative Filtering.....	137
6.1 Abstract	137
6.2 Introduction	137
6.3 Methods	141
6.3.1 EEG and fMRI data.....	141
6.3.2. Gradient artefact correction and suppression of residual artefacts	142
6.3.3. Optimised moving-average (OMA).....	143
6.3.4. The highly selective notch (HSN) filtering.....	146
6.3.5 Optimised exponential average (OEA).....	147
6.4 Comparative analysis, quantitative assessment, and clinical evaluation of the gradient artefact correction.....	149
6.4.1 Comparative analysis.....	149
6.4.2 Quantitative assessment	150
6.4.3 Clinical evaluation of the gradient artefact correction.....	150
6.5 Results	151
6.5.1 Quantitative assessment	157
6.5.2 Identification of epileptiform activity and clinical evaluation.....	160
6.6 Discussion	161
6.6.1 Limitations and future work.....	165
6.7 Conclusions	166
7 A Study of Attenuation of Residual Artefacts after Gradient Artefact Correction using a Non-Linear Filter based upon Differentiation between Consecutive Samples	169
7.1 Abstract	169
7.2 Introduction	170
7.3 Methods	173
7.3.1 EEG and fMRI data.....	173
7.3.2 Implementation of the average artefact subtraction methodology in this chapter ..	174
7.3.3 Estimation of the residual artefacts.....	176
7.3.4 Signal slope adaption (SSD) approach implementation	177
7.4 Results	181
7.4.1 Evaluation of the EEG signal preservation after SSD	189
7.5 Discussion	192
7.5.1 Limitations and future work.....	195
7.6 Conclusions	196
8 Gradient Artefact Suppression under the Occurrence of Abrupt Subject Head Movements.....	197

8.1 Abstract.....	197
8.2 Introduction	198
8.3 A study of gradient artefact correction under the occurrence of signal transients continuously inserted by abrupt head movements.....	200
8.3.1 EEG and fMRI data.....	200
8.3.2 Approach implementation	200
8.3.3 Results	205
8.3.4 Discussion	209
8.3.5 Conclusions	211
8.4 Other filtering strategies that might help to improve the gradient artefact correction under the occurrence of abrupt head movements	211
8.4.1 Linear superposition of an impulse signal.....	211
8.4.2 Sliding average window vs. optimised moving-average.....	212
8.4.3 Change in shape and amplitude of the gradient artefact	215
8.5 Final discussion and concluding remarks	216
9 Discussion and Conclusions	219
9.1 Performance and relative efficacy of the gradient artefact correction methods	219
9.2 Gradient artefact correction evaluation	225
9.3 Limitations, considerations, and directions for future work.....	226
9.4 Overall conclusions	228
References.....	231
List of the author's publications	253
Acknowledgments	257
About the author	259

CHAPTER 1

Introduction

Measurement and monitoring of brain activity are of fundamental importance to understand neuronal functions and neurophysiologic properties of the human brain. For those who deal with research, diagnosis, or treatment of brain disorders, neurological imaging techniques can provide valuable insight into the operation of the brain and the neurological status of the subject. According to the World Health Organization (WHO), brain and neurological disorders are a significant cause of disability in the global population and an emerging challenge to healthcare systems. For instance, recent estimates show that stroke is the second highest cause of morbidity and mortality worldwide, dementia, meningitis and migraine rank in the top-30 factors in disability-adjusted life years, and epilepsy in the top-50 out of 315 diseases and injuries studied (World Health Organization, 2017a; Kassebaum et al., 2015). Although research on the neurophysiologic properties of the human brain dates back centuries, brain imaging has only become available in the recent past. This sparked numerous breakthroughs in neurophysiologic brain mapping, and helped shaping a scientific basis for the modern technology to measure brain processes (Savoy, 2001; Turner and Jones, 2003; World Health Organization, 2006; Sanei and Chambers, 2007; Raichle, 2009; Gazzaniga et al., 2013; World Health Organization, 2017b).

A significant number of methods are currently available for structural and functional brain imaging and mapping; for example, electrocorticography (ECoG), electroencephalography (EEG), magnetoencephalography (MEG), magnetic resonance imaging (MRI), functional magnetic resonance imaging (fMRI), computerised tomography (CT), positron emission tomography (PET), doppler sonography (fTCD), electrical impedance tomography (EIT), functional near infrared spectroscopy (fNIRS), and optical imaging (Turner and Jones, 2003; Siedband, 2010; Villringer et al., 2010; Lloyd-Fox et al., 2010; Gibson et al., 2005; Gazzaniga et al., 2013). However, individual brain imaging methods do not provide a sufficiently broad and comprehensive view of brain processes and structures as they are limited to observing specific aspects of the brain function. Moreover, a single method suffers from the trade-off between good spatial resolution and good temporal resolution. Therefore, it has been

proposed to combine different brain imaging modalities in order to provide complementary neurophysiologic information and improve the spatiotemporal resolution, thus enhancing the ability to characterise brain processes (Villringer et al., 2010; Uludağ and Roebroeck, 2014).

In this regard, simultaneous acquisition of EEG and fMRI data (or co-registered EEG-fMRI) is considered to be a promising and powerful multimodal technique for neurophysiologic brain mapping. The high temporal resolution of EEG associated with the high spatial resolution of fMRI has been offering the opportunity to understand numerous questions in basic and cognitive neuroscience (Villringer et al., 2010; Pan et al., 2011). Co-registered EEG-fMRI was first applied in studies of epilepsy (Warach et al., 1996; Seeck et al., 1998). Over the past years, its application has been extended to many other neuroscientific fields such as cognitive measures of memory performance, learning capabilities, and decision-making; resting and sleep; pain research; and neuropsychiatric and mood disorders like schizophrenia, depression, and post-traumatic stress disorder (PTSD) (Ritter and Villringer, 2006; Horovitz et al., 2008; Villringer et al., 2010; Iannetti and Mouraux, 2010; Zotev et al., 2016; Pisauro et al. (2017); Zotev et al., 2018).

However, the application of co-registered EEG-fMRI faces a major challenge that limits its applications on a large scale: the occurrence of the gradient artefact in EEG data that are recorded simultaneously with fMRI data. The gradient artefact follows from the voltage interference induced by the magnetic field gradients and RF pulses used in MRI sequences, which is picked up in the human scalp (scalp potential) by the EEG electrodes during co-registered EEG-fMRI. In this thesis, the technical challenge of gradients artefact suppression will be addressed.

In the literature, a number of approaches have been proposed for this purpose, such as the often-used average artefact subtraction (AAS) and the fMRI artefact slice template removal (FASTR) methods. It has been demonstrated that these approaches substantially attenuate the artefact activity while preserving the EEG signal in the frequency band up to 80 Hz. Unfortunately, these existing gradient artefact correction methods do not allow assessment of the higher-frequency EEG band. For studies on brain processes characterised by higher frequencies (i.e. the gamma band and above in neuronal EEG), therefore, novel correction methodologies are required. The EEG gamma rhythm ranges from 30 up to 100 Hz and is crucial in clinical neurophysiology. It is also associated with event-related synchronisation of the brain, the so-called event-related potentials (ERPs). The study of high-frequency

oscillations (HFOs) between 100 and 500 Hz has recently received increased attention as well. EEG rhythms of up to 150 Hz are associated with attention and memory processes, whereas fast ripples in the frequency range of 200 – 500 Hz are mostly present in the onset region of epileptic seizures. Existing gradient artefact correction methods may leave residual artefacts in the gamma band and above and the use of conventional low-pass filters or further correction approaches may wash out components of interest of the neuronal EEG (Allen et al., 2000; Niazy et al., 2005; Spencer, 2015; Sanei and Chambers, 2007; Gotman, 2010). Until now, assessment of the higher-frequencies in the gamma band and HFOs has only been possible by employing customised MRI sequences that are not widely available to all investigators (Freyer et al., 2009; Spencer, 2015).

A second challenge in co-registration of EEG and fMRI data is an objective quality assessment of artefact correction methods. Artefact correction methods need to achieve a good balance between artefact suppression and EEG signal preservation. However, objective measures to compare artefact suppression while preserving the signal are scarcely used. This complicates a systematic and consistent performance evaluation of the gradient artefact correction methods. The risk of simultaneous removal of neuronal EEG activity during application of the gradient artefact correction method can therefore not be assessed. Moreover, the performance of gradient artefact correction among different EEG-fMRI acquisition scanner setups and vendors has been poorly evaluated (Ritter et al., 2010; Mandelkow et al., 2010; Ritter et al., 2007; Grouiller et al., 2007). This issue will also be addressed in this thesis.

1.1 Outline, objectives, and contributions of this work

1.1.1 Overview of EEG, fMRI, co-registered EEG-fMRI, and artefacts during co-registered EEG-fMRI

In **Chapter 2**, an overview is provided of EEG, fMRI, co-registered EEG-fMRI, and the artefacts that afflict the EEG and the fMRI acquisition during co-registration of EEG and fMRI. Firstly, the use of EEG, fMRI, and co-registered EEG-fMRI for mapping the brain activity is reviewed. Next, the main artefacts that occur in the co-registered EEG-fMRI environment are described, with a special focus on the characteristics of the gradient artefact.

1.1.2 Evaluation of the artefact attenuation and EEG signal preservation during gradient artefact correction

The first objective of this work is the proposal of a systematic procedure to evaluate the performance of gradient artefact correction approaches.

To this end, a critical literature overview of methods to suppress the gradient artefact and evaluate their performance is presented in **Chapter 3**. Most of the gradient artefact corrections evaluation approaches proposed in the literature do not take into account the preservation of the EEG signal after performing the gradient artefact correction. Moreover, the stochastic nature of the neuronal EEG is rarely taken into consideration when the degree of EEG preservation is assessed (Spencer, 2015; Ritter et al., 2010; Ritter et al, 2007; Grouiller et al., 2007; Mandelkow et al., 2010; Gonçalves et al., 2007). In order to assess the degree of EEG preservation and simultaneously measure the artefact attenuation, we have devised a novel and simple evaluation approach that accounts for the stochastic nature of the neuronal EEG. This procedure is used throughout this thesis, and can also be used as a systematic framework for performance evaluation of gradient artefact correction methods in general. Evaluation of the gradient artefact correction performance in EEG data sets recorded among different EEG-fMRI acquisition scanner setups and vendors is provided throughout the thesis as well.

In addition, some features of the existing methods for pulse artefact correction are described and discussed in **Chapter 3**. The pulse artefact in the EEG data is caused by the pulsatile movement of the blood in scalp arteries within the static magnetic field of the MRI equipment. The precise nature of the pulse artefact, however, remains an open question (Allen et al., 1998; Debener et al., 2010; Eichele et al., 2010; Spencer, 2015). As with the gradient artefact, a number of solutions have been proposed for the correction of this artefact, but these may not result in a good quality for the corrected EEG signal either. The evaluation of correction strategies as presented in Chapter 3 can also be applied for the pulse artefact.

1.1.3 Design of novel filtering techniques for suppression of the gradient artefact and other applications

The second and major objective of this thesis is the design and evaluation of novel filtering techniques for the suppression of the gradient artefact, in order to improve the quality of the EEG signal recorded simultaneously with fMRI data.

Some filtering techniques such as the finite impulse response (FIR) moving-average filter have the advantage of computational efficiency, thus are widely employed in signal processing in general. Therefore, we propose an FIR moving-average filter within an iterative filtering-based method to correct the gradient artefact and its correction-related residuals. In addition, we devised an approach exploiting the difference between consecutive samples of the digital signal to construct a non-linear low-pass filter. Implementation and application of these novel filtering approaches are presented in the following chapters:

Chapter 4: a novel comb-filtering design through iterative moving-average filtering. We describe in Chapter 4 the design of a novel comb-filtering technique named optimised moving-average (OMA). Implementation of OMA is based on an iterative filtering decomposition process (Lin et al., 2009), in which an FIR moving-average-based filter (referred to as double average filter) is iteratively applied to decompose a signal into intra-wave frequency modes or intrinsic mode functions. We show that exploitation of the first intrinsic mode function jointly to the double average filter enables the OMA comb-filter to provide larger attenuation in higher-frequency stop-bands than conventional comb-filtering approaches. Moreover, we demonstrate that other iterative moving-average filter-based approaches can be used to reduce the number of averages required during application of the time-domain averaging approach as well as be exploited to design a highly selective notch filtering (HSN) approach.

Chapter 5: gradient artefact correction using optimised moving-average filtering. In this chapter, it is demonstrated that the larger attenuation in higher-frequency stop-bands provided by the comb-filtering integrated in OMA is more effective than recent methods proposed in the literature in compensating the broadening of gradient spectral lines around the artefact bins associated with TR-slice in the EEG gamma band and above (Spencer, 2015; LeVan et al., 2016). TR-slice corresponds to the time of acquisition of a single MRI slice, and the results presented in Chapter 5 were obtained within a scenario in which the MRI parameter repetition time, TR, is set as a multiple of TR-slice. Furthermore, the proposed approach is shown to produce a better balance between suppression of the artefact and preservation of the neuronal EEG signal than template subtraction by AAS. Additional outcomes of this chapter indicate that our approach is capable of correcting the EEG data even within a scenario of misalignment between the EEG sampling interval and TR-slice, without accurate information about triggers and other MRI events, and without the use of customised fMRI pulse sequences (Spencer, 2015; Freyer et al., 2009).

Chapter 6: gradient artefact correction using iterative filtering in a broader case scenario. In Chapter 6, we describe a variant of the OMA approach addressing the gradient artefact activity associated with the MRI repetition time, TR. Design of such a variant is necessary to counterbalance the undesirable reduction of the attenuation in lower-frequency comb-filter stop-bands and the larger attenuation in higher-frequency comb-filter pass-bands observed for OMA when applied for TR. This OMA variant is tested in a scenario where it is not possible to switch off the dynamic stabilisation in the MRI equipment and, thereby, TR cannot be set as a multiple of TR-slice. Whereas the average template subtraction is usually applied using either TR or irregularly spaced artefact templates of length TR-slice, these approaches are less effective in obtaining a good quality for the corrected EEG than using regular templates of length TR-slice. The use of two averaging steps by AAS subsequently for TR and TR-slice is also shown to degrade the quality of the corrected EEG (Mandelkow et al., 2010). We demonstrate that OMA can be applied for both TR and TR-slice, thus achieving additional attenuation of the artefact activity associated with TR-slice.

In addition, we designed a highly selective notch (HSN) filtering as well as a novel low-pass filtering approach based on iterative application of the exponential average filter, the optimised exponential average (OEA), to attenuate residual artefacts in the artefact-corrected EEG. Although broadening of artefact spectral lines associated with TR-slice was effectively corrected by OMA, we noticed a trade-off between the number of iterations used during OMA application and the amount of residual artefacts left behind in the artefact frequency bins. Thus, we proposed the use of HSN and OEA in combination with OMA to obtain a better balance of this trade-off and to achieve a better preservation for the neuronal EEG, especially at higher frequencies. We show that our methodology to correct the gradient artefact can outperform the sliding averaging window by AAS as well as the often-used FASTR method. In this way, larger attenuation in the artefact frequency bins associated with TR-slice, better preservation of the higher-frequency EEG bandwidth, and improved robustness to alterations of the artefact waveform due to movements of the subject head could be achieved. Moreover, visual inspection performed by a trained EEG expert indicates that the proposed methodology can be used in studies involving identification of epileptiform activity.

Chapter 7: a study of residual artefacts attenuation using signal slope adaption. In Chapter 7, we investigate the large time course signal slopes associated with gradient artefact samples. These signal slopes have been exploited as a parameter of a non-linear filter to attenuate residual artefacts after gradient artefact correction. By making use of the difference

between consecutive samples of the digital signal, the resulting filtering approach termed signal slope adaption (SSD) is shown to be capable of selectively low-pass filtering the residual artefact activity associated with broadening of artefact spectral lines. Furthermore, we envisage that the SSD approach can be exploited for residual artefacts attenuation in the higher-frequency EEG bandwidth as well.

Chapter 8: gradient artefact correction during abrupt head motions. In Chapter 8, we elaborate on gradient artefact correction of EEG data affected by abrupt head movements by the subject. In this scenario, the gradient artefact correction often requires special processing that relies on the quantification of the head movement by sensors, camera track systems, or using MRI equipment movement-related information (Moosmann et al., 2009; Sun and Hinrichs, 2009; Spencer, 2015; Maziero et al., 2016). Here, we suggest a novel data-driven approach based on cubic splines in order to enhance the quality of the gradient artefact-corrected EEG under the occurrence of signal transients continuously inserted by abrupt head movements.

1.1.4 Concluding remarks and directions for future work

In **Chapter 9**, we conclude this thesis with an overall analysis, comparison, and discussion of the results. Practical limitations and directions of future work are also indicated. The major contribution of this work are the devised methodologies that can be employed to improve the quality of the EEG data recorded during fMRI as well as the devised strategies to objectively evaluate the performance of the gradient correction methods. The iterative filtering techniques presented in this thesis can for example be used in clinical epilepsy studies involving the use of co-registered EEG-fMRI data. Moreover, the novel filtering approaches can also be employed in other types of signal processing applications, such as comb-filtering, notch filtering, low-pass filtering, ECG peak detection, and harmonic analysis.

CHAPTER 2

EEG, fMRI, Co-Registered EEG-fMRI, and the Problem of Artefacts during Co-Registration of EEG and fMRI data

2.1 Electrical activity of the brain: the EEG signal

Electrical signal fluctuations from the brain observed by placement of electrodes on the scalp were described qualitatively for the first time by the English physiologist Richard Caton in 1875. However, the term *electroencephalogram*, (Greek, *en*, in; *kephale*, head; *gram*, writing, drawing) was introduced by the German psychiatrist Berger, who recorded the signal for the first time in 1924. After the first recording of the EEG signal, other researchers reproduced the results of Berger and confirmed that the brain activity measured on the scalp could be used as source of clinical information as well as for studies on brain functioning (Niedermeyer, 1999; Shipley, 2001; Haas, 2003).

2.1.1 The origin of the EEG signal

The human brain is constituted by five main parts: the cerebrum, the diencephalon (including the thalamus), the mesencephalon (midbrain), the cerebellum, and the brain stem. In particular, the cerebrum is divided into two hemispheres (left and right), whose outer surface shows a high convoluted pattern called cerebral cortex (Fig. 2.1). The cortex is mainly composed of cell bodies and dendrites (short branches) that together act as input structures of neurons (nerve cells), and constitute the grey matter. Any neuron has one branch that serves as the output fibre which sends information (projects) to other neurons, the axon. For connections among nearby neurons, axons are relatively short (e.g., a few centimetres) but often long distances need to be bridged (in adult humans sometimes up to one metre), in which case the axon usually is covered with a fatty, white substance (myelin), that enhances the speed of conduction of information along the axon.

The cortex is separated into regions by fissures, the sulci (singular, *sulcus*). Within these cortical regions, neurons are organised into columnar groups of cells (populations) that are

believed to be involved in one or another neurological and/or cognitive function. A cortical column has a perpendicular orientation with respect to the cortical surface and may contain two types of neurons:

- non-pyramidal neurons serve as cells that either process information within the population (inter-neurons) or receive information from other neuronal populations, either from other cortical areas (e.g., from the other hemisphere) or from the deeper structures such as the midbrain or brainstem. Non-pyramidal neurons often have remarkable shapes and both their dendrites and axon have no preferred orientation.
- pyramidal cells are the output units of a cortical population and are named after their anatomical shape. The cell body looks like a pyramid whose top (apex) points towards the cortical surface. The axon arises from the bottom of the pyramid and runs down, perpendicularly to the cortical surface. In pyramidal cells, two types of dendrites can be recognised:
 - o basal dendrites basically run parallel to the cortical surface;
 - o the apical dendrite arises from the top of the pyramid and runs perpendicularly to the cortical surface.

The cortex covers a massive collection of nerve fibres that lead to other parts of the brain and the human body (white matter). A longitudinal structure named corpus callosum connects the left and right cortical hemispheres by a large band of myelinated axons (Fig. 2.1). The cerebrum includes the regions for movement control, conscious awareness of sensation, complex analysis, and expression of emotions and behaviour (Sanei and Chambers, 2007; Rangayyan, 2002).

Information related to physiological control processes, thought processes, and external stimuli flows via the neurons (or nerve cells) and provokes synaptic activation in corresponding parts of the brain cortex. Such information is encoded as temporary changes in the voltage difference that under resting conditions is maintained across neuronal cell membranes. This resting membrane potential causes the intracellular fluid to be negative relative to the extracellular environment.

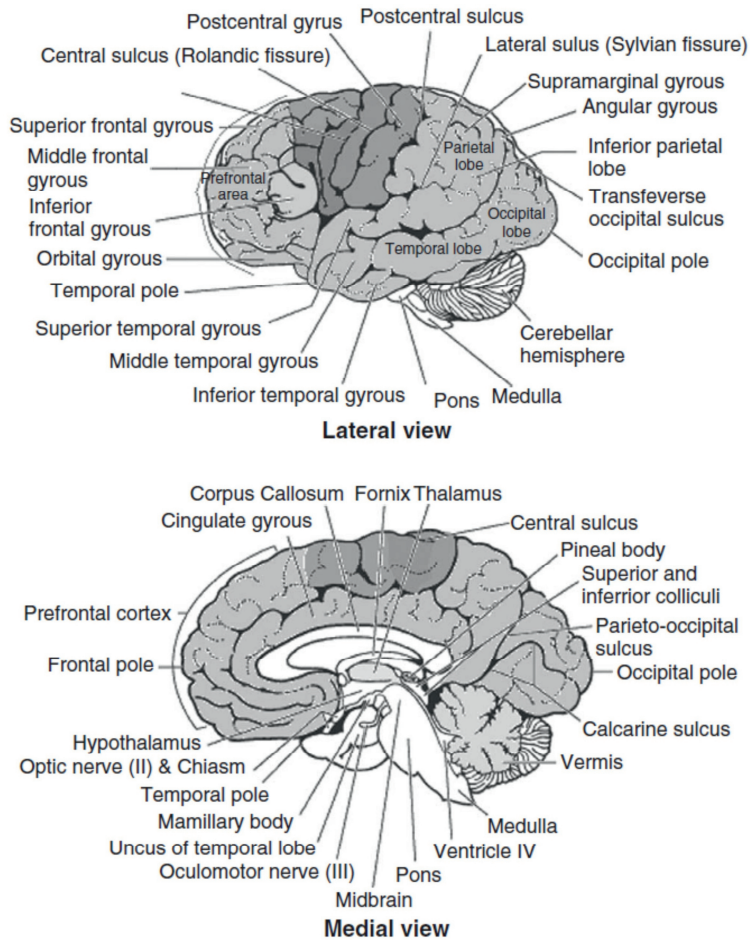


Figure 2.1: Lateral and medial views of the human brain. Adapted from Sanei and Chambers (2007).

In this context, two types of mechanisms in and around neuronal cell membranes must be mentioned:

- action potentials (APs) are short duration phenomena (at most a few milliseconds) that temporarily cause a reversal of the polarity of the membrane potential. An AP is initiated when the membrane potential depolarises (becomes less negative) beyond a threshold, after which an active process (the Hodgkin cycle) in and around the membrane takes over and autonomously generates a local, temporary neuronal voltage “spike”. Because of the local voltage differences that are generated between the active membrane area and the adjacent inactive membrane sections that still are at rest, local ion currents are generated

between adjacent membrane areas which, in turn, depolarise the neighbouring section thus initiating an AP there as well. This way an AP, once initiated, is actively conducted across the entire neuronal cell membrane. Action potentials are all-or-none phenomena: either they are present or not; they do not add up neither in time or in space;

- post-synaptic potentials (PSPs) are fluctuations in the membrane potential that occur at the receiving, post-synaptic side of the junction between two different neurons when the first, pre-synaptic, neuron receives an AP. An intricate biochemical process, often referred to as synaptic transmission, generates a small, but relatively slow (up to several tens of milliseconds) fluctuation of the membrane potential in the receiving, postsynaptic cell. Such a fluctuation can be either inhibitory (IPSP; the membrane potential becomes more negative) or excitatory (EPSP; the membrane potential becomes less negative). Due to the local membrane potential differences with adjacent post-synaptic membrane areas, local currents cause spreading of the PSP to nearby post-synaptic membrane sections. Contrary to APs, this conduction is passive and attenuates rapidly with increasing distance from the synapse. PSPs are graded phenomena: when a previous or a neighbouring PSP still is active, the effect of a second one is superimposed on the ongoing local phenomenon. This temporal and/or spatial summation may lead to a net depolarisation of the postsynaptic membrane beyond the threshold, thus initiating an AP which – as described above – is actively conducted across the entire post-synaptic membrane. This means that a post-synaptic AP always is preceded by a relatively slow, low-frequency sequence of stepwise changes (either depolarising or hyperpolarising membrane potential fluctuations which may take up to 100 milliseconds before the post-synaptic cell actually fires an AP. Usually, one single post-synaptic cell receives input from thousands of synapses leading to complex, but mainly slow temporal changes of post-synaptic membrane potentials.

Both APs and PSPs cause local currents in and around neuronal membranes. The extracellular currents are not restricted to the neighbourhood but spread through the entire extracellular space which must be regarded as one continuous space that mainly consists of water with various kinds of organic and inorganic substances solved in it. Due to the abundant presence of charged particles, the extracellular fluid of the brain tissue can be approximated as a linear conductor with a specific conductance, σ_b . Similar linear conductor models can be constructed for the structures that surround the brain: the Cerebro-Spinal Fluid (CSF), the skull and the scalp, each having their own specific conductances, σ_{csf} , σ_{skull} , and σ_{scalp} . The construction of

realistic conduction head models is an intricate process that up to now is topic for scientific debate. This, however, is beyond the scope of this thesis.

For this thesis, an important observation is that the electrical properties of the medium between the neurophysiological membrane mechanisms (either AP or PSP) and the scalp surface are purely resistive. Contrary to phenomena that occur across membranes, no capacitive or inductive effects occur in the extracellular environment. This means that there is only linear attenuation of electrical phenomena between source and scalp, no filtering. Using the laws of volume conduction (i.e. applying Maxwell's laws of electromagnetism in biological tissue), it can be proven that the level of attenuation approximately is inversely proportional to the square of the distance, D , between observation point and source. Another consequence of the linearity of the extracellular environment is that the conduction is instantaneous, implying that the sum of momentary AP and PSP activity contributes to the measurable electrical activity in or close to the brain. The EEG signal constitutes the measure of such an electrical activity over the scalp surface.

In summary, the following factors need to be taken into account to understand the various patterns that are measured in the main signal of interest in this thesis, the scalp surface EEG:

- In order to significantly contribute to the net extracellular currents, the direction of the individual extracellular source currents needs to be such that they enhance each other; the currents need to be more or less aligned towards the same direction.
- In each cell of a specific cortical population, APs either are ongoing or not. Because of their short duration, the probability of many APs to be active at the same time in multiple cells is low, except in situations of so-called hyper-synchronisation. This may occur for instance during an epileptic seizure.
- Conversely, it is more than likely that, within a cortical population, there are many PSPs simultaneously active. This in particular holds for the PSPs in the pyramidal cells, whose dendrites are aligned either perpendicularly (apical) or parallel (basal) to the cortical surface.

These factors lead to the conclusion that, in general, the neurophysiological sources of the EEGs are post-synaptic potentials, either inhibitory or excitatory, of the pyramidal cells in the cortex (Cluitmans, 2010).

2.1.2 Main features of the EEG signal

EEG signals can be recorded by placement of electrodes on the intact scalp^{*}, rather than the first time they were registered, using simple galvanometers. Two electrodes are responsible for measuring the signal, and a third electrode acts as signal-ground (reference). This configuration is so-called bipolar *montage* whereby the signal is measured between adjacent electrodes. Instead, if the signal is measured between the electrode and the reference, the montage is named unipolar (Sanei and Chambers, 2007; Clark Jr., 2010).

In clinical practice, several channels of the EEG are recorded simultaneously from various locations on the scalp for comparative analysis of activities in different regions of the brain (Rangayyan, 2002). Figure 2.2 depicts the conventional electrode setting so-called 10-20 system for 21 electrodes, recommended by The International Federation of Societies for Electroencephalography and Clinical Neurophysiology.

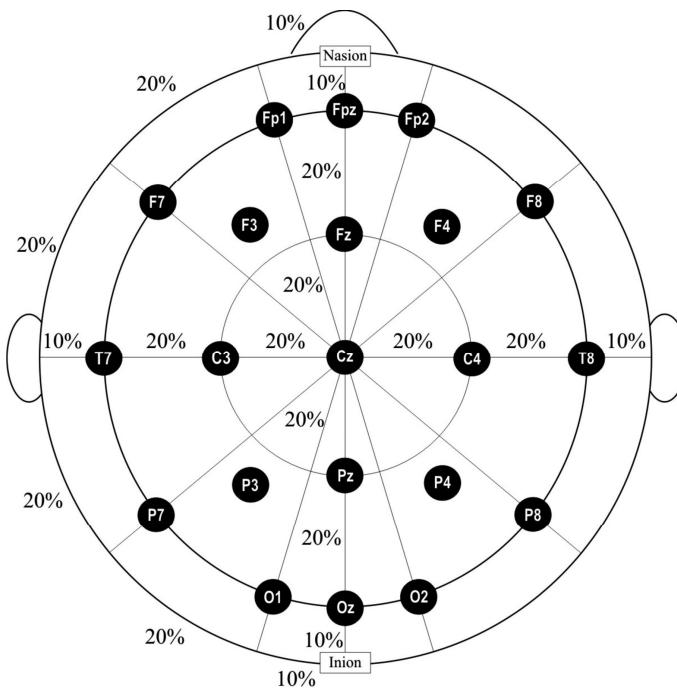


Figure 2.2: Conventional 10-20 EEG electrode placement. Adapted from Sanei and Chambers (2007) and Oostenveld and Praamstra (2001).

^{*} When the electrodes are placed on the exposed surface of the cortex, this type of bioelectric measurement is named *electrocorticogram* – ECoG (Clark Jr., 2010).

According to the 10-20 system, the EEG electrodes are positioned on the scalp at points 10 or 20% distant from each other related either to the total distance taken: from the inion (the bony protuberance in the middle of the back of the head) and the nasion (the bridge of the nose directly under the forehead); or to the total distance taken between the two pre-auricular points (the depression of the bone in front of the ear). A naming convention is adopted for each electrode: the letters refer to the underlying cerebral lobes, “Fp” for prefrontal; “F” for frontal; “C” for central; “P” for parietal; “T” for temporal; and “O” for occipital. Subscripts indicate whether the electrode is positioned on the left (odd numbers), on the right (even numbers) hemisphere of the head, or on the middle line (“z”). Two electrodes connected to the earlobes are often used as reference, but other choices of placement of the reference electrode, such as Fpz are also used (Sanei and Chambers, 2007).

In applications such as topographic methods to study spontaneous and evoked potentials, extra electrodes are placed between and equidistant the existing ones, which results in the 10-10 and 10-5 system (Oostenveld and Praamstra, 2001) (Fig. 2.3). For clinical purposes requiring robust and/or long-term EEG monitoring, the most commonly used scalp electrodes consist of Ag-AgCl disks, less than 3 mm in diameter, with long flexible leads that can be plugged into an amplifier. In routine recording of the electroencephalogram, the recording area on the surface of the scalp is initially degreased by cleaning it with alcohol. Afterwards, a conducting paste is applied on the recording area, and then the electrodes are affixed with glue (collodion). For short-term recordings and/or when patient-friendliness is crucial, ready-to use electrode-caps made from some kind of elastic fabric that contain all required electrodes has become increasingly popular (Clark Jr., 2010; Sanei and Chambers, 2007). Figure 2.4 depicts a lateral and anterior view of the 10-5 electrode system shown in Fig. 2.3b, together with a back view of an electrode-cap assembly placed on the head of the subject.

The EEG signal can be characterised as coloured with limited bandwidth, non-deterministic (stochastic), and non-stationary. It is normally displayed in the time-domain, and could be plotted on a plane paper with a grid, as was usually made in the old days of electroencephalography registration. Nowadays, computerised systems are the most common used manner for EEG visualisation, whereby the signal can be digitised, stored, and processed as well.

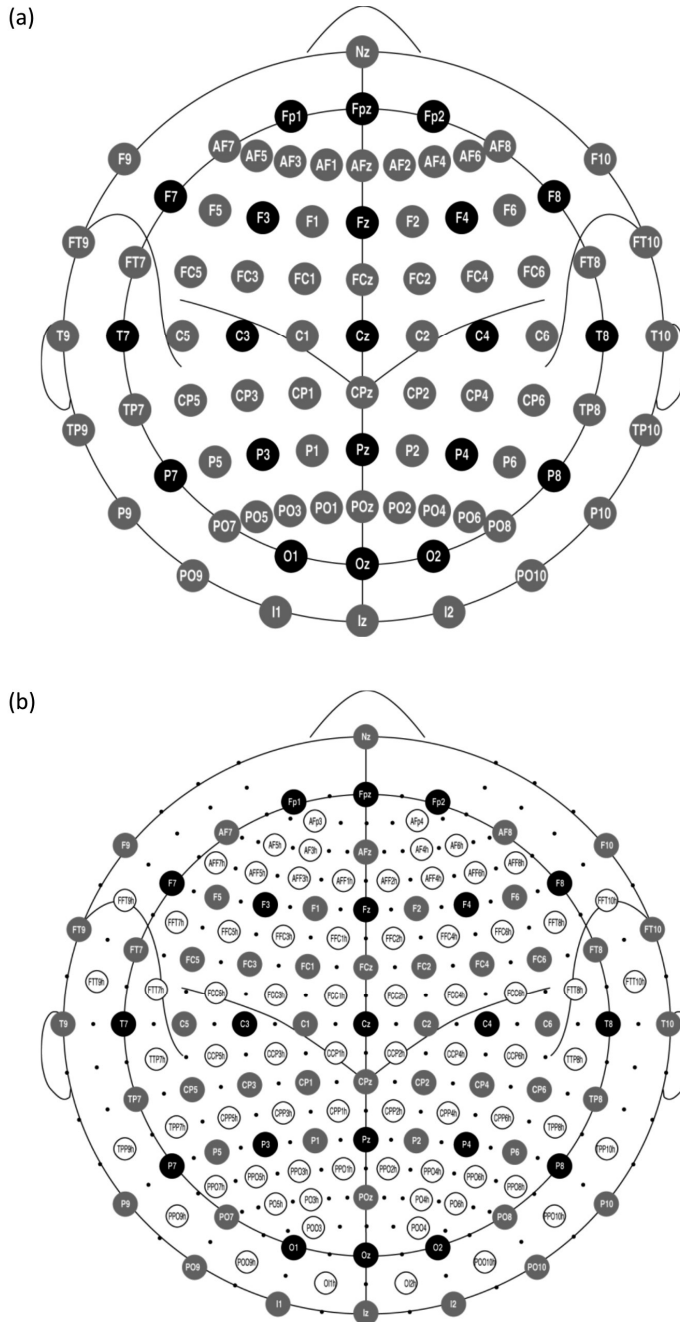


Figure 2.3: (a) 10-10 EEG electrode placement; (b) 10-5 EEG electrode placement. Black circles indicate positions of the original 10-20 system as depicted in Fig. 2.2; gray circles indicate the extra electrodes introduced in the 10-10 system; and open circles indicate additional positions used in the 10-5 system. Adapted from Oostenveld and Praamstra (2001).

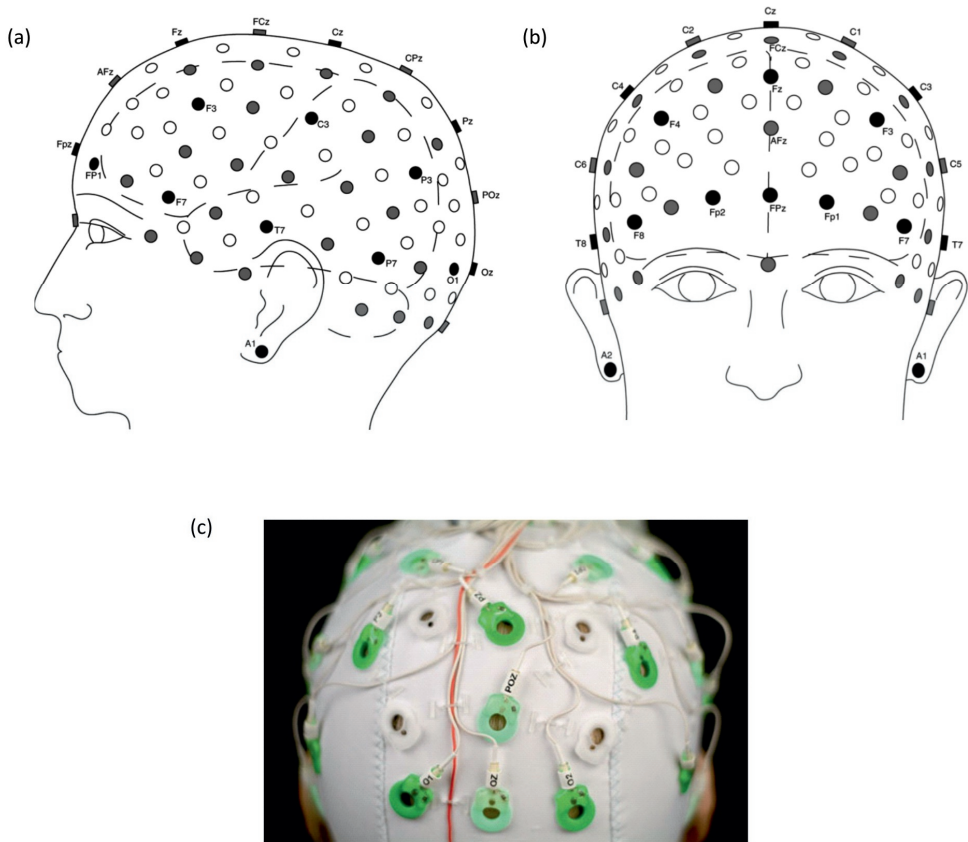


Figure 2.4: (a), (b) Lateral and anterior view of the head showing up the 10-5 EEG electrode placement according to Fig. 2.3b; (c) back view of an electrode-cap (BrainCap MR, Brain Products GmbH, Gilching, Germany) placed on the head of the subject. Adapted from Oostenvelde and Praamstra (2001) and Gutberlet (2010).

A relevant advantage of the EEG signal visualised in the time-domain is its good temporal resolution which allows measurement of the activity of large-scale neuronal networks at any moment with millisecond resolution, depending on the sampling rate of the EEG device (Michel and Brandeis, 2010; Sanei and Chambers, 2007; Cluitmans, 2010).

The amplitude of the EEG signal is much smaller in comparison with other bioelectrical signals, and commonly lies within 10 to 100 μV on the scalp. Thereby, amplifiers are required for a proper recording of the signal. After amplification, the EEG signal is converted from analogue to digital mode, performed by means of multichannel analogue-to-digital converters (ADC). Finally, the signal is calibrated and can be stored on a computer or made available for signal processing. It is noteworthy that, before ADC conversion, the amplified EEG signal

must be filtered using a low-pass filter (LP) to mitigate high-frequency noise components and aliasing effects. A high-pass filter (HP) is also implemented before or after sampling for ironing out undesired very low-frequency components (lower than 0.5 Hz). Notch filters with a null frequency of 50 Hz (or 60 Hz) are often necessary to ensure sufficient rejection of power-line interference (Sanei and Chambers, 2007).

In turn, the frequency range of the EEG signal typically extends from 0 to 150 Hz. For many applications, the effective bandwidth can be limited to 100 Hz or even half of this value. Therefore, a minimum sampling frequency of 100 Hz is often enough for sampling the EEG signals without violating the Nyquist criterion. Other commonly used sampling frequencies for EEG recordings are 250, 500, 1000, and 2000 Hz. Frequency contents of the EEG signal are associated with various physiological and mental processes whose response is translated in the electroencephalogram as several patterns of rhythmic or periodic activity. When the EEG is recorded with the subject relaxed or asleep, and there are no controlled conditions, it is characterised as a spontaneous ongoing activity of the brain, the *spontaneous EEG* (Olson, 2010; Sanei and Chambers, 2007; Clark Jr., 2010). In the spontaneous EEG (also called background EEG), some dominant EEG rhythms are commonly identified, associated with certain physiological and mental processes, and with the following frequency (f) bands (Sanei and Chambers, 2007; Rangayyan, 2002):

- Delta (δ): $0.5 \leq f < 4$ Hz: occurs during deep-sleep stages.
- Theta (θ): $4 \leq f < 8$ Hz: appears at the beginning stages of sleep, replacing alpha rhythms.
- Alpha (α): $8 \leq f \leq 14$ Hz: main resting rhythm of the brain, and is common in wakeful, resting adults, especially in the occipital area with bilateral synchrony.
- Beta (β): $14 \leq f \leq 30$ Hz: background activity that occurs in tense and anxious subjects.

Figure 2.5 shows the EEG signal with the typical amplitude levels and time basis for the four brain rhythms described above. The occurrence of a certain pattern usually depends on the region of the scalp in which the EEG is measured, and the waves also change with ageing.

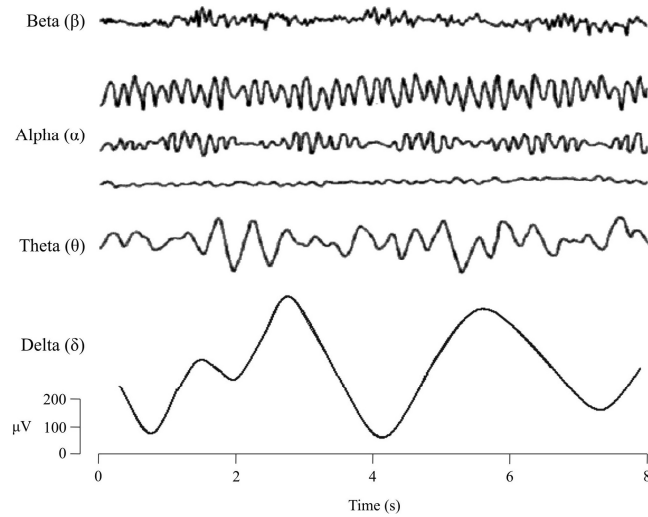


Figure 2.5: Typical dominant EEG rhythms observed in the spontaneous EEG. Adapted from Sanei and Chambers (2007).

Although with very low amplitudes, another EEG rhythm that can be useful in clinical neurophysiology is the gamma rhythm. It ranges from 30 to around 100 Hz, and its detection can be used to confirm certain brain diseases. The gamma rhythm can also be associated with event-related synchronisation of the brain, the so-called event-related potentials (ERPs). The study of high-frequency oscillations (HFOs) between 100 and 500 Hz has currently received increased attention as well. For instance, some EEG rhythms of physiological relevance up to 150 Hz are associated with attention and memory process, whereas fast ripples in the frequency range of 200 – 500 Hz are mostly present in the onset region of epileptic seizures (Sanei and Chambers, 2007; Gotman, 2010).

As for ERPs, they consist of measured responses in the EEG signal related to identifiable nervous system events such as electrical stimulation, initiation of movement, certain thought processes, et cetera. They are too small (1 – 30 μV) in comparison with the background EEG activity, and can be quantitatively characterised across three main dimensions: the amplitude, that provides an index of the extent of the neural activity; the latency, which indicates the time point at which the peak amplitude occurs; and the scalp distribution, that provides the pattern of the voltage gradient of a component over the scalp at any time instant (Sanei and Chambers, 2007). Evoked potentials (EPs) are a particular instance of ERPs, and can be defined as the response of the nervous system when an external stimulus (light, sound, electrical, or other) is applied to the subject. The frequency contents of ERPs and EPs differ

significantly from the spontaneous EEG and may include frequencies of up to 2 kHz (Sanei and Chambers, 2007; Rangayyan, 2002; Sörnmo and Laguna, 2005; Cluitmans, 2010).

2.1.3 EEG signal for identification of brain states and abnormalities, and other applications

EEG experts are familiar with manifestations of EEG rhythms in the electrical brain activity in the time-domain. This is typically done based upon human pattern recognition by screening all recorded EEG signals and interpreting their characteristics both in time and in distribution across the scalp. This so-called spatiotemporal interpretation is a delicate process that mainly relies on clinical evidence and experience rather than on physiological or physical models. Nevertheless, in some situations, it is difficult to understand and classify the EEG rhythms, even with trained eyes. In this scenario, the application of advanced signal processing tools has become very important for analysis of the EEG signal. The occurrence of rhythmical patterns associated with a specific EEG bandwidth induced the development of approaches and technologies related to the analysis of EEG signals in the frequency-domain. Thus, the usage of the Fourier transform and other spectral analysis techniques, as well as their combination with time-domain methods, have contributed to enhancement of the extraction and analysis of relevant features and clinical information in EEG signals (Sanei and Chambers, 2007).

The inspection and analysis of the EEG signal is useful for diagnosis of many brain disorders. Distortion and disappearance of normal rhythms, appearance and increase of abnormal rhythms, or disappearance of all rhythms are an indicative of abnormality. Thereby, the EEG signal is employed to diagnose mental disorders as well as for investigation of pathological process and metabolic disturbances to focal intracranial lesions, drugs and anesthesia effects, and information concerning etiology and chronicity (Sanei and Chambers, 2007; Cluitmans, 1990). The large range of applications encountered for the EEG signal ratifies the power of the use of electroencephalography in the areas of clinical neurophysiology and neuroscience research (Sanei and Chambers, 2007):

- (a) monitoring alertness, coma, and brain death;
- (b) locating areas of damage following head injury, stroke, and tumour;
- (c) testing afferent pathways;
- (d) monitoring cognitive engagement;

- (e) producing biofeedback situations;
- (f) controlling anesthesia depth;
- (g) investigating epilepsy and locating seizure origin;
- (h) testing epilepsy drug effects;
- (i) assisting in experimental cortical excision of epileptic focus;
- (j) monitoring the brain development;
- (k) testing drugs for convulsive effects;
- (l) investigating sleep disorders and physiology;
- (m) investigating mental disorders;
- (n) providing a hybrid data recording system together with other imaging modalities.

One of the most important uses of the encephalogram is the epilepsy diagnosis as well as the research of the focus in the brain causing epilepsy. Epilepsy is characterised by uncontrolled excessive activity by either a part or all of the central nervous system (CNS). A person pre-disposed to epilepsy has attacks when the basal level of excitability of all or part of the nervous system rises above a critical threshold. However, as long as the degree of excitability is held below this threshold, no attacks occur. The onset of a clinical epileptic seizure is often characterised by a sudden change of frequency and amplitude in the EEG measurement. The epileptic seizure normally occurs within the alpha wave frequency band with a slow decrease in frequency but an increase in amplitude during the seizure period. However, the onset region of an epileptic seizure can show up high-frequency oscillations (HFOs), as mentioned above (Clark Jr., 2010; Sörnmo and Laguna, 2005; Gotman, 2010).

A classical problem encountered in electroencephalography is the localisation of the accurate position of the current sources responsible for the generation of the related potentials on the scalp. In other words, in which exact regions or populations of neurons such potentials might be originated. Several works have been carried out to investigate the answer to this question, the so-called EEG inverse problem, whose solution could result in important breakthroughs in neurophysiologic and neurocognitive research (Lopes da Silva, 2010; Lopes da Silva and van Rotterdam, 1999; Pascual-Marqui, 1999). However, determination of the exact location of the current sources is difficult, and the lack of precise information regarding the geometry as well as the conductances, σ_{csf} , σ_{skull} , and σ_{scalp} , of the shells surrounding the brain makes the problem even worse to be solved. Moreover, the inverse problem has no unique solution, i.e. different combinations of intra-cerebral sources can result in the same potential distribution

on the scalp; and the EEG is a differential measure which is referenced to a reference point that never could be ideal.

This limited spatial resolution of the EEG has entailed recent efforts to combine this technique with others, like fMRI, in attempt to solve the EEG inverse problem (Niedermeyer, 1999; Michel and Brandeis, 2010; Ritter and Villringer, 2006).

2.2 Functional magnetic resonance imaging – fMRI

In comparison with the EEG, functional magnetic resonance imaging (or fMRI) is a brain activity mapping technique much more recent which started to be used in the beginning of the 1990s, albeit the idea that cerebral blood flow (CBF) could reflect neuronal activity began with experiments around one hundred years earlier, in 1890. In 1990, Ogawa et al. published a ground-breaking study reporting the use of magnetic resonance imaging (MRI) for spatial mapping of areas of brain activation in rats. According to this study, by using high speed MRI sequences, the brain activation areas could be mapped by the contrast caused by the blood oxygenation level in the magnetic resonance (MR) images. In 1991, Belliveau et al. reported, for the first time, the successful application of MRI for blood volume mapping during resting and activation in human brains, specifically in the visual cortex. Since then, fMRI has been consolidated as a widespread and most used tool for non-invasive imaging of human brain activity (Kim and Bandettini, 2006; Bandettini, 2009; Ritter and Villringer, 2006).

In 2017, there were already approximately 50,000 MRI units worldwide and, on average, 54% of the countries had at least one MRI unit. Those MRI devices have been performing hundreds of millions MRI scans per year, among which a considerable number is used for fMRI purposes. In addition to being non-invasive, some properties can help to explain the success of this technique: it utilises endogenous functional contrast; whole brain coverage; non-interference of spatially separate activation sites; and good spatial resolution that could be down to the scale of cortical columns and different cortical layers. Moreover, when compared to other methods of brain imaging like X-ray, computerised tomography (CT), and positron emission topography (PET), a great advantage of MRI is the use of non-ionising radiation by the scanners (Rinck, 2017; World Health Organization, 2017b; Hornak, 2010; Altman and Bernal, 2006).

2.2.1 The basis of MRI physics: the nuclear magnetic resonance (NMR)

The physical principles of MRI are underpinned by the nuclear magnetic resonance (NMR). NMR can be characterised as the interaction between an applied magnetic field and an atomic nucleus that possesses spin or “nuclear spin momentum”. The spin refers to the rotating of the nucleus around its own axis at a constant rate velocity like a spin top. It constitutes, thereby, a nuclear property of the atom, whose value depends on the precise atomic composition: the nucleus does not show spin if the number of neutrons and the number of protons are both even. However, if the number of neutrons plus the number of protons is odd, or the number of neutrons and the number of protons are both odd, the nucleus has a half-integer (e.g., $1/2$, $3/2$, $5/2$) or an integer spin (e.g., 1, 2, 3), respectively (Brown and Semelka, 2003; Goebel, 2007).

Parallel to its axis, the spin causes the appearance of a magnetic moment, as depicted in Fig. 2.6a. When the nucleus that possesses spin is placed inside a static magnetic field, \mathbf{B}_0 , it starts other type of rotational movement perpendicular to the magnetic field.

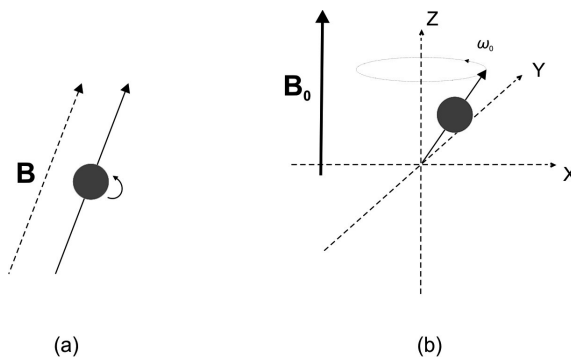


Figure 2.6: (a) Representation of the spin rotation and related magnetic moment \mathbf{B} ; (b) precession of the nucleus inside the applied magnetic field \mathbf{B}_0 and associated Larmor frequency (ω_0). Adapted from Brown and Semelka (2003).

This “precessing” movement, as it is also referred to, occurs because of the interaction of the magnetic field with the spinning positive charge of the nucleus. It has a constant frequency, ω_0 , named Larmor frequency which is proportional to \mathbf{B}_0 (Fig. 2.6b). As shown in Figs. 2.7a and 2.7b, if instead of just one nucleus, several nuclei are placed inside the static magnetic field, a non-zero net magnetic moment \mathbf{M}_0 will result from the sum of individual magnetic moments induced by each nuclear precessional movement (Goebel, 2007). The number of protons possessing magnetic moment with positive Z component is higher than those possessing negative Z component, so that the net magnetic moment \mathbf{M}_0 is parallel to \mathbf{B}_0 . \mathbf{M}_0 is

null when the value of the applied magnetic field is zero because, in the absence of \mathbf{B}_0 , nuclei that possess spins are randomly oriented and individual magnetic moments cancel each other out (Fig. 2.7c).

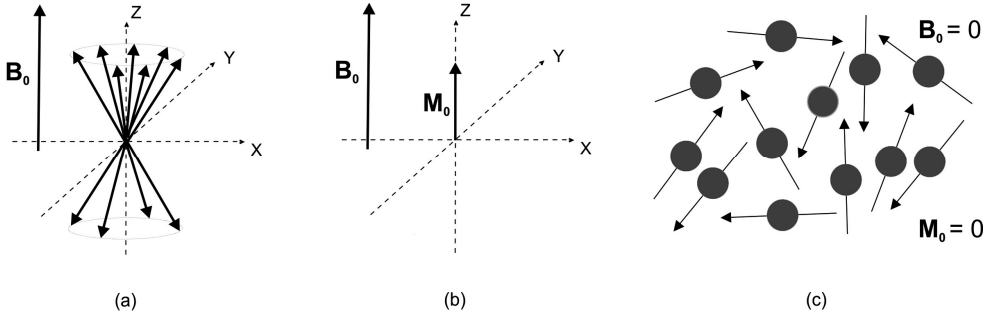


Figure 2.7: Net magnetic moment \mathbf{M}_0 resulting from the static magnetic field \mathbf{B}_0 above several nuclei: (a) individual magnetic moments; (b) resulting net magnetic moment \mathbf{M}_0 ; (c) the absence of the static magnetic field results in $\mathbf{M}_0 = 0$. Adapted from Brown and Semelka (2003).

The human body is primarily composed of water and secondly of fat, whose molecules contain hydrogen atoms. The most abundant isotope for hydrogen encountered in biological systems is the single proton ^1H (also known as “protium”) which has a spin equal to $1/2$ and is ideally suited for MRI because it possesses particularly favourable magnetic properties (Goebel, 2007; Brown and Semelka, 2003). Regarding the tissues of human body, the magnetic moment \mathbf{M}_0 can be associated with the static field \mathbf{B}_0 in accordance with Eq. (2.1):

$$\mathbf{M}_0 = \chi \mathbf{B}_0, \quad (2.1)$$

where χ is the bulk magnetic susceptibility. In turn, the precessional Larmor frequency, ω_0 , can be related to the magnitude of \mathbf{B}_0 by the expression:

$$\omega_0 = \gamma B_0, \quad (2.2)$$

where γ is a constant called gyromagnetic ratio, specific of each kind of atomic nucleus.

In short, the physics of a nuclear magnetic resonance measurement can be described in terms of energy transfer: the patient or sample is exposed to the magnetic excitation at the “correct frequency” that will be absorbed. A short time later, this energy is reemitted, in such a way that the associated electromagnetic signal can be detected and processed. The correct frequency is used to excite the protons with similar precessing frequency. Therefore, the

nuclear magnetic resonance (NMR) is named after the physic principle of frequency resonance that constitutes its basis (Goebel, 2007; Brown and Semelka, 2003).

Manipulation of the net magnetisation \mathbf{M}_0 allows the NMR signal acquisition. To this end, a magnetic excitation pulse \mathbf{B}_1 is applied perpendicular to the static magnetic field \mathbf{B}_0 of the MRI scanner, causing precession of spins in phase. Consequently, \mathbf{M}_0 turns towards the XY-plane perpendicular to \mathbf{B}_0 (Fig. 2.8). The magnetic excitation pulse contains a range of frequencies spread over a narrow bandwidth and centred at ω_0 , at which the protons absorb the energy by resonance. Because the precession frequency is in the range of radiofrequency waves, the magnetic excitation pulse \mathbf{B}_1 is also called radiofrequency (RF) pulse (Goebel, 2007; Brown and Semelka, 2003).

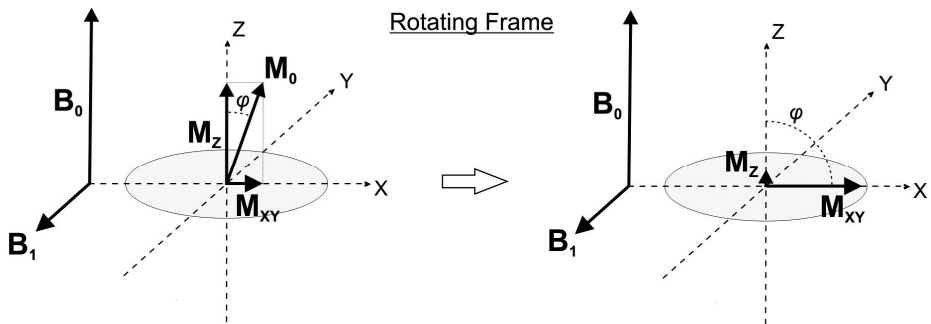


Figure 2.8: Manipulation of net magnetic moment \mathbf{M}_0 , resulting from the application of the RF pulse \mathbf{B}_1 perpendicular to the static magnetic field \mathbf{B}_0 . Adapted from Goebel (2007).

The strength and duration of \mathbf{B}_1 determines the rotation angle, φ , towards the XY-plane. For $\varphi = 90^\circ$, the net magnetic moment has only the transversal component \mathbf{M}_{XY} , located in the XY-plane. When \mathbf{B}_1 is turned off, the spins begin to return to their original equilibrium orientation, realigned to the static magnetic field. During this movement, termed dephasing or transversal relaxation, the precessing protons induce a detectable current flow that can be measured (received) in a coil (antenna) (Goebel, 2007). The current measured in the coil is also known as the free induction decay (FID) and is induced by the exponential decay of \mathbf{M}_{XY} :

$$\mathbf{M}_{XY} = \mathbf{M}_0 e^{-t/T_2^*}. \quad (2.3)$$

According to Eq. (2.3), the value of \mathbf{M}_{XY} depends on the values of \mathbf{M}_0 prior to the RF pulse and decays with the time constant or relaxation time T_2^* . Computation of the value of T_2^*

considers the presence of inhomogeneities in the static magnetic field and in biological tissues. Instead, if no inhomogeneities are considered, FID decays with the time constant T_2 with values in the range of 30 to 150 ms (Goebel, 2007). The relaxation time T_2 corresponds to the required time for \mathbf{M}_{XY} to decay to 37% of its initial value. However, the relaxation time T_2^* makes \mathbf{M}_{XY} decay faster because of the inhomogeneities.

Local field inhomogeneities lead to different precession frequencies, increasing the speed of dephasing. In parallel, local field inhomogeneities also have dependence on the local physiological state, in particular the state of local blood oxygenation. The state of local blood oxygenation itself depends on the state of local neuronal activity. As discussed later, it is an important observation for fMRI, so that measurements of change of the local magnetic field inhomogeneities (T_2^* parameter) provide an indirect measurement of local neuronal activity (Goebel, 2007; Brown and Semelka, 2003).

Besides the dephasing relaxation time T_2 , the longitudinal relaxation time T_1 is associated with the spin realignment to the static magnetic field \mathbf{B}_0 , after \mathbf{B}_1 is turned off. T_1 is defined as the required time for the component \mathbf{M}_Z to be re-established to 63% of the value of \mathbf{M}_0 , and ranges from 300 to 2000 ms (Goebel, 2007). Such a return process follows an exponential growth in accordance with the following expression:

$$\mathbf{M}_Z = \mathbf{M}_0 \left(1 - e^{-t/T_1}\right). \quad (2.4)$$

In addition to FID, another current flow can be measured in the receiver coil, once a 180° RF pulse is applied to reverse the dephasing effect of constant magnetic field inhomogeneities. This causes the dephased protons to flip about the X-axis or the Y-axis in the rotating frame of reference (Fig. 2.8). This reformation of phase induces a voltage named *spin echo* in the coil. In this case, the proton dephasing only occurs through T_2 because the contributors to T_2^* disappear due to the elimination of the inhomogeneities. An additional 180° will generate a second spin echo and so forth, as long as the energy of the signal is large enough. Spin echoes have amplitude smaller than the FID amplitude because of losses due to spin-spin interactions (Goebel, 2007; Brown and Semelka, 2003).

2.2.2 Magnetic resonance image reconstruction

Localisation of NMR signal sources with respect to different regions of the space, and subsequent construction of the MR image, is typically based upon field dependence. It can be

carried out by superimposition of small perturbations on the static magnetic field \mathbf{B}_0 , by magnetic field gradients. This provokes variation of the strength of the total applied magnetic field with the distance from the centre of the magnet. Spins protons exposed to a higher magnetic field precess faster than spins localised more distant from centre of the magnet. In this case, the Larmor frequency, ω_i , of a proton at a position \mathbf{r}_i , is given by Eq. (2.5):

$$\omega_i = \gamma(B_0 + \mathbf{G} \cdot \mathbf{r}_i), \quad (2.5)$$

where \mathbf{G} is a vector that computes the total gradient amplitude and direction (Goebel, 2007; Brown and Semelka, 2003).

The exact proton localisation can be accomplished through the use of three fundamental techniques: selective slice excitation, frequency encoding, and phase encoding. By means of the selective slice excitation, a gradient magnetic field known as the slice selection gradient is used in conjunction with frequency-selective excitation to select a slice of the imaged object. Eq. (2.6) describes the relationship between the slice thickness Δz , the amplitude of the slice selection gradient $\mathbf{G}_{s,z}$, applied along the Z-axis, and the frequencies bandwidth $\Delta\omega_s$, incorporated into the transmitted RF pulse:

$$\Delta\omega_s = \gamma\Delta(G_{s,z} \cdot \Delta z). \quad (2.6)$$

As $\Delta\omega_s$ is fixed, the slice thickness is determined by varying the amplitude of $\mathbf{G}_{s,z}$; therefore, the larger the slice selection gradient, the thinner the slice and vice-versa. A gradient along the the Z-axis will result in an axial slice, a gradient along the X-axis in a saggital slice, and a gradient along the Y-axis in a coronal slice. Oblique slices can be obtained by applying two or three gradients simultaneously. As depicted in Fig. 2.9, each position along the Z-axis has a unique resonance frequency.

Frequency encoding (or readout gradient) consists of a magnetic field gradient applied along one of the two remaining dimensions, while the slice selection gradient is applied to the first spatial dimension. The frequency encoding gradient is not used to selectively excite the protons. Instead, it is used for encoding a spatial dimension for those protons already excited in the slice. The third gradient magnetic field, known as phase encoding gradient, is added to the static magnetic field along the remaining spatial dimension in order to separate signal components originated from different positions along the second dimension in the imaging plane (Goebel, 2007).

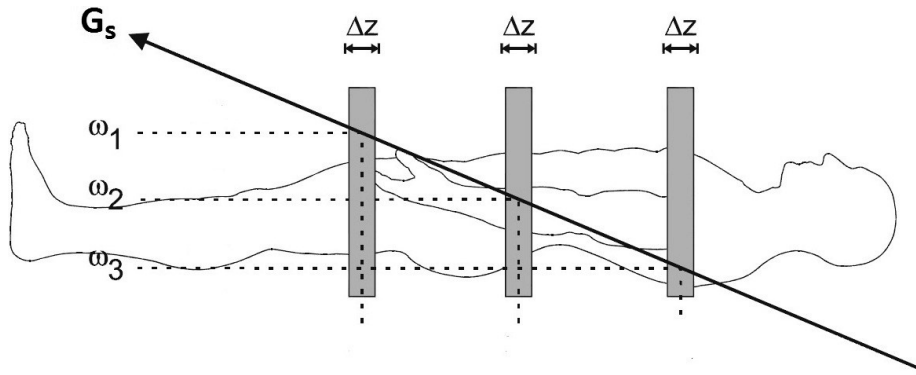


Figure 2.9: Slice selection process along the Z-axis. Adapted from Brown and Semelka (2003).

Not all RF energy is released and cannot be detected outside the body as RF waves. A part is given to the surrounding tissue, called “lattice”. The speed of T_1 recovery is determined by the spin-lattice interactions which are unique for every biological tissue. Hence, tissue-specific T_1 and T_2 values enable MRI to differentiate between types of tissue when properly designed MRI pulse sequences are used (Goebel, 2007). A pulse sequence consists of the combination and application of a 90° RF pulse together with the magnetic field gradients, data sampling periods, and the timing between each of them, which permits the acquisition of the MR image.

As mentioned by Spencer (2015), the most basic pulse sequence for MRI data acquisition is the Gradient Echo sequence, depicted in the scheme of Fig. 2.10a. After a slice being excited by the 90° RF pulse and the gradient slice selection, the spins are refocused along the Z-axis. Next, the phase encode gradient is applied along the Y-axis and the readout gradient along the X-axis. Reversion of the readout gradient gives rise to the spin echo measured in the receiver coil, and then the process of imaging reconstruction can be started. After being sampled, the data are stored in a two-dimensional acquisition matrix called k -space. Figure 2.10b shows the k -space filling according to the Gradient Echo sequence. Each time the pulse sequence of Fig. 2.10a is run, a line of the k -space is filled according to the varying amplitudes of the phase encode gradient lobe. Fourier transformation of the data encoded in the k -space allows the final reconstruction of the two-dimensional image space associated with the examined area. Therefore, magnetic resonance imaging can also be regarded as a frequency and phase map of the protons generated by unique magnetic fields at each point throughout the image (Spencer, 2015; Goebel, 2007; Brown and Semelka, 2003).

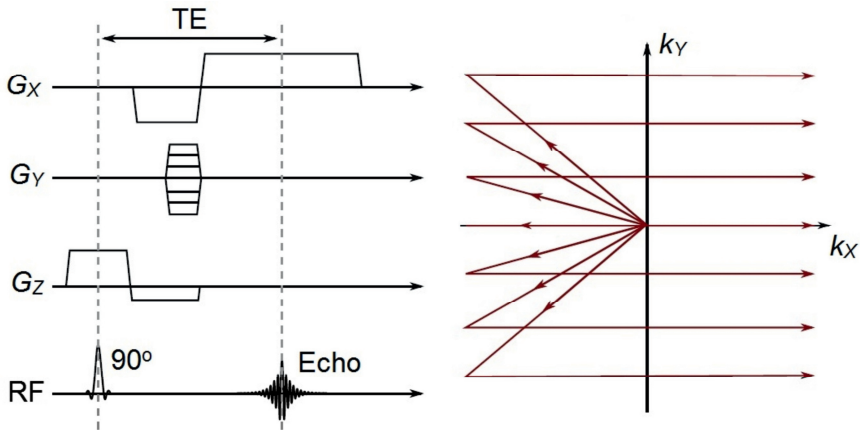


Figure 2.10: (a) Gradient Echo sequence; (b) k-space filling according to Gradient Echo sequence. Adapted from Spencer (2015).

The displayed image is composed by *pixels* (or digital picture elements) that represent volume elements of tissue (or *voxels*). The intensity of a pixel depends on the number of protons contained within the voxel, weighted by the relaxation times T_1 and T_2 for the tissues within the voxel. Regarding the resolution of the MR image, it may be expressed in two ways. The first way is the spatial resolution which may be expressed as the voxel size with units of mm/pixel. In case of 3D images, the spatial resolution can be expressed with a three-dimensional voxel size. The other way is the frequency resolution with units of Hz/pixel (Brown and Semelka, 2003).

The spatial resolution as well as the imaging contrast is influenced by the MRI parameters of a pulse sequence. For instance, among other factors, the image contrast depends upon the repetition time (TR) which is the time between successive applications of the pulse sequence, measured in ms. The slice thickness, measured in mm, influences the amount of energy absorbed by a voxel that generates the MRI signal. Likewise, the echo time (TE) has influence on the time for proton dephasing and the MRI signal amplitudes. TE corresponds to the time between the excitation RF pulse and the centre of the spin echo (see Fig. 2.10a). Proper values of TE are important to obtain a robust BOLD functional MRI contrast, as discussed in the next section. Many particular MRI parameters are determined by the scanner manufacturer and may be modified through the user-interface software (Brown and Semelka, 2003; Spencer, 2015).

2.2.3 Physiological background of fMRI

Enhanced synaptic activity resulting from stimulation of neurons leads to a local increase in energy consumption in functional areas. This physiological process requires the extraction of glucose and oxygen from the blood. After leaving the lungs, the oxygenated blood reaches the heart, and then it is pumped to all tissues of the body including the neuronal tissues. At the level of the capillary bed, the oxygen chemically stored in the blood is transferred to the cells. Then, it returns to the heart through the venous network and reaches the lungs again, where the respiratory cycle is restarted. The transport of oxygen is done in the blood by its chemical connection to the molecule of haemoglobin, Hgb. Thereby, within the arterial network and before getting the tissues, the blood has almost only oxyhaemoglobin (or oxygenated haemoglobin), HgbO_2 . After the extraction of oxygen by the cells, the blood contains a mixture of deoxyhaemoglobin (or deoxygenated haemoglobin) and oxyhaemoglobin (Berne et al., 2003).

The deoxyhaemoglobin has different magnetic properties in comparison with the oxyhaemoglobin: whereas the former is *paramagnetic*, i.e. causes an increase of the static magnetic field, the latter together with the brain tissue are *diamagnetic*, tending to provoke a slight decrease of the static magnetic field. Because more oxygen is transported to the site of activation via an increase of the cerebral blood flow (CBF), it leads to a washout of deoxygenated haemoglobin and an increasing concentration of oxygenated haemoglobin. Because of this, the field inhomogeneities are reduced and the magnetic properties of the blood and the brain tissue become more similar, enabling a stronger MRI signal measured in the site of activation. Thereby, local changes in oxygenated/deoxygenated haemoglobin ratio acts as an endogenous contrast agent, marking the neuronal activation associated with an external stimulus (task) or spontaneous brain activity in the MR image.

The mechanism described above enables the measurements of functional activation of synaptic areas by MRI. This mechanism is also known as blood oxygen level dependence (BOLD) effect, and is the most used technique to perform *functional magnetic resonance imaging (fMRI)* measurements in the human brain (Deichmann et al., 2010; Goebel, 2007). The BOLD effect can be characterised as a time course signal (Fig. 2.11) that represents the contrast associated with the response of the vascular system to the increased demand of energy during activation of synaptic areas.

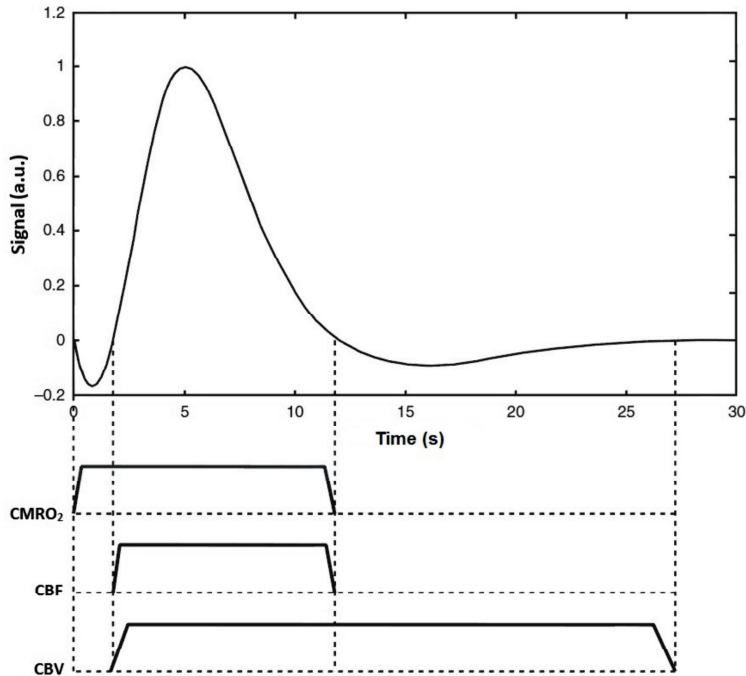


Figure 2.11: Typical BOLD hemodynamic response. It can be characterised as a time course signal that represents the contrast in the MRI image associated with the response of the vascular system to the increased demand of energy. Adapted from Deichmann et al. (2010).

The BOLD effect has dependence on the physiological parameter cerebral blood flow (CBF), and on the cerebral blood volume (CBV) which probably is a mechanical consequence of increased blood flow. Together with CBF and CBV, the cerebral metabolic rate of oxygen consumption (CMRO₂) is another important parameter that influences the BOLD response. As depicted in Fig. 2.11, the typical BOLD signal has a positive response that lasts around 5 to 10 s after an initial slight signal decrease (initial dip). By the remaining time up to 30 s after the onset of the stimulus, there is a signal undershoot. The respective variations of the physiological parameters CMRO₂, CBF, and CBV are also shown (Goebel, 2007; Deichmann et al., 2010; Spencer, 2015).

The physiology behind the BOLD effect is not ultimately understood and a suitable echo time (TE) is important to observe the BOLD contrast. Proper values of TE combined with the strength of the applied magnetic field can be used to enhance the measured BOLD signal. Multiple repeated stimulations also must be performed during fMRI measurements in order to

obtain a robust BOLD signal. To this end, the usage of special pulse sequences sensitive to BOLD such as the echo-planar imaging (EPI) and the spiral k-space filling sequence (SPRLIO) allows obtaining fMRI data with high signal-to-noise ratio (SNR) (Stippich, 2007; Deichmann et al., 2010; Solana et al., 2014).

EPI is the most common and one of the fastest pulse sequence used during fMRI scanning. This characteristic allows acquisition of all slices locations within a single repetition time (TR), thus being advantageous for acquisition of fMRI data (Spencer, 2015). The fMRI data corresponding to the scanned slices is called functional volume or functional 3D image. The repetition time TR of the pulse sequence matches the time of acquisition of a functional volume as well as the time interval separating successive excitations of the same MRI slice in the pulse sequence. Typical values of TR range from hundreds of milliseconds to several seconds. In turn, the time of acquisition of a single slice within TR is in the range of 50 – 150 ms (Brown and Semelka, 2003; Yan et al., 2009; Solana et al., 2014; Sladky et al., 2011).

2.2.4 Use of fMRI for research and clinical purposes

The BOLD signal can be statistically correlated with the chosen stimulation protocol. This enables the identification of those areas of the brain that show hemodynamic changes in synchrony with the task. In the literature, two major areas of research interest and applications in the field of functional magnetic resonance imaging are reported: cognitive neuroscience and medical sciences. In cognitive neurosciences, fMRI is used to understand aspects related to cognitive processes such as awareness, reasoning, learning, and behaviour. In turn, in the area of medical sciences, it is used to localise regions in the brain with clinical relevance. Some examples of application of fMRI are listed below:

- (a) functional neuroanatomy and brain mapping for determination of brain areas specialised for essential tasks (e.g., sensory, motor, and language) and cognitive neuroscience (Hirsch, 2006, Goebel, 2007; Turesky et al., 2018);
- (b) pre-surgical in epilepsy, associated with definition of eloquent cortical areas in epilepsy (Detre, 2004; Krakow, 2006; Kesavadas et al., 2007);
- (c) facilitating the selection of a safe treatment, planning and performing function, and preserving surgery in patients with brain lesion or tumour (Stippich, 2007);
- (d) inference in neuroimaging studies of cognitive processes (D’Esposito, 2006; Larcombe et al., 2018);

- (e) clinical and research application to psychiatry (Yurgelun-Todd et al., 2006; Papoutsis et al., 2018), memory in aging and dementia (Bondi et al., 2005; Saykin and Wishart, 2006; Galvin et al., 2011), pediatrics (Altman and Bernal, 2006; Kesavadas et al., 2007), pain (Davis, 2006), and pharmacology (Salmeron and Stein, 2006).

The high spatial resolution achieved during fMRI enables this imaging method to look in depth into subcortical structures in the order of millimetres. Recent studies have even suggested that intrinsic CBF changes are specific to sub-millimetre functional domains. However, the temporal resolution of fMRI is not considered to be good at all: as hemodynamic responses are sluggish, it is difficult to obtain very high temporal resolution, even if images can be obtained rapidly. Additionally, the exact time of neural activity from hemodynamic responses cannot be obtained easily because hemodynamic response varies depending on vascular structure in different regions of the brain and in different subjects (Kim and Bandettini, 2006).

2.3 Co-registered EEG-fMRI

Simultaneous acquisition of EEG and fMRI data (or co-registered EEG-fMRI) has been pointed out as a powerful and quite promising tool to solve numerous problems in cognitive and clinical neuroscience because of the higher temporal and spatial measurements of the brain activity when compared with the use of both techniques separately. In this way, the added value of co-registered EEG-fMRI is the possibility of employing two complementary brain imaging techniques to solve the EEG inverse problem as well as to augment the fMRI temporal scale by the high temporal resolution of the EEG data simultaneously acquired (Snyder and Raichle, 2010; Goebel and Esposito, 2010; Mulert et al., 2004).

Laufs et al. (2008) highlighted that as fMRI measures the haemodynamic changes associated with synaptic activity and EEG measures the electrical activity of a subset of neurons on the scalp, the exact relationship between such measurements remains to be determined. In this respect, two main perspectives have been adopted to integrate EEG and fMRI data: a) using fMRI to better determine the measured EEG activity; and b) trying to identify the common neural source of both EEG and fMRI signals in a broader sense, as depicted in Fig. 2.12.

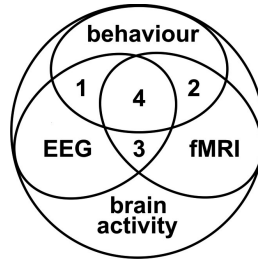


Figure 2.12: Analytical perspective on the integration of electrophysiological and fMRI data. Across all neural processes, only a fraction is reflected by EEG, fMRI, and behaviour. Some neural processes will manifest in EEG and behaviour (1) or fMRI and behaviour (2). Of the neural processes reflected in both EEG and fMRI there may also be measurable behavioural manifestations (4) or not (3). In both cases, 3 and 4, however, the correlation between EEG and fMRI is direct in that there is a common substrate of neural activity. If behaviour is related to neural processes that also manifest in EEG (1) and fMRI (2) independently, yet without being the identical processes at the source of EEG and fMRI effects, this situation can still result in an indirect but meaningful correlation between fMRI and EEG. Simultaneous multi-modal experiments benefit from situations where common neural processes are at the origin of EEG and fMRI signals but the most benefit is derived when these neural processes cannot be monitored by or recalibrated to behaviour (3). The difficulty in using either technique, EEG or fMRI, for predicting or constraining results in the other lies in the uncertainty as to whether one is recording data from situations 3 or 4 or from a joint situation of 1 and 2. In the latter case, prediction and constraint are not justified because the neural processes recorded in the two modalities are non-identical (Laufs et al., 2008).

Because of such characteristics, co-registered EEG-fMRI has attracted the interest of several researchers and clinicians over the past years. Initially, simultaneous application of EEG and fMRI as a multimodal brain activity mapping technique was proposed in studies focused on localisation of epileptic foci, and characterisation of the relationship between epileptic electric activity and hemodynamic response. Recently, it has been used to investigate numerous questions in basic and cognitive neuroscience such as cognitive measures of memory performance, learning capabilities, and resting and sleep (Warach et al., 1996; Seeck et al., 1998; Ritter and Villringer, 2006; Horowitz, 2008 ; Villringer et al., 2010; Snyder and Raichle, 2010; Hauf et al., 2012; Wiest et al., 2015; Jorge et al., 2014; Abreu et al., 2018).

Studies focused on pain research (Iannetti and Mouraux, 2010) and the relationship between the arousal level of a subject and the activation of brain regions in cognitive tasks (Matsuda et al., 2002) have been undertaken using co-registered EEG-fMRI as well. The high spatiotemporal resolution enabled by the co-registered EEG-fMRI has been also allowed a distinct analysis of disturbed brain function in neuropsychiatric diseases like schizophrenia, post-traumatic stress disorder (PSTD) and depression (Razavi et al., 2013; Zotev et al., 2016; Zotev et al., 2018). Other works involving the use of co-registered EEG-fMRI have been concerned with the research of EEG rhythms and ERPs and their relationship with the deoxygenated haemoglobin concentration changes (BOLD-fMRI) (Villringer et al., 2010).

Some exemplary applications of co-registered EEG-fMRI encountered in the literature are summarised in Table 2.1.

Table 2.1: Exemplary applications of co-registered EEG-fMRI encountered in the literature.

Application	References
Characterisation of the relationship between epileptic electric activity and hemodynamic response	Warach et al. (1996); Carmichael et al. (2008); Hauf et al. (2012)
Localisation of epileptic focus	Seeck et al. (1998); Zijlmans et al. (2007); Pittau et al. (2012); Centeno et al., (2016)
Research on memory and memory performance	Meltzer et al. (2007); Michels et al. (2010); Hanslmayr et al. (2012); Bergmann et al. (2012)
Study of learning capabilities and decision-making	de Souza et al. (2013); Bergmann et al. (2012); Frank et al. (2015); PISAURO et al. (2017)
Characterisation of the relationship between the arousal level of a subject and the activation of brain regions in cognitive tasks	Matsuda et al. (2002); Foucher et al. (2004); Mulert et al. (2004)
Characterisation of the relationship between EEG rhythms and the deoxy-Hb concentration changes (BOLD-fMRI)	Foucher et al. (2003); de Munck et al. (2007); Meltzer et al. (2007); Ritter et al. (2009); Hanslmayr et al. (2012)
Relationship between event-related brain activity and the deoxy-Hb concentration changes (BOLD-fMRI)	Portas et al. (2000); Allen et al. (2000); Mulert et al. (2004); Becker et al. (2005)
Research on resting and sleep stage studies	Portas et al. (2000); Fox and Raichle (2007); Horovitz et al. (2008); Dresler et al. (2012)
Study of mood disorders like depression, schizophrenia, and PTSD	Razavi et al. (2013); Zotev et al. (2016); Zotev et al. (2018)
Pain research	Christmann et al. (2007); Roberts et al. (2008); Iannetti and Mouraux (2010)

2.4 The quality of the EEG and fMRI signal during co-registered EEG-fMRI: the problem of artefacts

Parallel to the promising capability of using co-registered EEG-fMRI in neurophysiologic and neurocognitive research, consolidation and enlargement of the range of applications of such

multimodal technique still depends on the enhancement of the quality of the EEG signal acquired simultaneously with the fMRI data. During simultaneous acquisition of the EEG and fMRI, the EEG signal can be corrupted and distorted by three main types of artefacts which are induced by the magnetic fields of the MRI equipment: (i) the gradient or imaging acquisition artefact, caused by the variation of the gradient magnetic fields within the MRI scanner; (ii) the pulse artefact, caused by the pulsatile movement of the blood in scalp arteries within B_0 ; and (iii) the movement artefact, associated with the head subject movements within the static magnetic field (B_0) (Allen et al., 1998; Allen et al., 2000; Ritter et al., 2010; Eichele et al., 2010; Mulert and Hegerl, 2009; Spencer, 2015; Abreu et al., 2018). Each of these three types of artefacts is described below. In the end of the section, a short overview is provided as well about the occurrence of artefacts in the MRI signal due to interferences associated with the EEG system. Other sources of artefact are those related to vibrations associated with the helium pumps, patient ventilation systems, and room lights, which can be induced in the EEG signal even without the influence of MRI magnetic fields. As these other sources of artefact are outside the scope of this thesis, for further information about them, see Ritter et al. (2010) and Abreu et al. (2018).

2.4.1 The gradient artefact

The gradient artefact, also known as image acquisition artefact, provokes complete obscuration of the actual EEG signal, as depicted in Fig. 2.13. Faraday's Law can be used to predict the gradient artefact that results from the induction of an interference voltage $g_i(t)$ in the potential recorded in the scalp (scalp potential) in each EEG electrode, i : $g_i(t)$ is induced by the varying magnetic field \mathbf{B}_g associated with the MRI gradient magnetic fields and RF pulses in the circuit formed by the electrodes, leads, patient, and amplifier (Yan et al., 2009; Spencer, 2015):

$$g_i(t) = -\frac{\partial}{\partial t} \left(\int \mathbf{B}_g \cdot d\mathbf{A} \right). \quad (2.7)$$

In Eq. (2.7), \mathbf{A} represents the area over which the rate of change of the flux of \mathbf{B}_g occurs. As remarked by Yan et al. (2009), it is difficult, however, to apply Eq. (2.7) to the calculation of $g_i(t)$ because in a volume conductor scenario (i.e. applying Maxwell's Laws of electromagnetism in biological tissue) it is not straightforward to define the relevant value of

A . Moreover, the construction of realistic conduction head models is an intricate process that up to now is topic for scientific debate.

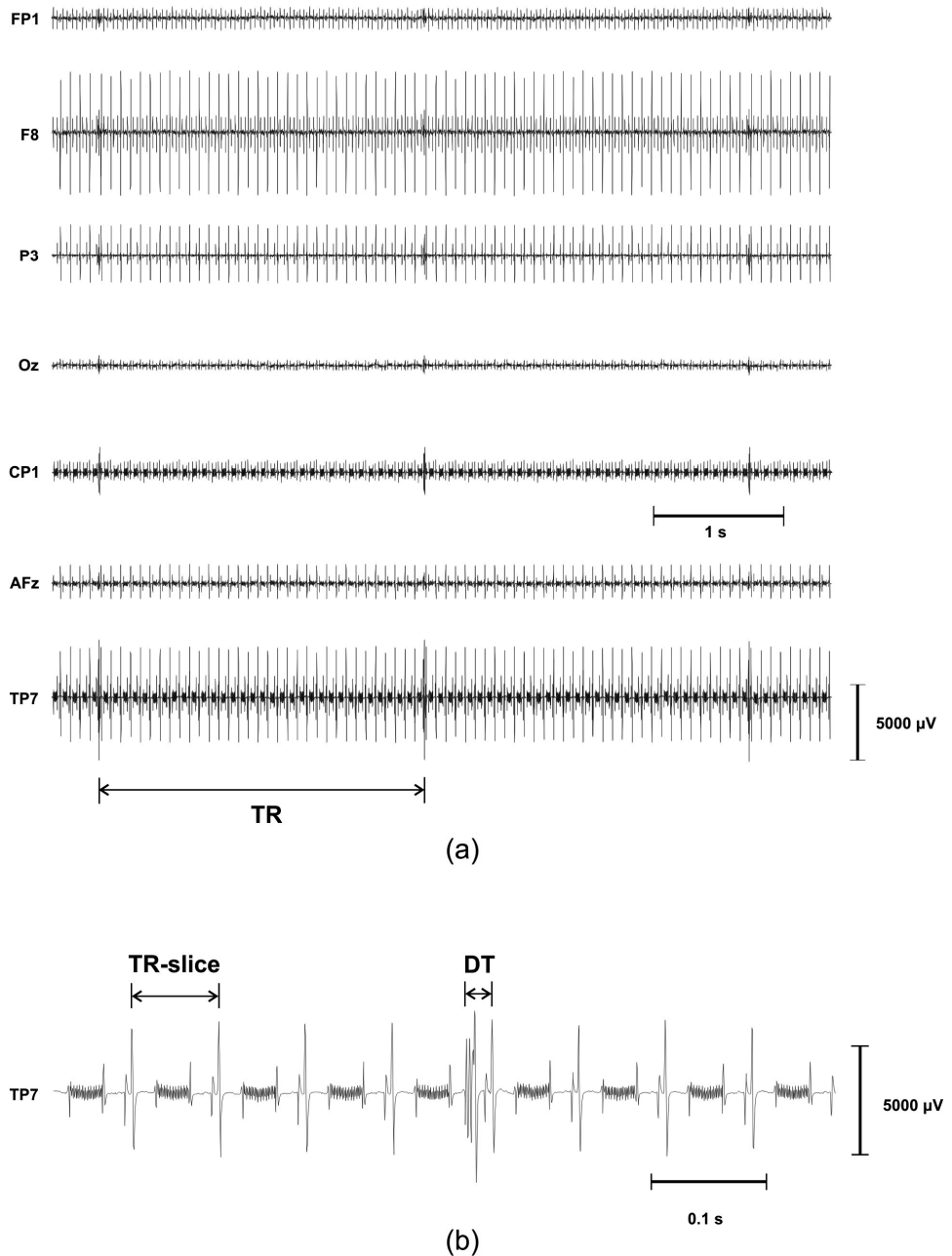


Figure 2.13: (a) Gradient artefact in ongoing scalp potential data. The MRI volume repetition time (TR) is indicated. (b) Zooming in the EEG electrode TP7 of (a) around the middle of the excerpt, showing the MRI slice-time (TR-slice) and the delay time (DT).

As mentioned above, EPI and SPRLIO pulse sequences are used to obtain fMRI data with high signal-to-noise ratio. For each of these techniques, the gradient magnetic fields and RF pulses used in these sequences induce a characteristic gradient artefact waveform in the scalp potential. Although such artefact waveform has different shapes considering the type of MRI pulse sequence used, the onset of the gradient artefact waveform corresponds precisely to the onset of a RF pulse in the measured scalp potential. Thus, the time between consecutive RF pulses (TR) matches the period of the artefact waveform that typically ranges from hundreds of milliseconds to several seconds.

As can be observed in the gradient artefact waveforms in Fig. 2.13, TR comprises the stack of repetitive individual MRI slices. The onset of each slice can be observed as signal peaks in the recorded scalp potential. As also mentioned earlier, the time of acquisition of a single slice (referred to as TR-slice or slice-time) lies in the range of 50 – 150 ms (Anami et al., 2003; Yan et al., 2009; Solana et al., 2014; Sladky et al., 2011). In Fig. 2.13, a delay time (DT) is indicated as well, between the end of the last slice within a certain volume and the onset of the first slice in the subsequent volume. DT occurs in the MRI sequence when it is not possible to switch off some parameters of the MRI scanner such as dynamic stabilisation. Dynamic stabilization makes use of additional RF pulses to measure and correct for any drift in the Larmor frequency caused by local changes in the static magnetic field. These local changes may occur, for example, because of the heating associated with passive shims (Spencer, 2015). The scalp potential excerpts shown in Fig. 2.13 were recorded during continuous (or non-interleaved) fMRI acquisition. The alternative fMRI acquisition method is characterised as periodic or interleaved, when non-scan periods are left for stimulus presentation between volumes (Becker et al., 2005; Eichele et al., 2010).

The amplitudes of the gradient artefact can be several orders of magnitude higher than the EEG signal. Artefact amplitudes associated with the gradient switching (about 10^3 to 10^4 μV) are generally much larger than those arising from RF pulses (up to 10^2 μV). The relative polarity and amplitude of the artefact induced in the EEG recordings varies across channels, mainly due to relative position of the EEG electrodes in the gradient magnetic fields, the corresponding electromagnetic coupling, and the permittivity associated with electrodes, leads, and patient. Another important characteristic of the gradient artefact is that it generates fast signal slopes (first derivative) in the order of 10^4 $\mu\text{V}/\text{ms}$ (Allen et al., 2000; Anami et al., 2003; Ritter et al., 2010; Eichele et al., 2010).

Regarding the frequency contents of the gradient artefact, discrete harmonic spectral lines arise at frequency intervals (or “frequency bins”) whose fundamental matches the multiples of the slice repetition frequency ($1/\text{TR}$ -slice). This feature can be observed in the power spectra of Fig. 2.14a around multiples of 20 Hz, and in Fig. 2.14b around multiples of 15.8 Hz. When the fMRI data is recorded with interleaved scan periods between volume acquisitions or in case of the occurrence of the delay time (DT), harmonics in the frequency range of the volume repetition frequency ($1/\text{TR}$) appear convolved with the harmonics bins of the slice repetition frequency, as also depicted in Fig. 2.14b (Anami et al., 2003; Niazy et al., 2005; Mandelkow et al., 2006; Mandelkow et al., 2010; Solana et al., 2014).

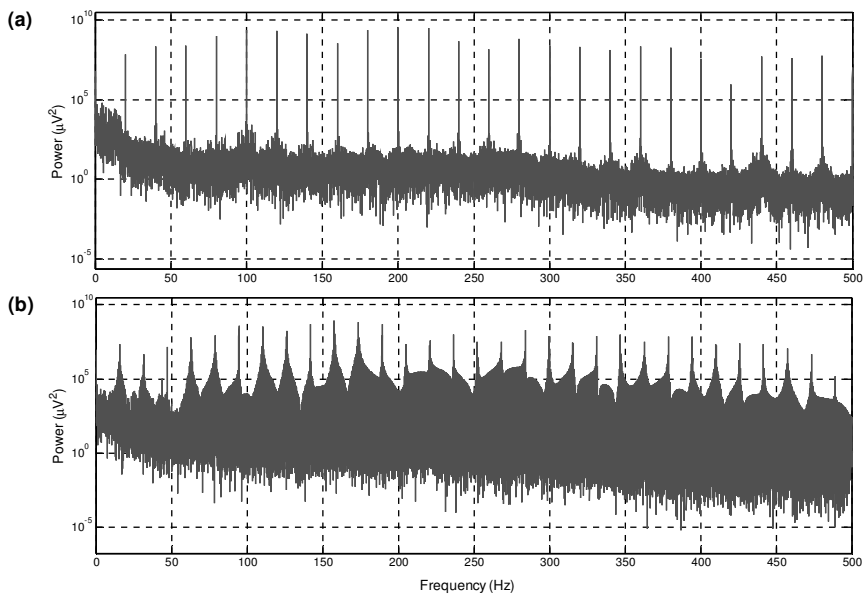


Figure 2.14: Power spectra of two scalp potential signals recorded during continuous fMRI acquisition. Harmonic artefact intervals (bins) corresponding to the slice repetition frequency ($1/\text{TR}$ -slice) can be observed in (a) around multiples of multiples of 20 Hz; and in (b) around multiples of 15.8 Hz. Additionally, the spectrum depicted in (b) contains harmonics of the volume repetition frequency ($1/\text{TR}$) convolved with the harmonic artefact bins associated with $1/\text{TR}$ -slice because of the occurrence of DT in the scalp potential recordings.

Although actual EEG frequencies below the first frequency bin associated with $1/\text{TR}$ -slice may be well preserved from the gradient artefact interference (Bagshaw and Bénar, 2010), an important feature of the gradient artefact is the broadening of the artefact spectral lines caused by small micro-movements, as described by Spencer (2015). Those tiny movements of the subject within the MRI scanner provoke random variations in the amplitude of the gradient artefact components. Conceptually, this can be similar to a random amplitude modulation. As

a result, spectral components of the gradient artefact are broadened, especially in higher-frequency spectral bins. Broadening of the gradient artefact spectral lines is the main cause of the partial failure of most gradient artefact correction methods, and is deeper detailed in Section 2.4.3.

In addition to the fMRI spectral signatures depicted in Fig. 2.14, the bandwidth of the actual EEG is exceeded by high-frequency artefact components associated with the readout gradient that typically lies in the range of 500 – 900 Hz; and overlapped by frequency components associated with RF pulses. Although RF emissions are in the order of tens of MHz, artefacts with smaller frequencies about 175 and 350 Hz can be caused by RF pulses in the scalp potential as well (Hoffmann et al., 2000). According to Anami et al. (2003), this seems to be attributable to the fact that the induced current caused by RF pulses is based on electrostatic or electromagnetic coupling. In this way, this current is supposed to be caused by a demodulation effect in the non-linear parts in the hardware system into the lower-frequency artefact within an EEG amplifier frequency range.

2.4.2 The pulse artefact

The fundamental cause of the pulse artefact, $p_i(t)$ – also referred to as ballistocardiogram or BCG artefact – is associated with the physical principle of the electromagnetism which states that an electromagnetic induction is generated whenever electrical current flows in a static magnetic field. In case of co-registered EEG-fMRI, the pulsatile blood flowing in the scalp vessels acts such as an electrical current, and its interaction with the MRI static magnetic field B_0 induces the pulse artefact in the EEG signal (Allen, 2010). Therefore, since it is caused by the static magnetic field B_0 , the pulse artefact is visible on the EEG signal recorded inside the MRI scanner even in the absence of gradient switching.

Some possible mechanisms of pulse artefact generation have been suggested in the literature. Amongst them, three mechanisms are the most plausible pulse artefact sources (Yan et al., 2010): (i) voltages induced by rotation of the head in the magnetic field, which is driven by the momentum changes of blood as it is pumped by the heart and shunted into arteries in the head; (ii) the pulsatile blood flow in superficial arteries that gives rise to potential variation at the surface of the scalp; and (iii) voltages generated by head movement associated with pulse driven expansion of the scalp. According to the findings of Yan et al. (2010), head rotation is

likely to be the dominant source of the PA, although contributions from scalp expansion and blood flow in superficial arteries cannot be neglected.

Figure 2.15 depicts EEG excerpts containing the pulse artefact. The pulse artefact contributes with amplitudes in the order of $50 \mu\text{V}$ (at 1.5 T) and $200 \mu\text{V}$ (at 3 T), and frequencies close to the range of the ECG signal. As can be observed in Fig. 2.15, it possesses resemblance to epileptic spikes and its feature is synchronised with the ECG signal recorded simultaneously with the EEG data, following the fluctuations of the heart rate (Debener et al., 2007; Debener et al., 2010; Eichele et al., 2010). The peak of the artefact in the EEG occurs with a time delay relatively to the R-peak in the ECG. The onset of the pulse artefact approximately corresponds to the onset of the systole, i.e. the onset of the blood ejection phase. The artefact polarity and amplitude can vary across individuals EEG electrodes (Fig. 2.15). This variation is observed for different types of MRI scanners as well.

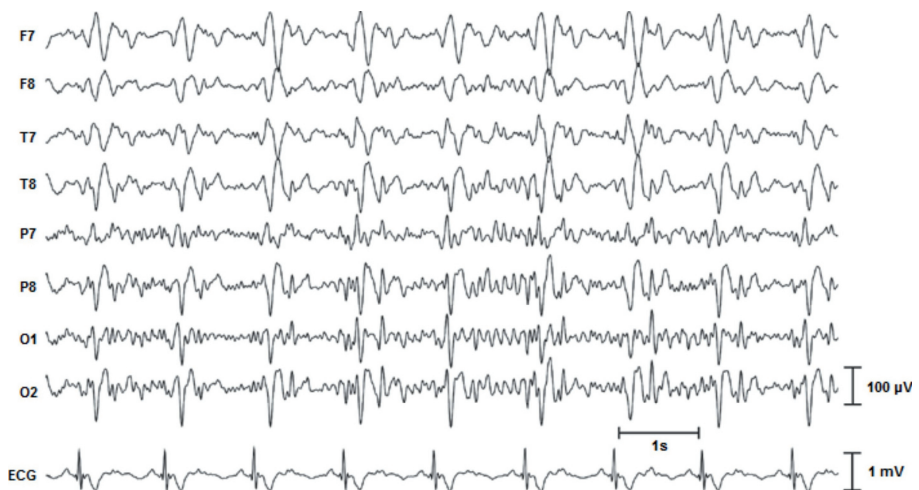


Figure 2.15: Pulse artefact in ongoing EEG data. Adapted from Debener et al. (2010).

The EEG signal recorded in electrodes far from the EEG reference electrode expresses larger pulse artefact amplitudes, and a high-field MRI scanner causes larger pulse artefact amplitudes than a scanner with a lower field (Debener et al., 2010; Eichele et al., 2010).

2.4.3 The movement artefact

When the head of the subject moves within the scanner during simultaneous EEG-fMRI data acquisition, the geometry of electrodes and cables in the static magnetic field is changed,

inducing a transient electromotive force which affects the amplitude and the topography of both gradient artefact and pulse artefact. The alterations introduced by such a transient are termed movement or motion artefact. The strength of the transient voltage varies across the EEG channels according to a number of factors, like the strength of the static magnetic field B_0 , the amount of motion, the velocity, and the conductive loop area (Moosmann et al., 2009; Sun and Hinrichs, 2009; Mullinger et al., 2011; Eichele et al., 2010; Laufs et al., 2008; Chowdhury et al., 2014; Maziero et al., 2016; Daniel et al., 2019).

To prevent the occurrence of this transient voltage, some procedures have been adopted to stabilise the subject head, such as the use of a vacuum cushion or pillow; and to fix EEG device and wires by using sandbags (Anami et al., 2002; Bénar et al., 2003; Ritter et al., 2010). In addition to the movement artefact, two types of vibration-induced motion can induce transients in the EEG signal. Vibration-induced motion can be related to the MRI scanner cryogen pump, a problem that could be bypassed by transiently switching off the cooling system. Vibration can also be caused by the gradient switching itself, which cannot be fully avoided.

The alterations in the gradient artefact waveform caused by the movement artefact may compromise the performance of most gradient artefact correction strategies because they are based upon the assumption of constant nature of the artefact waveform, as discussed in Chapter 3. Thereby, the quality of the gradient artefact-corrected EEG may be compromised by the endogenous and inevitable movement artefact induced by subtle head motions (referred to as “micro-movements”) and related to respiration as well. In case of the occurrence of large signal transients caused by abrupt subject head motions, the EEG signal may even be corrupted beyond recovery (Spencer, 2015; Sun and Hinrichs, 2009; Mullinger et al., 2011; Eichele et al., 2010).

2.4.3.1 Micro-movements of the subject head and broadening of gradient artefact spectral lines

As mentioned above, to redress the occurrence of the movement artefact, $m_i(t)$, the use of a head vacuum cushion has been proposed in such a way as to prevent the influence of subject head movements over $s_i(t)$ and, in consequence, on the morphology of the gradient artefact waveform (Anami et al., 2002; Ritter et al., 2010). By using such a procedure, it is possible to avoid the occurrence of greater head motions, thus obtaining a gradient artefact waveform

more reproducible and stationary, characteristic on which most of post-processing gradient artefact correction methods rely. However, as remarked by Spencer (2015), small head micro-movements cannot be cancelled out when using head vacuum cushions even with the most cooperative subjects. This endogenous and inevitable influence of subtle head tiny movements is related to respiration and small movements of the subject head (Eichele et al., 2010).

Those tiny movements provoke random variations in the amplitude of the gradient artefact components, which conceptually can be similar to a random amplitude modulation. As a result, spectral components of the gradient artefact are broadened, especially in higher-frequency spectral bins associated to the slice repetition frequency ($1/\text{TR-slice}$). To explain the random modulation in the amplitude of gradient artefact components owing to head micro-movements, Spencer (2015) has used the model for the scalp potential of Eq. (2.8):

$$s_i(t) = [a + C(t)]g_i(t), \quad (2.8)$$

where $s_i(t)$ is the scalp potential recorded in the electrode i ; a is a scaling factor which depends upon the position of the EEG leads and the shape of the volume conductor, thus varying with respect to the conductive paths generated by the subject head and EEG leads relative to the magnetic field gradients; $C(t)$ is a zero mean, random process associated with the influence of the micro-movements of the subject head; and $g_i(t)$ is the gradient artefact. For the sake of simplicity, the component $e_i(t)$ of $s_i(t)$ associated with the actual EEG signal corresponding to the electrode i has been neglected in Eq. (2.8) (Spencer, 2015). Thus, the power spectrum of $s_i(t)$ can be estimated by calculating the autocorrelation function R_s from Eq. (2.8):

$$R_s(k) = a^2 R_g(k) + R_C(k)R_g(k). \quad (2.9)$$

To calculate $R_g(k)$ and $R_C(k)$, the following assumptions have been made:

- (i) $R_g(k)$ is periodic, real, and even because of the characteristics of the gradient artefact $g_i(t)$. Thus, it can be written as a combination of l cosine waves:

$$R_g(k) = \sum_l g_{i,l} \cos(l\omega_f k), \quad (2.10)$$

where

$$\omega_f = \frac{2\pi}{\text{TR-slice}}. \quad (2.11)$$

(ii) $C(t)$ is stationary in wide-sense, in such a way that an autoregressive model of the white Gaussian noise $U(t)$ with variance σ_U^2 would be its simplest representation:

$$C(t) = \sum_{l=0}^{\infty} \rho^l U(t-k), \quad (2.12)$$

with $\rho < 1$. Thus, R_C can be estimated as:

$$R_C(k) = \frac{\sigma_U^2}{1-\rho^2} e^{|k|\ln \rho}. \quad (2.13)$$

Replacing Eqs. (2.10) and Eq. (2.13) in Eq. (2.9), and applying the Fourier transform, the power spectrum $S_i(\omega)$ of $s_i(t)$ is then calculated as:

$$S_i(\omega) = \frac{2\pi\sigma_U^2}{1-\rho^2} \sum_l g_{i,l} \left[\frac{\ln \rho}{(\ln \rho)^2 + (\omega + l\omega_f)^2} + \frac{\ln \rho}{(\ln \rho)^2 + (\omega - l\omega_f)^2} \right]. \quad (2.14)$$

As indicated in the equation above, the power spectrum $S_i(\omega)$ consists of a summation of Lorentzians centred at frequencies multiples of ω_f , whose amplitudes are dependent upon the magnitude of the frequency component around which they are centred (Spencer, 2015). Therefore, according to Eq. (2.14), the effect of the component $C(t)$ in Eq. (2.9) is to provoke the broadening of the l gradient artefact harmonics with fundamental frequency at ω_f , which constitutes the artefact frequency bins associated with TR-slice (see Section 2.4.1).

Thereby, the influence of the micro-movements of the subject head on broadening of the gradient artefact spectral lines as indicated in Eq. (2.14) should be predicted by any approach designed to correct the gradient artefact. Otherwise, this broadening effect may give rise to

residual artefacts in the estimate of the corrected EEG, $\hat{e}_i(t)$. As discussed in Chapter 3, this fact helps to explain why the established average artefact subtraction (AAS) and other gradient artefact correction methods are not able to effectively suppress the gradient artefact from the EEG recordings (Spencer, 2015).

2.4.3.2 Abrupt head movements and their effect on the morphology of the gradient artefact

The morphology of the gradient artefact waveform along the recorded scalp potential may be profoundly altered because of the occurrence of head movements that are beyond certain amplitude, rather than the micro-movements discussed in the previous section. Such alterations (hereafter called *abrupt head movements*) can be observed as two different components or variants. The first variant is observed when the subject makes a small change in position during acquisition of a certain volume N_1 , so that the shape of the gradient artefact waveform changes over time (Spencer, 2015; Maziero et al., 2016; Moosmann et al., 2009):

$$s_i(t) = \begin{cases} e_i(t) + g_{i,1}(t), & \text{if } t < t_1 \\ e_i(t) + g_{i,2}(t), & \text{if } t \geq t_1 \end{cases}, \quad (2.15)$$

where $e_i(t)$ corresponds to the EEG component in $s_i(t)$; and $g_{i,1}(t)$ and $g_{i,2}(t)$ correspond, respectively, to the gradient artefact before and after the position change of the subject head at time t_1 within the volume N_1 . This effect may also compromise the performance of the gradient artefact correction methods based upon subtraction of an average artefact template because the artefact template cannot characterise individual occurrences of the artefact waveform over time (Spencer, 2015; Yan et al., 2009).

The second variant of abrupt head movements occurs when the subject makes a large change in position, which results in signal transients that are slowly and continuously inserted in $s_i(t)$ (Spencer, 2015):

$$s_i(t) = e_i(t) + g_i(t) + m_{tr}(t), \quad (2.16)$$

where $m_{tr}(t)$ represents the large signal transients. Additionally, over a certain amplitude and faster occurrence over time, $m_{tr}(t)$ may be likened to the superposition of an impulse signal, $\delta_{tr}(t)$, in the scalp potential:

$$s_i(t) = e_i(t) + g_i(t) + \delta_{tr}(t). \quad (2.17)$$

A deeper discussion about the effect of these components of the movement artefact under the occurrence of abrupt head movements over the quality of the gradient artefact-corrected EEG is provided in Chapter 8.

2.4.4 Artefacts in the MR image due to the EEG system

The effects of the EEG equipment on the fMRI data quality are more subtle in comparison with the artefacts induced in the EEG recordings during co-registered EEG-fMRI (Mullinger and Bowtell, 2010; Abreu et al., 2018). As remarked by Carmichael (2010), the overall effect of the introduction of an EEG system in the fMRI scanner is a reduction in the signal-to-noise ratio (SNR) of the MRI signal. In particular, the presence of an EEG system can interact with the static magnetic field (B_0) and varying magnetic fields of the MRI equipment, which can have a subsequent impact on the image quality.

If the lead wires, electrodes, or conductive gel of the EEG system have a significantly different magnetic susceptibility from the tissues of the head, unwanted magnetic field inhomogeneity are induced in the static magnetic field. Such B_0 -inhomogeneities may cause image distortion as well as result in local signal loss (Mullinger and Bowtell, 2010). The latter effect causes increased loading of the RF coil used for signal reception and a reduction in the global SNR of the MRI data, as a consequence. The extent of signal drop-out and image distortion resulting from magnetic susceptibility effects depends on how greatly the magnetic susceptibilities of the materials used differ. Hence, provided that the materials used for EEG electrodes and gel are carefully chosen and tested, there is only a small increase in B_0 -inhomogeneity within the human brain, which limits the impact on image quality (Carmichael, 2010; Mullinger and Bowtell, 2010).

In turn, degradation of MR images due to interactions with the EEG hardware is related to the B_1 -homogeneity induced as external RF interference. Corruption of MRI data sets occurs whenever interfering spurious RF signals at, or close to, the Larmor frequency reach the RF coil. Sources of interference can include radio stations, electrical motors, electrical lighting, and computers. Interference from such external sources is normally prevented from reaching the RF coil by sitting the scanner inside a RF shielded room. Likewise, electrical devices such as EEG amplifiers sited close to the subject can also generate RF interference (Mullinger and Bowtell, 2010).

MRI-compatible EEG systems have been developed and employ fiber-optic cables to transfer data from the EEG amplifier, placed inside the shielded room in which the scanner is, to a recording system placed outside. Thus, this prevents transmission of externally generated RF interference into the shielded room, and has also the advantage of electrically isolating the subject from the EEG recording system. In addition, a high degree of RF screening of the EEG amplifier, along with the incorporation of RF filters, is used to prevent any interference generated by the amplifier electronics from reaching the RF coil (Mullinger and Bowtell, 2010; Carmichael, 2010). Further analysis has shown the electrodes of the conventional 64 EEG system generally have very little effect on the B_1 -homogeneity.

However, the longer copper leads used to connect to the ECG and EOG electrodes on one commercially available EEG cap were shown to cause significant B_1 -homogeneity. In consequence, signal loss has been observed in the areas of the brain directly beneath the wires (Mullinger and Bowtell, 2010). In parallel, effects of high density EEG systems on the quality of the (f)MRI signal have been also reported (Luo and Glover, 2012; Klein et al., 2015). As remarked by Luo and Glover (2012), high density EEG systems with 128 and 256 channels have become available and increasingly used in EEG-fMRI experiments because they permit to provide higher spatial resolution on recording the scalp EEG, and thus might improve the accuracy of the cortical response localisation. However, the presence of more metallic conduction wires in the high density EEG cap can produce a strong electromagnetic shielding effect in the areas near the conducting wires. This may result in large decrease of the anatomic MRI signal (about 40%) when the EEG cap is used, in comparison with a scenario without the EEG cap (Luo and Glover, 2012). Moreover, a significant and consistently higher value of the SNR for both the structural (spatial SNR) and functional (temporal SNR) images can be achieved when the subject is not wearing the EEG cap (Klein et al., 2015). A high density EEG cap can also lead to B_0 and B_1 -homogeneities, thus showing that the EEG cap has a negative impact on both the static magnetic field and the radio frequency (RF) pulse (Klein et al., 2015, Mullinger et al., 2008a).

CHAPTER 3

Gradient Artefact Suppression and Correction Evaluation**3.1 Abstract**

Over the past years, the promising capability of using co-registered EEG-fMRI in neurocognitive research and correlated studies has attracted the interest of a large number of neuroscientists and clinicians. However, additional work remains to be done in order to improve the quality of the EEG signal, especially concerning the occurrence of artefacts. Artefacts induced by the magnetic fields of the MRI scanner, in particular the gradient artefact, may corrupt the EEG data and make it difficult to obtain an effective artefact correction together with an adequate preservation of the neuronal EEG. Although several correction approaches have been devised for suppression of the gradient artefact, their improvement and development of novel correction methods are required to enhance the quality of the corrected EEG signal, mainly regarding the access of higher-frequencies in the EEG gamma band and above. In this chapter, we make a review of the existing methodologies proposed for correction of the gradient artefact. In parallel, we present an overview of the usual methods employed to evaluate the gradient artefact correction performance. To date, this kind of assessment has been seldom performed systematically or consistently, in part due to the difficulties associated with the stochastic and non-stationary nature of the neuronal EEG. Because of this, in many EEG-fMRI studies the quality of the artefact-corrected EEG is assessed by visual inspection only. Moreover, generalisation of the correction results for different types of EEG data has been poorly made as well. Thereby, we propose in this chapter a simple and effective method for assessment of the preservation of the EEG signal, which is capable of accounting for the stochastic and non-stationary nature of the neuronal EEG. A short review of the existing approaches to correct the pulse artefact is also provided.

3.2 Introduction

The promising capability of revealing new insights in neurocognitive studies has attracted the interest of several researchers and clinicians to co-registered EEG-fMRI in recent years, mainly due to the possibility of integrating the high temporal resolution of the EEG with the high spatial resolution of fMRI (Villringer et al., 2010; Pan et al., 2011). Nonetheless, consolidation and broadening of the range of applications of EEG-fMRI still depend on enhancement of the quality of the EEG signal, in particular regarding the occurrence of the gradient artefact, such as depicted in Fig. 3.1:

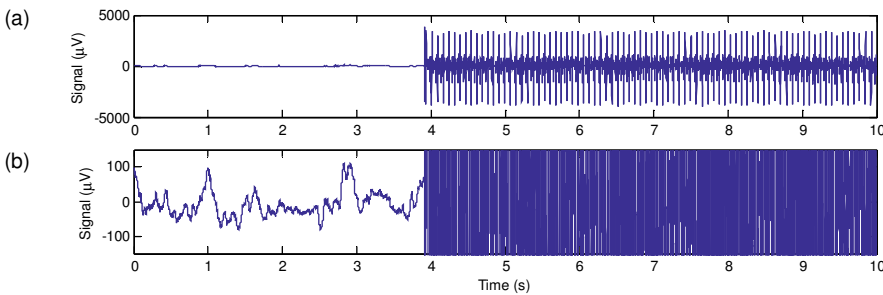


Figure 3.1: (a) Scalp potential recording (electrode position F8) showing the occurrence of the gradient artefact, starting about 3.9 s; (b) zooming in the signal-axis of (a), highlighting the amplitude of the EEG signal in comparison with the amplitude of the gradient artefact.

The signal picked up by each electrode i of a set of scalp electrodes leads to recording of the analogue scalp potential, $a_i(t)$. Such analogue input of the recording system represents the voltage difference across one or two “active” electrodes and one reference electrode. The difference between these two setups is that differential amplifiers are used to minimise the common mode components in the electrical potential difference when two electrodes are used.

Before being displayed, as shown in Fig. 3.1, $a_i(t)$ is first amplified, filtered, and digitised by the recording hardware. Depending on the age/generation of the EEG recording equipment, the amplitude resolution of the used A/D converters varies: 12 and 16 bit systems are still in use (meant for only EEG), but most modern systems are either 24 or 32 bit. The sampling frequency, f_s , usually is the same for all channels in one recording device; this means that the measured signal with the highest upper bandwidth limit determines f_s for all channels. Low-pass (LP) filtering is used at least at the desired Nyquist frequency, and high-pass filtering (HP) is often utilised to suppress direct current (DC) and very slow electrode drift

components. The MRI magnetic field gradients and RF pulse that induce the gradient artefact have frequency characteristics that largely exceed the bandwidth of the neuronal EEG, as described in Section 2.4.1. Thereby, in EEG and fMRI data co-registration it is important to employ an analogue band limiting filter in the signal path of the EEG system to attenuate the energy associated with artefact high-frequency activity as well as to prevent aliasing effects of artefactual components in the measured $a_i(t)$. To this end, an analogue low-pass filtering typically with cut-off frequency 250 Hz is normally utilised to attenuate the artefact by at least a factor of ten (Mullinger et al., 2011; Gutberlet, 2010; Anami et al., 2003).

The digitised and pre-filtered version of $a_i(t)$ will be referred to as $s_i(t)$ to avoid confusion with the unfiltered, raw analogue scalp potential. Although we in fact deal with digitised signals that consist of discrete time series of the analogue signal $a_i(t)$, in this chapter we will stick the time-continuous notation for the various signals and signal-components in the signal processing models (rather than discrete time-signals). This is done because not all components in our models are (or can be) sensed/digitised explicitly, and sometimes indirect measures on the different components of the measured signals are available at different sampling rates.

When the scalp potentials fluctuation can mainly be ascribed to intracranial bioelectrical ionic currents, $s_i(t)$ is usually approximated as being the actual (neuronal) EEG signal, $e_i(t)$:

$$s_i(t) = e_i(t). \quad (3.1)$$

As mentioned in Section 2.1, the actual EEG consists of a non-stationary, coloured stochastic signal with limited bandwidth. When recorded with no controlled conditions, $e_i(t)$ is characterised as a spontaneous ongoing activity of the brain, the spontaneous EEG. In addition to this spontaneous EEG activity, low signal amplitude responses related to identifiable nervous system events such as electrical stimulation, initiation of movement, and certain thought processes can also be measured in the scalp potential as hidden responses in the spontaneous EEG. These responses are called event-related potentials (ERPs) and have quite lower amplitude in comparison with the spontaneous EEG. A particular instance of ERPs is the evoked potentials (EPs) that can be defined as the response of the nervous system when an external stimulus (light, sound, electrical) is applied to the subject. Auditory evoked potentials (AEPs) and visual evoked potentials (VEPs) are commonly used modalities of EPs corresponding, respectively, to the evoked potentials by light and sound stimuli. The main

difference between ERPs and EPs lies in the application area: the use of ERPs is mostly concerned with neurocognitive research, whereas EPs are extensively used for diagnostic and monitoring purposes in clinical routine (Rangayyan, 2002; Sanei and Chambers, 2007; Sörnmo and Laguna, 2005; Cluitmans, 2010). ERPs and EPs typically are identified by averaging epochs of the measured signal which are time-locked to the event or stimulus. The typical amplitude and frequency contents associated with the actual EEG are indicated in Table 3.1.

Table 3.1: Typical amplitude and frequency contents associated with the actual EEG.

Actual EEG ($e_i(t)$)	Condition	Clinical		Research	
		Amplitude range (μV)	Frequency range (Hz)	Amplitude range (μV)	Frequency range (Hz)
Spontaneous EEG peak-to- peak (20 s)	Non-epilepsy	10 – 150	0.5 – 45	10 – 100	0.01 – 150
	True epileptic seizures (not psychogenic)	10 – 250	0.5 – 120	10 – 200	0.5 – 150
	Coma/brain death	< 2	0 – 20	Not available	Not available
Auditory Evoked Potentials	All	0.5 – 1.0	20 – 5000	0.5 – 1.0	20 – 5000
Visual Evoked Potentials	All	0.5 – 2	10 – 100	0.5 – 2	10 – 100
Event Related Potentials	All	0.5 – 5	0.01 – 150	0.5 – 5	0.01 – 150

Because the scalp potential may also be affected by disturbances from other physiological current sources $q_i(t)$, such as the ECG, the EMG, and the EOG signal, Eq. (3.1) cannot be used as a general model to describe $s_i(t)$. Moreover, electrical potential fluctuations across the scalp caused by electrochemical disturbances in the electrode-skin junction, the so-called movement-electrochemical artefact, $m_i(t)$, may affect $s_i(t)$ as well. Thereby, $q_i(t)$ and $m_i(t)$ must be included in Eq. (3.1), resulting in:

$$s_i(t) = e_i(t) + q_i(t) + m_i(t). \quad (3.2)$$

During co-registered EEG-fMRI, $s_i(t)$ may further be obscured by the other sources of disturbance indicated in Section 2.4:

- a) Voltage differences across the scalp caused by the time-varying magnetic field gradients and RF pulses during the scanning process. The gradient artefact, $g_i(t)$, is the most severe and obscure all other components in the measured electrode signals.

- b) Voltage differences across scalp electrodes caused by inductive currents (Hall Effect) through loops of blood vessels within and around the skull and the cables that connect the electrodes with the measurement equipment. Those loops have strong inductive properties due to the conductive nature of blood and the measurement cables that consequently can be regarded as “coils”. The natural mechanical pulsations in the arteries and arterioles cause changes in the inductive properties of those loops that to a great extent (but not always exactly) are synchronised with heart rate. This in fact is an interaction between the MRI static magnetic field B_0 and the dynamic-biological changes in the electromagnetic properties of the tissue within the magnet. These cause the so-called pulse artefact, $p_i(t)$. Although this artefact is less severe in terms of amplitude characteristics when compared to $g_i(t)$, it is more difficult to handle because there are many biological and physiological variables that determine its characteristics (Allen et al., 1998; Debener et al., 2010).
- c) Voltage fluctuations due to temporary changes in the electromagnetic electrode-scalp characteristics due to movements within the magnet. These fluctuations correspond to $m_i(t)$, described above. Within an MRI environment, however, movements of the subject head also introduce (temporary) changes in the electromagnetic coupling between scalp measurement circuits and the static MRI field B_0 (Yan et al., 2009; Spencer, 2015).

Therefore, taking into account the MRI sources of interferences, Eq. (3.2) results in the extended model depicted in Fig. 3.2. Or in formula:

$$s_i(t) = e_i(t) + q_i(t) + m_i(t) + p_i(t) + g_i(t). \quad (3.3)$$

To estimate $e_i(t)$ from $s_i(t)$, the usual approach is to neglect at least one and, most of the times, two or more artefact components. In the current framework, this can be easily done by zeroing the components not taken into consideration. Therefore, under the assumption of independent artefact sources, this means that any reconstruction algorithm also aims at preserving the neglected artefacts. Hence, they must be removed separately to estimate $e_i(t)$. This is the usual approximation regarding gradient artefact methodologies to correct $g_i(t)$ (Ritter et al., 2010).

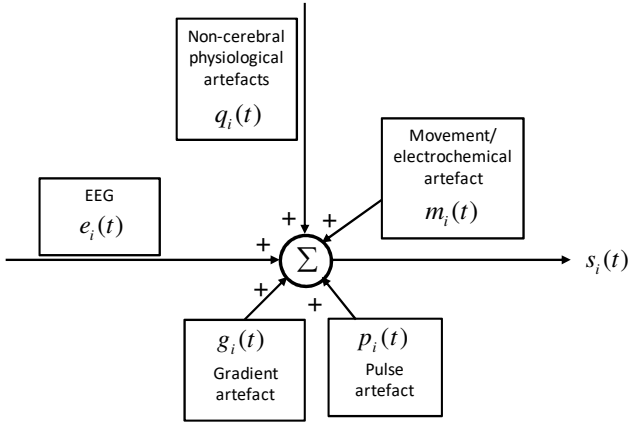


Figure 3.2: General model for the sources of the measured signal $s_i(t)$ during co-registered EEG-fMRI.

However, the effect of one artefact interference source over another should be taken into consideration if the assumption of independence between the artefact sources is not valid. It is the case of the influence of the movement artefact over the gradient artefact, when micro-movements of the head as well as abrupt movements cannot be neglected. In these scenarios, specific models must be used to account for such an influence (Spencer, 2015), as discussed in Chapters 6 and 8.

After carrying out the suppression of $g_i(t)$, the gradient artefact correction methodologies should have their performance evaluated in order to obtain a measure of both artefact reduction and degree of preservation of the actual EEG signal in $\hat{e}_i(t)$. Although some approaches have been proposed to this end, to date a consistent or systematic evaluation has been seldom performed (Ritter et al., 2007; Ritter et al., 2010; Freyer et al., 2009). In Section 3.5, we provide an overview and critical analysis of the existing approaches for evaluation of the gradient artefact correction methods. Next, in Section 3.6, we describe and propose a systematic procedure for evaluation of gradient artefact correction methods, which has been used in the current thesis.

In the following sections, we provide a review of the existing methodologies to correct the gradient artefact (Section 3.3), and a brief overview of the existing approaches to attenuate the pulse artefact (Section 3.4).

3.3 Overview of the existing methods for gradient artefact correction

3.3.1 Artefact attenuation at the source

In the literature, a number of approaches have been suggested to minimise the inductive effects of the gradient artefact at the source. For instance, minimisation of the conductor loop area can be used to reduce the artefact amplitude, which can be implemented by laying out and immobilising the EEG leads, twisting leads, and using a bipolar electrode configuration (Mullinger et al., 2014; Goldman et al., 2000; Bénar et al., 2003; Ritter et al., 2010; Chowdhury et al., 2015). Mullinger et al. (2011) described a positioning adjustment procedure of the subject within the MRI scanner which results in reduced amplitude of the gradient artefact. According to this study, up to 40% of the gradient artefact amplitude can be attenuated by axially positioning the subjects, so that the nasion is shifted from the scanner iso-centre towards the feet.

Chowdhury et al. (2014) have proposed the use of an EEG cap that incorporates electrodes embedded in an external layer and can record the gradient artefact separately from the EEG signal. Thus, subtraction between the signals recorded by internal and corresponding external electrodes allows substantial attenuation of the artefact. As mentioned by Spencer (2015), however, although this method sounds quite promising to attenuate the gradient artefact, it requires the use of specialised hardware that is within the prototyping stages and is not yet available to all investigators.

Depending on the application, an interleaved or sparse approach whereby the MRI signal acquisition is suspended at regular intervals could be used as well (Becker et al., 2005; Ritter and Villringer, 2006). This setup results in periodic EEG excerpts free of gradient artefacts, and are suitable for certain forms of brain activity, such as slowly varying rhythms and evoked responses. The delayed onset of fMRI acquisition associated with the neural response does not pose a problem in this case scenario because it can be assumed that the peak of the BOLD changes associated with the neural activity of interest occurs with the same time delay as those of normal stimuli. Nevertheless, interleaved protocols are generally less flexible and experimentally efficient than continuous measurements. In studies in which unintentional fluctuations in attention and vigilance gain more relevance, longer acquisition times are required.

Thereby, dedicated post-processing solutions have to be developed and employed in order to effectively perform the suppression of the gradient artefact (Ritter et al., 2010).

3.3.2 Model of the actual situation in post-processing solutions

Instead of using the extended model of Eq. (3.3), most of the post-processing solutions for gradient artefact correction neglect $q_i(t)$ and simply assume that any measured scalp potential signal for channel i , $s_i(t)$, is the (linear) sum of four independent components:

1. The actual (neuronal) EEG, $e_i(t)$.
2. Gradient artefact, $g_i(t)$.
3. Pulse artefact, $p_i(t)$.
4. Movement artefact, $m_i(t)$.

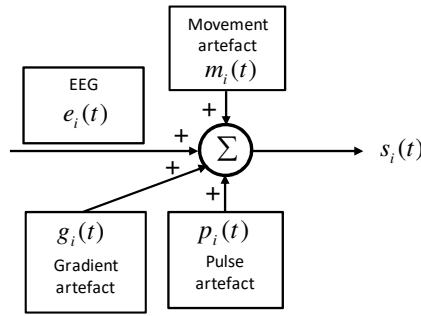


Figure 3.3: Usual model encountered in the literature for the sources of the measured signal $s_i(t)$, during correction of $g_i(t)$.

In formula:

$$s_i(t) = e_i(t) + g_i(t) + p_i(t) + m_i(t). \quad (3.4)$$

The main problem at hand is to estimate $e_i(t)$ from $s_i(t)$. Although a number of methods have been developed to correct $g_i(t)$, $p_i(t)$, and $m_i(t)$ in single EEG channels, the spatial aspects of $g_i(t)$, $p_i(t)$, and $m_i(t)$ (i.e. differences across various scalp electrodes) are still poorly understood. In current artefact correction methods, these aspects typically are covered by introducing one or more time-varying parameters in the signal models that may be estimated from the actual data (Yan et al., 2009; Spencer, 2015).

3.3.3 Usual approximation considered by the existing methods to correct the gradient artefact

As mentioned in Section 3.2, several approaches only take $g_i(t)$ in consideration, thus simplifying the problem of constructing an estimate $\hat{g}_i(t)$ for the gradient artefact. Then, $\hat{g}_i(t)$ is subtracted from the measured signal to obtain an estimate of the actual EEG, $\hat{e}_i(t)$. Hence, the model of Eq. (3.4) results in:

$$\begin{aligned} m_i(t) &= 0; \quad p_i(t) = 0; \\ \hat{e}_i(t) &= s_i(t) - \hat{g}_i(t). \end{aligned} \tag{3.5}$$

This leads to the correction scheme in the time-domain depicted in Fig. 3.4:

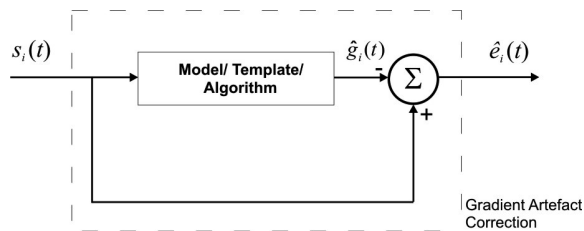


Figure 3.4: Correction scheme of the usual approximation to estimate and suppress $g_i(t)$ in the time-domain.

As indicated in this scheme, $\hat{g}_i(t)$ is constructed and subtracted from $s_i(t)$ by using a **Model/Template/Algorithm** to obtain the estimate of the neuronal EEG, $\hat{e}_i(t)$. In this and in following figures, the larger block indicated by the dashed line represents the operations used to perform the gradient artefact correction whereby the input $s_i(t)$ results in the output $\hat{e}_i(t)$. Estimation and subtraction of an estimate of $g_i(t)$ can alternatively be implemented in frequency-domain using the Fourier transform (FT) and the inverse Fourier transform (IFT):

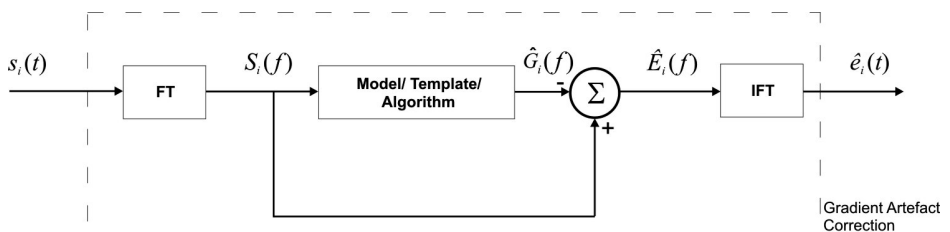


Figure 3.5: Correction scheme of the usual approximation to estimate and suppress $g_i(t)$ in frequency-domain.

In the next section, we present an overview of the various methods to generate the estimate $\hat{g}_i(t)$ or $\hat{G}_i(f)$.

3.3.4 Subtraction in time-domain-based methods

3.3.4.1 Average artefact subtraction and its variants

According to the average artefact subtraction (AAS) methodology, an average template in the time-domain that describes the gradient artefact waveform is used as the estimate $\hat{g}_i(t)$ (Allen et al., 2000). The AAS method assumes that the artefact and the EEG signal are uncorrelated, so that the subtraction of the averaged template yields an estimation of the corrected EEG. This approach can be likened to a comb-filter based upon a coherent detection process whereby the harmonic artefact interference is attenuated (Braun, 1975; Braun, 2011; Spencer, 2015). The average template is constructed by dividing $s_i(t)$ into averaging epochs that correspond to periods in which the repetition of the artefact waveform is observed. As described by Allen et al. (2000), the length M of the epochs considered for averaging is usually set: either as TR-slice (when it is possible to disable the dynamic stabilisation of the MRI equipment, thus making TR as a multiple of TR-slice); or as TR (when it is not possible to disable the dynamic stabilisation and DT occurs – see Fig. 2.13, or when an interleaved fMRI acquisition is used).

As the AAS method has also strong dependency on the assumption of gradient artefact stationarity, variations in the amplitude and shape of the artefact waveforms used for averaging may lead to inaccurate template estimation which results in residual artefacts in $\hat{e}_i(t)$ after subtraction of $\hat{g}_i(t)$. An important point with respect to correction methods that rely on the stationary nature of the artefact waveform over time such as the AAS is the accurate identification of $g_i(t)$ characteristics in the scalp electrode signals. Thereby, the artefacts waveforms must be precisely and reproducibly sampled to provide a more accurate template $\hat{g}_i(t)$.

Because of the relatively low sampling frequency in EEG systems in comparison with the acquisition clock that controls the MRI scanning process, the gradient artefact waveform is not always digitised precisely from epoch to epoch. Additionally, given the fast slopes of the gradient artefact in the order of $10^4 \mu\text{V/ms}$, an imprecise sampling of $s_i(t)$ may result in

strong variability of the artefact waveform across epochs. Thus, the temporal localisation with accuracy significantly better than a hundred milliseconds is required for adequate identification of the onset of each occurrence of the artefact (Mullinger et al., 2008b; Eichele et al., 2010). A logical solution to this problem is to use phase-locking hardware systems whereby the EEG system sampling frequency and the MRI scanner acquisition clock are exactly synchronised. Hence, TR (or TR-slice) is set as a multiple of the EEG system sampling interval in the recorded $s_i(t)$, before estimating and subtracting $\hat{g}_i(t)$ (Anami et al., 2003; Mandelkow et al., 2006; Mandelkow et al. 2010; Solana et al., 2014):

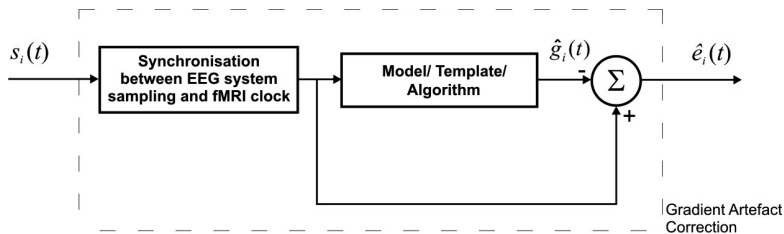


Figure 3.6: Correction scheme in which a synchronisation procedure of the EEG system sampling frequency and the MRI scanner acquisition clock is taken into consideration before construction and subtraction of $\hat{g}_i(t)$.

This synchronised setup between EEG system sampling and fMRI clock results in more reproducible artefact waveforms, more accurate average template, and a cleaner $\hat{e}_i(t)$ from residual artefacts after AAS (Anami et al., 2003; Mandelkow et al., 2006; Mullinger et al., 2008b; Gebhardt et al., 2008; Solana et al., 2014). Mandelkow et al. (2006) reported a usable bandwidth in the corrected EEG up to around 150 Hz after AAS by using synchronisation between the EEG sampling interval and the fMRI clock. In a previous work, Anami et al. (2003) suggested the combination of a synchronised acquisition setup with a special MRI pulse sequence and EEG acquisitions at the rate 1 kHz. This yields artefact amplitude attenuation to less than 5%, exclusively in the period in which the artefact resides around the baseline level. However, because this approach (referred to as “stepping-stop technique”) makes use of customised MRI sequences, it imposes restrictions on the MRI sequences, in addition to not being generally available to all investigators. Moreover, it requires the use of interleaved approaches as well as effective artefact post-processing after subtraction of $\hat{g}_i(t)$.

Parallel to phase-locking synchronisation, other publications have employed a kind of retrospective synchronisation by taking into account artefact waveform phase correction via temporal alignment by interpolation, or by considering timing error correction (Allen et al.,

2000; Negishi et al., 2004; Gonçalves et al., 2007; Huang et al., 2012). To correct the timing error, Gonçalves et al. (2007) have proposed calculation of a cost function Ψ with respect to DT and TR-slice (see Fig. 3.3) whereby the ratio $\hat{e}_i(t)/s_i(t)$ could be minimised:

$$\Psi(\text{DT, TR-slice}) = \frac{\sum_{i,j} (\hat{e}_{i,j}(\text{DT, TR-slice}))^2}{\sum_{i,j} (s_{i,j})^2} \times 100. \quad (3.6)$$

In this equation, j runs over the number of samples corresponding to the one volume repetition time (TR). Instead of a cost function, Negishi et al. (2004) suggested the use of an analogue 125 Hz low-pass filter before sampling of $s_i(t)$ to enable more reliable timing error detection. The usage of higher sampling rates has also been proposed to obtain a more accurate sampling of the gradient artefact waveform. Thus, during co-registered EEG-fMRI, scalp potential sampling rates are larger (at 5000 Hz) than those used for EEG routine recordings (between 250 and 2000 Hz). However, the limits in the usual sampling rates of the EEG pose restrictions to this approach, in addition to being lesser economically achieved than clock synchronisation (Sanei and Chambers, 2007; Gutberlet, 2010). Other AAS variants have addressed the correction of remaining residual artefacts after template subtraction by taking into consideration the spatial characteristics of the gradient artefact waveform. In this way, some studies have proposed the use of a sliding average window, independent component analysis (ICA), principal component analysis (PCA), beamformer spatial filtering, selective average subtraction, and a basis set of artefact templates correlated to head movements (Becker et al., 2005; Mantini et al., 2007; Niazy et al., 2005; Freyer et al., 2009; Brookes et al., 2008; de Munck et al., 2013; Spencer, 2015).

As mentioned in Chapter 2, the movement artefact, $m_i(t)$, modulates and provokes alterations in the morphology of the artefact waveform over the artefact period, in such a way that the average artefact template may not characterise individual occurrences of the artefact waveform. In this scenario, abrupt movements of the subject's head have a significant influence over the precision of averaged artefact templates and can result in large residual artefacts in the gradient artefact-corrected EEG by AAS. In addition, micro-movements of the subject head gives rise to broadening of the gradient artefact spectral lines, leading to the occurrence of residual artefacts in $\hat{e}_i(t)$ after template subtraction (see Section 2.4.3). Hence, the influence of $m_i(t)$ cannot be neglected as usually assumed in Eq. (3.5) (Yan et al., 2009; Moosmann et al., 2009; Sun and Hinrichs, 2009; Spencer, 2015; Maziero et al., 2016). Even

though some works have reported the access of the higher-frequency bandwidth of the neuronal EEG in $\hat{e}_i(t)$ after application of the AAS method (Mandelkow et al., 2006; Freyer et al., 2009), it is generally difficult to access EEG a bandwidth higher than 80 Hz because of the broadening of the gradient artefact spectral lines and the occurrence of related residual artefacts which tend to be in the EEG gamma band and frequencies above (Spencer, 2015).

Average-template-based correction methods are the most established methodology to suppress the gradient artefact. As shown in Table 3.2, the average artefact subtraction and its variants can be even grouped in a larger category classified as subtraction in time-domain methods. As its name suggests, this category also comprises other methodologies whereby $\hat{g}_i(t)$ is constructed and subtracted from $s_i(t)$ by using an artefact model in the time-domain.

3.3.4.2 Cubic spline template estimation

Koskinen and Vartiainen (2009) have described the use of a cubic spline to approximate the gradient artefact waveform, instead of constructing an average template. In this way, the artefact waveforms, corresponding to the epochs into which $s_i(t)$ is divided, are used to train a cubic spline model representative of $\hat{g}_i(t)$. A cost function Ψ is used to calculate the spline parameters, in such a way that the error between the model and the artefact waveform samples is minimised:

$$\Psi = a \sum_{i,j} [s_{i,j} - r(b_{i,j})]^2 + (1-a) \int [D^2 r(t)]^2 dt. \quad (3.7)$$

In Eq. (3.7), r corresponds to the spline model; j runs over the number of samples corresponding to one slice-time (TR-slice); b is a parameter that computes the time difference between the sample j and the beginning of the epoch to which the sample j belongs; a is a spline parameter; and D^2 stands for the second derivative of r . Similarly to the AAS method implementation, this approach is based upon the assumption of artefact waveform stationarity, as well as makes use of timing error correction.

3.3.4.3 Sum-of-sinusoids modelling estimation

As suggested by El-Tatar and Fokapu (2011), a sum-of-sinusoids modelling approach is used to approximate the average artefact waveform. In this way, those authors proposed to

construct the artefact template $\hat{g}_i(t)$, by minimisation of the mean square error between the sum-of-sinusoids model and the average artefact epoch.

3.3.4.4 Singular value decomposition

Liu et al. (2012) devised a gradient artefact correction method based on singular value decomposition (SVD). According to this approach, $s_i(t)$ is divided into epochs corresponding to the artefact waveforms that are arranged into a data matrix where each column corresponds to one epoch, and the lines match the number of points within each epoch. Application of SVD into the data matrix results in a sum of orthogonal components that are then classified as artefactual or not according to the slowly varying temporal patterns of the gradient artefact waveform across epochs. Last, a set of orthogonal basis functions is extracted from the artefactual components, whose linear combination is used to construct $\hat{g}_i(t)$.

3.3.5 Filtering in frequency-domain-based methods (Fourier filtering)

This category of gradient artefact correction methodologies covers those methods that make use of the Fourier transform (FT) and inverse Fourier transform (IFT) to implement the gradient artefact estimation in frequency-domain, as depicted in Fig. 3.5. FT is applied in $s_i(t)$ and IFT in $\hat{E}_i(f)$ in such a way that the estimate $\hat{G}_i(f)$ can be calculated and subtracted from $S_i(f)$. Thus, the output of the inverse Fourier transform corresponds to the estimate of the neuronal EEG, $\hat{e}_i(t)$.

Construction of the estimate $\hat{G}_i(f)$ has been implemented:

- (i) either by assuming that the frequencies in which the artefact activity is observed are totally associated with the gradient artefact, so that $\hat{G}_i(f)$ is constructed by setting the spectral power at those frequencies to zero (Hoffmann et al., 2000);
- (ii) or by estimation and subtraction of an average artefact template in frequency-domain (Sijbers et al. 1999; Sijbers et al., 2000).

The filtering in frequency-domain-based methods mentioned above are indicated in Table 3.2 as well.

Table 3.2: Summary of the gradient artefact methodologies proposed in the literature.

Category	Method	Variant	Principle/Assumption	References
Subtraction in time- domain	Imaging artefact reduction (IAR)		Estimation and subtraction of an average artefact template in the time-domain/ artefact waveform stationarity; uncorrelation between EEG and artefact; time-domain averaging	Allen et al. (2000)
		Synchronisation followed by AAS	Synchronisation of EEG system and fMRI scanner clocks before performing construction of the average artefact template	Anami et al., (2003); Mandelkow et al. (2006); Mullinger et al., (2008b); Gebhardt et al., (2008); Huang et al. (2012); Solana et al. (2014)
		Sliding average window	Estimation of a moving average artefact template based on a limited number of epochs	Becker et al. (2005)
	Average artefact subtraction (AAS)	Timing error correction	More accurate computing of timing error correction	Negishi et al. (2004); Gonçalves et al. (2007)
		Independent component analysis (ICA)	Independent component analysis (ICA) is used to describe and correct residual artefacts	Mantini et al. (2007)
		Principal component analysis (PCA) and difference model subtraction (DMS)	PCA and DMS are used to estimate basis set functions to describe residual artefacts owing to small temporal variations in the artefact of different artefact waveforms.	Niazy et al. (2005); Spencer (2015)
		High-frequency artefact residuals analysis	Use of PCA for processing of high-frequency residual artefacts	Freyer et al. (2009)
	Beamformer spatial filtering	Spatial filtering of electrical sources associated with residual artefacts	Brookes et al. (2008)	
	Selective average subtraction	EEG artefacts are grouped in clusters with the highest possible similarity before averaging	de Munck et al. (2013)	
	Online subtraction of artefact waveform	The estimated average artefact template is fitted and online subtracted from the EEG recordings	Garreffa et al. (2003); Anwar et al. (2009)	
Filtering in the frequency- domain (Fourier filtering)	Artefact estimation using cubic spline	–	Artefact waveform stationarity; uncorrelation between EEG and artefact	Koskinen and Vartiainen (2009)
	Sum-of-sinusoids modelling	–	Estimation of artefact components using sinusoids/Estimation of sinusoids using mean square error	El-Tatar and Fokapu (2011)
	Singular value decomposition and correlation analysis	–	Estimation of the gradient artefact using singular value decomposition and canonical correlation analysis	Liu et al. (2012) and Li et al. (2017)
	Suppression of the spectral power associated with the artefact frequencies	–	Correction of artefact frequencies by setting their power spectrum to zero	Hoffmann et al. (2000)
	Average artefact subtraction in frequency-domain	–	Estimation and subtraction of an average artefact template in frequency-domain/ Stationarity of the spectral artefact signature	Sijbers et al. (1999); Sijbers et al. (2000)

Fourier filtering methods may have the disadvantage of suppressing part of the actual EEG together with the gradient artefact due to the spectral overlap between both signals. Furthermore, the estimate $\hat{e}_i(t)$ obtained by frequency-domain filtering may suffer from ringing artefacts (Bénar et al., 2003; Ritter et al., 2010).

3.4 Overview of the existing approaches for pulse artefact correction

The pulse artefact, $p_i(t)$, can be attenuated at the source in a similar way as performed for the gradient artefact. In this way, it is carried out by carefully laying out and immobilising the leads, twisting the leads, using a bipolar electrode chain arrangement, and a head vacuum cushion. As remarked by Yan et al. (2010), limiting head motion as much as is tolerable by the subject can clearly help to reduce the amplitudes of the induced pulse artefact. Nevertheless, like the gradient artefact, it is more common to combine these efforts with post-processing correction methods to obtain the suppression of $p_i(t)$ (Bénar et al. 2003; Debener et al., 2010). Post-processing correction of $p_i(t)$ is typically performed after carrying out the gradient artefact correction, and thus applied in the estimate $\hat{e}_i(t)$. Below, we provide a brief discussion about the usual post-processing methods for correction of $p_i(t)$ reported in the literature.

3.4.1 *The pulse artefact (PA) subtraction correction method and its variants*

Allen et al. (1998) proposed a subtraction in time-domain-based correction method for suppression of $p_i(t)$ referred to as pulse artefact (PA) subtraction that assumes a constant and periodic nature for the artefact waveform. According to this method, a pulse artefact template is estimated along a preceding range of the EEG signal and this template is then subtracted from the ongoing electroencephalogram at those regions in which the artefact occurs. Therefore, such a method resembles the AAS approach proposed for gradient artefact correction (Allen et al., 2000), and has become seminal on cleaning up the pulse artefact. This procedure for correction of $p_i(t)$ requires simultaneous recording of EEG and ECG signals, and also takes into account the assumption that both EEG and pulse artefact are not correlated (Debener et al., 2010).

The PA subtraction shows limitations related to the violation of the basic assumptions on which the method is based: spatial and temporal instability of the pulse artefact, reliable and precise detection of the onset of each cardiac cycle, and lack of correlation between stimulus (and response) and cardiac activity. Furthermore, the ECG peak detection approaches relies on the typical morphology of the ECG waveform which may fail because of the distorted ECG shape inside a strong magnetic field. Deviations from the stability assumption result in inaccurate artefact estimation and, thereby, lead to greater residual artefacts after subtraction. In this way, longer averaging times can produce an inaccurate template due to the spatial and temporal variations of the pulse artefact, on one hand. On the other hand, shorter averaging times pose a risk of filtering out components of interest of the neuronal EEG together with the pulse artefact itself (Debener et al., 2010; Eichele et al., 2010; Laufs et al., 2008; Yan et al., 2010).

To overcome spatial variability problems, Niazy et al. (2005) proposed the use of principal component analysis (PCA) channel-wise for generation of the PA template as well. This approach was called optimal basis set (OBS) method, referring to the first few principal components as representations of several distinct pulse artefact templates. Such templates try to account for the greater temporal variance in the artefact shape in any given EEG channel, and are jointly used to suppress the pulse artefact from the EEG data. The artefact spatial variability has also been addressed by Wan et al. (2006), who proposed a non-linear wavelet-based approach combined with spatial average subtraction to describe the residual variances. Rather than a template calculated by simple average, estimations based on weighted averages and median values have been respectively described by Goldman et al. (2000) and Sijbers et al. (2000).

With respect to the temporal inter-beat variability of the R – R interval, the length of the pulse artefact template may also need some adjustment. In this way, the use of an adaptive Kalman filter has been proposed to account for the temporal instability of the pulse artefact (Bonmassar et al., 2002; Masterton et al., 2007). Implementation of such an approach requires an extra motion sensor signal as a reference signal. Vincent et al. (2007) has devised a moving general linear model (mGLM) approach which addresses the specific issue of $p_i(t)$ that lasts longer than a cardiac cycle. An alternative approach has been proposed by de Munck et al. (2013) to provide a more precise timing of overlapping artefacts, being able to eliminate such a temporal constraint. To this end, initially, hierarchical clustering has been applied to

discriminate the different spatiotemporal patterns of $p_i(t)$ as well as detect outliers. In addition, an ordinary least-squares (OLS) estimator has been used to estimate the overlapping between pulse artefact waveforms.

Another variant of the PA subtraction method has been described by Oh et al. (2014), who proposed to take into account delay variations between the QRS complex and a pulse artefact-peak, instead of using the mean interval (Allen et al., 1998). According to this approach, individual delays and artefact window lengths are estimated by using temporal characteristics of the ECG signal recorded within the MRI scanner and of the pulse artefact. Afterwards, those parameters are used to classify and group similar pulse artefact shapes that are then used to calculate the corresponding average artefact template.

3.4.2 Other solutions for pulse artefact correction

Instead of using principal component analysis (PCA) to specifically account for template spatial variability, Bénar et al. (2003) have proposed the use of PCA as well as independent component analysis (ICA) for overall correction of the pulse artefact. As reported by Brookes et al. (2008), correction of $p_i(t)$ can also be achieved by using a spatial beamformer technique which uses spatial filters to extract the components of the artefact according to its spatial characteristics. Therefore, rather than using an artefact template, these approaches aim at suppressing a number of prototypical topographies in which the pulse artefact can be characterised (Eichele et al., 2010).

According to Debener et al. (2010), in principle, some problems inherent in implementation and performance of the PA subtraction due to the template variability can be avoided by using PCA and ICA instead. Another advantage associated with PCA and ICA-based techniques is that exact knowledge about the onset of each cardiac cycle is not necessarily required. The assumption behind these techniques is that the contribution of the pulse artefact activity is statistically independent of (or in the case of PCA uncorrelated to) ongoing EEG activity (Eichele et al., 2010). However, combination of different methodologies such as AAS or OBS with ICA and PCA seems to be more attractive for a number of authors, as it provides several advantages that may otherwise be impossible to achieve using each technique separately, even at higher field strengths (Eichele et al., 2010).

3.4.3 Remaining challenges on suppression of the pulse artefact

Although well-established and widely used for pulse artefact correction, the PA subtraction method shows to be ineffective under deviations from the basic assumptions, as discussed above. Deviations from the spatial and temporal stability assumptions result in inaccurate estimation of $p_i(t)$ and, therefore, may lead to residual artefacts after template subtraction. Shortening the moving average window size cannot fully redress this problem because a smaller moving average window would leave more residual EEG activity in the template. In addition to instability of the artefact, any degree of correlation between cardiac and neuronal activity can be problematic from the point of view of EEG data quality. Nonetheless, these effects can be reduced by using proper experimental designs in EPs studies (Debener et al., 2010). On the other hand, the cardiac cycle onset can be difficult to be identified due to ECG channel contamination resulting from gradient switching and the effect of B_0 , leading to missed cycles or inaccurate template estimation window alignment. Accurate marker position improves the quality of the pulse artefact correction, in particular regarding residual noise in the high-frequency range of the EEG signal. Efforts to ensure good ECG recording quality with a focus on a clear R-wave through careful consideration of the positioning of electrodes are worthwhile (Debener et al., 2010; Eichele et al., 2010).

Also, there is a lack of consistency in the evaluation of pulse artefact suppression methods, which tend to focus on the reduction of $p_i(t)$ in detriment of assessments of EEG signal preservation (Debener et al., 2010; Abreu et al., 2016). Some methodologies such as a wavelet-based non-linear reduction of the pulse artefact, beamformer filtering, and Kalman filtering are also computationally demanding (Wan et al. 2006; Brookes et al., 2008; Bonmassar et al., 2002; Debener et al., 2010; Eichele et al., 2010). While several groups have reported success in using ICA for pulse artefact suppression, some results have been less positive. A possible reason for this discrepancy is the field strength of the scanners used in these studies (Debener et al., 2010). Currently, the available evidence suggests that the spatial filtering approaches such as ICA and PCA are not as efficient as template subtraction methods, in particular at scanner fields of 3 T and higher.

Improvement of artefact correction techniques may result from a better understanding of the mechanisms that give rise to the MRI induced artefacts (Yan et al., 2009). In other words, a better knowledge about the different mechanisms causing the pulse artefact should help to optimise recording conditions as well as offline data correction approaches, and thus

contribute to a better EEG signal quality. Given the promises of simultaneous EEG-fMRI, this seems a worthwhile goal (Eichele et al., 2010).

3.5 Overview and critical analysis of the existing approaches for evaluation of gradient artefact correction methods

The key question that arises after carrying out the gradient artefact correction using those methods of Table 3.2 is how to evaluate the accuracy and performance of the methodologies to construct $\hat{g}_i(t)$ (or $\hat{G}_i(f)$) as well as the quality of the estimate $\hat{e}_i(t)$, the corrected EEG. As remarked by Ritter et al. (2010), to date, evaluation of the performance of the gradient artefact correction methods has been seldom made in a systematic or consistent way. Furthermore, generalisation of the correction results for different types of EEG data has been poorly made (Mandelkow et al., 2010; Ritter et al., 2007; Freyer et al., 2009). In many EEG-fMRI studies, a single algorithm is chosen without proper justification, and often the quality of gradient artefact correction is assessed by visual inspection only. In the other cases, different approaches have been used to evaluate the gradient artefact correction methods quantitatively. In general, three types of measurement can be distinguished (Ritter et al., 2007; Grouiller et al., 2007): (i) the amount of artefact reduction; (ii) the degree of EEG signal preservation; and (iii) the use of phantoms and simulated data.

3.5.1 Measurement of the artefact reduction

Measurement of the artefact reduction is carried out by assessing the attenuation of gradient artefact parameters or characteristics that can be identified in the scalp potential $s_i(t)$, corrected EEG, $\hat{e}_i(t)$, and their respective power spectra. It is usually performed in two ways:

- a) By calculating the attenuation in voltages associated with the estimated artefact (Allen et al, 2000; Anami et al., 2003; Chowdhury et al., 2014). Accordingly, the artefact reduction can be assessed by attenuation in amplitude (difference between maximum and minimum value) of the estimated gradient artefact $\hat{g}_i(t)$; or by the amplitude of voltages associated with residual artefacts in the signal $\hat{e}_i(t)$. For instance, calculation of the amplitude of the difference between $s_i(t)$ and $\hat{e}_i(t)$ allows identifying how the artefact has been attenuated. Alternatively, the RMS value of the estimate $\hat{g}_i(t)$ can

also be used to assess the artefact attenuation. Those procedures are usually performed for a certain number of $s_i(t)$ and $\hat{e}_i(t)$ excerpts from different EEG channels and, at last, the median (or average) value of the attenuation in amplitude for all channels and excerpts is used to assess the overall attenuation across the EEG electrodes.

- b) By calculating the median spectral power attenuation within a specific frequency bin associated with the artefact activity (Niazy et al., 2005; Mandelkow et al., 2006; Mullinger et al., 2011). As described in Section 2.4.1, large artefact spectral peaks can be observed in the power spectrum of the scalp potential, $S_i(f)$, at harmonic frequency bins around multiples of the slice repetition frequency, $1/TR$ -slice. Accordingly, the assessment of artefact reduction can be performed by comparing the spectral power within the frequency bins before (P_B) and after (P_A) application of the gradient artefact correction. Niazy et al. (2005) assumed the frequency bins as the region ± 1 Hz around the multiples of $1/TR$ -slice. For instance, in Fig. 3.7, P_B and P_A should be calculated taking into account the frequency range corresponding to the artefact bins in $S_i(f)$ (red dot trace) and in $\hat{E}_i(f)$ (blue trace), respectively. In this figure, the artefacts bins can be observed at multiples of 13.2 Hz.

The values of P_B and P_A are then used to calculate the spectral power attenuation that can be computed in percentage or in decibels:

$$\text{Attenuation} = 100 \times \text{absolute} \left(\frac{P_B - P_A}{P_B} \right) \% , \quad (3.8)$$

$$\text{Attenuation} = -20 \times \log \left(\frac{P_A}{P_B} \right) \text{ dB} . \quad (3.9)$$

Such a procedure is performed for a number of $s_i(t)$ and $\hat{e}_i(t)$ excerpts picked up from different EEG electrodes, which are then used to compute the overall median or average attenuation.

The schemes corresponding to the measurement of artefact reduction as described above are depicted in Fig. 3.8.

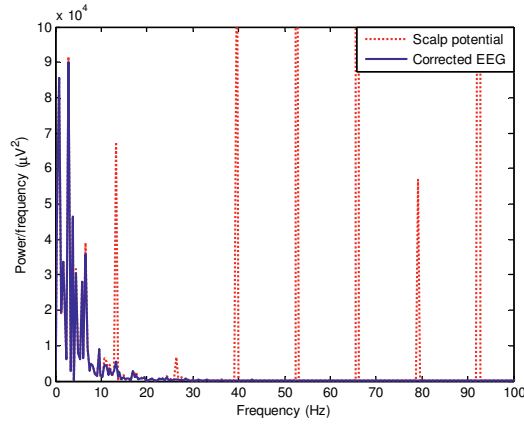


Figure 3.7: Measurement of the artefact reduction by comparing the power spectrum of the scalp potential (red dot trace), $S_i(f)$, and of the corrected EEG (blue trace), $\hat{E}_i(f)$. In this case, the artefact attenuation is calculated for the harmonic frequency bins, around the spectral peaks observed at multiples of 13.2 Hz in the power spectrum of the scalp potential.

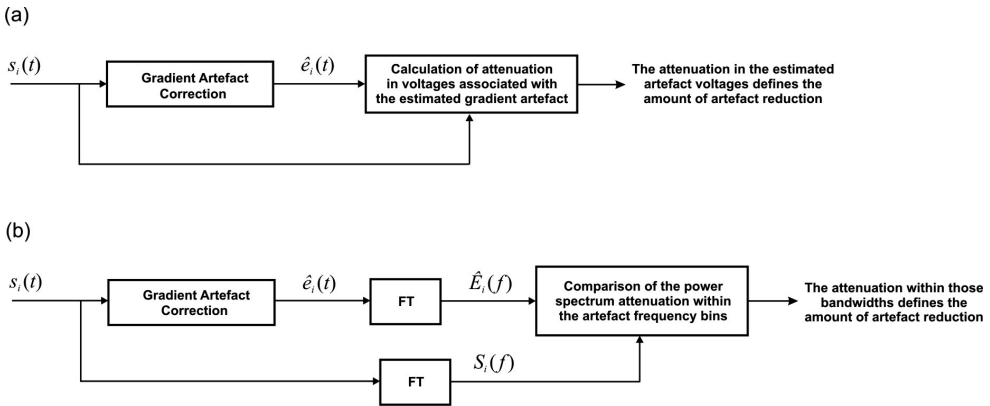


Figure 3.8: Schemes for measurement of the artefact reduction: (a) by assessing the attenuation in amplitude of voltages associated with the estimated artefact; (b) by assessing the attenuation of the power spectrum within a specific bandwidth associated with the gradient artefact activity. The blocks labelled as **Gradient Artefact Correction** match the larger block indicated as dashed lines in Figs. 3.4, 3.5, or 3.6.

3.5.1.1 Critical analysis

The amount of reduction in voltages of the estimated artefact over time and within the artefact bins are corresponding measures in the time and frequency-domain, respectively. Thereby, the periodicity of the gradient artefact in the time-domain is translated as the harmonic artefact

bins in frequency-domain, in such a way that the simultaneous usage of such measures might represent redundant information.

However, artefact spectral power that leaks around the multiples of the frequency $1/TR$ -slice might be not accounted for when calculating the attenuation in voltages over time. On the other hand, strong attenuation within the harmonic artefact intervals might mask the suppression of spectral power of EEG signal components that are overlapped by any harmonic artefact interval. Thus, the measurement of the gradient artefact reduction as described above should be always followed by the measurement of preservation of the characteristic of interest of the actual EEG in $\hat{e}_i(t)$ (Ritter et al., 2007).

3.5.2 Measurement of the EEG signal preservation

The measurement of preservation of the actual EEG signal in $\hat{e}_i(t)$ is usually performed in the following ways:

- a) By injection (linear addition) of a reference EEG signal, $e_{i,\text{ref}}(t)$, with a known dominant characteristic in scalp potential recordings, $s_i(t)$, with the gradient artefact (Fig. 3.9a). This results in a modified scalp potential signal, $s_{i,\text{mod}}(t)$, which is then subjected to the artefact correction. The estimated signal after artefact correction ($\hat{e}_i(t) + \hat{e}_{i,\text{ref}}(t)$) is used to retrieve the dominant characteristic which is then compared with its original value in $e_{i,\text{ref}}(t)$. Thus, the dominant characteristic of $e_{i,\text{ref}}(t)$ is used to generate a kind of “contrast” that would be observed in the estimate $\hat{e}_i(t) + \hat{e}_{i,\text{ref}}(t)$ (or in $\hat{E}_i(f) + \hat{E}_{i,\text{ref}}(f)$), after application of the gradient artefact correction method.

In the literature, sinusoids have been suggested as the reference EEG, $e_{i,\text{ref}}(t)$, within implementation of this procedure. Accordingly, sine waves with different frequencies at each bandwidth of interest of the neuronal EEG are used to generate a contrast in the spectrogram of the signal $\hat{e}_i(t) + \hat{e}_{i,\text{ref}}(t)$. Hence, it permits to identify whether the traces in the spectrogram corresponding to the injected sinusoids are disrupted by the gradient artefact correction method (Ritter et al., 2007).

b) By comparing the spectral power in the bandwidth of interest, or by comparing the RMS values over time, taking into account the following conditions of the EEG signal (Ritter et al., 2007; Allen et al., 2000; Freyer et al., 2009):

- the reference EEG, $e_{i,\text{ref}}(t)$: here, the usual reference EEG consists of scalp potentials excerpts recorded in MRI non-scan intervals (with no application of magnetic field gradients and RF pulses);
- the corrected EEG, $\hat{e}_i(t)$: obtained from application of the gradient artefact correction in scalp potential recordings with the gradient artefact, $s_i(t)$;
- the signal $\hat{e}_{i,\text{ref}}(t)$: obtained from application of the gradient artefact correction in the reference EEG, $e_{i,\text{ref}}(t)$.

When using the spectral power (Fig. 3.9b), initially, the power spectra $E_{i,\text{ref}}(f)$, $\hat{E}_i(f)$, and $\hat{E}_{i,\text{ref}}(f)$ are calculated for $e_{i,\text{ref}}(t)$, $\hat{e}_i(t)$, and $\hat{e}_{i,\text{ref}}(t)$, respectively. Then, for each of those power spectra, the total power within the bandwidth of interest of the neuronal EEG is computed. Finally, the median (or average) power within the EEG bandwidth of interest is calculated for $E_{i,\text{ref}}(f)$, $\hat{E}_i(f)$, and $\hat{E}_{i,\text{ref}}(f)$, taking into consideration a number of excerpts of $e_{i,\text{ref}}(t)$, $\hat{e}_i(t)$, and $\hat{e}_{i,\text{ref}}(t)$, and picked up across the different EEG electrodes.

The spectral power difference can be computed as a ratio (Ritter et al., 2007):

$$\text{Ratio} = \left(\frac{P_1}{P_2} \right), \quad (3.10)$$

where P_1 and P_2 correspond to the median/average power spectrum calculated for the EEG bandwidth of interest in $E_{i,\text{ref}}(f)$, $\hat{E}_i(f)$, and $\hat{E}_{i,\text{ref}}(f)$:

Median/average power spectrum	Compared spectra according to the EEG bandwidth of interest		
P_1	$\hat{E}_i(f)$	$\hat{E}_{i,\text{ref}}(f)$	$\hat{E}_{i,\text{ref}}(f)$
P_2	$E_{i,\text{ref}}(f)$	$E_{i,\text{ref}}(f)$	$E_{i,\text{ref}}(f)$

The spectral power difference can also be calculated by using Eq. (3.11) (Allen et al., 2000):

$$\text{Difference} = 100 \times \text{absolute} \left(\frac{P_2 - P_1}{P_2} \right) \% , \quad (3.11)$$

where P_1 and P_2 have correspondence with $\hat{E}_i(f)$ and $E_{i,\text{ref}}(f)$, respectively:

Median/average power spectrum	Compared spectra according to the EEG bandwidth of interest
P_1	$\hat{E}_i(f)$
P_2	$E_{i,\text{ref}}(f)$

According to Ritter et al. (2007), comparison between the power spectra of $e_{i,\text{ref}}(t)$ and $\hat{e}_i(t)$ is carried out in order to identify differences between artefact corrected epochs and the reference EEG. In turn, the power spectra of $\hat{e}_i(t)$ and $\hat{e}_{i,\text{ref}}(t)$ are compared for identification of systematic differences between these types of signals after application of the gradient artefact correction. Last, comparison between the power spectra of $\hat{e}_{i,\text{ref}}(t)$ and $e_{i,\text{ref}}(t)$ allows evaluation of the EEG preservation after application of the gradient artefact correction. Besides the usage of spectral power analysis, Freyer et al. (2009) proposed to use ratios of the median RMS values of $e_{i,\text{ref}}(t)$, $\hat{e}_i(t)$, and $\hat{e}_{i,\text{ref}}(t)$ to produce additional measures of degree of EEG preservation and artefact attenuation.

- c) Alternatively, measurement of the EEG signal preservation is assessed by the comparison of single events that occurs in $e_{i,\text{ref}}(t)$ and $\hat{e}_i(t)$, or in $e_{i,\text{ref}}(t)$ and $\hat{e}_{i,\text{ref}}(t)$ (Fig. 3.9c). Here, the reference EEG signal, $e_{i,\text{ref}}(t)$, is recorded outside MRI scanning intervals as well. In turn, $\hat{e}_{i,\text{ref}}(t)$ can be obtained from the linear addition of sinusoid waves (playing the role of $e_{i,\text{ref}}(t)$) that simulates single events in $s_i(t)$. Analysis and evaluation of the following single events have been suggested:
- (i) ERPs and VEPs (Gonçalves et al., 2007; Mantini et al., 2007; Koskinen and Vartiainen, 2009; Ryali et al., 2009; Freyer et al., 2009). As described in Section 3.2, ERPs and VEPs are low signal magnitude responses (see Table 3.1) related to identifiable nervous system events that can be measured in the spontaneous EEG. Because both ERPs and VEPs suffer from a poor signal-to-noise ratio (SNR), even in a non-MRI environment, an averaging over the duration (latency time) of the ERPs/VEPs is required to raise them above the spontaneous EEG. To establish a

comparison of ERPs/VEPs identified in $e_{i,\text{ref}}(t)$, $\hat{e}_i(t)$, or $\hat{e}_{i,\text{ref}}(t)$, the parameters signal-to-noise ratio and mean squared error have been used:

Signal-to-noise ratio (SNR):

$$\text{SNR} = \frac{\sigma_{e_{i,\text{ref}}}}{\sigma_{(e_{i,\text{ref}} - \hat{e}_i)}}, \quad (3.12)$$

where the numerator is the standard deviation of ERPs/VEPs identified in $e_{i,\text{ref}}(t)$; and the denominator corresponds to the standard deviation of the difference between ERPs/VEPs identified in $e_{i,\text{ref}}(t)$ and $\hat{e}_i(t)$. The signal-to-noise ratio calculated as described in Eq. (3.12) represents a summary of discrepancies between ERPs/VEPs measured in $e_{i,\text{ref}}(t)$ and $\hat{e}_i(t)$ in time (Ryali et al., 2009; Grouiller et al., 2007). However, because it is a normalised number, it does not quantify the absolute value of the residual noise. In parallel, since EPs and ERPs result from an averaging procedure, they are prone to a natural uncertainty;

$$\text{SNR} = \frac{\text{cov}(e_{i,\text{ref}}, \hat{e}_{i,\text{ref}})}{\sigma_{e_{i,\text{ref}}} \cdot \sigma_{\hat{e}_{i,\text{ref}}}}, \quad (3.13)$$

where cov is the covariance between the of ERPs/VEPs identified in $e_{i,\text{ref}}(t)$ and $\hat{e}_{i,\text{ref}}(t)$; and $\sigma_{e_{i,\text{ref}}}$ and $\sigma_{\hat{e}_{i,\text{ref}}}$ are, respectively, the standard deviation of ERPs/VEPs identified in $e_{i,\text{ref}}(t)$ and $\hat{e}_{i,\text{ref}}(t)$. The signal-to-noise ratio calculated by Eq. (3.13) corresponds to a measure of cross-correlation between of ERPs/VEPs as well, and allows an evaluation of frequency characteristics between $e_{i,\text{ref}}(t)$ and $\hat{e}_{i,\text{ref}}(t)$. Values of SNR closer to the unity means higher similarity between $e_{i,\text{ref}}(t)$ and $\hat{e}_{i,\text{ref}}(t)$.

Mean squared error (MSE):

$$\text{MSE} = \frac{1}{N} \sum_{n=1}^N (e_{i,\text{ref},n} - \hat{e}_{i,\text{ref},n})^2, \quad (3.14)$$

where n runs over the samples of ERPs/VEPs; and N is the total number of samples of ERPs/VEPs. The mean squared error (MSE) yields an estimate of the

difference between ERPs/VEPs in time, by quantifying an average squared error of such difference. As calculated in Eq. (3.14), smaller values of MSE indicate higher correspondence between the ERPs/VEPs identified in $e_{i,\text{ref}}(t)$ and $\hat{e}_{i,\text{ref}}(t)$.

- (ii) Identification of epileptiform activity or number of epileptic spikes (Bénar et al., 2003; Hoffmann et al., 2000). The onset of a clinical epileptic seizure is often characterised by a sudden change of frequency and amplitude in the scalp potential, referred to as epileptic spikes (Sanei and Chambers, 2007). Observation and correlation of epileptiform activity or epileptic spikes with the fMRI signal is important in studies focused on localisation of epileptic foci. Thereby, a gradient artefact correction method should allow observing a number of epileptic spikes in $\hat{e}_i(t)$ with high sensitivity and positive predictivity when compared with $e_{i,\text{ref}}(t)$. Identification of the epileptic spikes is usually performed by visual inspection of a trained observer (Bénar et al., 2003). An average rate consisting of the number of identified epileptic spikes per minute has been suggested by Bénar et al. (2003) to compare the number of epileptic spikes observed in $e_{i,\text{ref}}(t)$ and $\hat{e}_i(t)$ (Eq. (3.15)). Thus, a satisfactory EEG signal preservation is indicated when closer average rates are calculated for $e_{i,\text{ref}}(t)$ and $\hat{e}_i(t)$.

$$\text{Average rate} = \frac{\text{number of identified spikes}}{\text{min}}. \quad (3.15)$$

- (iii) Identification of alpha rhythms (Chowdhury et al., 2014; Niazy et al., 2005). Strong alpha activity (see Section 2.1.2) can be measured in healthy individuals at rest with their eyes closed, and is suppressed by opening the eyes. Thereby, the alpha activity should be observed in the corrected EEG $\hat{e}_i(t)$ as well.

3.5.2.1 Critical analysis

The use of single events to perform the measurement of the EEG preservation in $\hat{e}_i(t)$, as indicated in Fig. 3.9c, applies when such events are the signal component of interest in $\hat{e}_i(t)$, as used for epileptic spikes. Nevertheless, the use of single events might not be applicable when the signal component of interest in $\hat{e}_i(t)$ is the spontaneous EEG. In this case, the assessment of the dominant characteristic (Fig. 3.9a) by injection of a set of continuous sinusoids might be used to allow the assessment of EEG preservation, as performed by Ritter et al. (2007).

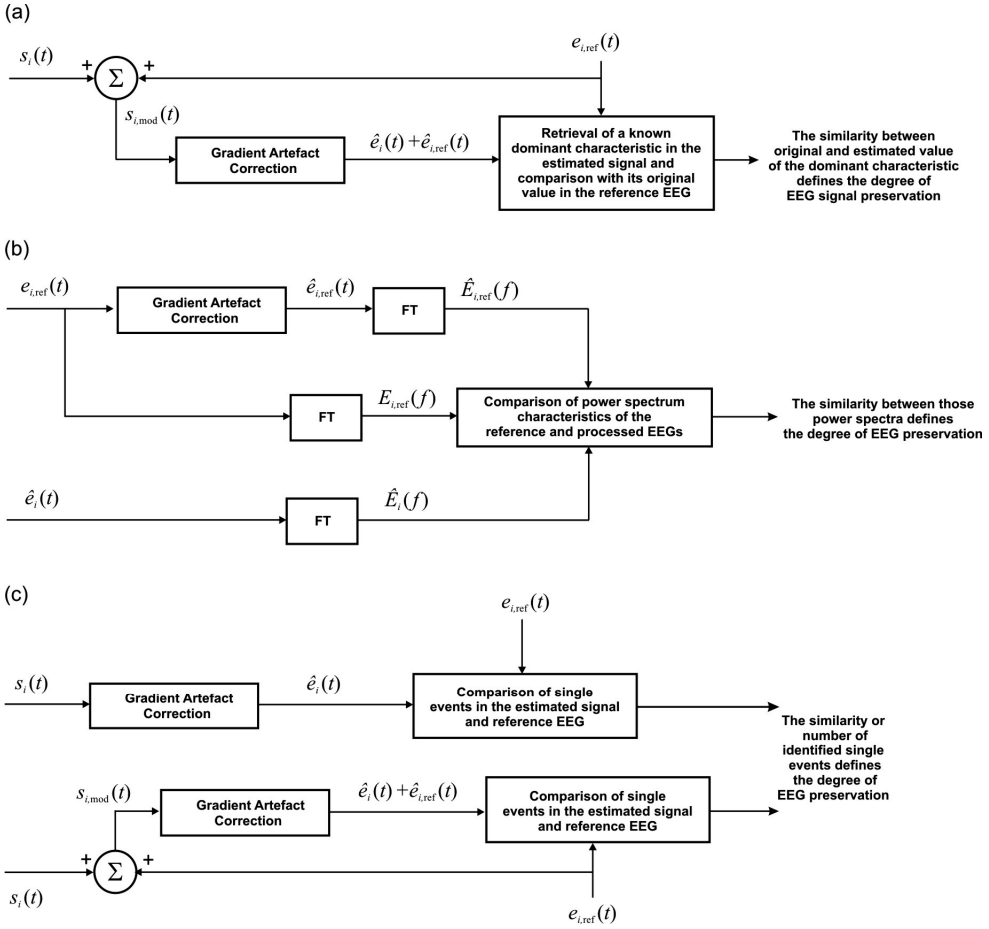


Figure 3.9: Schemes for measurement of EEG signal preservation: (a) by injection of $e_{i,ref}(t)$ in $s_i(t)$ and retrieval of a dominant characteristic; (b) by comparison of the power spectra of the signals $e_{i,ref}(t)$, $\hat{e}_{i,ref}(t)$, and $\hat{e}_i(t)$; (c) by comparison of single events in $\hat{e}_i(t)$ and $e_{i,ref}(t)$, or in $e_{i,ref}(t)$ and $\hat{e}_{i,ref}(t)$. The blocks labelled as **Gradient Artefact Correction** match the larger block indicated as dashed lines in Figs. 3.4, 3.5, or 3.6.

However, a quantitative evaluation of EEG preservation should also be taken into account jointly to this approach. Additionally, the use of sinusoids as a simulated EEG reference does not take into consideration the stochastic and non-stationary nature of the neuronal EEG. Further, when the spontaneous EEG is the signal component of interest in $\hat{e}_i(t)$, both analysis in time and frequency-domain should be complementarily conducted to assess the degree of EEG preservation in $\hat{e}_i(t)$.

Quantification of the EEG power spectrum in certain spectral bands, as shown in the scheme of Fig. 3.9b, allows obtaining a comparison between the power in frequencies of the reference and the estimated EEG. However, the lack of knowledge of the true EEG signal makes it difficult to compare the power spectra of artefact-corrected EEG excerpts with the spectra of the EEG recorded inside or outside the scanner. Furthermore, because the spectral analysis represents an average measure, it should be performed together with evaluation of EEG signal preservation in the time-domain. Thus, residual spectral power associated with the artefact might be masked when the spectral analysis is used alone, as well as when RMS amplitude values over time are used alone. Application of the gradient artefact correction approach directly in the reference EEG has also the disadvantage of not accounting for the influence of the gradient artefact and its dependence upon subject head micro-movements (see Section 2.4.3).

3.5.3 Use of phantoms and simulated data

Recordings made in phantoms and/or simulated data have also been employed to evaluate the performance of gradient artefact correction methods. In this scenario, measurement of the artefact reduction and the EEG signal preservation can be performed simultaneously (Ritter et al., 2010). In addition, the voltage recorded by the scalp electrodes is influenced by the magnetic induction of MRI magnetic field gradients and RF pulses, but not by the other current sources indicated in Eq. (3.3), or by magnetic coupling with the subject.

Scalp potential electrodes positioned in phantoms that must have a shape consistent with the human head (e.g. melon, watermelon, water balloon, or agar) are used to record a reference gradient artefact, $g_{i,\text{ref}}(t)$, when placed inside the MRI scanner. Next, the measured $g_{i,\text{ref}}(t)$ is linearly added to a reference EEG, $e_{i,\text{ref}}(t)$, generating a simulated scalp potential, $s_{i,\text{mod}}(t)$, as depicted in Fig. 3.10.

Last, application of the gradient artefact correction approach in $s_{i,\text{mod}}(t)$ produces the estimates $\hat{e}_{i,\text{ref}}(t)$ and $\hat{g}_{i,\text{ref}}(t)$. Thereby, the assessment of artefact reduction in the estimate can be evaluated by comparing $g_{i,\text{ref}}(t)$ with $\hat{g}_{i,\text{ref}}(t)$. In parallel, evaluation of EEG preservation can be performed by comparing $e_{i,\text{ref}}(t)$ and $\hat{e}_{i,\text{ref}}(t)$.

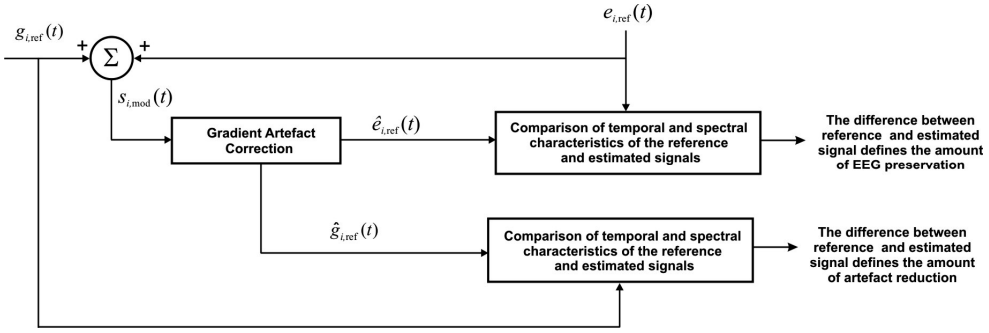


Figure 3.10: Scheme for evaluation of gradient artefact correction using phantoms or simulated data. The block labelled as **Gradient Artefact Correction** match the larger block indicated as dashed lines in Figs. 3.4, 3.5, or 3.6.

Instead of recording in phantoms, the usage of mathematically simulated data as estimation of $g_{i,ref}(t)$ and/or $e_{i,ref}(t)$ has also been proposed (Grouiller et al., 2007). Alternatively, sinusoids (as mentioned above) or simulated epileptic spikes can be superimposed on $e_{i,ref}(t)$ and used to either retrieve a dominant entry or identify single events.

3.5.3.1 Critical analysis

The use of simulations and recordings in phantoms has been proposed by several authors to minimise the effects of pulse, movement artefacts, and other sources of interference (Fig. 3.2) on the evaluation of the performance of the gradient artefact correction. This scenario offers the opportunity of assessing both artefact reduction and EEG signal preservation simultaneously. However, this approach has the main disadvantage of a lack of realism, in terms of the complexity of the actual EEG signal, other sources of interference, and inter-subject and inter-recording variability (Ritter et al., 2010).

A summary of the approaches described above for gradient artefact correction evaluation is shown in Table 3.3.

Table 3.3: Summary of the approaches for gradient artefact correction evaluation proposed in the literature.

Measurement	Approach	Principle	References
Amount of artefact reduction	Assessment of the median/average attenuation of artefact voltages	Calculation of the amplitude or RMS value of the gradient artefact estimate, $\hat{g}_i(t)$; calculation of the amplitude of voltages associated with gradient residual artefacts	Allen et al. (2000); Anami et al. (2003)
	Assessment of the median/average spectral power attenuation within the artefact frequency bins associated with the 1/TR-slice	Calculation of the power spectrum in a bandwidth associated with the artefact activity in $S_i(f)$ and $\hat{E}_i(f)$	Niazy et al. (2005); Mandelkow et al. (2006); Mullinger et al. (2011)
Degree of EEG signal preservation	Linear addition of $e_{i,ref}(t)$ in $s_i(t)$ and retrieval of a dominant characteristic of $e_{i,ref}(t)$	The dominant characteristic of $e_{i,ref}(t)$ is used as a contrast to be identified in $\hat{e}_i(t) + \hat{e}_{i,ref}(t)$	Ritter et al. (2007)
	Comparison of the power spectra of the signals $e_{i,ref}(t)$, $\hat{e}_i(t)$, and $\hat{e}_{i,ref}(t)$	The similarity of the power spectra $E_{i,ref}(f)$, $\hat{E}_i(f)$, and $\hat{E}_{i,ref}(f)$ are used to assess the EEG preservation	Allen et al. (2000); Garreffa et al. (2003); Ritter et al. (2007); Freyer et al. (2009); Becker et al. (2005)
	Identification and comparison of single events in $e_{i,ref}(t)$ and $\hat{e}_i(t)$, or $\hat{e}_{i,ref}(t)$	Comparison of VEPs and ERPs observed in $e_{i,ref}(t)$, $\hat{e}_i(t)$, or $\hat{e}_{i,ref}(t)$	Gonçalves et al. (2007); Mantini et al. (2007); Koskinen and Vartiainen (2009); Ryalı et al. (2009); Anwar et al. (2009); Liu et al. (2012); Solana et al. (2014)
		Comparison of the number of epileptic spikes observed in $e_{i,ref}(t)$ and $\hat{e}_i(t)$	Hoffmann et al. (2000); Béнар et al. (2003)
Use of phantoms or simulated data		Identification of alpha activity in $\hat{e}_i(t)$	Chowdhury et al. (2014); Niazy et al. (2005)
	Simultaneous comparison of $g_{i,ref}(t)$ and $\hat{g}_{i,ref}(t)$, and of $e_{i,ref}(t)$ and $\hat{e}_i(t)$	Use of data recorded from phantoms or mathematically simulated	Grouiller et al. (2007); Mandelkow et al. (2010); Gonçalves et al. (2007); Spencer (2015)

3.6 Methodology for evaluation of gradient artefact correction methods proposed for the current thesis

In the previous sections, we have provided an overview of the existing approaches for evaluation of gradient correction methods. Some characteristics discussed above could be taken into account to outline a framework for a systematic correction evaluation:

1. As complimentary measures of gradient artefact correction performance, measurement of the artefact reduction as well as of the neuronal EEG signal preservation shall be jointly undertaken (Ritter et al., 2007).
2. The EEG signal component of interest is a crucial factor for the correct choice of the reference signals.
3. In the current thesis, the focus is on the spontaneous EEG. Thus, entire EEG excerpt lengths should be analysed as the characteristic of interest, rather than single events. Hence, we should search for an approach implementation that might more broadly and accurately address the complexity of the spontaneous EEG.
4. As discussed above, a difficulty that arises with regard to the analysis of the spontaneous EEG is its stochastic and non-stationary nature. To handle this matter, analyses in time and frequency-domain shall be complementarily carried out to assess the artefact reduction as well as the EEG signal preservation.
5. The complexity of the neuronal EEG and the influence of the pulse and movement artefact as well as of other sources of interference are underestimated in case of using phantoms and simulated EEG data. Measures in phantoms and mathematically simulated data of the gradient artefact were not available in the current work either.
6. In this scenario, to perform the measurement of EEG preservation in the time-domain, the evaluation approach should allow the rejection of $\hat{g}_i(t)$ and $\hat{e}_i(t)$, and preservation of $\hat{e}_{i,\text{ref}}(t)$. Thus, the reference EEG, $e_{i,\text{ref}}(t)$, and its estimate, $\hat{e}_{i,\text{ref}}(t)$, could be compared.

Following the considerations above, our proposal for evaluation of gradient artefact correction in this thesis is described as follows.

3.6.1 Assessment of the artefact reduction

The assessment of the artefact reduction has been carried out by using the procedures described in the paragraphs a) and b) of Section 3.5.1. Such procedures were used as complimentary measures in time and frequency-domain.

Regarding the procedure described in paragraph a), the attenuation of artefact voltages was calculated using the amplitude of the estimate $\hat{g}_i(t)$ as well as its RMS value. In case of the procedure of paragraph b), the attenuation was calculated in decibels (Eq. (3.9)). Real data consisting of the scalp potentials recorded during MRI scanning has been utilised to perform this analysis.

3.6.2 Measurement of EEG signal preservation

To carry out the measurement of EEG signal preservation, we have proposed the use of the scheme depicted in Fig. 3.11 (see Section 5.4.2):

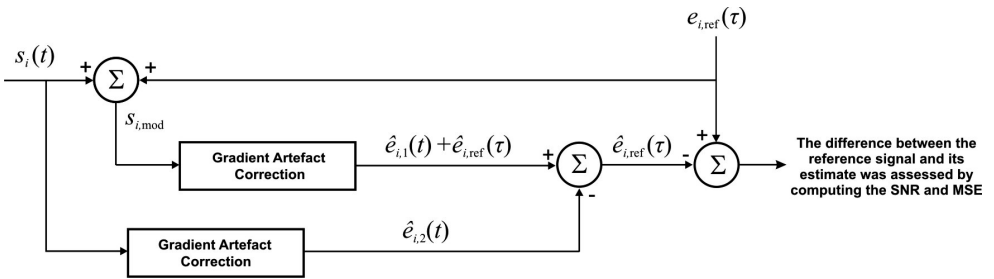


Figure 3.11: Proposed scheme for measurement of the EEG signal preservation by linear addition of $e_{i,\text{ref}}(\tau)$ in $s_i(t)$. Both $e_{i,\text{ref}}(\tau)$ and $s_i(t)$ were picked up from the same EEG electrode in different times, t and τ . The blocks labelled as **Gradient Artefact Correction** match the larger block indicated as dashed lines in Figs. 3.4, 3.5, or 3.6.

As indicated in Fig. 3.11, the reference EEG signal, $e_{i,\text{ref}}(\tau)$, was linearly added to the measured scalp potential, $s_i(t)$, thus generating the modified signal $s_{i,\text{mod}} = s_i(t) + e_{i,\text{ref}}(\tau)$. This modified signal was provided as real EEG data recorded inside the MRI scanner during non-scan periods. In Fig. 3.11, thus τ indicates that the reference EEG has been recorded at a different time than $s_i(t)$. The gradient artefact correction method was then applied to $s_{i,\text{mod}}$ and $s_i(t)$, respectively, resulting in the estimates $\hat{e}_{i,1}(t) + \hat{e}_{i,\text{ref}}(\tau)$ and $\hat{e}_{i,2}(t)$. Thus, the subtraction between these estimates allows obtaining an estimate of the reference signal, $\hat{e}_{i,\text{ref}}(\tau)$, that was finally compared with $e_{i,\text{ref}}(\tau)$. Eqs. (3.13) and (3.14) have been used to calculate the SNR and the MSE as complimentary measures of temporal and frequency contents of $e_{i,\text{ref}}(\tau)$ and $\hat{e}_{i,\text{ref}}(\tau)$. In addition to being of simple implementation, the advantage of using the evaluation scheme of Fig. 3.11 is that it allows the assessment of larger EEG experts by accounting the stochastic

nature of the neuronal EEG signal, and not single events only. The scheme shown in Fig. 3.11 has been used to assess the EEG preservation in Chapters 5 and 7. In Chapter 6, along with identification of epileptiform activity (see Section 3.6.3, below), we provided the assessment of the EEG preservation in $\hat{e}_i(t)$ by the quantification of the EEG power spectrum in a certain bandwidth.

As described in the next chapters, most of the proposed strategies for gradient artefact correction are frequency-domain filtering-based approaches in which synchronisation between the acquisition clock of the MRI equipment and the EEG system sampling frequency has also been taken into account. Thereby, we have used the scheme of Fig. 3.5 as well as the scheme of Fig. 3.12 – in which the block corresponding to the synchronisation procedure is indicated – within the design of our approaches for gradient artefact suppression:

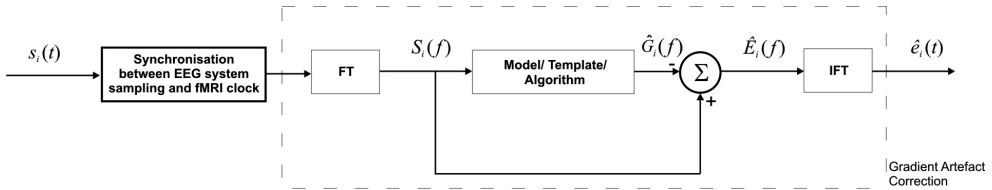


Figure 3.12: Correction scheme to estimate and suppress $g_i(t)$ in frequency-domain, taking into account a synchronisation procedure between the EEG system sampling frequency and the MRI acquisition clock.

Hence, considering the scheme of Fig. 3.11, the blocks labelled as **Gradient Artefact Correction** also match the larger block indicated as dashed lines in the scheme of Fig. 3.12.

3.6.3 Visual inspection by a trained EEG expert

As assessment of evaluation of the gradient artefact correction performance, we also used visual inspection to check the quality of the gradient artefact-corrected EEG, $\hat{e}_i(t)$. In this way, a trained EEG expert was requested to identify the occurrence of epileptiform activity in $\hat{e}_i(t)$, thus providing a clinical indication of quality of the signal used in epilepsy studies, as described in Chapter 6.

3.7 Concluding remarks

As discussed in this chapter, the proposal of techniques for estimation and suppression of the gradient artefact from scalp potential recordings has been recurrently reported in the literature. However, the improvement of the quality of the EEG signal obtained after application of the gradient artefact correction is still an open matter, especially concerning a better balance for the trade-off between artefact suppression and preservation of the neuronal EEG. In this way, efforts in this regard might result in a more effective access of higher-frequency neuronal EEG activity in the gamma band and above. In the next chapters, the design and implementation of novel filtering approaches for gradient artefact correction are proposed in order to achieve a better balance for the trade-off between artefact suppression and preservation of the neuronal EEG.

Regarding the evaluation of the gradient artefact correction methods, the use of a more systematic approach could make it easier to compare the different methodologies used for correction of the gradient artefact, as well as to facilitate the selection of a certain method amongst the existing ones, according to the quality required for the EEG signal. With this intent, our methodology described in Section 3.6 has been proposed and employed to evaluate the gradient artefact correction approaches utilised in this thesis. Besides, the evaluation scheme for EEG preservation depicted in Fig. 3.11 might also be used within the evaluation of other types of artefact correction procedures and in other signal processing analyses, as remarked in Chapter 9.

Application of the gradient artefact correction methods in EEG data sets recorded by using MRI scanners from different vendors is also provided in Chapters 5 – 8.

CHAPTER 4

Enhancement of the Comb-filtering Selectivity using Iterative Moving-Average for Periodic Waveform and Harmonic Elimination^{*}

4.1 Abstract

A recurring problem regarding the use of conventional comb-filter approaches for elimination of periodic waveforms is the degree of selectivity achieved by the filtering process. Some applications, such as the suppression of the gradient artefact from scalp potential recordings, require a highly selective comb-filtering that provides effective attenuation in the stop-bands and gain close to unity in the pass-bands. In this chapter, we present a novel comb-filtering implementation whereby we propose to exploit the iterative filtering application of FIR moving-average-based approaches in order to enhance the comb-filtering selectivity. Our results indicate that the proposed comb-filtering implementation can approximate the filter gain in the pass-bands to unity. A cascaded implementation using the proposed approach shows to further increase the attenuation in the filter stop-bands. Moreover, broadening of the comb-filtering stop-bands bandwidth around -3 dB according to the fundamental frequency of the stop-band can be achieved by our devised method, in addition to providing no distortion effects in the signal phase. Such comb-filtering characteristics are investigated in Chapter 5 within the proposed approach to attenuate the gradient artefact. The iterative application of time-domain averaging reveals to enable the use of a smaller number of averages during application of such a method. The proposed method can be used to design a novel notch filtering approach with enhanced selectivity as well.

^{*} This chapter was based on the paper:

Ferreira, J.L., Wu, Y., R., and Aarts, R.M. (2018). Enhancement of the Comb-filtering Selectivity using Iterative Moving-Average for Periodic Waveform and Harmonic Elimination. *J. Healthc. Eng.* 2018: article ID 7901502, 1-14.

4.2 Introduction

In biomedical signal processing and signal processing in general, comb-filtering approaches represent an important class of filters that plays a relevant role in different fields, such as extraction or elimination of periodic signal components, speech enhancement, audio and speech signal processing, decimation processes, prediction and estimation of geophysical signals, and power-line rejection (Rangayyan, 2002; Braun, 2011; Meher et al., 2011; Proakis and Manolakis, 1996; Zeng et al., 2017). In its simplest form, a comb-filter can be viewed as a combination of notch filters in which the null frequencies occur periodically across the filter bandwidth. Another and often-used comb-filtering approach is the conventional FIR moving-average filter indicated in Eq. (4.1):

$$y_n = \frac{1}{M} \sum_{k=0}^{M-1} x_{n-k}, \quad (4.1)$$

whose representation in z -domain and discrete time realisation are shown, respectively, in Eq. (4.2) and Fig. 4.1.

$$\frac{Y(z)}{X(z)} = \frac{1}{M} \frac{(1 - z^{-M})}{(1 - z^{-1})} = H_{MAF}(z), \quad (4.2)$$

with $M = f_s/f_M$, where f_s is the sampling frequency, and f_M is the fundamental of the periodic null frequencies.

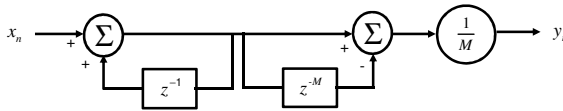


Figure 4.1: Discrete time realisation of the moving-average filter described in Eq. (4.2).

The comb-filter realisation indicated in Eq. (4.2) is widely employed because of its computational efficiency. As limitations, however, Eq. (4.2) provides a magnitude response with low attenuation in the filter stop-bands as well as non-uniform gain and high attenuation in the pass-bands, as indicated in Fig. 4.2.

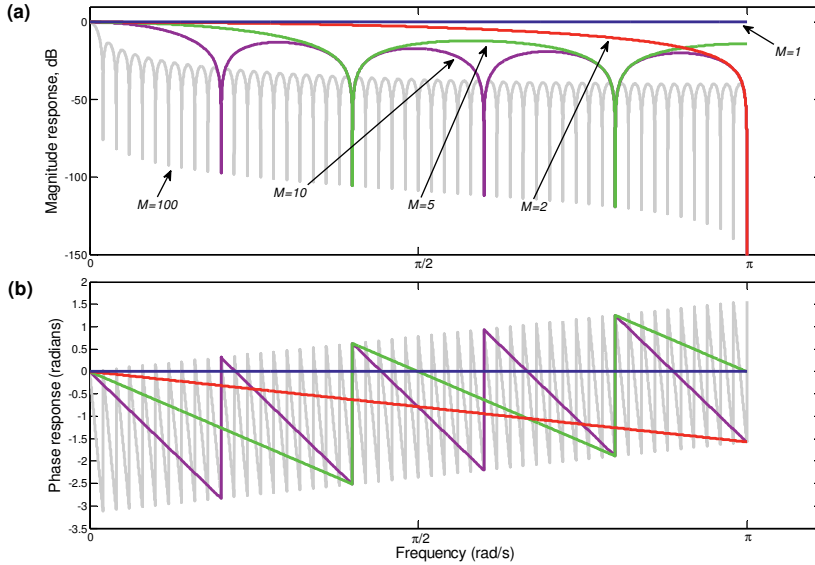


Figure 4.2: Frequency response of $H_{MAF}(\omega)$ for some values of M : (a) magnitude response; (b) phase response.

In addition, despite the piece-wise linearity of the phase characteristic, it can provoke increased phase delay for higher values of M . A filter that provokes no effects on the signal phase helps to preserve features over time in the output filtered waveform exactly where they occur in the input unfiltered signal. Thus, usually, zero-phase (non-causal) filters are preferable for many applications in electrophysiology (Widmann et al., 2015).

Therefore, the frequency response characteristics shown in Fig. 4.2 may be undesirable in certain applications, and are far from those of an ideal comb-filter: zero gain at notch frequencies, uniform and unity gain in the pass-bands, and no effects on the signal phase (Proakis and Manolakis, 1996; Rangayyan, 2002). To make the comb-filter realisation of Eq. (4.2) more selective or closer to the ideal behaviour, some strategies have been suggested in the literature. For instance, it can be achieved by the introduction of poles in the transfer function of the comb-filter realisation of Eq. (4.2), as indicated in Eq. (4.3) (Proakis and Manolakis, 1996; Tahir and Mazumder, 2014; Prodić et al., 2003):

$$H_{MOD}(z) = \frac{1 - z^{-M}}{1 - z^{-1}} \frac{1 - r \cdot z^{-1}}{1 - (r \cdot z^{-1})^M}, \quad (4.3)$$

where the value of the parameter r is contained in the interval $[0, 1)$. As mentioned by Proakis and Manolakis (1996), the insertion of poles in Eq. (4.2) has the effect of introducing a resonance in the vicinity of the null, thus provoking reduction of the bandwidth of the stop-bands. Therefore, the zeros $z = e^{j2\pi k/M}$ placed at the unit circle in the z -plane will have in their vicinity the poles $z = r \cdot e^{j2\pi k/M}$. The comb-filter approach described in Eq. (4.3) has been successfully used in several applications, such as in harmonic compensators and rectifiers in power systems (Prodić et al., 2003; Tahir and Mazumder, 2014). However, one of the limitations of this approach is the decreased attenuation in the stop-bands, as the value of r increases towards 1. Furthermore, there is a trade-off between the values of M and r , which is contingent to the performance requirement of the filter: on one hand, the use of higher values of M makes this method computationally expensive regarding memory usage. On the other hand, the exponential decrease of the power r^M makes the filter be implemented by using lower-resolution computer unit. Thus, there exists a compromise between the value of M and the computer unit resolution (Tahir and Mazumder, 2014).

Another proposed strategy to improve the selectivity of the comb-filtering provided by Eq. (4.2) is the time-domain averaging approach. Time-domain averaging consists of a kind of comb-filtering approach based on a coherent detection process whereby estimation and elimination of the periodic activity is carried out by averaging repetitive sequences of a periodic signal, $p(t)$, observed in the input signal, $x(t)$:

$$x(t) = p(t) + e(t). \quad (4.4)$$

In Eq. (4.4), $e(t)$ represents the non-periodic component of $x(t)$ which could be a noise signal or some stochastic process. Under the assumption that $p(t)$ and $e(t)$ are uncorrelated, summing up N subsequent segments $x(t_k)$ corresponding to the periodic signal results in coherent summation of $p(t)$ (Braun, 1975). Thus, the estimate of $p(t)$ obtained by time-domain averaging can be calculated by the following discrete representation:

$$\hat{P}_n = \frac{1}{N} \sum_{k=0}^{N-1} x_{n-kM}. \quad (4.5)$$

Or in z -domain:

$$H_p(z) = \frac{1}{N} \frac{(1 - z^{-NM})}{(1 - z^{-M})}. \quad (4.6)$$

The frequency response associated with the non-periodic component is derived from the subtraction between the discrete representation x_n and Eq. (4.5):

$$\hat{e}_n = x_n - \hat{p}(t) = x_n - \frac{1}{N} \sum_{k=0}^{N-1} x_{n-kM} = y_n. \quad (4.7)$$

Thus,

$$\frac{Y(z)}{X(z)} = 1 - H_p(z) \Rightarrow H_{TDA}(z) = 1 - |H_p(z)|, \quad (4.8)$$

where $H_{TDA}(z)$ is the magnitude response of the comb-filtering for elimination of the periodic component.

Time-domain averaging is a well-established comb-filtering approach which has been widely used to estimate and extract periodic signals encountered in phenomena involving some rotating machinery (Braun, 1975; McFadden, 1987). Time-domain averaging-based approaches have been also proposed to estimate and eliminate the gradient artefact from the EEG signal, such as the average artefact subtraction (AAS) method (Allen et al., 2000; Becker et al., 2005). As described in Section 2.4.1, the gradient artefact consists of a periodic waveform which is induced in the voltage recorded in the human scalp by the rapidly varying magnetic field gradients and radiofrequency pulses used in MRI sequences during simultaneous acquisition of EEG and fMRI data (Anami et al., 2003; Yan et al., 2009). One limitation of time-domain averaging is its high dependency on accurate sampling of the periodic waveform $p(t)$. The occurrence of jitter errors may result in imprecise sampling of the averaging waveforms which can impair the effectiveness of the method. Thus, the period of the repetitive waveform must be an exact multiple of the sampling interval. In parallel, the period of $p(t)$ must be precisely known, requiring an external trigger or reference signal provided by an additional hardware (Braun, 1975; Mandelkow et al., 2006). In case of suppression of the gradient artefact from the EEG signal, subject movements or small drifts may also compromise the performance of the algorithm because they change the morphology and shape of the artefact, in such a way that it is not possible to obtain an accurate estimate of

$\hat{p}(t)$. Subject movements or small drifts also provoke broadening of the harmonic artefact spectral lines (Spencer, 2015), whose attenuation may not be effectively accounted for by the AAS time-domain averaging-based comb-filter, as remarked in Section 3.3.4. In consequence, residual artefacts are left behind in the corrected EEG after subtraction of the estimated periodic waveform \hat{p}_n .

In this chapter, we present a novel comb-filtering implementation to improve the selectivity of the comb-filtering provided by Eq. (4.2). As described in Section 4.3, implementation of such a comb-filter has been based on an iterative filtering decomposition process (Lin et al., 2009) whereby an estimation of the filtered signal can be obtained by the iterative application of an FIR moving-average filter-based approach named double average filter. Comparison between our comb-filtering implementation and those existing methodologies to enhance the selectivity of Eq. (4.2) described above shows that our approach could be used in scenarios in which those approaches might be not effective, such as during broadening of harmonic spectral lines associated with the gradient artefact. Additionally, the iterative application of time-domain averaging demonstrates to enable the use of a smaller number of averages during application of such a method, as discussed in Sections 4.4 and 4.5.

4.3 Methods

In recent research (Lin et al., 2009), iterative filtering decomposition has been proposed as an alternative implementation for empirical mode decomposition (Huang et al., 1998). According to this methodology, a series \mathbf{L}_i of low-pass filters (or moving-average filters) is used to decompose a signal in intra-wave frequency modes or intrinsic mode functions (IMFs). Here, we have exploited the estimation of the first IMF, \mathbf{F}_1 , by application of the filter $(1 - \mathbf{L}_1)$ in the input signal \mathbf{x} :

$$\mathbf{F}_1 = \lim_{j \rightarrow \infty} (1 - \mathbf{L}_1)^{j-1} \mathbf{x}, \quad (4.9)$$

where \mathbf{L}_1 corresponds to an FIR moving-average-based filter. The convergence of the iterative filtering decomposition is ensured by the coefficients (masks) of the filter \mathbf{L}_1 having value between 0 and 1, and has been demonstrated by Lin et al. (2009).

4.3.1 Design of a novel comb-filtering approach for elimination of periodic waveforms

As \mathbf{L}_1 , initially we investigated the forward-backward application of the moving-average filter indicated in Eq. (4.1) in the input signal, x_n (Ferreira et al., 2014a; Ferreira et al., 2016). This procedure allows obtaining a filtered signal with zero-phase distortion which is a characteristic of an ideal comb-filter. The forward-backward application of Eq. (4.1) in x_n can be expressed as:

$$\begin{aligned} y_n &= \frac{1}{M} \sum_{k=0}^{M-1} \left[\frac{1}{M} \sum_{k=0}^{M-1} x_{n-k} \right]_{n+k} \\ &= \frac{1}{M} \sum_{k=-M+1}^{M-1} \left(\frac{M-|k|}{M} \right) x_{n+k}. \end{aligned} \quad (4.10)$$

Equation (4.10) is also referred to as double average filter (Lin et al., 2009; Wang et al., 2012), where the coefficients of x_{n+k} correspond to a triangular window of length $2 \times M$. By applying the z -transformation in Eq. (4.10), it results in the following transfer function:

$$H_D(z) = \frac{1}{(M)^2} \frac{(1-z^{-M})(1-z^M)}{(1-z^{-1})(1-z)}, \quad (4.11)$$

whose discrete time realisation is depicted in Fig. 4.3.

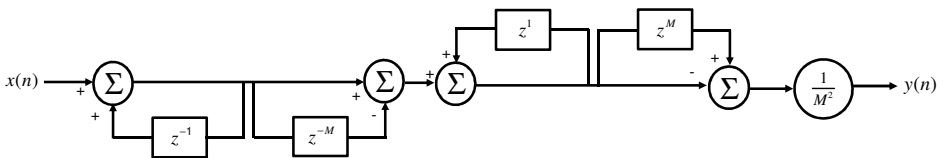


Figure 4.3: Discrete time realisation of Eq. (4.11).

The frequency response of $H_D(z)$ is derived from Eq. (4.11) by setting $z = e^{j\omega}$. Hence:

$$H_D(\omega) = \frac{1}{(M)^2} \frac{\sin^2\left(\frac{\omega M}{2}\right)}{\sin^2\left(\frac{\omega}{2}\right)}. \quad (4.12)$$

Figure 4.4 depicts the magnitude response of $H_D(\omega)$, calculated according to Eq. (4.12), for some values of M . It also shows the presence of spaced zeros at the frequency $2\pi/M$. For a hypothetical value $M = 1$, $H_D(\omega)$ becomes an all-pass band filter:

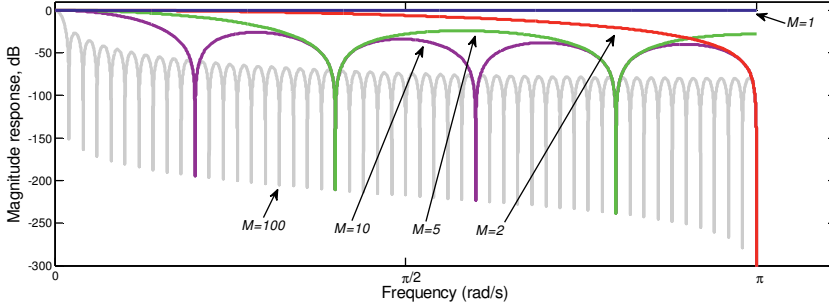


Figure 4.4: Magnitude response of $H_D(\omega)$ for some values of M .

The phase response of $H_D(\omega)$ possesses a zero-phase characteristic, as a result of the forward-backward application of the moving-average filter of Eq. (4.1):

$$\theta_D(\omega) = \tan^{-1} \left\{ \frac{\text{Im}[H_D(\omega)]}{\text{Re}[H_D(\omega)]} \right\} = 0. \quad (4.13)$$

Therefore, Eq. (4.11) describes a moving-average filter that provides no distortion effects in the phase of the signal in the whole filter pass-band. Equation (4.11) is also a non-causal filter because each sample in the filtered output signal is calculated from preceding and future samples of the unfiltered input signal (Widmann et al., 2015; Proakis and Manolakis, 1996).

Replacing Eq. (4.11) by \mathbf{L}_1 in Eq. (4.9), and taking into account a number J of iterations, it can be rewritten as (Ferreira et al., 2014a):

$$F_1(z) = (1 - H_D(z))^J X(z) \Rightarrow \frac{F_1(z)}{X(z)} = (1 - H_D(z))^J = H_1(z). \quad (4.14)$$

Equation (4.14) corresponds to the transfer function that relates the extracted periodic waveform, $p(t)$, and the input signal, $x(t)$, as indicated in Eq. (4.4). Therefore, after elimination of $p(t)$, the output $y(t)$ of the proposed comb-filter is related to $x(t)$ as (Ferreira et al., 2016):

$$Y(z) = (1 - H_1(z))X(z) \Rightarrow \frac{Y(z)}{X(z)} = 1 - H_1(z) = H_c(z). \quad (4.15)$$

To improve the attenuation in the stop-bands, we investigated application of $H_c(z)$ within the cascade implementation indicated in Eq. (4.16):

$$H_L(z) = [H_c(z)]^L, \quad (4.16)$$

where L is the number of cascades.

Because Eq. (4.15) has been derived from Eq. (4.11), which has zero-phase distortion characteristic, it does not cause any distortion effects on the filtered signal phase either. The same behaviour occurs for Eq. (4.16), so that the cascade application of $H_c(z)$ does not affect the phase of the filtered signal.

4.3.2 Iterative application of time-domain averaging

As an alternative for the filter \mathbf{L}_1 in Eq. (4.9), we have also investigated the use of the time-domain averaging filter described in Eq. (4.8). To this end, we have taken into account a number J of iterations of Eq. (4.9) which was rewritten as:

$$F_2(z) = (1 - H_{TDA}(z))^J X(z) \Rightarrow \frac{F_2(z)}{X(z)} = (1 - H_{TDA}(z))^J = (H_p(z))^J = H_2(z). \quad (4.17)$$

Thereby, by eliminating the estimated periodic signal, the output will be related to the input as:

$$\frac{Y(z)}{X(z)} = 1 - H_2(z) = H_{RTDA}(z). \quad (4.18)$$

4.3.3 Using the proposed method to design a novel notch filtering approach

As remarked by Braun (2011), the frequency response provided by Eqs. (4.7) and (4.8) corresponds to the convolution between the frequency response depicted in Fig. 4.2 and a train of unit pulses separated by the period M . Making use of this idea, we also investigated the convolution of a single pulse, δ , and the magnitude response indicated in Fig. 4.2a to design a novel notch filtering approach approximated to the ideal case:

$$H_3(\omega) = \delta(\omega) * |H_{MAF}(\omega)|. \quad (4.19)$$

Figure 4.5 shows this convolution, where the unit pulse has been located at the frequency ω_0 , and $|H_{MAF}(\omega)|$ was calculated for $M=2$. As can be noticed in Fig. 4.5b, Eq. (4.19) corresponds to a band-pass filter with unit amplitude and central frequency at ω_0 .

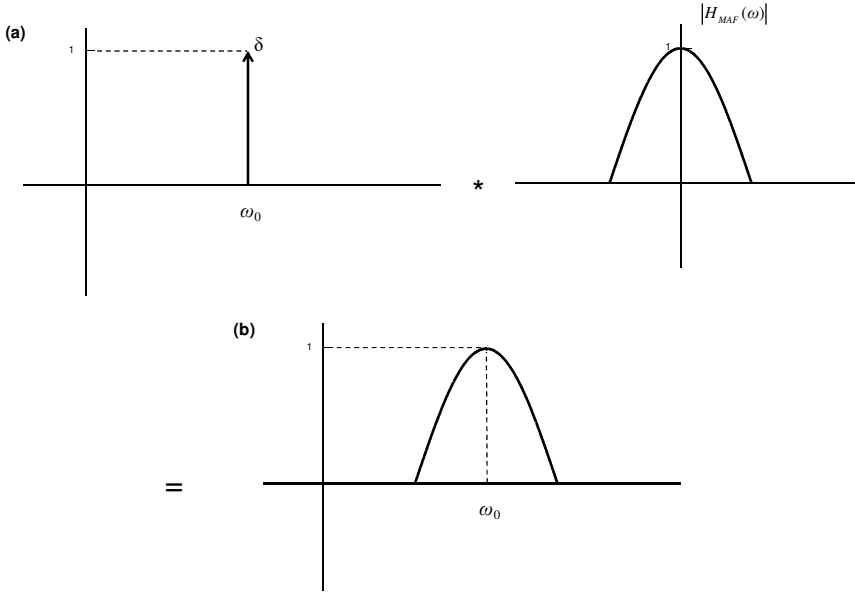


Figure 4.5: Convolution between the unit pulse δ (located at the frequency ω_0) and $|H_{MAF}(\omega)|$ ($M=2$). It results in a band-pass filter with central frequency at ω_0 .

Replacing \mathbf{L}_1 in Eq. (4.9) by $(1 - H_3(z))$, and taking into account a certain number J of iterations, it results in the notch filter $H_{NTC}(z)$ of Eq. (4.20):

$$F_3(z) = [1 - (1 - H_3(z))]^J X(z) \Rightarrow \frac{F_3(z)}{X(z)} = (H_3(z))^J \Rightarrow H_{NTC}(z) = 1 - (H_3(z))^J. \quad (4.20)$$

Like in Eq. (4.16), we investigated the application of Eq. (4.20) in a cascade implementation to enlarge the attenuation at the notch frequency, as indicated in Eq. (4.21):

$$H_{NL}(z) = [H_{NTC}(z)]^L. \quad (4.21)$$

4.4 Results

4.4.1 Frequency characteristics of the novel comb-filtering approach

All frequency responses depicted below have been calculated using a number of samples $N_s = 300000$ samples, so that ω was set as $\omega = [-\pi, \pi]$, with frequency interval at $2\pi \times (1 / N_s)$. In these figures, only the frequencies ranging from 0 to π are shown. The simulations were performed in MATLAB (The MathWorks Inc., Natick, USA) environment.

In Fig. 4.6, the magnitude response of $H_C(z)$ (Eq. (4.15)) is depicted, taking into account $M = 10$ and $M = 100$, and some values of J . It can be observed that increasing of J is followed by substantial increasing of the filter gain, which attains 0 dB as well as become more uniform in the different pass-bands. On the other hand, increasing of J is also followed by reduction in the attenuation in the filter stop-bands. On the extreme case, when $J \rightarrow \infty$, Eq. (4.15) tends to become an all-pass band filter, as shown in Fig. 4.7a. By fixing the value of J and varying M , Eq. (4.15) shows to provide more uniform gain in the pass-bands for smaller values of M , as observed in Fig. 4.7b.

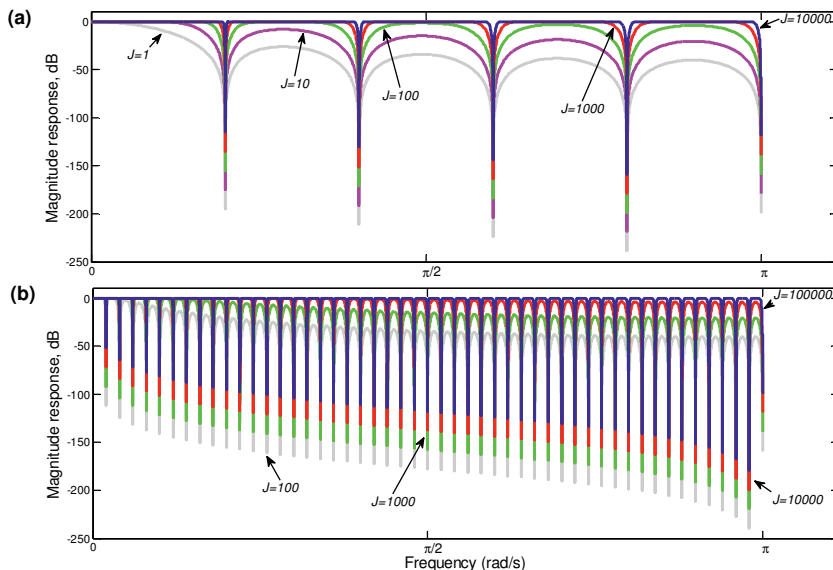


Figure 4.6: Magnitude response of $H_C(\omega)$, taking into account (a) $M = 10$; and (b) $M = 100$, and some values of J .

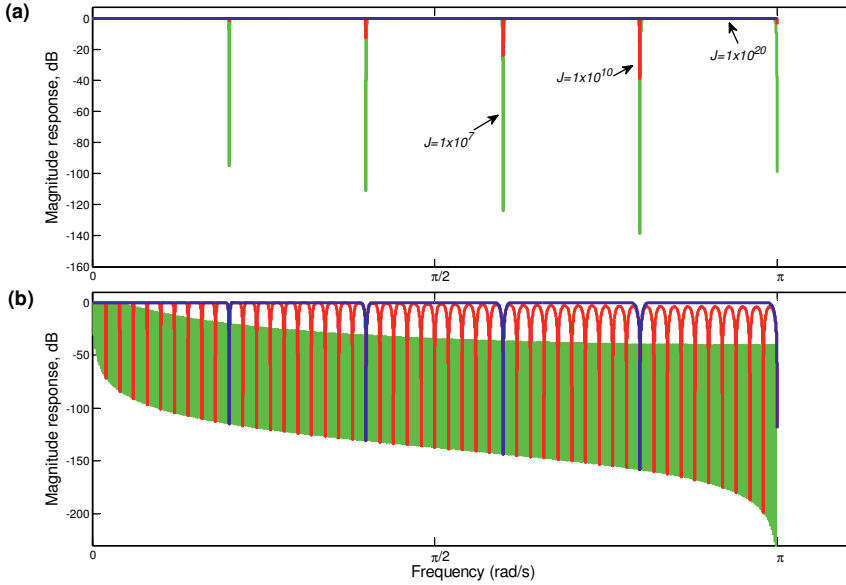


Figure 4.7: (a) Magnitude response of $H_C(\omega)$ for $M=10$ and some values of J ($J \rightarrow \infty$); (b) magnitude response of H_C for $J=10000$ and some values of M : $M=10$ (blue trace), $M=100$ (red trace), and $M=1000$ (green trace).

4.4.2. Iterative application of time-domain averaging

By setting $z = e^{j\omega}$ in Eq. (4.6), the magnitude and phase response of the periodic component $\hat{p}(t)$ obtained by time-domain averaging are, respectively, derived as:

$$\Rightarrow |H_p(\omega)| = \frac{1}{N} \left| \frac{\sin\left(\frac{\omega NM}{2}\right)}{\sin\left(\frac{\omega M}{2}\right)} \right|, \quad (4.22)$$

and

$$\Rightarrow \theta_p(\omega) = \tan^{-1} \left\{ \frac{\text{Im}[H_p(\omega)]}{\text{Re}[H_p(\omega)]} \right\}. \quad (4.23)$$

Figure 4.8 depicts the magnitude and phase response of Eqs. (4.22) and (4.23), taking into account $M=10$, for $N=4$ (dark trace), $N=8$ (green trace), and $N=16$ (gray trace).

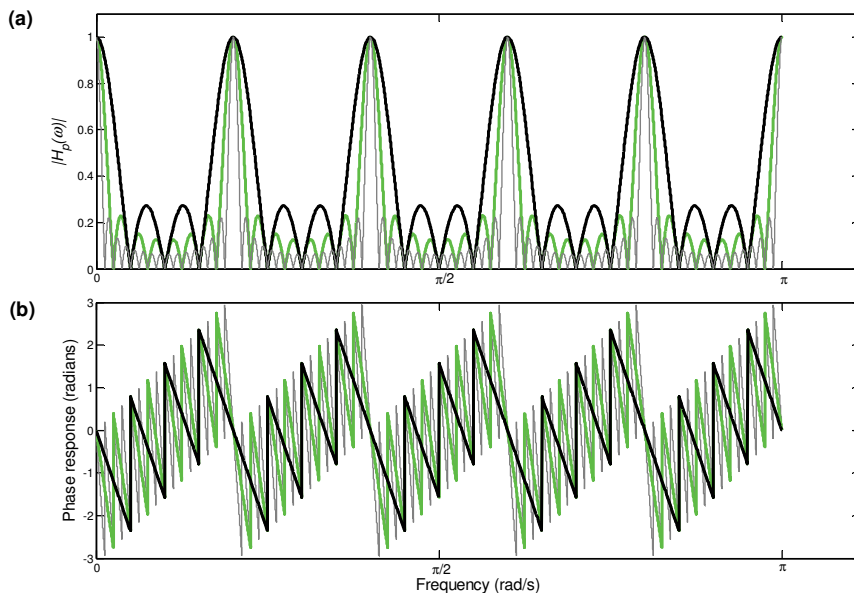


Figure 4.8: Frequency response $|H_p(\omega)|$ for $M = 10$, taking into account $N = 4$ (dark trace), $N = 8$ (green trace), and $N = 16$ (gray trace): (a) magnitude response; (b) phase response.

The main lobes of the magnitude response $|H_p(\omega)|$ lie spaced at the frequency $2\pi/M$, and have unit amplitude. By increasing N , the amplitude of the side-lobes is reduced as well as the main lobes become narrower. Regarding the phase response, it is not linear, but has approximated piece-wise linearity between the null frequencies of the lobes (Braun, 1975; McFadden, 1987; Proakis and Manolakis, 1996). In turn, Fig. 4.9 shows the frequency response associated with the non-periodic component $e(t)$, as indicated in Eq. (4.8).

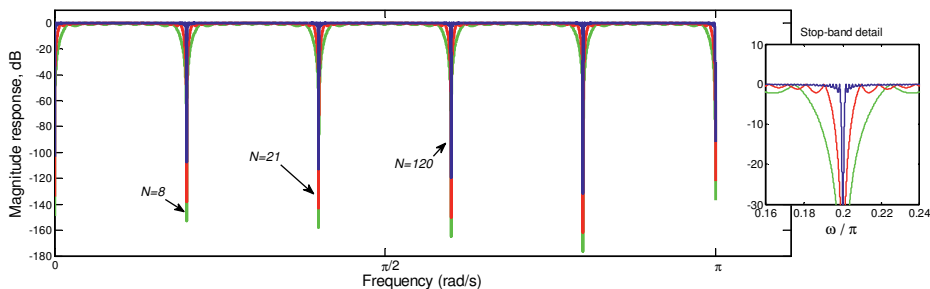


Figure 4.9: Magnitude response of $H_{TDA}(z)$ for $M = 10$ and some values of N .

Figure 4.10 depicts the frequency response provided by Eq. (4.17), taking into account $M = 10$ and $N = 4$, for $J = 1$ (dark trace), $J = 3$ (green trace), and $J = 8$ (gray trace). It can be noticed that increasing of J in Eq. (4.17) has a similar effect to increasing N in Eq. (4.22), by reducing the amplitude of the side-lobes and narrowing the main lobe. Regarding the phase response, it remains piece-wise linear after increasing of J . In Fig. 4.11, the frequency response corresponding to Eq. (4.18) is depicted, for $M = 10$, $N = 8$, and some values of J .

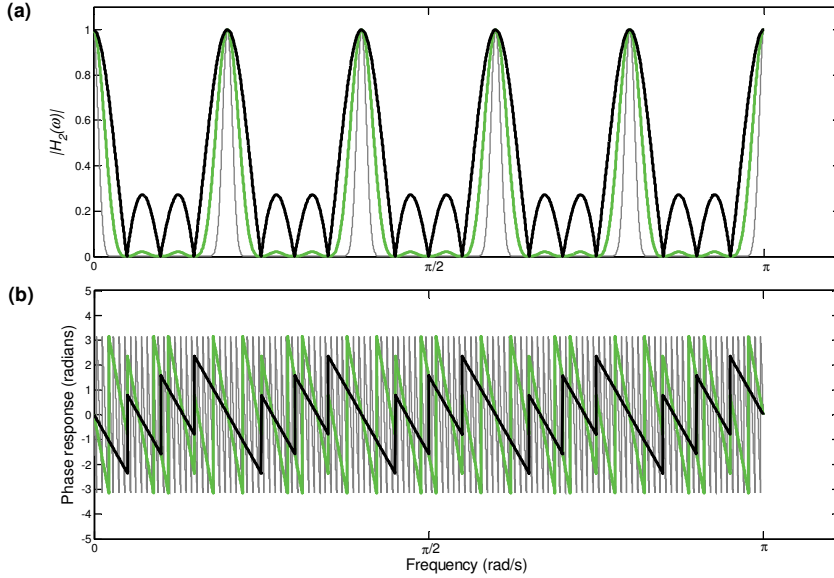


Figure 4.10: Frequency response of Eq. (4.17), taking into account $M = 10$, $N = 4$, for $J = 1$ (dark trace), $J = 3$ (green trace), and $J = 8$ (gray trace): (a) magnitude response; (b) phase response.

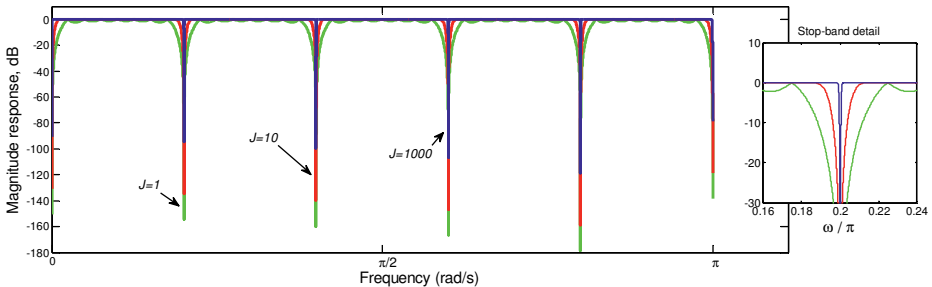


Figure 4.11: Magnitude response of $H_{RTDA}(\omega)$, taking into account $M = 10$, $N = 8$, and some values of J .

It can be observed that as J increases, the filter gain is approximated to the unity along the pass-bands as well as the stop-bands become narrower. Therefore, increasing of J in Eq. (4.18) attests a similar effect to that provided by increasing of N in Eq. (4.8).

4.4.3 Notch filter characteristics obtained by iterative moving-average

The magnitude response corresponding to $H_{NTC}(z)$ is depicted in Fig. 4.12, taking into account $M = 2$, some values of J , and $N_s = 300000$ samples for $|H_{MAF}(\omega)|$ as well. The stop-band of the notch filter was located at $\omega_0 = \pi/2$. It can be observed that the bandwidth of the notch filter stop-band is narrowed by increasing the value of J , as well as Eq. (4.20) tends to become an all-pass band filter when $J \rightarrow \infty$. This notch filter does not cause any effects on the phase of the signal.

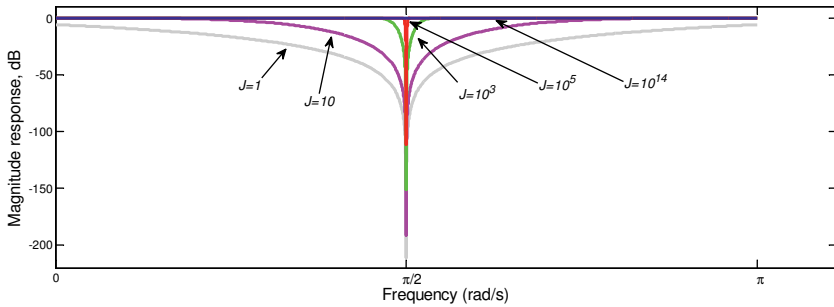


Figure 4.12: Magnitude response of $H_{NTC}(\omega)$ (Eq. (4.20)), taking into account $M = 2$, some values of J , and $\omega_0 = \pi/2$.

4.5 Further comparative analyses and discussion

As indicated in Figs. 4.6 and 4.9, by increasing the parameters J (Eq. (4.15)) and N (Eq. (4.8)), the gain in the filter pass-bands provided, respectively, by H_C and H_{TDA} increases and attains the unity (0 db). Simultaneously, a reduction of attenuation in the stop-bands is also observed. Nevertheless, rather than the response of H_{MOD} of Eq. (4.3) (Prodić et al., 2003; Tahir and Mazumder, 2014), there is no effects on the phase response corresponding to H_C and H_{TDA} , which remains zero radians for any values of frequency. On the other hand, H_{TDA} (Eq. (4.8)) cannot be applied in a cascade implementation due to the ripple that occurs below and around

0 dB in the pass-bands (see stop-band detail in Fig. 4.10), which can compromise the gain uniformity along the pass-bands. As H_C shows no ripple along the pass-bands and no phase-distortion, these characteristics allow the application of H_C in a cascade implementation (Eq. (4.15)) to improve the attenuation in the stop-bands. H_{MOD} (Eq. 4.3), in turn, cannot be applied within a cascade implementation without causing some distortion in the signal phase alike.

It is noteworthy that the forward-backward filtering described in Eq. (4.10) has been used to derive Eq. (4.11). As such, the magnitude response of Eq. (4.11) (H_D) has a (real) squared magnitude response of the original filter H_{MAF} (Eq. (4.2)) (Smith, 1999). However, Eq. (4.11) is later used in Eq. (4.14) to provide the novel comb-filtering approach based upon iterative filtering. Thus, the magnitude response H_C of Eq. (4.14) does not possess a squared response like H_D . Rather, the magnitude response of Eq. (4.14) is a combination of every component iteratively obtained by using Eq. (4.11) as L_1 in Eq. (4.9).

Figures 4.8 – 4.11 show that the iterative application of time-domain averaging, according to Eq. (4.18), represents an alternative to using higher values of N because it permits to obtain narrower comb-filter stop-bands as well as phase distortion approximately zero along the filter pass-bands. Thus, in addition to enhancing the comb-filter selectivity, time-domain averaging applied with a J number of iterations enables to use a smaller number of averaging periods. Figure 4.13 depicts the difference amongst H_{MOD} , H_{TDA} , H_C , and H_L regarding the bandwidth in the stop-bands around -3 dB. The analysis depicted in this figure has taken into account $M = 20$. In case of H_{MOD} , above around $r = 0.95$, the bandwidth around -3 dB is equal for all stop-bands. In turn, for H_{TDA} (and H_{RTDA}), such a bandwidth is approximately similar for all stop-bands, irrespective of the value of N (and J). On the other hand, for H_C , the width of the stop-bands around -3 dB depends on the frequency of the stop-band as well as the value of J . The attenuation in the stop-bands (as well as the gain in the pass-bands) may lie below -3 dB for smaller values of J (see Fig. 4.6). As the gain in the pass-bands approximates to 0 dB when J increases, the bandwidth of the stop-bands around -3 dB becomes narrower. However, it is not the same for all stop-bands, but it enlarges according to the fundamental frequency (f_d) of the stop-band (Fig. 4.13c). Such a difference is even higher for smaller values of J . Therefore, as shown in Fig. 4.13c, the higher the fundamental

frequency of the stop-band, the broader is its respective bandwidth.

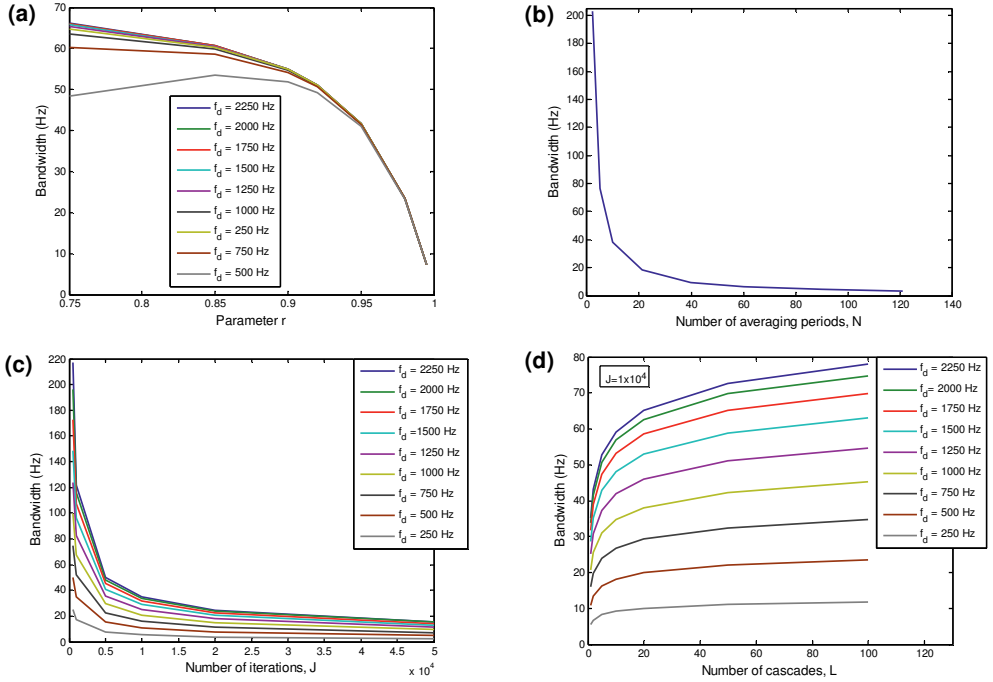


Figure 4.13: Bandwidth of the stop-bands around -3 dB ($M = 20$), for (a) H_{MOD} , (b) H_{TDA} , (c) H_C , and (d) H_L ($J = 1 \times 10^4$). $f_s = 5$ kHz.

In Fig. 4.14, an exemplary setting of parameters r , N , J , and L are used to illustrate the bandwidth of the stop-bands according to the fundamental frequency (f_d). As predicted by Eq. (4.16), the stop-band width is further enlarged when H_C is applied within the cascade implementation (H_L), especially in stop-bands with higher fundamental frequency (Figs. 4.13d and 4.14). As can also be observed in Fig. 4.14, H_C , H_L , and H_{MOD} do not provide a stop-band around 0 Hz, whereas it is produced by H_{TDA} and H_{RTDA} .

Regarding the computational effort, we verified that H_C and H_L are less computationally demanding than H_{MOD} , H_{TDA} , and H_{RTDA} . This can be ascribed to the computational efficiency of Eq. (4.11) which precisely requires the double of the computations of Eq. (4.2), as indicated in Figs. 4.1 and 4.3. The worst case of computational effort was for H_{MOD} , whose

application was seriously compromised because of expensive computational memory demand by higher values of M (Prodić et al., 2003; Tahir and Mazumder, 2014).

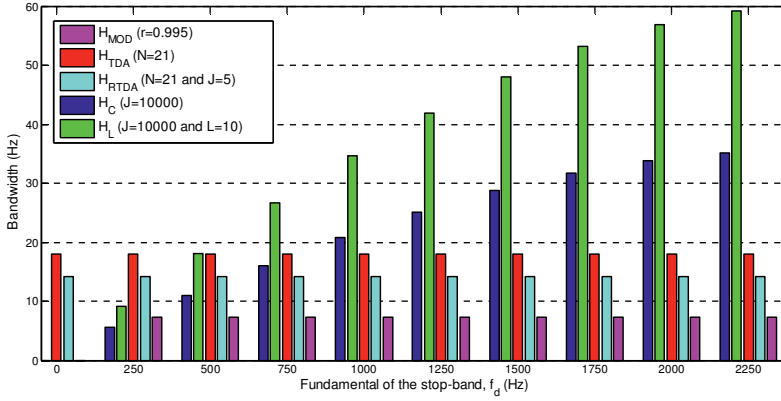


Figure 4.14: Bandwidth of the stop-bands around -3 dB ($M = 20$) for an exemplary setting of parameters r , N , J , and L . $f_s = 5$ kHz.

Because a comb-filter can also be implemented as a combination of notch filters, the selectivity provided by Eq. (4.21) could be used to design a highly selective comb-filtering approach with a variable bandwidth for the different filter stop-bands. Regarding the use of values of $M > 2$ in Eq. (4.20), we observed that some ripple around and below 0 dB may appear in the frequency response of H_{NTC} for smaller values of J , which can cause non-uniform gain along the pass-bands within the cascade implementation indicated in Eq. (4.21). Case higher values of J are used in this scenario, the filter gain becomes uniform, but the notch filter stop-band would have narrower bandwidth than when $M = 2$ in Eq. (4.21).

A limitation of the comb-filtering provided by Eqs. (4.11), (4.14), and (4.15) is concerned with the use of non-causal filters in real-time applications. Because Eq. (4.11) is a non-causal filter, Eqs. (4.14) and (4.15) also correspond to non-causal filters. As non-causal filters require full data (past and future samples of the unfiltered signal) they cannot be implemented in real-time applications. In the same way, the frequency-domain implementation of the filtering design method by using iterative filtering proposed in this chapter cannot be used in real-time applications as well because it also requires full data usage (Rangayyan, 2002). Non-causal filters might also cause side-effects by smearing some features in the filtering signal back in time (Rousselet, 2012; Widmann et al., 2015). An assessment about the preservation of the electrophysiological signal (neuronal EEG) in the comb-filtered signal by

(4.14) and (4.15) is performed in Chapter 5 (see Section 5.5).

In future work, Eq. (4.20) should have its performance compared with other notch filter approaches (Vlček and Zahradník, 2004), as well as Eq. (4.21) should be used and evaluated in applications where notch or comb-filtering is required. Additionally, other filters L_1 in Eq. (4.9) should be investigated and evaluated for the iterative comb-filtering implementation proposed here. Eqs. (4.15) and (4.16) should also be used and have its performance evaluated in signal processing applications where broadening of harmonic spectral lines is observed. This characteristic is further investigated in Chapters 5 and 6 for attenuation of the gradient artefact activity associated with broadening of artefact spectral lines caused by tiny subject head movements. As a further suggestion for future work, iterative time-domain averaging should be assessed by using other kinds of moving-averaging filters, such as the exponential averaging and running averaging (Braun, 2011).

4.6 Conclusions

A number of biomedical and other signal processing applications require the use of comb-filtering approaches that perform elimination or extraction of periodic waveforms with high degree of selectivity. As regards the elimination of periodic waveforms, the comb-filter should be able to suppress the harmonics associated with the periodic signal and, simultaneously, preserve the stochastic component or noisy signal according to the level of quality required by the application. Thus, it is important to make sure that the performance of the comb-filtering approach meets the selectivity requirements of the application. Since such requirements are not always met by the existing methods, investigation and proposal of novel approaches to improve the comb-filtering selectivity have been often described in the literature.

In this work, we have proposed and demonstrated how iterative filtering decomposition can be used to improve the selectivity of comb-filtering approaches as well as to design a novel notch-filter, which are based on the conventional FIR moving-average filter. The novel comb-filtering approach we devised has demonstrated to provide unit gain in the pass-bands, no effects on the signal phase, and broadening of the stop-band bandwidth around -3 dB according to the fundamental frequency of the stop-band. Moreover, a cascade implementation of the proposed approach permits to further increase the attenuation provided

in the stop-bands. In parallel, the iterative application of time-domain averaging allows using a smaller number of averaging epochs in order to estimate the periodic signal component. Hence, when a number of iterations are taken into consideration, the noise component can be attenuated with a factor higher than the square roots of the number of averaging epochs. Last, the novel notch filter implementation by iterative decomposition shows to provide a selective filtering with a large range of values for the stop-band bandwidth around -3 dB.

CHAPTER 5

Gradient Artefact Correction and Evaluation of the EEG Recorded Simultaneously with fMRI Data using Optimised Moving-Average*

5.1 Abstract

Over the past years, co-registered EEG-fMRI has emerged as a powerful tool for neurocognitive research and correlated studies, mainly because of the possibility of integrating the high temporal resolution of the EEG with the high spatial resolution of fMRI. However, additional work remains to be done in order to improve the quality of the EEG signal recorded simultaneously with fMRI data, in particular regarding the occurrence of the gradient artefact. We presented, in this chapter, the results of application of the novel comb-filtering implementation described in Chapter 4 for suppression of the gradient artefact in the EEG signal. This novel comb-filtering approach, hereafter named optimised moving-average filtering (OMA), is demonstrated to estimate and cancel out the gradient artefact activity associated with the TR-slice by integration of the time course EEG. Additionally, OMA is capable of performing the attenuation of the periodic artefact activity without accurate information about MRI triggers. By using the proposed approach, it is possible to achieve a better balance than the slice-average subtraction as performed by the established AAS method, regarding EEG signal preservation together with effective suppression of the gradient artefact. Since the stochastic nature of the EEG signal complicates the assessment of EEG preservation after application of the gradient artefact correction, we also propose a simple and effective method to account for it.

* This chapter was partly based on the papers:

Ferreira, J.L., Aarts, R.M., and Cluitmans, P.J.M. (2014a). Optimized moving-average filtering for gradient artefact correction during simultaneous EEG-fMRI. Proc. BRC 2014 Conf.: 1-6.

Ferreira, J.L., Wu, Y., Besseling, R.M.H., Lamerichs, R., and Aarts, R.M (2016). Gradient artefact correction and evaluation of the EEG recorded simultaneously with fMRI data using optimised moving-average. J. Med. Eng. 2016: article ID 9614323, 1-17.

5.2 Introduction

Integration of functional magnetic resonance imaging (fMRI) with electroencephalography (EEG) has offered the possibility of understanding new insights in neuroscientific studies because of the higher temporal and spatial measurements of brain activity when compared with the use of each technique separately. Rather than only an additional tool, co-registered EEG-fMRI has shown to be a promising and powerful technique for the mapping of brain activity, and has drawn the attention of several researchers and clinicians in recent years (Gotman and Pittau, 2011; Wiest et al., 2015; Matsuda et al., 2002; Murta et al., 2015; Goebel and Esposito, 2010; Mulert and Hegerl, 2009; Ritter and Villringer, 2006). Meanwhile, consolidation of simultaneous EEG-fMRI and enlargement of its range of applications still depend on enhancing the quality of the EEG signal acquired simultaneously with the fMRI data.

The MRI scanner constitutes quite a hostile environment for EEG because of the voltages induced by the magnetic fields used for acquisition of fMRI data. Such voltages correspond to three different types of artefact and may corrupt and distort the EEG signal, measured by the scalp electrodes. The first type of artefact is the *movement artefact* associated with motion of the subject head, electrodes, and wires into the static magnetic field (B_0) of the MRI scanner, which introduces temporary voltage fluctuations in the measured scalp potential (Sun and Hinrichs, 2009; Eichele et al., 2010; Maziero et al., 2016; Daniel et al., 2019). A second type of artefact is the *pulse* or *ballistocardiogram artefact*, caused by the pulsatile movement of the blood in scalp arteries within B_0 (Allen et al., 1998; Mahadevan et al., 2008; Oh et al., 2014). Finally, the *gradient* or *imaging acquisition artefact* is the voltage induced in the measured scalp potential by the application of rapidly varying magnetic field gradients for spatial encoding of the MRI signal, and radiofrequency pulses (RF) for spin excitation (Allen et al., 2000; Yan et al., 2009; Ritter et al., 2010). An in-depth analysis of the movement artefact as well as of the pulse artefact is out of the scope of this work, and further details about their characteristics and methods to suppress them can be found in the abovementioned references.

Regarding the gradient artefact, its amplitudes can be several orders (up to 10^4 μV) higher than the neuronal EEG signal. The gradient fields and RF pulses used in the MRI pulse sequences induce a characteristic and repetitive artefact waveform in the electrical potential picked up by the scalp EEG electrodes (scalp potential) which is approximately the

differential waveform of the corresponding gradient pulse (Anami et al., 2003). The onset of the artefact waveform corresponds to the occurrence of a RF pulse in the MRI sequence, such that the time separating consecutive RF pulses (termed repetition time – TR) matches the period of the artefact waveform. Typical values of TR range from hundreds of milliseconds to several seconds. The stack of repetitive individual MRI slices within a single TR occurs in the recorded scalp potential as signal peaks, and the time corresponding to the acquisition of one slice or slice-time (TR-slice) lies in the range of 50 – 150 ms. In the frequency-domain, the repetitive feature of the gradient artefact can be observed as discrete harmonic artefact frequency intervals, or “frequency bins”. The fundamental of each respective frequency bin corresponds to multiples of the inverse of the slice repetition time ($1/\text{TR-slice}$). For periodic or interleaved fMRI acquisition, in which delays are left between MRI volumes, harmonics in the frequency range of $1/\text{TR}$ appear convolved with the frequency bins associated with the slice repetition frequency, $1/\text{TR-slice}$ (Yan et al., 2009; Ritter et al., 2010; Anami et al., 2003; Sanei and Chambers, 2007; Solana et al., 2014).

In the literature, a number of solutions have been proposed to attenuate the effects of the gradient artefact at the source. For instance, it is possible to reduce its magnitude by laying out and immobilising the EEG leads, twisting the leads or modifying the lead paths, using a bipolar electrode configuration, and using a head vacuum cushion (Ritter et al., 2010; Mullinger et al., 2014; Chowdhury et al., 2015). The use of interleaved fMRI acquisition approaches has shown to be suitable for certain forms of brain activity, such as slowly varying rhythms and evoked responses. However, they are generally less flexible and experimentally efficient than continuous measurements (Eichele et al., 2010; Becker et al., 2005). According to Mullinger et al. (2011), the amplitudes of the gradient artefact can also be attenuated by adjusting the subject position within the MRI scanner. Chowdhury et al. (2014) have proposed the use of an EEG cap that incorporates electrodes embedded in an external layer and can record the gradient artefact separately from the EEG signal. Thus, subtraction between the signals recorded by internal and corresponding external electrodes allows the attenuation of the artefact. Although these solutions permit to achieve a considerable attenuation of the gradient artefact, its effective suppression and EEG correction must be performed by using dedicated post-processing signal approaches.

The average artefact subtraction (AAS) methodology (Allen et al., 2000) is the most established post-processing technique for gradient artefact suppression. Such an approach makes use of the assumption of periodic and stationary nature of the artefact to calculate an

average template from occurrences of the artefact waveform, which is then subtracted from the scalp potential. It also assumes the artefact and the EEG signal are not correlated, so that the subtraction of the averaged template permits an estimation of the corrected EEG (Braun, 1975). The performance of the AAS method highly depends on the reproducibility of the artefact waveform from epoch to epoch, which can be facilitated by utilising a setup that yields more accurate sampling of the gradient artefact waveform over time. Anami et al. (2003) and Mandelkow et al. (2006) have demonstrated that the use of synchronisation between the MRI clock and the EEG sampling frequency allows more precise sampling of the artefact and construction of a more accurate artefact template, in consequence. Thus, a cleaner EEG can be obtained after application of AAS in the recorded scalp potential. The performance of AAS has also high dependency on changes in the subject position. Head motions of the subject provoke alterations in the morphology of the artefact waveform over the artefact period, in such a way that the average artefact template cannot characterise individual occurrences of the artefact waveform. To address this problem, Allen et al. (2000) and Becker et al. (2005) proposed the use of a sliding average window implementation whereby the artefact template may be individually calculated for a particular occurrence of the artefact waveform. However, the correct choice of the number of averaging epochs poses difficulties to implementation of this approach because few windows can result in removal of the neuronal EEG, whereas the use of many windows can lead to remaining residual artefacts after AAS. Hence, to effectively suppress the gradient artefact with an adequate preservation of the neuronal EEG, additional approaches like low-pass filtering with a cut-off frequency around 50 – 80 Hz and adaptive noise cancelling must be employed to attenuate residual artefacts (Allen et al., 2000; Yan et al., 2009; Mullinger et al., 2014; Becker et al., 2005; Gebhardt et al., 2008; Mullinger et al., 2008b; Huang et al., 2012; Niazy et al., 2005).

Some variants of AAS have been devised in attempt to improve the accuracy of template calculation by using principal component analysis (Niazy et al., 2005), independent component analysis (Mantini et al., 2007), and spatial filtering (Brookes et al., 2008). To correct the jitter between EEG sampling frequency and MRI clock, more precise computing of the timing error has been addressed by Negishi et al. (2004), Gonçalves et al. (2007), and Huang et al. (2012). Nevertheless, estimation of an optimal artefact template is still the object of study. In addition, the study of ultra-high frequency neuronal activity as currently performed (Freyer et al., 2009) requires the use of interleaved approaches as well as customised MRI sequences that are generally not available to all investigators. Thus, further

improvements of AAS and development of novel correction methods are still required and highly desirable to enhance the quality of the EEG signal, mainly regarding EEG signals with low amplitude and with frequency activity in the gamma band (30 – 100 Hz), and high-frequencies oscillations between 100 and 500 Hz (Mullinger et al., 2014; Freyer et al., 2009).

Because of the risk of simultaneous removal of neuronal EEG activity during application of the gradient artefact correction approach, assessment of the preservation of the EEG signal should be carried out together with the effectiveness of the artefact suppression. This, however, has seldom been made systematically or in a consistent way (Freyer et al., 2009; Ritter et al., 2007; Grouiller et al., 2007; Bénar et al., 2003). In many EEG-fMRI studies, a single algorithm is chosen without proper justification, and often the quality of gradient artefact correction and EEG preservation is assessed by visual inspection only. The classical (gold standard) way of analysing EEG signals relies on visual judgement and recognition of sometimes very subtle or short duration phenomena such as spike-wave patterns in epilepsy studies or K-complexes in sleep research. Nonetheless, those patterns may easily be distorted or obscured after application of the artefact correction approach. A difficulty that arises with regard to the analysis of spontaneous EEG excerpts is the stochastic and non-stationary nature of the neuronal EEG. On the other hand, identification of single events in the corrected EEG is not suitable for a scenario in which the signal of interest is the spontaneous EEG and, thus, larger EEG excerpts over time should be analysed. Additionally, the lack of knowledge of the true EEG signal makes it difficult to compare the power spectra of artefact-corrected EEG excerpts with the spectra of the EEG recorded inside or outside the scanner. Thereby, a more systematic approach to assess and compare the performance of the gradient artefact correction methods is advised in some applications, rather than only relying on the analysis of single events or the quantification of EEG power in certain spectral bands. Moreover, to date, generalisation of the correction results for different types of EEG data has been poorly made as well (Ritter et al., 2010; Ritter et al., 2007; Grouiller et al., 2007; Bénar et al., 2003).

This chapter presents a novel methodology for gradient artefact correction based upon the novel comb-filtering approach presented in Chapter 4, hereafter referred to as *optimised moving-averaging (OMA) filtering*. As mentioned in Chapter 4, OMA filtering constitutes a modality of iterative filtering decomposition (Lin et al., 2009; Wang et al., 2012), and has been exploited in a research project that our group has undertaken to investigate characteristics and features of the gradient artefact that might be used to attenuate, correct, and improve the quality of the corrected EEG signal (Ferreira et al., 2014a; Ferreira et al.,

2014b; Ferreira et al., 2013a; Ferreira et al., 2012). Optimised moving-average makes use of the forward-backward application of an FIR moving-average named double average filter (Eq. (4.10)) that is likened to an integration procedure to suppress the artefact and estimate partial components of the corrected EEG at the same time. Iterative application of such a procedure allows estimation of the corrected EEG as a sum of the calculated partial components. Rather than estimation of an average template, as performed by the AAS implementation, the artefact is calculated not for epochs, but sample-by-sample, as described in the Section 5.3. To assess the degree of EEG preservation, we have devised a novel and simple evaluation approach that allows accounting for the stochastic nature of the neuronal EEG, and was used to perform a comparative analysis of OMA with AAS. Comparison between the performance of OMA and AAS shows that our method can provide an improved balance for the trade-off suppression of the artefact and preservation of the neuronal EEG signal, as shown in Section 5.5. In parallel, the use of low-pass filtering or another correction approach to suppress residual artefacts after application of OMA can be avoided, and thus our method potentially better preserves highly relevant high-frequency EEG features. Furthermore, the results indicate that our approach is capable of correcting the EEG data even within a scenario of misalignment between EEG sampling interval and the MR slice-time, and without accurate information about MRI triggers. Analysis of the application of the gradient artefact correction in EEG data sets recorded by using MRI scanners from two different vendors is also provided in Section 5.5.

5.3 Methods

5.3.1 EEG and fMRI data

Our devised methodology was tested in two types of EEG data simultaneously acquired with fMRI data. The EEG data sets were kindly provided and given consent for publication by Brain Products GmbH, Gilching, Germany. Data acquisition was conducted in accordance with the Declaration of Helsinki, approved by the responsible Ethics Committee, and the subjects gave their informed written consent before participating in the study. One of the EEG data sets was recorded within a Philips scanner (hereafter referred to as Philips data), whereas the other EEG data set was recorded within a GE scanner (hereafter referred to as GE data). The EEG data in both the Philips and GE scanner were recorded in two volunteers by using a MRI-compatible 64 channels EEG system (BrainAmp MR, Brain Products GmbH, Gilching,

Germany). An MRI-compatible EEG cap (BrainCap MR, EASYCAP GmbH, Herrsching, Germany) containing sintered Ag-AgCl electrodes was used to pick up the scalp potential. The EEG cap was arranged in accordance with the standard 10-5 electrodes positioning, with the FCz position used as reference and the ground electrode located at the AFz position. The impedance of all electrodes was set below 30 k Ω , and one additional electrode was placed on the subject back to record the ECG signal. The EEG amplifiers were positioned inside the scanner bore near the middle axis and connected via fibber optic to a PC interface located outside the scanner room. SyncBox (Brain Products GmbH, Gilching, Germany) was used to synchronise the internal sampling clock of the EEG amplifier and the MRI scanner 10 MHz master clock. The signal acquisition was performed using a sampling rate at 5000 Hz and measurement resolution at 0.5 μ V. Hardware-filtering in the frequency band between 0.016 Hz and 250 Hz was applied before data digitalisation to prevent saturation and reduce the gradient artefact amplitude. During acquisition, the volunteers were instructed to perform a simple opening/closing eyes manoeuvre at regular time intervals. Regarding acquisition of fMRI data, the following setups were used:

A) Philips data: acquisition of the Philips data set was carried out using a 3 T Achieva Scanner (Philips, Eindhoven, The Netherlands). One volunteer was scanned using a functional echo-planar imaging (EPI) sequence with 40 transversal slices and volume repetition time (TR) equal to 2000 ms. The MRI clock and the EEG sampling frequency have been synchronised, so that TR was set as a multiple of the EEG sampling interval. fMRI data acquisition was continuously performed, and TR was adjusted as a multiple of the slice-time (TR-slice). Hence, TR-slice was equal to 2000 ms/ 40 slices = 50 ms. Acquisition of the Philips data was approximately performed during 4 minutes.

B) GE data: acquisition of the GE data set was carried out using a 3 T Discovery MR750 Scanner (GE, Waukesha, USA). A second volunteer was scanned using an EPI sequence with 28 transversal slices and volume repetition time (TR) equal to 2000 ms. fMRI data acquisition was continuously performed, and the MRI clock and the EEG sampling frequency have been synchronised for a period equal to 500 ms, corresponding to seven times TR-slice. Thereby, although TR was approximately adjusted as a multiple of the slice-time (TR-slice), TR-slice was not aligned and did not match a multiple of the EEG sampling interval. Acquisition of the GE data was approximately performed during 10 minutes.

5.3.2 Proposed methodology for gradient artefact correction

The proposed methodology for gradient artefact correction was implemented in two steps: (i) *peak detection and TR-slice estimation*; and (ii) *optimised moving-average filtering*. The recorded scalp potential, s_n , in one specific EEG channel was mathematically modelled as a linear superposition of the neuronal EEG, e_n , and the induced voltage associated with the gradient artefact interference, g_n :

$$s_n = e_n + g_n. \quad (5.1)$$

For the sake of notation simplification, henceforth we have omitted the subscript i indicative of the EEG electrode. Likewise, we will use the time-discrete notation, where n is the time sample.

5.3.3 Peak detection and TR-slice estimation

An initial detection of the peaks corresponding to the onset of the MRI slices observed in the recorded scalp potential must be performed according to the proposed methodology. Such detection permits estimation of the slice-time (TR-slice) according to the time basis of the EEG sampling system utilised for acquisition of the EEG data. Within a scenario of alignment between the MRI slice-time and the EEG system sampling interval, the estimated TR-slice precisely corresponds to a multiple of the EEG sampling interval (Mandelkow et al., 2006; Gebhardt et al., 2008; Mullinger et al., 2008b). However, when there is misalignment between the MRI slice-time and the EEG sampling interval, the value estimated for TR-slice may not match a multiple of the sampling interval and, thereby, vary. This variation can be accounted for application of the optimised moving-average filtering, as described in the following section.

5.3.4 Optimised moving-average filtering (OMA)

Figure 5.1 shows an excerpt of the scalp potential picked up from the Philips data, in which TR is a multiple of TR-slice. The time measured between two consecutive peaks in the signal matches the slice-time or TR-slice. Assuming that the artefact waveform is stationary, any moving-average window M with length equal to TR-slice along the signal contains the artefact waveform period, but with a different onset of those samples localised in the signal peaks.

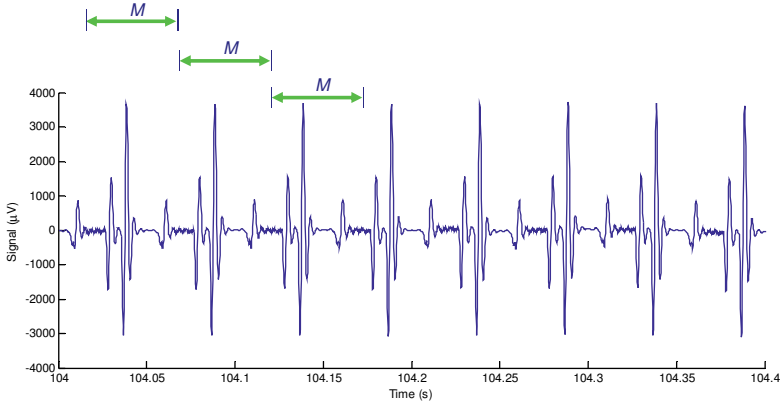


Figure 5.1: Scalp potential excerpt recorded during continuous acquisition of fMRI data. Assuming that the artefact waveform is stationary, any moving-average windows of length M ($=$ TR-slice) along the signal contains the artefact waveform corresponding to one slice, but with onset other than those samples localised in the signal peaks.

Thereby, assuming that the gradient artefact waveform is stationary and has zero mean, integration of Eq. (5.1) over the period M results in cancellation of the artefact waveform. Also assuming that the terms of Eq. (5.1) are uncorrelated, the resulting value of the integral along the scalp potential, \mathbf{s} , corresponds to a mean estimate of the neuronal EEG, $\overline{\hat{e}_n}$. This integral can be described as an FIR moving-average filter with order M :

$$\frac{1}{M} \sum_{k=0}^{M-1} s_{n-k} = \frac{1}{M} \sum_{k=0}^{M-1} (e_{n-k} + g_{n-k}), \quad (5.2)$$

$$= \frac{1}{M} \sum_{k=0}^{M-1} (e_{n-k}) + \frac{1}{M} \sum_{k=0}^{M-1} (g_{n-k}) = \overline{\hat{e}_n}. \quad (5.3)$$

Because of the phase distortion caused by the moving-average filter (Oppenheim and Schaffer, 1999; Rangayyan, 2002; Proakis and Manolakis, 1996), the mean value $\overline{\hat{e}_n}$ is not in phase with the neuronal EEG, e_n . To make them in phase, the moving-average must be backward applied in Eq. (5.3):

$$\frac{1}{M} \sum_{k=0}^{M-1} \overline{\hat{e}_{n+k}} = \frac{1}{M} \sum_{k=0}^{M-1} \left[\frac{1}{M} \sum_{k=0}^{M-1} s_{n-k} \right]_{n+k} \quad (5.4)$$

$$\begin{aligned}
&= \frac{1}{(M)^2} (s_{n-M+1} + 2s_{n-M+2} + \dots + (M-1)s_{n-1} + (M)s_n + (M-1)s_{n+1} + \dots + 2s_{n+M-2} + s_{n+M-1}) \\
&= \frac{1}{(M)^2} \sum_{k=-M+1}^{M-1} (M-|k|)s_{n+k} = e_{\text{comp},1,n} .
\end{aligned} \tag{5.5}$$

Thereby, according to Eqs. (5.4) and (5.5), forward-backward application of the moving-average filter in the recorded scalp potential results in the signal $\mathbf{e}_{\text{comp},1}$ that is in phase and constitutes a mean approximation of the neuronal EEG (Ferreira et al., 2014a):

$$\mathbf{e}_{\text{comp},1} \approx \hat{\mathbf{e}} . \tag{5.6}$$

Equation (5.5) corresponds to the double average filter indicated in Eq. (4.10) and acts as a smoothing filter, in such a way that the signal $\mathbf{e}_{\text{comp},1}$ contains low-frequency activity associated with $\hat{\mathbf{e}}$. In turn, the frequency activity associated with the gradient artefact is contained in the signal, $\mathbf{e}_{\text{high},1}$, resulting from the subtraction of $\mathbf{e}_{\text{comp},1}$ from \mathbf{s} :

$$\mathbf{e}_{\text{high},1} = \mathbf{s} - \mathbf{e}_{\text{comp},1} . \tag{5.7}$$

Since high-frequency components associated with $\hat{\mathbf{e}}$ remain in $\mathbf{e}_{\text{high},1}$, it is possible to obtain an estimate of such components by the iterative application of Eq. (5.5) in $\mathbf{e}_{\text{high},1}$. The second component, $e_{\text{comp},2,n}$, results from the application of Eq. (5.5) in $\mathbf{e}_{\text{high},1}$:

$$e_{\text{comp},2,n} = \frac{1}{(M)^2} \sum_{k=-M+1}^{M-1} (M-|k|)e_{\text{high},1,n+k} , \tag{5.8}$$

and the signal $\mathbf{e}_{\text{high},2}$ can be obtained afterwards:

$$\mathbf{e}_{\text{high},2} = \mathbf{e}_{\text{high},1} - \mathbf{e}_{\text{comp},2} . \tag{5.9}$$

This procedure was repeated so forth, for a number j of iterations, allowing estimation of the component $\mathbf{e}_{\text{comp},j}$:

$$e_{\text{comp},j,n} = \frac{1}{(M)^2} \sum_{k=-M+1}^{M-1} (M-|k|)e_{\text{high},j-1,n+k} . \tag{5.10}$$

As mentioned in Chapter 4, this procedure also constitutes a modality of iterative filtering decomposition (IFD) in which Eq. (5.5) is termed double average filter (Lin et al., 2009; Wang et al., 2012). The convergence of IFD has been demonstrated in Lin et al. (2009), and is ensured by the coefficients (masks) of the double average filter having value between 0 and 1.

Finally, the estimate $\hat{\mathbf{e}}$ of the corrected EEG can be calculated by the sum of the J estimated components:

$$\hat{\mathbf{e}} = \sum_{j=1}^J \mathbf{e}_{\text{comp},j} . \quad (5.11)$$

Implementation of Eq. (5.11) can be visualised in the scheme of Fig. 5.2.

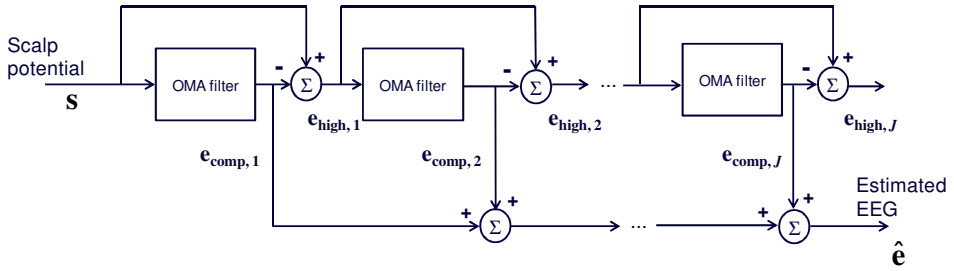


Figure 5.2: Scheme of the optimised moving-average filtering (OMA) during gradient artefact correction: estimation of the actual EEG ($\hat{\mathbf{e}}$) is carried out by iterative application of Eq. (4.10) in the scalp potential and successive $\mathbf{e}_{\text{high},j}$, followed by subtraction of the components $\mathbf{e}_{\text{comp},j}$. The blocks labelled as *OMA filter* represent the forward-backward moving-average filtering, as described in Eq. (4.10).

Application of the z -transform in the OMA filter, described in Eq. (5.10), permits to find its transfer function:

$$H_{OMA}(z) = \frac{1}{(M)^2} \frac{(1-z^{-M})(1-z^M)}{(1-z^{-1})(1-z)}, \quad (5.12)$$

which corresponds to Eq. (4.11). Making use of Eq. (5.12), the frequency response of H_{OMA} can be calculated by setting $z = e^{j\omega}$, as described in Eqs. (4.12) and (4.13). Figure 5.3 shows the magnitude and phase response of H_{OMA} that is, therefore, similar to the frequency response calculated for $H_D(z)$ in Eq. (4.11):

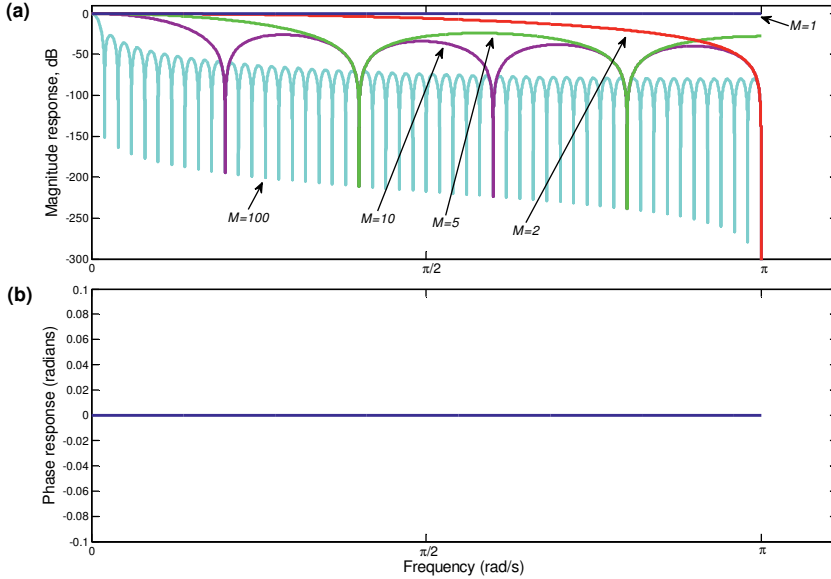


Figure 5.3: Frequency response of the OMA filter for some values of M : (a) magnitude response; (b) phase response. The phase response is the same for any values of M .

From Eq. (5.7), we can find the transfer function between $\mathbf{e}_{\text{high},1}$ and \mathbf{s} :

$$H_1 = 1 - \left[\frac{1}{(M)^2} \frac{(1 - z^{-M})(1 - z^M)}{(1 - z^{-1})(1 - z)} \right] = 1 - H_{OMA}(z). \quad (5.13)$$

Hence, $\mathbf{e}_{\text{high},J}$ corresponds to:

$$E_{\text{high},J}(z) = [1 - H_{OMA}(z)]^J S(z). \quad (5.14)$$

Therefore, Eqs. (5.12), (5.13), and (5.14) allow removing the J cascade components shown in Fig. 5.2 and establishing the transfer function between $\hat{\mathbf{e}}$ and \mathbf{s} :

$$\frac{\hat{E}(z)}{S(z)} = 1 - [1 - H_{OMA}(z)]^J = H_C(z). \quad (5.15)$$

In Fig. 5.4, the magnitude response of $H_C(z)$ in Eq. (5.15) is illustrated, taking into account $M = 250$ (value of TR-slice estimated for the Philips data) and some values of J .

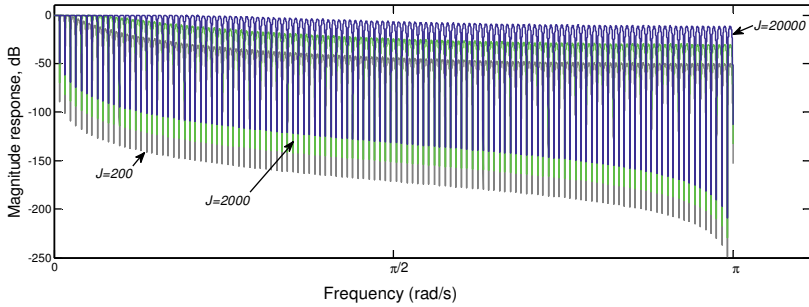


Figure 5.4: Magnitude response of Eq. (5.15), taking into account $M = 250$, and some values of J .

It can be observed that increasing of J is followed by substantial droop reduction (increasing gain) in the filter pass-bands, likewise as depicted in Fig. 4.6. On the other hand, increasing of J is also followed by reduction in the attenuation in the filter stop-bands.

To improve the attenuation in the stop-bands, $H_c(z)$ has been also applied in the cascade implementation indicated in Eq. (5.16):

$$H_L(z) = [H_c(z)]^L, \quad (5.16)$$

where L is the number of cascades. Therefore, Eqs. (5.15) and (5.16) correspond, respectively, to Eqs. (4.15) and (4.16), and Eq. (5.16) equals Eq. (5.15) when $L = 1$. Figure 5.5 depicts the magnitude response of $H_L(z)$, for $L = 2$ and $L = 5$, taking into account $M = 250$, and some values of J . As noticed, Eq. (5.16) can be used to provide reduced droop in the pass-bands together with higher attenuation in the stop-bands according to the values of J and L . Additionally, Eqs. (5.15) and (5.16) possess a zero-phase characteristic as well, similar to that observed in Fig. 5.3b.

Therefore, Eqs. (5.15) and Eq. (5.16) can be used to estimate the artefact-corrected EEG in z -domain. On the other hand, in the time-domain, the corrected EEG, $\hat{\mathbf{e}}$, can be calculated by using either Eq. (5.11) or Eq. (5.17):

$$\hat{\mathbf{e}} = \mathbf{s} - \mathbf{e}_{\text{high},J}. \quad (5.17)$$

As indicated in Eqs. (5.10) and (5.12), the estimate $\mathbf{e}_{\text{comp},j}$ is calculated sample-by-sample, rather than calculation and subtraction of an average artefact template. Thus, the optimised moving-average filtering implementation depicted in Fig. 5.2 permits an individual

calculation and subtraction of the artefact for each signal sample rather than epochs averaging, as performed by AAS.

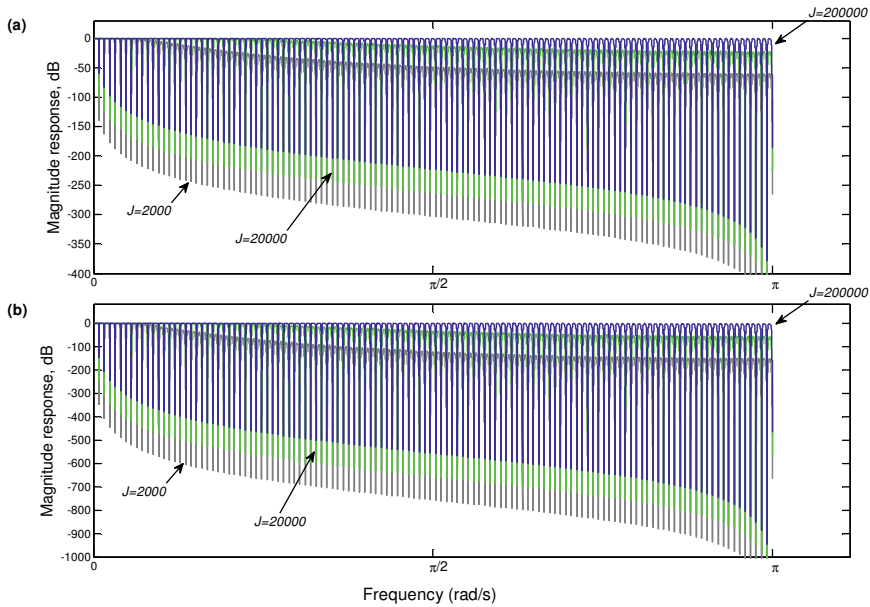


Figure 5.5: Magnitude response of Eq. (5.16) for (a) $L = 2$ and (b) $L = 5$, taking into account $M = 250$ and some values of J .

Hence, the inherent uncertainty associated with averaged samples and the influence of alterations of the artefact waveform caused by subject head motions might be minimised by using the proposed approach. To assess the performance of the proposed approach in a scenario of misalignment between the EEG sampling interval and the slice-length, OMA has been applied by using Eq. (5.16), taking into consideration some values of L , as shown in Section 5.5.

5.4 Evaluation of the gradient artefact correction and comparative analysis

According to Ritter et al. (2007), two measures must be complementarily used to evaluate the performance of the gradient artefact correction approach: (i) the effectiveness of gradient artefact attenuation; and (ii) the degree of preservation of the neuronal EEG after artefact correction.

5.4.1 Assessment of the artefact attenuation

To assess the gradient artefact attenuation, the RMS and amplitude of the artefact voltage over time were calculated taking into account the subtraction between s and the estimation of the corrected EEG, \hat{e} . Also we performed calculation of the spectral power attenuation around the fundamental of the frequency bins associated with the slice repetition frequency ($1/TR$ -slice). To this end, we have estimated and took into consideration a bandwidth of ± 1 Hz around the fundamental of each frequency bin. Calculation of the spectral power attenuation was carried out for the frequency bins below 500 Hz. Although a band limiter set at 250 Hz was employed during data acquisition, we would rather evaluate the attenuation in frequency bins up to 500 Hz because of the artefactual energy that may remain above the band limiter edge frequency (Gutberlet, 2010). Equation (5.18) was used to compute the spectral power attenuation in decibel:

$$\text{Attenuation} = -20 \times \log \left(\frac{P_A}{P_B} \right) \text{ dB}, \quad (5.18)$$

where P_B and P_A correspond to the spectral power within the harmonic artefact bins, before and after application of the gradient artefact correction, respectively.

5.4.2 Evaluation of the EEG preservation

The scheme depicted in Fig. 4.6 (see Fig. 3.11) was used to perform the quantitative evaluation of the EEG preservation:

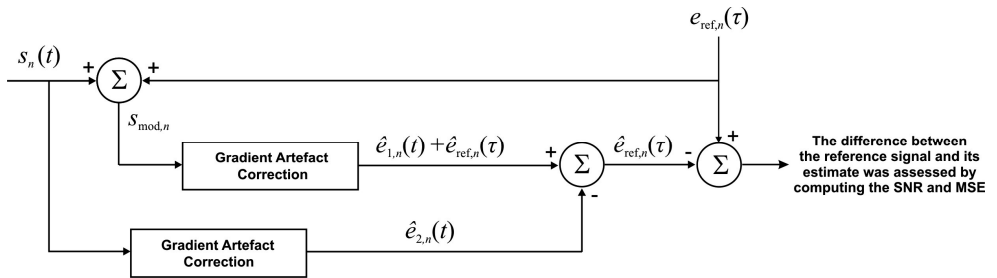


Figure 5.6: Proposed scheme for measurement of the EEG signal preservation by linear addition of an artefact-free EEG excerpt, $e_{ref,n}$, in the recorded scalp potential, s_n . Both $e_{ref,n}$ and s_n were picked up from the same EEG channel at different times, t and τ . The blocks labelled as **Gradient Artefact Correction** match one specific gradient artefact correction approach (OMA or AAS).

As indicated in this figure, a reference EEG signal, $e_{\text{ref},n}$, has been linearly added to the measured scalp potential, s_n , thus generating the modified signal $s_{\text{mod},n}$. As $e_{\text{ref},n}$, we used EEG excerpts recorded inside the MRI scanner during non-scan periods. Thereby, the letters τ and t indicate that the reference EEG excerpt has been recorded at a different time than s_n . The gradient artefact correction was then applied to $s_{\text{mod},n}$ and s_n , resulting in the estimates $\hat{e}_{1,n} + \hat{e}_{\text{ref},n}$ and $\hat{e}_{2,n}$, respectively. Thereby, the subtraction between these estimates allows obtaining an estimate of the reference signal, $\hat{e}_{\text{ref},n}$, which was finally compared with $e_{\text{ref},n}$. Equations (5.19) and (5.20) were used to calculate the signal-to-noise ratio (SNR) and the mean squared error (MSE) as complimentary measures of temporal and frequency contents of $\hat{e}_{\text{ref},n}$ in comparison with $e_{\text{ref},n}$:

$$\text{SNR} = \frac{\text{cov}(\mathbf{e}_{\text{ref}}, \hat{\mathbf{e}}_{\text{ref}})}{\sigma_{\mathbf{e}_{\text{ref}}} \cdot \sigma_{\hat{\mathbf{e}}_{\text{ref}}}}, \quad (5.19)$$

$$\text{MSE} = \frac{1}{N} \sum_{n=1}^N (e_{\text{ref},n} - \hat{e}_{\text{ref},n})^2. \quad (5.20)$$

The SNR calculated by Eq. (5.19) corresponds to a measure of cross-correlation and allows an evaluation and comparison of frequency characteristics between $e_{\text{ref},n}$ and $\hat{e}_{\text{ref},n}$ (Proakis and Manolakis, 1996). Values of SNR closer to unity mean higher similarity between $e_{\text{ref},n}$ and $\hat{e}_{\text{ref},n}$. In turn, smaller values of MSE computed according to Eq. (5.20) indicate higher correspondence between $e_{\text{ref},n}$ and $\hat{e}_{\text{ref},n}$ over time. In addition to being of simple implementation, the evaluation scheme of Fig. 5.6 has the advantage of allowing the assessment of longer EEG excerpts by accounting for the stochastic nature of the neuronal EEG signal, and not single events only.

5.4.3 Comparative analysis

The results obtained by application of OMA were compared with those obtained by subtraction of a mean template, according to the average artefact subtraction (AAS) methodology (Allen et al., 2000; Becker et al., 2005). Both OMA and AAS were applied to the Philips data and GE data set. For implementation of OMA, we developed and applied the proposed methodology to the EEG recordings in MATLAB (The MathWorks Inc., Natick, USA) environment. In turn, the average artefact subtraction was carried out by utilising the software Brain Vision Analyzer 2 (Version 2.1.0.327; Brain Products GmbH, Gilching, Germany). As benchmark, a sliding moving-average window implementation of 21 epochs

was used for construction of the average artefact template. The reason for using 21 epochs was based upon the default settings of the Brain Vision Analyzer. The epoch length to be averaged and construct the artefact template was set at 50 ms (TR-slice) for the Philips data, and 500 ms for the GE data. Such values were chosen to match the minimum period in which the fMRI data were synchronised as a multiple of the EEG sampling interval, so that the influence of head motions in longer sliding average windows might be prevented.

After application of OMA and AAS, assessment of artefact attenuation and evaluation of the EEG preservation, as described above, were carried out using MATLAB. All 63 EEG channels were used to perform the analysis of the GE data. For the Philips data, the channel TP8 was excluded from the analysis because the entire recordings were corrupted by artefacts which made it impossible to pick up a signal excerpt representative of $e_{\text{ref},n}$.

5.5 Results

Figure 5.7a depicts an exemplary scalp potential excerpt, Philips data, electrode position Fz. In Fig. 5.7b, the power spectrum of the signal of Fig. 5.7a is shown, and the harmonic activity associated with the gradient artefact can be visualised as spectral peaks at multiples of the fundamental frequency equal to 20 Hz, corresponding to the frequency bins associated with $1/\text{TR-slice}$. By performing the peak detection associated with the gradient artefact in the signal of Fig. 5.7a, TR-slice was estimated in even lengths of 250 samples, thus confirming the alignment between TR-slice and the EEG sampling interval for the Philips data. Hence, for application of the optimised moving-average (OMA), we set $M = 250$. Figure 5.8a depicts the artefact-corrected EEG by using Eq. (5.15), for $J = 200$, $J = 2000$, and $J = 200000$.

It can be seen in Fig. 5.8b that the harmonic activity associated with the gradient artefact has been attenuated for the used values of J . Increasing the value of J shows a better preservation of the power activity along the spectrum of the corrected EEG signal, mainly at high-frequencies. Smaller attenuation in the frequency bins associated with $1/\text{TR-slice}$ is also noticed when the value of J is increased, which agrees with the comb-filtering response depicted in Fig. 5.4 as well.

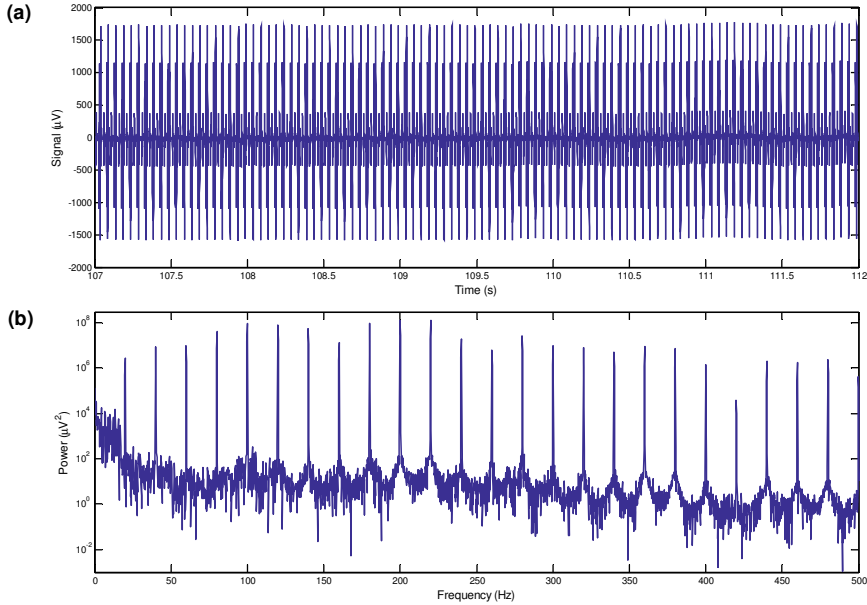


Figure 5.7: (a) Scalp potential excerpt picked up from the EEG electrode Fz of the Philips data; (b) power spectrum of the signal (a), showing up the harmonic artefact activity associated with the gradient artefact at multiples of $1/TR$ -slice (TR -slice = 250 samples), equal to 20 Hz for the Philips data.

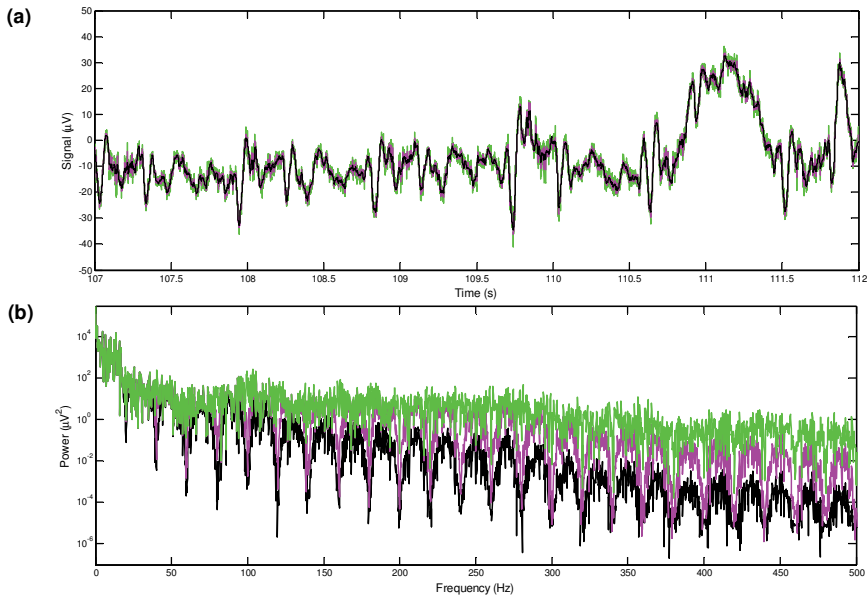


Figure 5.8: (a) Scalp potential excerpt of Fig. 5.7a after application of OMA, taking into account Eq. (5.15), for $J = 200$ (dark trace), $J = 2000$ (pink trace), and $J = 200000$ (green trace); (b) power spectra corresponding to the signals of (a).

Therefore, the choice of the value of J should be made in such a way as to provide effective attenuation of the artefact activity in the frequency bins and adequate preservation of the EEG signal. However, Eq. (5.15) might not provide enough attenuation of the artefact, and Eq. (5.16) can be used instead, as shown in the next example.

An illustrative scalp potential excerpt picked up from the GE data, EEG electrode position Fp1, is depicted in Fig. 5.9a, and its corresponding power spectrum is shown in Fig. 5.9b.

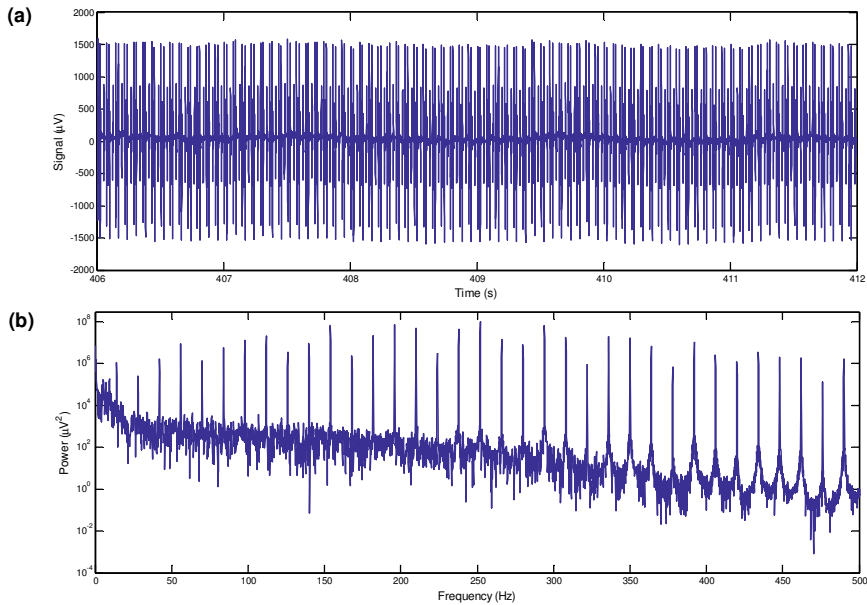


Figure 5.9: (a) Scalp potential excerpt picked up from the EEG electrode Fp1 of the GE data; (b) power spectrum of the signal (a), showing up the harmonic artefact activity associated with the gradient artefact at multiples of $1/TR$ -slice (TR -slice = 357 ± 1 samples), approximately equal to 14 Hz for the GE data.

For these data, the slice-length has not been aligned with the EEG sampling interval, in such a way that the value of TR -slice was estimated at 357 ± 1 samples. To demonstrate the performance of the proposed method to suppress the gradient artefact in this scenario, we used Eq. (5.16), taking into account $M = 357$ and $J = 200000$, for $L = 1$ (Eq. (5.15)), $L = 5$, and $L = 100$. Figure 5.10a depicts the corresponding power spectra of the corrected EEG. For $L = 1$, the gradient artefact was not effectively attenuated by OMA, so that residual spectral power artefact remained in most of artefact frequency bins (dark trace). Figure 5.10b shows a detail of the time course corrected EEG signals around 408 s in which the presence of such residuals can also be noticed (thin dark traces). Nevertheless, higher values of L allow

increased attenuation of the harmonic artefact activity (Figs. 5.10a and 5.10b). For $L = 5$ (pink trace), residual spectral power associated with the artefact were substantially attenuated in the bandwidth up to 300 Hz. In turn, when $L = 100$ (green trace), such attenuation was even higher, and artefact harmonic activity in the frequency bins could be strongly reduced in the bandwidth below 500 Hz.

As observed in the spectrum details around 56 and 336 Hz (Fig. 5.10a), by increasing L , it provokes larger attenuation around the frequency bins. Thereby, Eq. (5.16) can be used to account for the enlargement of the spectral artefact harmonic lines by the alignment error between the EEG sampling interval and TR-slice, thus being able to correct the scalp potential within this scenario. No signal interpolation for correction of the artefact waveform phase has been performed. Figure 5.10c depicts the power spectra of the corrected EEG after application of OMA (blue trace, $J = 200000$ and $L = 100$) and the mean template subtraction by AAS (red trace) in the signal of Fig. 5.9a. As can be noticed for the signal corrected by the AAS method, residual power associated with the artefact activity arose in higher-frequencies bins, above around 200 Hz. In Fig. 5.10d, a detail around 408 s of the time course of the corrected EEG by OMA and AAS is also depicted. Some small amount of residual artefacts corresponding to the artefact residual power can be noticed in the time course signal corrected by AAS. Rather, those residuals could be attenuated by using OMA.

Both OMA and AAS play a role of comb-filtering approaches (Braun, 1975; Ferreira et al., 2014a) whereby harmonic frequency components associated with the slice repetitive frequency ($1/\text{TR-slice}$) can be attenuated. On one hand, AAS implementation consists of a coherent detection-based comb-filtering process (Braun, 1975; Braun, 2011) that is carried out by subtraction of the template with period TR-slice. As such, the AAS method is highly dependent on precise sampling of the scalp potential as well as accurate alignment amongst the averaging epochs to construct the average template. Moreover, small drifts and subject head motions can provoke broadening of the high-frequency artefact spectral lines, in such a way that AAS may fail to attenuate them, and residual artefacts arise in the corrected EEG as a consequence (Spencer, 2015). This helps to explain why AAS is not effective in eliminating the high-frequency artefact activity shown in Figs. 5.10c and 5.10d, whose attenuation is more affected by imprecise sampling than low-frequency artefact activity as well (Mandelkow et al., 2006; Huang et al., 2012). On the other hand, OMA performs comb-filtering making use of the filtering implementation described above. By using proper values of M , J , and L in Eq. (5.16), thereby, it allows OMA to effectively account for the attenuation of high-

frequency artefact activity, as depicted in Fig. 5.10.

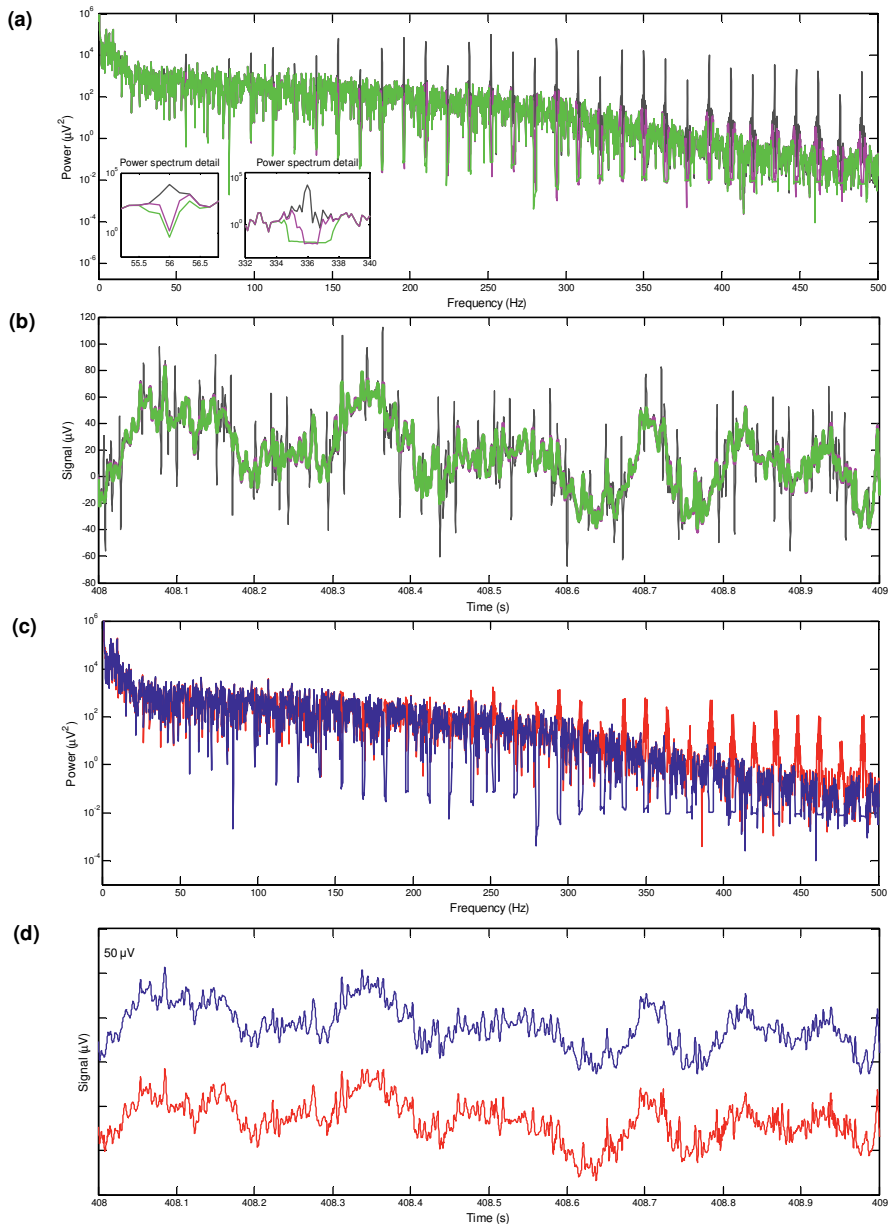


Figure 5.10: (a) Power spectrum of the scalp potential of Fig. 5.9a after application of OMA, taking into account Eq. (5.16) and $J = 200000$, for $L = 1$ (dark trace), $L = 5$ (pink trace), and $L = 100$ (green trace); (b) detail in the time course corrected EEG by OMA with similar setup and colour code as indicated in (a); (c) power spectrum of the scalp potential of Fig. 5.9a taking into account Eq. (5.16) for $L = 100$ (blue trace), and power spectrum of the corrected EEG by AAS (red trace); (d) detail in the time course corrected EEG by OMA (blue trace) and AAS (red trace).

The results presented in Tables 5.1 – 5.5 for the OMA correction (Eq. (5.16)) refer to $J = 200000$ and $L = 1$ (Philips data), and $J = 200000$ and $L = 100$ (GE data).

Table 5.1: Median artefact voltages attenuation over time.

Method	Philips data		GE data	
	RMS (μV)	Amplitude (μV)	RMS (μV)	Amplitude (μV)
OMA	622.5291	5167.6000	207.1564	1847.9000
AAS	622.5524	5172.3000	207.1422	1858.1000

Table 5.2: Median attenuation in the artefact frequency bins.

EEG data set					
Philips data			GE data		
Frequency Bin (Hz)	OMA	AAS	Frequency Bin (Hz)	OMA	AAS
	Attenuation (dB)	Attenuation (dB)		Attenuation (dB)	Attenuation (dB)
20	45.3751	57.5263	14.01	16.9613	16.1357
40	78.9570	91.8088	28.01	33.6730	32.4054
60	85.6000	96.0201	42.02	60.0656	55.6886
80	98.2415	111.0143	56.02	62.9907	61.6082
100	98.3248	110.7207	70.03	47.2065	40.3737
120	110.7477	121.1444	84.03	67.6971	63.3023
140	117.0230	126.7208	98.04	70.2665	64.4877
160	104.1135	110.7799	112.04	77.2094	71.3954
180	112.6177	119.6797	126.05	76.8379	64.6367
200	120.2490	126.1687	140.06	71.6883	61.2908
220	122.7164	127.8049	154.06	92.4285	82.1534
240	120.7178	123.6904	168.07	73.6179	57.6112
260	122.9039	125.0317	182.07	103.6173	77.8464
280	116.5943	117.3843	196.08	104.8400	82.8587
300	130.2747	129.5068	210.08	111.4681	81.6893
320	141.4297	139.5853	224.09	111.8922	80.3991
340	140.0759	136.2834	238.10	127.1047	78.2103
360	142.5260	138.4374	252.10	143.5516	85.3269
380	144.0613	137.4788	266.11	149.7997	78.9997
400	140.8645	132.8269	280.11	153.8597	79.6079
420	137.6477	128.4942	294.12	174.5559	84.2324
440	142.1547	131.7775	308.12	163.7475	77.0851
460	142.6946	131.4058	322.13	173.4991	79.8261
480	141.9741	130.2354	336.13	173.0371	82.8779
500	131.2361	117.6283	350.14	179.3995	81.8668
			364.15	176.0360	81.8207
			378.15	160.9627	79.0052
			392.16	181.9554	80.8334
			406.16	163.7591	77.9195
			420.17	175.0643	79.6067
			434.17	175.9680	79.2014
			448.18	171.1805	78.3351
			462.18	171.7091	78.1379
			476.19	153.6883	77.2672
			490.20	171.5568	77.0958

As observed in Table 5.1, the median RMS and amplitude calculated for the artefact voltages estimated by both approaches are quite similar. However, when the power spectra of the corrected signals are compared, the attenuation of the artefact activity in the frequency bins by the AAS and OMA is different (Table 5.2). Although both approaches show to provoke attenuation approximately similar in some artefact frequency bins, OMA provided more attenuation than AAS in higher-frequency bins.

Table 5.3: Median SNR and MSE considering the evaluation of the EEG preservation according to the scheme of Fig. 5.6.

Method	Philips data		GE data	
	SNR	MSE (μV^2)	SNR	MSE (μV^2)
OMA	0.9999	0.1498	0.9993	1.1062
AAS	0.9990	2.3031	0.9960	7.1058

Table 5.4: SNR and MSE for some EEG electrodes (Philips data), considering application of low-pass filtering in $e_{ref,n}$ and $\hat{e}_{ref,n}$.

Measure	Method	EEG Electrode	Filter cut-off frequency					
			No LP	150 Hz	120 Hz	100 Hz	70 Hz	50 Hz
SNR	OMA	Fp1	0.9999	1.0000	1.0000	1.0000	1.0000	1.0000
		F3	0.9998	0.9999	0.9999	0.9999	0.9999	0.9999
		Oz	0.9999	0.9999	0.9999	0.9999	0.9999	0.9999
		CPz	0.9997	0.9999	0.9999	0.9999	1.0000	1.0000
		Fz	0.9997	0.9999	1.0000	1.0000	1.0000	1.0000
		FC5	0.9992	0.9998	0.9998	0.9998	0.9998	0.9998
		AF3	0.9998	0.9999	0.9999	0.9999	0.9999	0.9999
	AAS	Fp1	0.9993	0.9994	0.9995	0.9995	0.9995	0.9995
		F3	0.9988	0.9990	0.9991	0.9991	0.9991	0.9992
		Oz	0.9987	0.9989	0.9989	0.9989	0.9990	0.9990
		CPz	0.9977	0.9981	0.9982	0.9983	0.9984	0.9984
		Fz	0.9987	0.9990	0.9991	0.9991	0.9991	0.9992
		FC5	0.9975	0.9986	0.9988	0.9989	0.9990	0.9990
		AF3	0.9991	0.9992	0.9993	0.9993	0.9994	0.9994
MSE (μV^2)	OMA	Fp1	0.5078	0.2047	0.1686	0.1537	0.1407	0.1359
		F3	0.5841	0.3335	0.3123	0.3020	0.2913	0.2867
		Oz	0.4108	0.1962	0.1794	0.1734	0.1694	0.1685
		CPz	0.1355	0.0283	0.0225	0.0202	0.0184	0.0179
		Fz	0.1091	0.0183	0.0148	0.0132	0.0119	0.0114
		FC5	2.3462	0.7015	0.5607	0.5026	0.4500	0.4299
		AF3	0.3380	0.1484	0.1305	0.1230	0.1161	0.1135
	AAS	Fp1	3.6086	2.8759	2.6540	2.5278	2.3824	2.3155
		F3	3.2115	2.6447	2.4861	2.3915	2.2782	2.2246
		Oz	3.7296	3.1849	2.9991	2.8894	2.7599	2.6993
		CPz	0.9186	0.7407	0.6878	0.6575	0.6225	0.6063
		Fz	0.4204	0.3190	0.2957	0.2826	0.2675	0.2606
		FC5	7.7577	4.0962	3.4639	3.1535	2.8346	2.7007
		AF3	1.9105	1.5336	1.4264	1.3652	1.2941	1.2611

Table 5.5: SNR and MSE for some EEG electrodes (GE data), considering application of low-pass filtering in $e_{ref,n}$ and $\hat{e}_{ref,n}$.

Measure	Method	EEG Electrode	Filter cut-off frequency					
			No LP	150 Hz	120 Hz	100 Hz	70 Hz	50 Hz
SNR	OMA	Fp1	0.9990	0.9997	0.9998	0.9998	0.9998	0.9998
		F3	0.9974	0.9994	0.9996	0.9996	0.9997	0.9997
		Oz	0.9980	0.9992	0.9993	0.9993	0.9993	0.9994
		CPz	0.9968	0.9992	0.9994	0.9995	0.9996	0.9997
		Fz	0.9977	0.9991	0.9991	0.9991	0.9990	0.9990
		FC5	0.9958	0.9989	0.9990	0.9990	0.9990	0.9989
		AF3	0.9990	0.9997	0.9998	0.9998	0.9998	0.9998
	AAS	Fp1	0.9960	0.9961	0.9962	0.9962	0.9962	0.9962
		F3	0.9977	0.9981	0.9982	0.9982	0.9982	0.9983
		Oz	0.9861	0.9861	0.9861	0.9861	0.9861	0.9861
		CPz	0.9949	0.9952	0.9953	0.9953	0.9953	0.9954
		Fz	0.9953	0.9956	0.9956	0.9957	0.9957	0.9957
		FC5	0.9974	0.9979	0.9979	0.9980	0.9980	0.9981
		AF3	0.9969	0.9971	0.9971	0.9971	0.9971	0.9971
MSE (μV^2)	OMA	Fp1	8.1852	2.2973	1.9257	1.8225	1.7843	1.7917
		F3	3.1040	0.6376	0.4770	0.4207	0.3828	0.3740
		Oz	2.5445	0.9858	0.8820	0.8359	0.7909	0.7727
		CPz	0.7211	0.1624	0.1208	0.1007	0.0807	0.0726
		Fz	0.6469	0.2537	0.2448	0.2493	0.2621	0.2703
		FC5	8.6758	2.2185	1.9761	1.9478	1.9942	2.0390
		AF3	2.3881	0.6828	0.5910	0.5671	0.5628	0.5685
	AAS	Fp1	32.2881	30.8757	30.5258	30.3384	30.1333	30.0426
		F3	2.7148	2.1758	2.0877	2.0445	2.0002	1.9816
		Oz	18.2050	17.7786	17.6364	17.5485	17.4401	17.3874
		CPz	1.1722	1.0444	1.0174	1.0024	0.9855	0.9779
		Fz	1.3609	1.2396	1.2154	1.2021	1.1870	1.1801
		FC5	5.4794	4.1711	3.9548	3.8491	3.7422	3.6981
		AF3	7.5164	7.1415	7.0543	7.0059	6.9510	6.9259

To perform the quantitative evaluation of EEG preservation, we used the scheme depicted in Fig. 5.6, and calculated the median values of SNR (Eq. 5.19) and MSE (Eq. 5.20) between $e_{ref,n}$ and $\hat{e}_{ref,n}$. The results of such measures are shown in Tables 5.3, 5.4, and 5.5. In Tables 5.4 and 5.5, we show the individual results for some exemplary channels, Fp1, F3, Oz, CPz, Fz, FC5, and AF3. In these tables, we also included the values of SNR and MSE, considering application of low-pass (LP) filtering in $e_{ref,n}$ and $\hat{e}_{ref,n}$. The LP filter cut-off frequencies are indicated, and were used to assess the EEG preservation in a different EEG bandwidth for both OMA and the AAS method. Calculation of the median global values shown in Table 5.3 also took into account the results considering LP filtering. It can be observed that the overall values of SNR and MSE for the OMA method are better than those for AAS.

It is also noteworthy that low-pass filtering of $e_{ref,n}$ and $\hat{e}_{ref,n}$ substantially increased the SNR and decreased the MSE considering the OMA approach, unlike the AAS method. Therefore,

by using OMA, the signals $e_{\text{ref},n}$ and $\hat{e}_{\text{ref},n}$ have become more similar after LP filtering, attesting even better preservation of the neuronal EEG in low-frequencies. We also noticed that the mean subtraction by AAS produced signals $e_{\text{ref},n}$ and $\hat{e}_{\text{ref},n}$ less similar because of the higher influence of small drifts and subject head motions. This led to the small differences of the values of SNR and the MSE for the considered LP cut-off frequencies, as observed in Tables 5.4 and 5.5 (AAS).

Figure 5.11 shows a comparison of the typical attenuation in the frequency bins by using OMA (Eq. 5.15) and AAS, taking into account different values of J and different number of averaging epochs, as well as similar EEG preservation (same SNR and MSE).

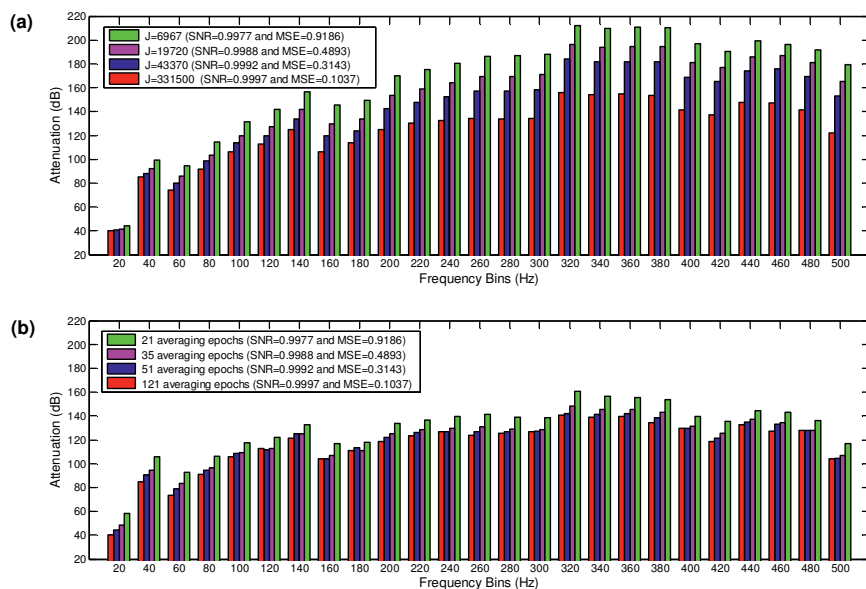


Figure 5.11: Attenuation in the frequency bins by application of (a) OMA and (b) AAS for an EEG excerpt picked up from the channel CPz (Philips data), taking into account different values of J and number of averaging epochs. Although OMA and AAS can provide similar EEG preservation (same value of SNR and MSE), OMA is more effective in attenuating the artefact in the overall frequency bins, mainly at higher frequencies than 100 Hz.

The results shown in Fig. 5.11 were obtained from an EEG excerpt from the channel CPz of the Philips data. As observed, even though OMA and AAS can provide similar EEG preservation according to the values of J and the number of averaging epochs, respectively, OMA shows larger attenuation than AAS in the overall frequency bins, mainly in frequencies higher than 100 Hz. Additionally, the larger the values of J , the higher the difference of attenuation by OMA in a certain frequency bin. In turn, the attenuation by AAS is more

uniform among different number of averaging epochs taking into consideration a certain frequency bin. The attenuation provided by AAS shows to be slight higher and less uniform than OMA only for the frequency bins 20 and 40 Hz. Therefore, Fig. 5.11 demonstrates that the proposed comb-filtering approach can be more effective in attenuating the artefact activity, and simultaneously to achieve EEG preservation as similar as that provided by the AAS method.

5.6 Discussion

As the repetitive gradient artefact waveform recorded in the scalp potential during continuous acquisition of EEG-fMRI is approximately the differential waveform generated within the MRI sequence (Anami et al., 2003), a proper integration over the artefact period might theoretically be used to cancel out the artefact, as indicated in Fig. 5.1 and Eq. (5.3). To implement such integration, we have investigated and proposed the use of the forward-backward application of a moving-average filter in the scalp potential, described in Eq. (5.5). When this procedure is iteratively carried out, as depicted in the scheme of Fig. 5.2, it permits to suppress the gradient artefact from the scalp potential and obtain an estimation of the neuronal EEG (Ferreira et al., 2014a). Such kind of moving-average procedure is referred to as iterative filtering decomposition, which has been investigated as an alternative implementation for empirical mode decomposition (Lin et al., 2009; Wang et al., 2012). It also constitutes a comb-filtering approach whereby harmonic signal components can be filtered out, as shown in Chapter 4. As observed in Figs. 5.4 and 5.5, the OMA comb-filtering approach described in Eqs. (5.15) and (5.16) can provide increased gain in the filter pass-bands together with effective attenuation in the stop-bands, in addition to possessing a zero-phase characteristic (Fig. 5.3). Thus, it is able to effectively suppress the harmonic artefact activity associated with the repetitive artefact waveform that occurs in the slice repetition time (TR-slice), as observed in Figs. 5.7 – 5.11 and Tables 5.1 and 5.2.

When compared with subtraction of an average artefact template, according to the AAS method implementation (Allen et al., 2000; Becker et al., 2005), both OMA and AAS show quite a similar RMS and amplitude attenuation associated with the gradient artefact over time (Table 5.1). Meanwhile, OMA shows different attenuation in the artefact frequency bins in comparison with AAS, as can be observed in Table 5.2 and Fig. 5.11. As a consequence, our

method can lead to a different preservation of the EEG signal than AAS, as indicated by the SNR and MSE (Table 5.3, 5.4, and 5.5). In addition, taking into account similar EEG preservation (same SNR and MSE), OMA shows to be more effective in attenuating the artefact in the overall frequency bins (Fig. 5.11), especially at higher frequencies (above 100 Hz). Thus, this characteristic can avoid the use of further processing methods such as adaptive noise cancelling (ANC) and low-pass (LP) filtering that may contribute to suppress high-frequency activity of the neuronal EEG. This is a substantial conceptual advantage compared to AAS in which post-processing is essential to remove residual artefacts (Allen et al., 2000; Mandelkow et al., 2006; Gebhardt et al., 2008; Niazy et al., 2005). Therefore, these results indicate that OMA can lead to a better balance for the trade-off artefact attenuation versus EEG preservation, thus outperforming the average template subtraction by AAS. Better preservation of the corrected EEG in low-frequencies was also achieved by OMA, as shown in Tables 5.3, 5.4, and 5.5. The SNR closer to unity and the smaller values of the MSE reflect smaller difference between the reference EEG, $e_{ref,n}$, and its estimate, $\hat{e}_{ref,n}$, after application of OMA than AAS. Thus, it confirms an improved preservation and less distortion of the EEG signal by using OMA.

Furthermore, baseline correction has not been performed before application of OMA, whereas it has been carried out before AAS. This evidences that OMA is more robust to the alterations of the artefact waveform caused by small drifts and movements of the subject head. The inherent uncertainty (standard deviation) associated with averaging epochs caused by alterations in the artefact waveform because of small drifts as well as subject head motions may lead to an inaccurate estimation of the average artefact template (Yan et al., 2009). Contrary to AAS, gradient artefact estimation by our method does not rely on calculation of an average template. Rather, implementation of OMA is individually performed sample-by-sample according to application of the OMA filter indicated in Eq. (5.10), whose uncertainty is influenced by artefact waveform alterations that occur in samples of the scalp potential ranging from s_{n-M+1} to s_{n+M-1} . In case of AAS, it is affected by artefact waveform alterations that occur in those $2m+1$ sliding average windows considered for average template construction, whose samples range from s_{n-mM} to s_{n+mM} (see Section 8.4.2). Hence, it explains why OMA is less affected by small drifts and subject head movements than AAS.

As reported by Mandelkow et al. (2006), synchronisation between the EEG sampling interval and the MRI acquisition clock leads to increasing of the usable bandwidth in the corrected

EEG up to around 150 Hz after average template subtraction. Because OMA is capable of provoking larger attenuation of the artefact activity in higher-frequency bins, this shows that the proposed approach could be used to produce further broadening of the usable bandwidth of the corrected EEG. As shown in Figs. 5.10 and 5.11, by using OMA, substantial attenuation in the artefact frequency bins could be achieved in the bandwidth below 500 Hz. The study of high frequency neuronal activity between 100 and 500 Hz has currently received increased attention and requires the use of customised MRI sequences that are generally not available to all investigators (Anami et al., 2003; Mullinger et al., 2014; Freyer et al., 2009). Furthermore, it makes use of an interleaved fMRI protocol which has shown to be less effective and flexible than continuous fMRI measurements (Eichele et al., 2010). Therefore, the usage of OMA could be useful in EEG-fMRI studies that address those high-frequencies oscillations. As depicted in Fig. 5.10, implementation and application of OMA also has no dependency on interpolation or slice-timing correction between the slice-length and the EEG sampling interval (Allen et al., 2000; Becker et al., 2005; Gebhardt et al., 2008; Gonçalves et al., 2007). This characteristic suggests that our approach could produce effective results even when there are jitter errors between MRI clock and EEG sampling rate. Albeit reduction of jitter by using hardware synchronisation solutions has become increasingly available as well as OMA shows to provide better results within a scenario of alignment between TR-slice and the EEG sampling interval (Philips data), Eq. (5.16) reveals to represent a general analytical expression that allows estimation and suppression of the gradient artefact in scenarios either with or without the occurrence of such timing errors. Moreover, our method is data-driven, not requiring accurate information about MRI triggers and events to be implemented (Allen et al., 2000; Mandelkow et al., 2006; Mullinger et al., 2008b; Freyer et al., 2009).

The approach depicted in Fig. 5.6 proposed for evaluation of EEG preservation shows to simplify the implementation of this measurement, so that there is no need to perform comparison of the spectral power of excerpts of the reference EEG, $e_{\text{ref},n}$, with that of corrected EEG excerpts, \hat{e}_n , as is usually performed in the literature (Allen et al., 2000; Freyer et al., 2009; Ritter et al., 2007). Since the power spectrum represents an average measure of the frequencies contained in the time-domain signal, spectral power associated with artefact residuals might be masked in the power spectrum of \hat{e}_n , which can compromise this kind of analysis. Application of the artefact correction approach directly in the reference EEG (Freyer et al., 2009; Ritter et al., 2007) also has the disadvantage of not accounting for the influence of the artefact, which might impair the accuracy of the assessment of EEG preservation by

using such a procedure. Furthermore, the stochastic nature and the lack of knowledge of the neuronal EEG makes it imprecise to compare the power spectrum of the artefact-corrected EEG with the spectrum of the reference EEG recorded inside or outside the scanner. Therefore, evaluation of EEG preservation by quantification of power in certain spectral bands should always be performed together with evaluation of EEG preservation in the time-domain in order to obtain a more precise measurement. On the other hand, the assessment of single events is not suitable to account for the stochastic and non-periodic nature of the neuronal EEG (Ritter et al., 2007). All these characteristics can be effectively accounted by using the time-domain scheme depicted in Fig. 5.6.

The selectivity of the OMA filtering, i.e. the amount of attenuation of the gradient artefact together with the degree of EEG preservation, is influenced by the slice-length (TR-slice or M), and the values of J and L . Therefore, combination of proper values of those parameters should be taken into account to obtain an optimal balance between artefact attenuation and EEG preservation. In this respect, the assessment indicated in Tables 5.2 – 5.5 and Fig. 5.11 could be used to choose the values of J and L according to the value estimated for M , as well as to obtain an optimal selectivity. Additionally, the EEG sampling frequency should be taken into account as well because it can influence on the value of M . Some preliminary investigations suggested us that OMA appears to effectively produce EEG correction for lower EEG sampling frequencies (around 500 Hz), provided that the gradient artefact waveform is well reproduced in the scalp potential. Further, OMA might be applied when a delay time (DT – see Section 2.4.1) occurs between volume acquisitions, by setting M for both TR-slice and TR, without substantial degradation of the EEG quality. This characteristic is better assessed in Chapter 6. As further suggestion for future work, OMA should be applied and generalised for other types of EEG data recorded in other types of MRI scanners as well as for correction of other types of periodic artefacts, such as the artefact that affects the scalp potential during electrical impedance tomography (Fabrizi et al., 2010).

Due to the computational efficiency of the OMA filter described in Eq. (5.12), Eqs. (5.15) and (5.16) are not computationally demanding either, in addition to possessing quite low complexity of implementation. Thus, large values of the parameters J and L do not compromise the computational processing time of Eqs. (5.15) and (5.16). As a result, the time to compute Eqs. (5.15) and (5.16) is quite low and comparable with the processing time of the mean template subtraction performed by the Brain Vision Analyzer software. Equations (5.15) and (5.16) also allow using non-integer values of M , according to the estimated value

of TR-slice, which can be used to reduce the effect of jitter errors on the comb-filtering performance as well (Braun, 1975). Rather, the use of Eq. (5.11) may be followed by some problems such as the substantial ringing effects in the signal ends caused by the iterative application and subtraction of the components of the corrected EEG, as well as the increased computational load when larger values of J and L are used. Thereby, the frequency-domain implementation indicated by Eqs. (5.15) and (5.16) should be preferably used than Eq. (5.11) to minimise such problems.

As another limitation, we noticed that the use of larger values of M in Eq. (5.12) provokes strong reduction of the attenuation provided by $H_{OMA}(z)$ in lower-frequency comb-filter stop-bands as well as larger attenuation in higher-frequency comb-filter pass-bands. This effect is particularly important when M equals the value of the parameter TR, and is deeper addressed in Section 6.3.3. In parallel, the performance of OMA might be compromised when the occurrence of EEG amplifier saturation, as also observed for the AAS method. Thus, band limiters are needed to reduce the EEG system dynamic range and prevent saturation of the EEG amplifier during EEG data acquisition.

5.7 Conclusions

In this chapter, we have shown the effectiveness of using optimised moving-average filtering (OMA) for suppression of the gradient artefact from the scalp potential recorded during continuous EEG-fMRI. OMA constitutes a comb-filtering approach, whose application in the scalp potential allows suppression of the gradient artefact and simultaneous estimation of the neuronal EEG. When compared with the average template subtraction as performed according to the established average artefact subtraction (AAS) methodology, OMA is shown to be capable of obtaining an improved balance compared to AAS for the trade-off between effective suppression of the gradient artefact and preservation of the EEG signal. In this respect, OMA can provide larger attenuation in higher-frequency artefact bins and be less affected by artefact waveform alterations owing to small drifts and subject head motions. In addition to being data-driven and not requiring accurate information about MRI trigger and events, OMA also is shown to be capable of correcting the EEG signal in scenarios either with or without misalignment between the EEG sampling interval and the MRI slice-time. Last, besides effectively accounting for the stochastic and non-periodic nature of the neuronal EEG,

the proposed approach for evaluation of EEG signal preservation is shown to simplify the implementation of this measurement. Such characteristics indicate that our methodology can help to improve the quality of the EEG signal recorded during fMRI as well as the performance evaluation of the gradient artefact correction approaches, and thus contribute to the consolidation of co-registered EEG-fMRI.

CHAPTER 6

Evaluating the Relative Efficacy and Clinical Usefulness of the Gradient Artefact Correction using Iterative Filtering*

6.1 Abstract

Although co-registered EEG-fMRI has been considered a tool to solve numerous problems in cognitive and clinical neuroscience, some limitations such as the occurrence of artefacts still impair the use of such a technique in a broader range of applications. In particular, the gradient artefact may compromise obtaining an EEG signal with good quality, even after application of the existing correction methods proposed in the literature. In this chapter, we make an assessment of the relative efficacy of the novel methodology we propose to attenuate the gradient artefact and residual artefacts in the corrected EEG by using iterative filtering. As an extension of the OMA method proposed in Chapter 5, such a methodology makes use of further iterative filtering techniques which are based upon a modality of iterative filtering decomposition process. When compared with the often-used AAS and FASTR correction methods, the proposed methodology provides better preservation of high-frequency activity in the corrected EEG together with effective gradient artefact attenuation. Moreover, it has improved robustness under the occurrence of abrupt movements of the subject head. Besides, epileptiform activity could be fairly well identified by visual inspection of a clinical EEG expert.

6.2 Introduction

Simultaneous acquisition of EEG and fMRI data (co-registered EEG-fMRI) has been considered a promising and powerful technique to solve numerous problems in cognitive and clinical neuroscience. Combination of the high temporal resolution of the EEG with the high

* This chapter was based on the paper:

Ferreira, J.L., Besseling, R.M.H., Wu, Y., Arends, J., Carrette, E. (2018). Evaluating the relative efficacy and clinical usefulness of the gradient artefact correction using iterative filtering. To be submitted.

spatial resolution of the fMRI has enabled the possibility of measuring the activity of large-scale neuronal networks with millisecond resolution and, simultaneously, to look deep into subcortical structures on the order of millimetres. In the beginning, co-registered EEG-fMRI was used in studies of epilepsy. Over the past years, however, several other clinical applications and neuroscientific studies have made use of this technique as well (Snyder and Raichle, 2010; Warach et al., 1996; Seeck et al., 1998; Wiest et al., 2015; Ritter and Villringer, 2006).

Besides its promising capability of offering new insights into brain functioning, co-registered EEG-fMRI is a challenging technique, mainly because of the quality of the EEG signal that is compromised by the occurrence of artefacts induced by the magnetic fields of the MRI scanner (Allen et al., 2000; Anami et al., 2002; Debener et al., 2010; Sun and Hinrichs, 2009). The magnetic field gradients and RF pulses used in MRI pulse sequences induce an interference voltage in the electrical potential recorded in the scalp electrodes (scalp potential), which is termed *gradient* or *imaging acquisition artefact*. As described in Section 2.4.1, the gradient artefact is characterised as an approximately repetitive waveform in the time course scalp potential, whose period corresponds to the repetition time (TR) of the MRI pulse sequence, and may have amplitudes about hundreds of orders higher than the neuronal EEG signal. In the frequency-domain, the spectral activity associated with the gradient artefact appears in harmonic frequency bands (or frequency bins) spaced at $1/TR$, and convolved with spectral frequency bands at $1/TR$ -slice corresponding to the inverse of the period between two MRI slice acquisitions (TR-slice) (Anami et al., 2003; Ritter et al., 2010). In turn, the *pulse* and the *movement artefact* caused by abrupt subject head movements are mainly ascribed to the static magnetic field of the MRI scanner. An in-depth analysis of the pulse and the movement artefacts are outside the scope of this work, and additional information and methods to correct them can be obtained in the references mentioned above.

In attempt to attenuate the gradient artefact at the source, reduction of the induction effects of the MRI magnetic fields, as well as the use of interleaved approaches whereby silent scanning periods are left between fMRI data acquisitions, has been suggested in the literature (Mullinger et al., 2014; Mullinger et al., 2011; Ritter et al., 2010). Attenuation of the induction effects, however, is not able to effectively suppress the artefact from the EEG signal, requiring the use of post-processing techniques to correct it. In parallel, interleaved approaches have shown to be less flexible and experimentally efficient than continuous fMRI acquisition (Eichele et al., 2010; Becker et al., 2005). The use of a special EEG cap has also

been proposed, whereby it is possible to record the gradient artefact separately. Then it is subtracted from the recorded scalp potential corrupted by the gradient artefact (Chowdhury et al., 2014). Although this technique has shown to be quite promising, it requires specialised hardware that are not yet widely available. The use of a head vacuum cushion has also been proposed to prevent the influence of subject head movements on the morphology of the gradient artefact waveform (Anami et al., 2002). Thus, it is possible to obtain an artefact waveform more reproducible and stationary, characteristic on which most of post-processing gradient artefact correction methods artefact rely. As remarked by Spencer (2015), however, small head micro-movements cannot be cancelled out when using head vacuum cushions even with the most cooperative subjects. Those tiny movements provoke random variations in the amplitude of the gradient artefact components, which conceptually can be similar to a random amplitude modulation. As a result, spectral components of the gradient artefact are broadened, especially in higher-frequency spectral bins. As mentioned in Section 2.4.3, the endogenous and inevitable influence of subtle head tiny movements is related to respiration and small movements of the subject head (Eichele et al., 2010; Spencer, 2015).

Broadening of the gradient artefact spectral lines is the main cause of the partial failure of the average artefact subtraction (AAS) method which is the most established post-processing gradient artefact correction approach. AAS is based upon the assumption of stationary nature of the gradient artefact waveform as well as of the neuronal EEG and the gradient artefact to be uncorrelated. According to the AAS implementation, an average artefact waveform (or average template) is constructed and subtracted from the scalp potential to produce a clean EEG signal (Allen et al., 2000; Becker et al., 2005; Freyer et al., 2009). This approach can be likened to a comb-filter based upon a coherent detection process whereby the harmonic artefact interference is attenuated (Braun, 1975; Braun, 2011). Although the gradient artefact can be substantially suppressed by the comb-filtering attenuation provided by AAS, it is not effective in addressing the broadening of the spectral lines caused by tiny subject head movements, in such a way that residual artefacts may be left behind in the EEG signal after AAS application (Spencer, 2015). For suppression of these residual artefacts, low-pass (LP) filtering and adaptive noise cancelling (ANC) are usually employed (Allen et al., 2000; Niazy et al., 2005; Huang et al., 2012).

To improve the AAS performance, a number of techniques have been proposed such as synchronisation between the MRI acquisition clock and the EEG sampling frequency (Anami et al., 2003; Mandelkow et al., 2006). Accordingly, when the repetition time TR (or TR-slice)

of the MRI sequence is set as a multiple of the EEG sampling interval, it allows obtaining a more reproducible artefact waveform by mitigating the occurrence of jitter problems. Mandelkow et al. (2006) have reported a usable bandwidth in the corrected EEG up to around 150 Hz after average template subtraction by using synchronisation between the EEG sampling interval and the MRI clock. However, it is generally difficult to access a bandwidth of the neuronal EEG higher than 80 Hz because of the occurrence of residual artefacts that tend to be in the EEG gamma band (30 – 100 Hz) (Spencer, 2015). The study of high-frequency oscillations (HFOs) in the EEG between 100 and 500 Hz has currently received increased attention, and is associated with attention and memory process as well as with the onset of epileptic spikes (Sanei and Chambers, 2007; Gotman, 2010). Even though the access of HFOs as well as ultra-high-frequency EEG oscillations has been demonstrated by Freyer et al. (2009), this method combines interleaved approaches with customised MRI sequences that are not widely available to all investigators. Other additional approaches have been devised in attempt to correct the residual artefacts by construction of an optimal basis set (OBS) using principal component analysis, by making use of independent component analysis, and by utilising spatial filtering (Eichele et al., 2010; Niazy et al., 2005). These approaches, however, are generally not able to provide a corrected EEG signal with usable frequency bandwidth higher than the gamma band. Even though the FMRI Artifact Slice Template Removal – FASTER (Niazy et al., 2005) has been often employed to correct the gradient artefact, its performance has strong dependency on subject head movements and may not be capable of addressing the broadening of artefact spectral lines either. Thereby, the corrected EEG by FASTER may be susceptible to the occurrence of residual artefacts alike, requiring the use of LP filtering around 70 Hz and ANC to effectively correct them.

In Chapter 5, we described the use of a novel comb-filtering approach (OMA) based upon the iterative application of a moving-average filter, to improve the attenuation of the gradient artefact activity in the frequency bins associated with the slice-length (TR-slice). OMA has shown to provide larger attenuation than AAS in higher-frequency bins in which there is broadening of artefact spectral lines, and simultaneously to obtain a better preservation of the EEG signal. In this chapter, we propose to employ a variant of OMA along with other iterative filtering techniques to attenuate the gradient artefact in a scenario where it is not possible to switch off the dynamic stabilisation in the MRI equipment. Within this scenario, TR-slice may no longer be an integer of the EEG sampling interval. Hence, subtraction of an average template by AAS should be applied using either the repetition time TR or irregularly

spaced templates of length TR-slice which are less effective in obtaining a good quality for the corrected EEG than using regular epochs of length TR-slice (Mandelkow et al., 2010; Spencer, 2015). In Sections 6.3 and 6.5, we describe and demonstrate how OMA could be applied for both TR and TR-slice in order to obtain an adequate quality for the artefact-corrected EEG. The design of the variant of OMA as well as of the other novel filtering techniques are based upon a kind of iterative filtering decomposition process recently proposed in the literature (Lin et al., 2009; Ferreira et al., 2016; Ferreira et al., 2018). As shown in Section 6.5, a substantial attenuation of the gradient artefact together with a better preservation of the EEG signal above 80 Hz can be provided by using the proposed methodology, thus outperforming AAS and the FASTR method. Our approach is also shown to be capable of limiting the region of influence of abrupt head movements. In parallel, it also allows the identification of epileptiform activity in the time course EEG comparable to that provided by FASTR, according to the visual inspection of a clinical EEG expert. Thereby, this indicates that the proposed methodology could be used in clinical epilepsy studies, as discussed in Sections 6.5 and 6.6.

6.3 Methods

6.3.1 EEG and fMRI data

To implement and apply the proposed methodology, EEG data have been simultaneously acquired with fMRI data from a volunteer who was an epilepsy patient. Given the type of epilepsy, interictal epileptiform activity was expected during data acquisition. The recordings were conducted in accordance with the Declaration of Helsinki, and made with the approval of the local ethics committee and informed consent by the volunteer. The subject was scanned within a 3 T MAGNETOM Trio Scanner (Siemens, Erlangen, Germany) during approximately 62.2 minutes using a functional echo-planar imaging (EPI) sequence with 40 transversal slices and volume repetition time (TR) equal to 2500 ms. fMRI data acquisition was continuously performed. First, a structural scan (T_1) was taken, followed by a functional scan (T_2^*) simultaneous with the EEG recording. The MRI clock and the EEG sampling frequency have been synchronised, so that TR was set as a multiple of the EEG sampling interval. TR was not adjusted as a multiple of the slice-time (TR-slice) because it has not been possible to switch off the dynamic stabilisation. To record the EEG data, a MRI-compatible

32 channels EEG system (BrainAmp MR, Brain Products GmbH, Gilching, Germany) with electrodes positioned according to the standard 10-20 international system as well as a MRI-compatible EEG-cap part of the EEG system was used. The EEG data were recorded in 31 EEG channels, and one additional electrode was used to record the ECG signal. The EEG signal acquisition was performed using a sampling rate at 5000 Hz.

6.3.2. Gradient artefact correction and suppression of residual artefacts

The idea behind most of gradient artefact correction methods, including the established average artefact subtraction (AAS) method (Allen et al., 2000; Niazy et al., 2005), consists of the application of a comb-filtering approach with improved performance to account for the attenuation of the harmonic artefact activity associated with the periodic nature of the gradient artefact. Within the scenario under study in which the dynamic stabilisation has not been switched off in the MRI equipment during data recording, the EEG data has been provided with an artefact waveform in which the repetition time TR was not a multiple of the slice-length (TR-slice). Thereby, the gradient artefact correction should be able to predict the attenuation of the artefact activity associated with both TR and TR-slice.

In addition, because of the occurrence of tiny micro-movements associated with the subject head, Eq. (6.1) should be used to model the recorded scalp potential, s_n (Spencer, 2015):

$$s_n = [a + C_n] g_n + e_n, \quad (6.1)$$

where a is a scaling factor which depends upon the position of the EEG leads and the shape of the volume conductor, thus varying with respect to the conductive paths generated by the subject head and EEG leads relative to the magnetic field gradients; C_n is a zero mean, random process associated with the influence of the micro-movements of the subject head; g_n is the gradient artefact; and e_n is the actual EEG. Therefore, the model of Eq. (6.1) describes a random amplitude modulation in g_n caused by the subject head micro-movements. Assuming the gradient artefact and the EEG signal are not correlated, e_n is not affected by such variations in the amplitude, as indicated in Eq. (6.1). Taking into account the autocorrelation of s_n and applying the Fourier transform, the corresponding power spectrum, $S(\omega)$, can be estimated as (Spencer, 2015):

$$S(\omega) = \frac{2\pi\sigma_U^2}{1-\rho^2} \sum_l g_l \left[\frac{\ln \rho}{(\ln \rho)^2 + (\omega + l\omega_f)^2} + \frac{\ln \rho}{(\ln \rho)^2 + (\omega - l\omega_f)^2} \right] + E(\omega), \quad (6.2)$$

where the first term in the right hand side represents the spectral component associated with the gradient artefact; $E(\omega)$ is the spectral component associated with the neuronal EEG; U corresponds to the white Gaussian noise with variance σ_U^2 , $\rho < 1$, associated with C_n ; g_l is the l -th component of the gradient artefact harmonics; and ω_f is fundamental frequency of each harmonic frequency bin. As described by Spencer (2015), in Eq. (6.2), C_n has the effect of contributing to spectral broadening in $S(\omega)$ around the l artefact harmonics with fundamental frequency at ω_f , which constitutes the artefact frequency bins associated with TR-slice.

Thus, the comb-filtering performed by the gradient artefact correction should also be capable of predicting the broadening of the artefact spectral lines caused by micro-movements of the subject head, as indicated in Eq. (6.2), to effectively attenuate the spectral artefact activity. Otherwise, the gradient artefact correction may fail and, as a result, residual artefacts remain in the artefact-corrected EEG. Such residual artefact activity may impair to access an EEG bandwidth higher than 80 Hz in the EEG signal corrected by AAS (Spencer, 2015). Moreover, a balance for the trade-off between amount of artefact suppression and EEG signal preservation should also be taken into account in order to avoid unwanted removal of components of interest in the EEG signal.

Below, we describe the proposed filtering techniques to suppress the component associated with the gradient artefact as indicated in Eqs. (6.1) and (6.2), attenuate eventual residual artefacts in the estimate of e_n , and increase its usable bandwidth: the *optimised moving-average (OMA) filtering*; the *highly selective notch (HSN) filtering*, and the *optimised exponential average (OEA) filtering*. OMA, HSN, and OEA were implemented in MATLAB (The MathWorks Inc., Natick, USA) environment.

6.3.3. Optimised moving-average (OMA)

As described in Chapter 5, optimised moving-average (OMA) consists of a comb-filtering technique based upon iterative application of a moving-average filter, whose notch

frequencies are located at $1/\text{TR}$ -slice (Ferreira et al., 2016; Ferreira et al., 2018). When this procedure is iteratively applied in the scalp potential, s_n , recorded with TR-slice as a multiple of the EEG sampling interval, it permits to simultaneously suppress the gradient artefact and estimate the corrected EEG. This approach can also be implemented in the frequency-domain, and does not require accurate information about triggers and other MRI events in comparison with the artefact template subtraction performed by AAS. In addition, OMA provides larger attenuation in higher-frequency artefact bins, so that it has shown to better address the broadening of higher-frequency spectral lines associated with the gradient artefact (Eq. (6.2)) than subtraction of an average artefact template (Ferreira et al., 2016).

According to OMA implementation (see Section 5.3.4), the artefact-corrected EEG, $\hat{\mathbf{e}}_{\text{correct}}$, is related to the scalp potential, \mathbf{s} , by Eq. (6.3):

$$H_C(z) = \frac{\hat{E}_{\text{correct}}(z)}{S(z)} = 1 - [1 - H_{\text{OMA}}(z)]^J, \quad (6.3)$$

where $\hat{E}_{\text{correct}}(z)$ is the z -domain representation of $\hat{\mathbf{e}}_{\text{correct}}$; $S(z)$ is the z -domain representation of \mathbf{s} ; J is the number of iterations used; and $H_{\text{OMA}}(z)$ is described in Eq. (5.12). The frequency response of the OMA filter is derived from Eq. (6.4) by setting $z = e^{j\omega}$, resulting in:

$$\Rightarrow H_{\text{OMA}}(\omega) = \frac{1}{(M)^2} \frac{\sin^2\left(\frac{\omega M}{2}\right)}{\sin^2\left(\frac{\omega}{2}\right)}. \quad (6.4)$$

A cascade implementation of Eq. (6.3) permits to enlarge the attenuation in the filter stop-bands:

$$H_L(z) = [H_C(z)]^L, \quad (6.5)$$

where L is the number of cascades (Ferreira et al., 2016; Ferreira et al., 2018).

Here, we modified Eq. (6.3) to achieve the attenuation of the gradient artefact activity associated with the volume repetition TR as well. Since TR is much larger than TR-slice, the value of M in Eq. (6.4) is also enlarged by setting M equal to TR. This provokes strong reduction of the attenuation provided by $H_{\text{OMA}}(z)$ in lower-frequency comb-filter stop-bands

as well as larger attenuation in higher-frequency comb-filter pass-bands when using Eq. (6.4) (Ferreira et al., 2018). To counterbalance this effect, we modified Eq. (6.4) to Eq. (6.6):

$$\Rightarrow H_{OMA}(\omega) = \frac{1}{(M)^2} \frac{\sin^p\left(\frac{\omega M}{2}\right)}{\sin^2\left(\frac{\omega}{2}\right)}, \quad (6.6)$$

where the exponent p equals to 4, 6, or 8 depending on how large the value of M is. To attenuate the artefact activity associated with TR, thereby, we have set $M = \text{TR}$ and applied OMA to \mathbf{s} using Eqs. (6.5) and (6.6). Next, by setting $M = \text{TR-slice}$, we applied OMA using Eqs. (6.4) and (6.5) to the resulting signal in order to attenuate the artefact activity associated with TR-slice. The value of TR was estimated using the recorded scalp potential as well, thus according to the time basis of the EEG sampling system (Ferreira et al., 2016). It is worthy of note that there is no difference in the order of application of OMA for TR or TR-slice firstly because Eqs. (6.4) – (6.6) have linear response.

Although broadening of artefact spectral lines could be accounted for by using OMA, we noticed that the use of smaller values of J might provoke larger attenuation of EEG frequencies around artefact frequency bins, especially at higher frequencies, and simultaneously low-pass filtering higher-frequencies of interest in the corrected EEG. On the other hand, eventual residual artefacts might be left behind around the frequency bins when larger values of J are used (Ferreira et al., 2016; Ferreira et al., 2018). In addition to such a trade-off, extra interference sources may afflict the EEG during co-registered EEG-fMRI, such as vibrations owing to the MRI scanner gradient switching, and cryogen and air flow pumps (Eichele et al., 2010; Spencer, 2015). These sources of interference are difficult to be predicted by any gradient artefact correction approaches and, therefore, further methods and procedures should be used to minimise those interferences. Contrary to the cryogen and air flow pumps that can be switched off, vibrations associated with the MRI scanner gradient switching can only be partially reduced by shock-absorbing mattress or suspension of the scanner bed, which is technically challenging and impractical in most applications. The use of conventional notch and low-pass filtering approaches might not be advisable in those scenarios because they may provoke substantial attenuation of components of the neuronal EEG and make it difficult to access EEG spectral activity above the gamma band (Spencer, 2015).

Thereby, we have made use of other iterative filtering approaches that might be capable of producing substantial attenuation of eventual residual artefacts after application of OMA and simultaneously improving the preservation of the spectral energy in the artefact-corrected EEG. Such filtering techniques are the highly selective notch (HSN) filtering and the optimised exponential average (OEA) filtering, described as follows.

6.3.4. The highly selective notch (HSN) filtering

As described in Section 4.4.3, convolution between a unit pulse, δ , with the magnitude response $|H_{MAF}(\omega)|$ of Eq. (4.2), calculated for $N=2$, provides a band-pass filter with unit amplitude and central frequency at ω_0 (see Fig. 4.5). By applying Eq. (4.19) within an iterative filtering procedure, as indicated in Eqs. (4.9) and (4.20), this results in the notch filter $H_{NTC}(z)$:

$$H_{NTC}(z) = 1 - (H_1(z))^J. \quad (6.7)$$

The magnitude response corresponding to $H_{NTC}(z)$ can be seen in Fig. 4.12. This notch filter does not cause any effects on the phase of the signal. Thus, as indicated in Eq. (4.21), Eq. (6.7) can be used in a cascade implementation as well:

$$H_{NL}(z) = [H_{NTC}(z)]^L, \quad (6.8)$$

where L is the number of cascades. Thus, Eq. (6.13) can produce a notch filter with a large range of values for the stop-band bandwidth around -3 dB. This characteristic enables Eq. (6.8) to provide a highly selective notch filtering to extract specific frequencies of the corrected EEG. In this fashion, the amount of energy filtered by the notch filter could be selectively tapped by setting proper values of J and L in Eq. (6.8) which permits to vary the bandwidth around -3 dB and, thereby, the degree of attenuation provided by the filter.

Another way we devised to implement a highly selective notch filtering was the usage of Eq. (6.12) combined with a power spectrum threshold to indicate the amount of energy to be extracted in that specific frequency. For instance, in case of the gradient artefact residuals, we assumed that the spectral energy associated with the gradient artefact activity lay above the set power spectrum threshold, and the energy underneath this threshold ought to be associated with the neuronal EEG. Thus, the attenuation provided by the notch filter should be able to

reduce the energy associated with the residual artefact frequencies until the set threshold. To calculate the threshold, the power spectrum corresponding to a reference EEG excerpt recorded inside the MRI scanner during non-scan periods (baseline EEG power spectrum) might be used. In parallel, to find the correct attenuation of the filter, initially we have searched for a value of minimal attenuation provided by Eq. (6.8) whereby the energy in a specific frequency could be attenuated until the set threshold. This can be carried out by varying the values of J and L , as mentioned above. Afterwards, our algorithm sought and selected those frequencies in the region around the frequency bins that had spectral energy above the threshold. Equation (6.8) was then applied to the corrected EEG after OMA, ($\hat{\mathbf{e}}_{\text{correct}}$) to reduce the energy in those selected frequencies. This procedure was iteratively performed, until the power spectrum of those selected frequencies was below the set threshold. To estimate the power spectrum of $\hat{\mathbf{e}}_{\text{correct}}$ in which HSN were to be applied, we have used the Fast Fourier transformation E_k calculated by Eq. (6.14):

$$E_k = \sum_{n=1}^I \hat{e}_{\text{correct}} \omega_I^{(n-1)(k-1)}, \quad (6.9)$$

where I is the length of $\hat{\mathbf{e}}_{\text{correct}}$; and $\omega_I = e^{-j2\pi/I}$. Equation (6.9) was implemented using the function `fft` of MATLAB. I was also used as the number of points of the FFT, and a Hamming window of the same length was used to minimise the spectral leakage. The power spectrum was calculated as:

$$P_k = \frac{E_k \cdot \bar{E}_k}{I}, \quad (6.10)$$

where \bar{E}_k is the complex conjugate of E_k .

6.3.5 Optimised exponential average (OEA)

Because of the occurrence of residual artefacts associated with the broadening of the gradient artefact spectral lines as indicated in Eq. (6.2), the corrected EEG may not have a power spectrum that is inversely proportional to the frequency ($1/f$) after gradient artefact correction, as is typically observed for the neuronal EEG (Gutberlet, 2010; Mandelkow et al., 2006). Although a conventional low-pass (LP) filter is able to attenuate residual artefact frequencies that are above its cut-off frequency, it does not predict any decrease of the EEG power spectrum as $1/f$. Thus, the LP filter must be applied with cut-off frequency right in the region

of the spectrum in which those deviations above $1/f$ occur, and tend to be in the EEG gamma band and above (Spencer, 2015). In parallel, frequencies of the corrected EEG higher than the filter cut-off frequency are strongly attenuated because they lie in the transition and stop-band of the LP filter. As such, we have investigated and made use of the exponential average filter as a low-pass filter to approximate the EEG power spectrum to $1/f$. An exponential average filter can be described by the following equation (Braun, 2011):

$$y_n = -ay_{n-1} + (1-a)x_n, \quad (6.11)$$

where $a = (1-1/C)$, and C is a constant. Application of the z -transformation in Eq. (6.11) results in:

$$H_{EA}(z) = \frac{Y(z)}{X(z)} = \frac{1-a}{1-az^{-1}}. \quad (6.12)$$

Like in Eq. (4.19), we have performed the convolution between a unit pulse, δ , with the magnitude response $|H_{EA}(\omega)|$:

$$H_2(\omega) = \delta(\omega_0) * |H_{EA}(\omega)|. \quad (6.13)$$

The central frequency response ω_0 in Eq. (6.13) has now been set at $\omega_0 = 0$, in such a way that it provides the low-pass filter response depicted in Fig. 6.1a (blue trace) which is a well-known characteristic of an exponential average. The magnitude response of an FIR LP filter cut-off frequency about 70 Hz (21-coefficient – dark trace; 56-coefficient – red trace; and 91-coefficient – green trace) implemented using the MATLAB function `FIR1` are depicted in Fig. 6.1a as well for comparison purposes. In Fig 6.1b, it can be observed that by iteratively applying Eq. (6.13), as described in Eq. (6.14) and its cascade implementation (Eq. (6.15)):

$$H_{OEA}(z) = 1 - \left[1 - (H_2(z))^K \right]^J, \quad (6.14)$$

$$H_{LO}(z) = (H_{OEA}(z))^L, \quad (6.15)$$

the low-pass characteristics of Eq. (6.13) can be changed, permitting to increase or decrease the low-pass filter attenuation along the pass-band, transition band, and stop-band (Fig. 6.1b). Thereby, by using proper values of C , K , J , and L in the optimised exponential average (OEA) filtering approach indicated in Eqs. (6.14) and (6.15), residual artefacts along the EEG gamma

band and above might be more selectively filtered according to different responses obtained for OEA, rather than the FIR LP filter that only attenuates frequencies around and over the filter cut-off frequency (Fig. 6.1a). This characteristic of OEA, therefore, could be used to produce larger attenuation of residual artefacts in intermediary frequencies together with smaller attenuation at higher frequencies than the FIR LP filter, approximating the EEG power spectrum to $1/f$. It is noteworthy that Eqs. (6.14) and (6.15) does not produce any distortion effects in the phase of the signal either.

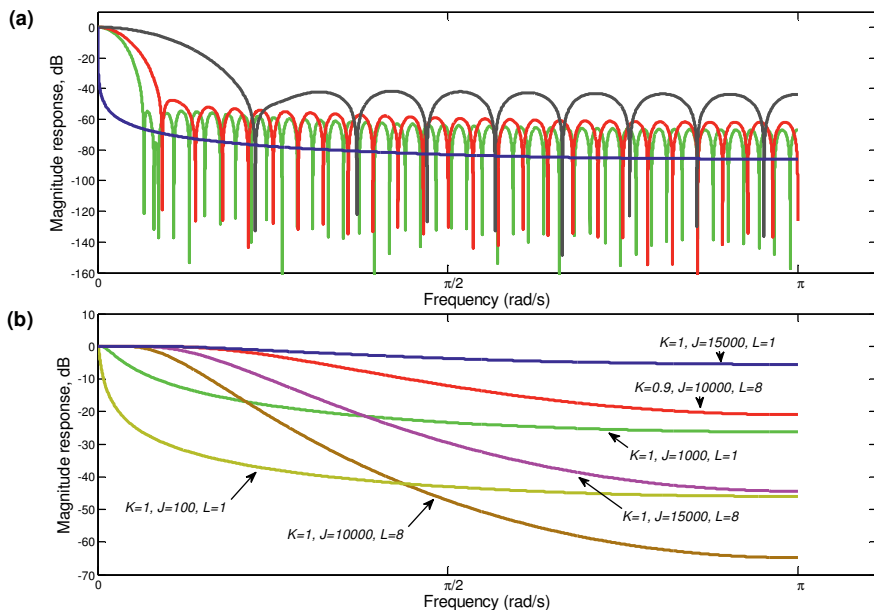


Figure 6.1: Magnitude response of: (a) $H_2(\omega)$ (Eq. (6.13)) – blue trace, and an FIR LP filter (21-coefficient – dark trace; 56-coefficient – red trace; and 91-coefficient – green trace); b) $H_{LO}(z)$ (Eq. (6.15)), taking into account some values of K , J , and L , and $C = 10000$.

6.4 Comparative analysis, quantitative assessment, and clinical evaluation of the gradient artefact correction

6.4.1 Comparative analysis

As a measure of relative efficacy, we compared our results with those obtained by application of the MATLAB-based plug-in FMRI Artefact Slice Template Removal (FASTR, Center for Functional MRI of the Brain, Oxford, UK). FASTR is a part of the FMRIB toolbox (Version

2.00) of the open source toolbox EEGLab (Version 14.1.1b) (Delorme and Makeig, 2004). Initially, this algorithm performs the artefact template subtraction according to the AAS method. To this end, the epoch length to construct the artefact template was set at 2500 ms (TR) which matched the used volume-start marker in the EEG data. A sliding average with window size of 61 epochs and an interpolation factor equal to 4 were used. The reason for using 61 epochs was a minimum of 60 averages that is generally required to attenuate brain signals effectively in the artefact template, corresponding to a scaling of the standard deviation by approximately 0.13 (Spencer, 2015, Mullinger et al., 2008c). Besides the average artefact template subtraction, FASTR performs the correction of residual artefacts based upon an optimal basis set (OBS) using principal component analysis (PCA). In short, PCA is used to carry out the identification of small temporal variations in the artefact of different artefact waveforms. These variations allow the calculation of the optimal basis set that is then fitted to and subtracted from the corrected EEG. Next, low-pass (LP) filtering with recommended cut-off frequency at < 70 Hz and adaptive noise cancelling (ANC) should be performed to improve the correction of the residual artefacts (Niazy et al., 2005). Both our methodology and FASTR were applied in EEG excerpts of 4 minutes-length.

6.4.2 Quantitative assessment

The resulting restored EEG signals, $\hat{\epsilon}_n$, from application of the gradient artefact correction according to our methodology and the FASTR method were used to estimate the evaluation metrics of artefact attenuation and EEG preservation. The gradient artefact attenuation was assessed by calculation of the attenuation in the frequency bins associated with TR-slice up to 500 Hz. To this end, a bandwidth of ± 1 Hz around the fundamental of each frequency bin was taken into consideration (Niazy et al., 2005). In turn, assessment of the EEG preservation was carried out by the quantification of the EEG power spectrum in a certain bandwidth: delta (0.5 – 4 Hz), theta (4 – 8 Hz), alpha (8 – 14 Hz), beta (14 – 30 Hz), gamma (30 – 100 Hz), high-frequency-1 – Hf1 (100 – 200 Hz), and high-frequency-2 – Hf2 (200 – 500 Hz).

6.4.3 Clinical evaluation of the gradient artefact correction

To perform a clinical evaluation, the time course restored EEG signals $\hat{\epsilon}_n$, were brought to a clinical EEG expert for visual inspection. The expert was requested to identify the occurrence of epileptiform activity in $\hat{\epsilon}_n$, thus providing a clinical indication of the quality of signal used in these studies (Bénar et al., 2003).

6.5 Results

Figure 6.2a shows an exemplary excerpt of the recorded scalp potential corrupted by the gradient artefact, electrode position T7. An exemplary of the power spectrum of the recorded scalp potential, electrode position T7, is depicted in Fig. 6.2b. Figure 6.3 depicts the gradient artefact correction in the scalp potential, electrode position T7, performed according to our methodology and the FASTR plug-in in the following scenarios: AAS alone; combination of AAS and OBS (AAS+OBS); OMA (for TR: $M = 12500$, $p = 6$, $J = 2 \times 10^9$, and $L = 1$; and for TR-slice: $M = 310$, $J = 2 \times 10^5$, and $L = 1$). As can be seen in Fig. 6.3a, the correction provided by AAS was not effective in suppressing the artefact, and a substantial amount of residual artefacts is observed in the corrected EEG, rather than the correction provided by the combination AAS+OBS and by OMA.

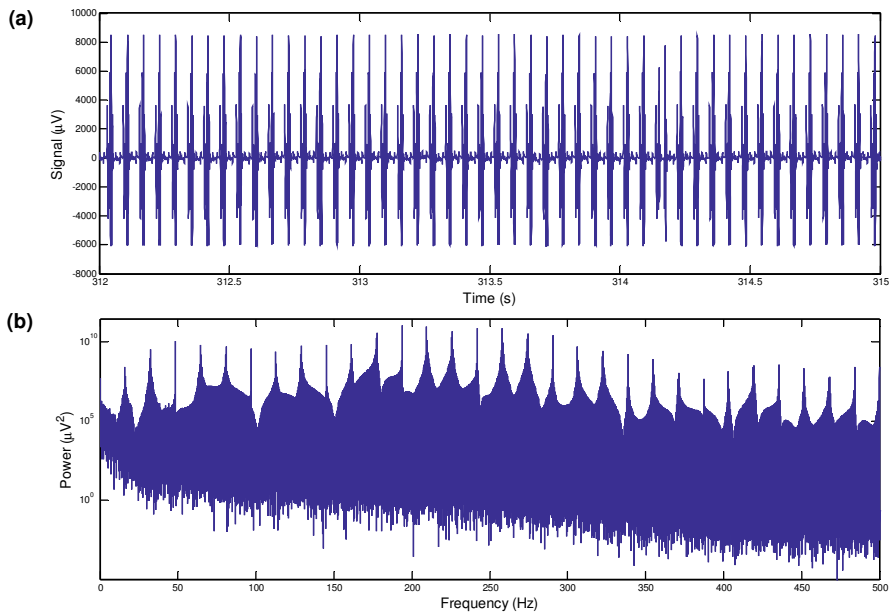


Figure 6.2: (a) Exemplary excerpt of the time course recorded scalp potential, electrode position T7; (b) exemplary power spectrum of the scalp potential, electrode position T7.

In Figs. 6.3b and 6.3c, a cleaner EEG was also obtained by OMA, whereas some residuals can be observed for the signals corrected by AAS and AAS+OBS. The residuals shown in Fig. 6.3c are related to broadening of the spectral lines associated with TR-slice (Eq. (6.2)).

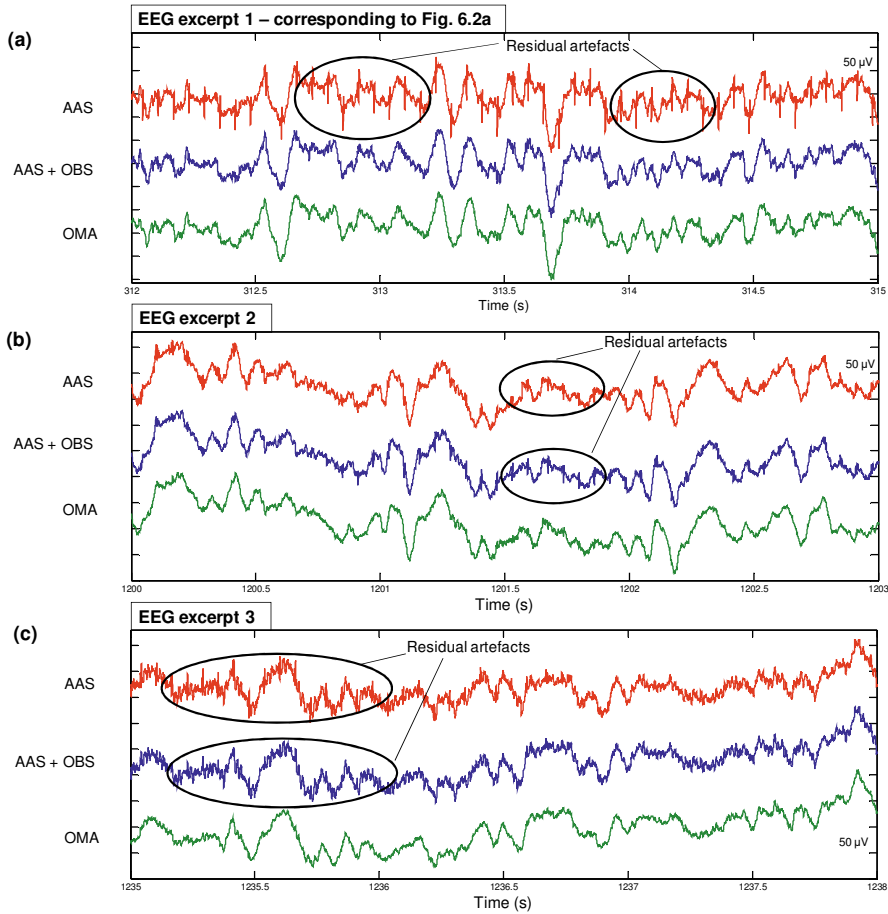


Figure 6.3: (a) Exemplary excerpt of the time course recorded scalp potential, electrode position T7; (b) exemplary power spectrum of the scalp potential, electrode position T7.

Because OMA is able to better account for the suppression of the artefact activity associated with TR-slice, it has been capable of better attenuating such residuals. This can also be observed in Fig. 6.4 in which the EEG excerpt corresponds to the electrode position FC5. In the time course EEG as well as in the power spectrum, a larger amount of residuals can be observed in the signals corrected by AAS and AAS+OBS, rather than OMA.

As some spectral lines associated with TR-slice have showed up larger broadening, a small amount of residual artefacts still remained in EEG corrected by OMA, as observed in Fig. 6.4a and 6.4d. To redress these residual artefacts, thereby, we applied OMA along with the highly selective notch filtering (OMA+HSN) and with both HSN and the optimised exponential average (OMA+HSN+OEA), resulting in the corrected EEG signals of Fig. 6.5a

(light green and brown trace, respectively). For this case scenario, OEA was set as: $C = 10000$, $K = 1.7$, $J = 0.2$, and $L = 10000$.

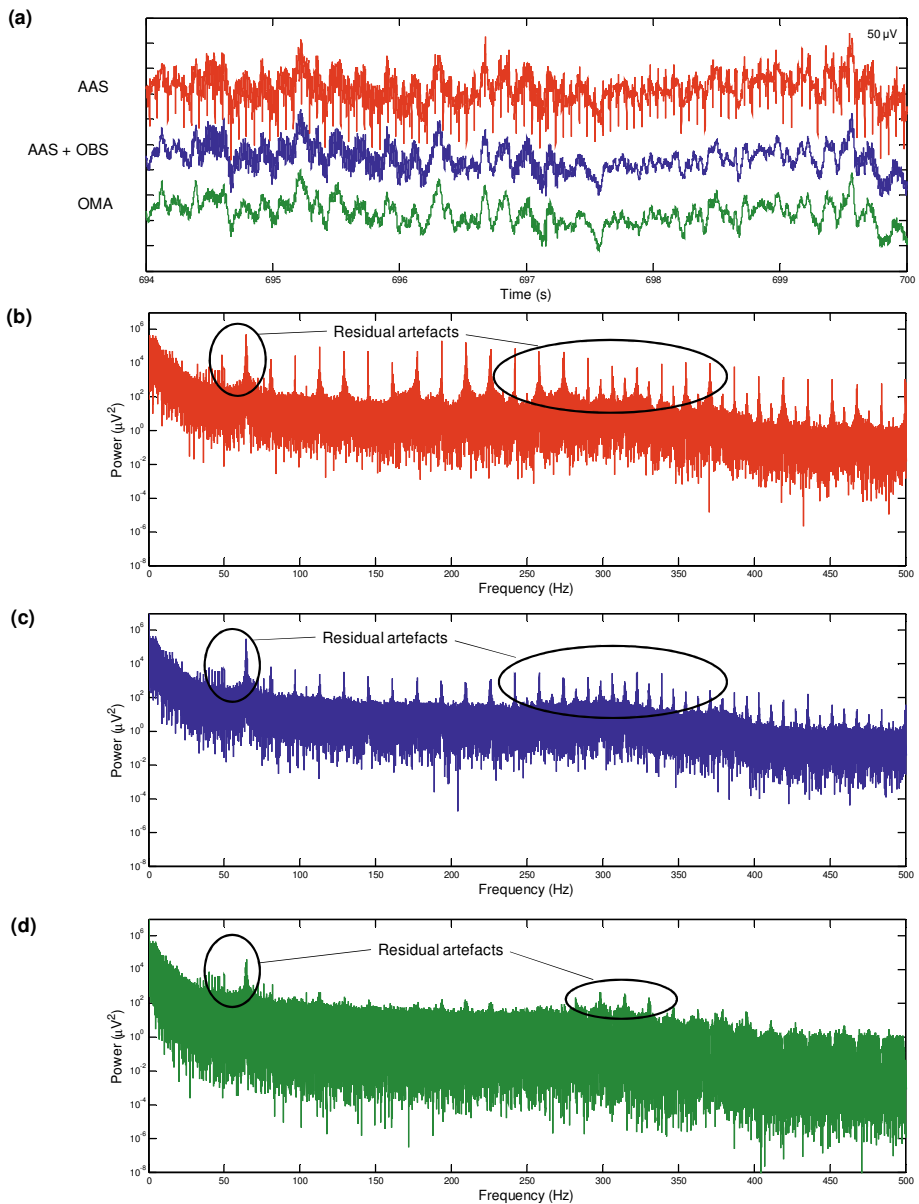


Figure 6.4: Corrected EEG (electrode position FC5) within some scenarios: (a) AAS, AAS combined with OBS (AAS+OBS), and OMA; (b) power spectrum of the signal corrected by AAS; (c) power spectrum of the signal corrected by AAS+OBS; (d) power spectrum of the signal corrected by OMA.

It can be observed that those residuals shown in Fig. 6.4a and 6.4d have been strongly attenuated. In Fig. 6.5a, the residual correction obtained by application of adaptive noise cancelling (ANC) and low-pass (LP) filtering in the signal corrected by AAS+OBS of Fig. 6.4a is shown as well. LP filtering was set with two values of cut-off frequency for comparison purposes: 250 Hz and 70 Hz (recommended in the FASTR plug-in).

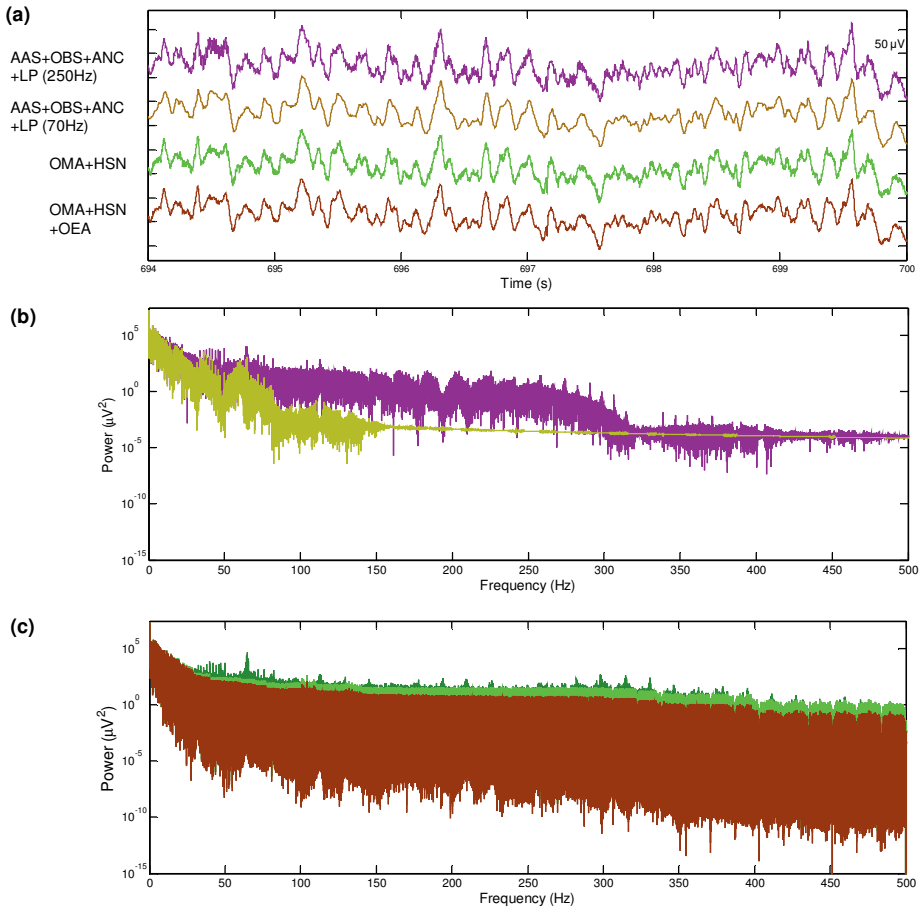


Figure 6.5: Corrected EEG (electrode position FC5) within some scenarios: (a) AAS+OBS+ANC+LP filtering (FASTR), OMA+HSN, and OMA+HSN+OEA; (b) power spectrum of the signals corrected by FASTR (LP filtering cut-off 250 Hz – pink) and by FASTR (LP filtering cut-off 70 Hz – dark yellow); (c) power spectrum of the signals corrected by OMA (dark green), OMA+HSN (light green), and OMA+HSN+OEA (brown trace).

By using ANC and LP filtering cut-off 250 Hz, some residual artefacts can still be observed in the corrected signal; whereas for the correction by ANC and LP filtering cut-off 70 Hz, the residuals have been strongly attenuated, but at the expense of some signal degradation in the

gamma band (30 – 100 Hz) and above. This can be clearly observed in the power spectra depicted in Fig. 6.5b. Rather, the signals corrected by the combination OMA+HSN and OMA+HSN+OEA have been better preserved, especially at higher frequencies.

In Fig. 6.6, EEG excerpts of the electrode positions CP1 and C4 were used to illustrate the influence of alterations that continuously occur in the artefact waveform morphology due to subject head movements over the performance of the gradient artefact correction. In case of Fig. 6.6, OMA was set for TR: $M = 12500$, $p = 6$, $J = 2 \times 10^9$, $L = 1$; and for TR-slice: $M = 310$, $J = 2 \times 10^4$, and $L = 1$). As depicted in Figs. 6.6a and 6.6b, the correction of AAS was affected by the occurrence of head movements in such a way that the artefact-corrected signal possesses a “step” around the times 544 s and 864 s, respectively, as indicated. The signal corrected by the combination AAS+OBS does not show up such a step, as with the correction provided by OMA alone. Figure 6.6c depicts the EEG correction under the occurrence of transients in the recorded potential due to an abrupt head movement around 1904 s (Fig. 6.6d). The influence of these transients was propagated along the time course corrected EEG matching all averaging epochs used to estimate the artefact template by AAS, which were in the same framework where the movement occurred. These movement influence can be observed at time intervals regularly spaced equal to the repetition time TR ($= 2.5$ s) in Fig 6.6c. Neither the combination AAS+OBS nor AAS+OBS+ANC+LP (FASTR) were capable of attenuating these residual artefacts, as indicated.

On the contrary, we observed that most of the entire length of the EEG corrected by OMA was not corrupted by the influence of abrupt head motions which have been noticed only nearby and locally in the region of the signal in which the abrupt movement occurred (around ± 20 s the site of the abrupt movement occurrence). Thus, the performance of OMA is shown to be less susceptible to alterations in the morphology of the artefact waveform than AAS (Ferreira et al., 2016), in addition to being more robust in limiting the region of influence of abrupt head motions than AAS and FASTR.

Last, we can also observe in Fig. 6.6c that FASTR has been able to attenuate the residual artefact contribution associated with the broadening of spectral lines, but at the expense of suppression of higher-frequencies alike (as indicated in Fig. 6.5). Rather, such residuals are not seen in the corrected EEG by OMA alone depicted in Fig. 6.6c.

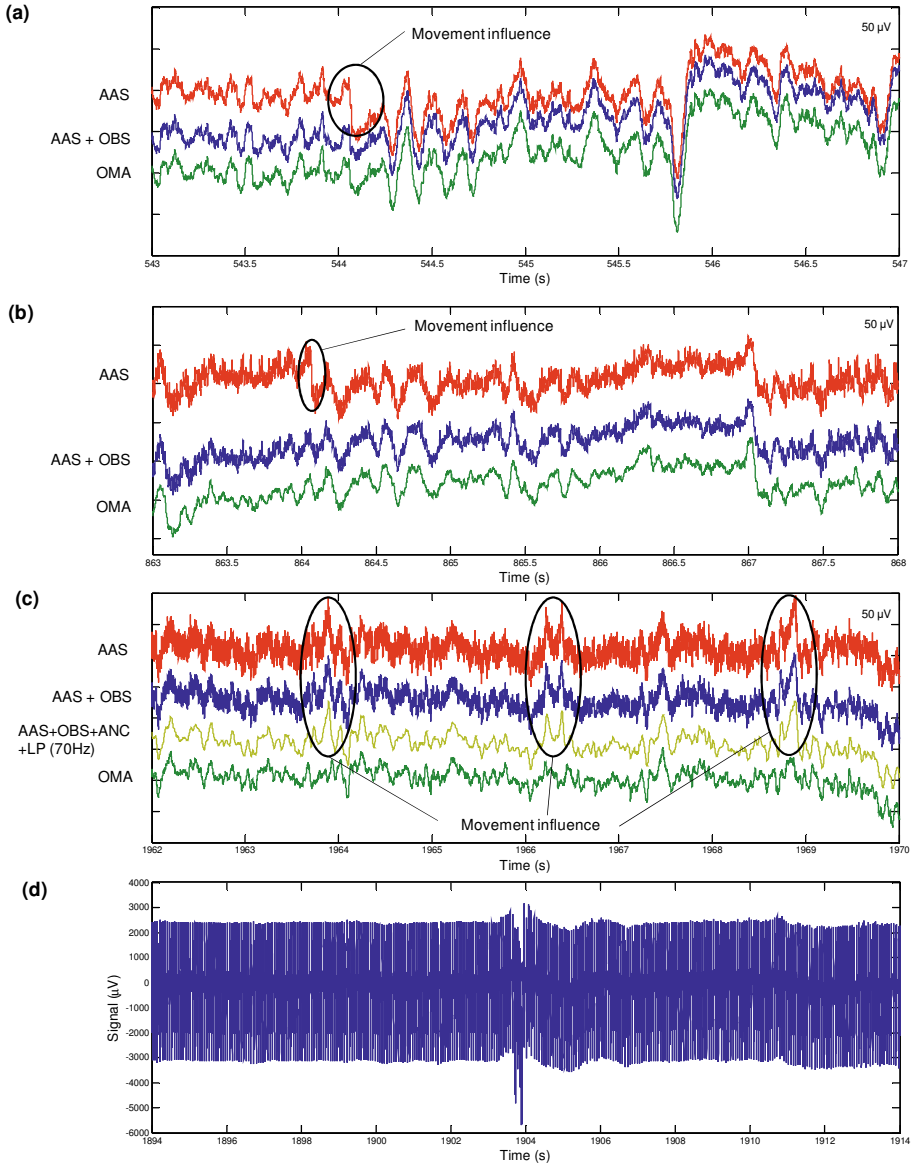


Figure 6.6: Performance of the gradient artefact correction under the occurrence of alterations of the artefact waveform due to abrupt movements of the subject head. (a) Corrected EEG (electrode position CP1) within some scenarios: AAS, AAS combined with OBS (AAS+OBS), and OMA; (b) corrected EEG (electrode position C4) within some scenarios: AAS, AAS combined with OBS (AAS+OBS), and OMA. In (a) and (b), the influence of the movement can be observed in the signal corrected by AAS; (c) corrected EEG (electrode position CP1) within some scenarios: AAS, AAS combined with OBS (AAS+OBS), AAS+OBS+ANC+LP filtering (cut-off frequency 70 Hz), and OMA. The influence of transients due to an abrupt head movement that occurred around the time 1904 s – shown in (d) – has propagated and is observed in the signal corrected by AAS, AAS+OBS, and AAS+OBS+ANC+LP filtering – shown in (c).

6.5.1 Quantitative assessment

The evaluation metrics used to perform the quantitative assessment are shown in Tables 6.1 and 6.2, and in Figs. 6.7 and 6.8. In Table 6.1, the median attenuation in the artefact frequency bins is shown for the methods AAS, AAS+OBS, FASTR (AAS+OBS+ANC+LP filtering 70 Hz cut off), OMA, and OMA+HSN+OEA. In turn, Table 6.2 contains the quantification of the EEG power spectrum in certain spectral bands of the corrected EEG by using those methods as well. To calculate the values shown in Tables 6.1 and 6.2, OMA was set with $M = 12500$, $p = 6$, $J = 2 \times 10^9$, and $L = 1$ for TR; and $M = 310$, $J = 2 \times 10^5$, and $L = 1$ for TR-slice. All 31 EEG channels were used to perform the calculations.

Table 6.1: Median attenuation in the artefact frequency bins, taking into account all 31 EEG channels.

Frequency Bin (Hz)	AAS	AAS+OBS	FASTR	OMA	OMA+HSN+OEA
	Attenuation (dB)				
16.13	50.7352	50.7283	63.6740	51.1389	52.3798
32.26	76.8044	76.9261	111.2301	78.2699	82.3502
48.39	94.9217	96.2663	158.3823	98.5108	104.9412
64.52	82.4702	83.7273	134.0989	91.5779	107.8699
80.65	100.7179	104.0741	157.6734	108.2884	118.0990
96.77	94.0843	97.8854	195.9507	103.4230	113.4788
112.90	86.0906	91.4230	200.1521	96.1344	107.0718
129.03	96.3771	100.9330	210.6327	108.5335	120.4659
145.16	106.0348	111.7487	226.8173	120.2622	132.8102
161.29	114.1487	119.3433	242.5342	126.5353	139.5446
177.42	116.2986	128.0128	249.5689	133.1763	146.7330
193.55	116.4265	130.1584	253.1660	138.6117	152.6805
209.68	116.1064	130.2667	256.5099	137.5850	152.1181
225.81	112.9144	121.2780	248.1759	134.5860	149.5532
241.94	114.4375	123.2277	249.2439	137.0389	152.4031
258.06	115.0146	129.0782	254.9462	140.9926	156.7328
274.19	115.9931	127.1585	252.1766	138.7349	154.8287
290.32	114.5683	119.5524	242.6050	137.8445	154.2659
306.45	110.5731	114.8271	237.6550	133.7534	150.4931
322.58	106.1828	111.2197	229.1634	133.1626	150.2039
338.71	98.2242	105.6046	225.3679	129.1293	146.4487
354.84	94.2745	98.4832	216.8488	125.7343	143.3237
370.97	91.9462	96.7020	217.9331	125.0865	142.9363
387.10	94.8896	100.7345	214.7092	132.1282	150.2195
403.23	109.6036	112.2031	223.2496	140.6863	159.0148
419.35	112.3900	118.6223	224.9659	150.0005	168.5576
435.48	108.6084	112.8974	227.4562	149.7288	168.5000
451.61	103.7853	107.2856	216.2013	141.9930	160.9733
467.74	105.4005	109.4738	213.0502	142.9066	162.0913
483.87	111.1620	115.7936	218.4599	147.2665	166.6407
500.00	113.2789	121.7474	223.1719	153.5717	173.1344

Table 6.2: Median power spectrum estimated for some EEG frequency bands, taking into account all 31 EEG channels.

Frequency Band	AAS	AAS+OBS	FASTR	OMA	OMA+HSN+OEA
	Power (μV^2)				
Delta (0.5 – 4 Hz)	5.3499×10^7	5.3533×10^7	6.4765×10^7	5.7578×10^7	5.7578×10^7
Theta (4 – 8 Hz)	3.8436×10^7	3.8424×10^7	4.4484×10^7	4.1298×10^7	4.1225×10^7
Alpha(8 – 14 Hz)	2.4026×10^7	2.3981×10^7	2.2765×10^7	2.5215×10^7	2.4583×10^7
Beta(14 – 30 Hz)	7.4765×10^6	7.4632×10^6	3.2984×10^6	7.3867×10^6	5.9815×10^6
Gamma(30 – 100 Hz)	4.1938×10^6	4.0426×10^6	5.5634×10^5	2.6371×10^6	1.1153×10^6
Hf1 (100 – 200 Hz)	1.9946×10^6	1.1293×10^6	4.3840×10^1	9.1838×10^5	2.3111×10^5
Hf2 (200 – 500 Hz)	1.3419×10^6	5.3085×10^5	1.1887×10^0	2.6505×10^5	4.5629×10^4

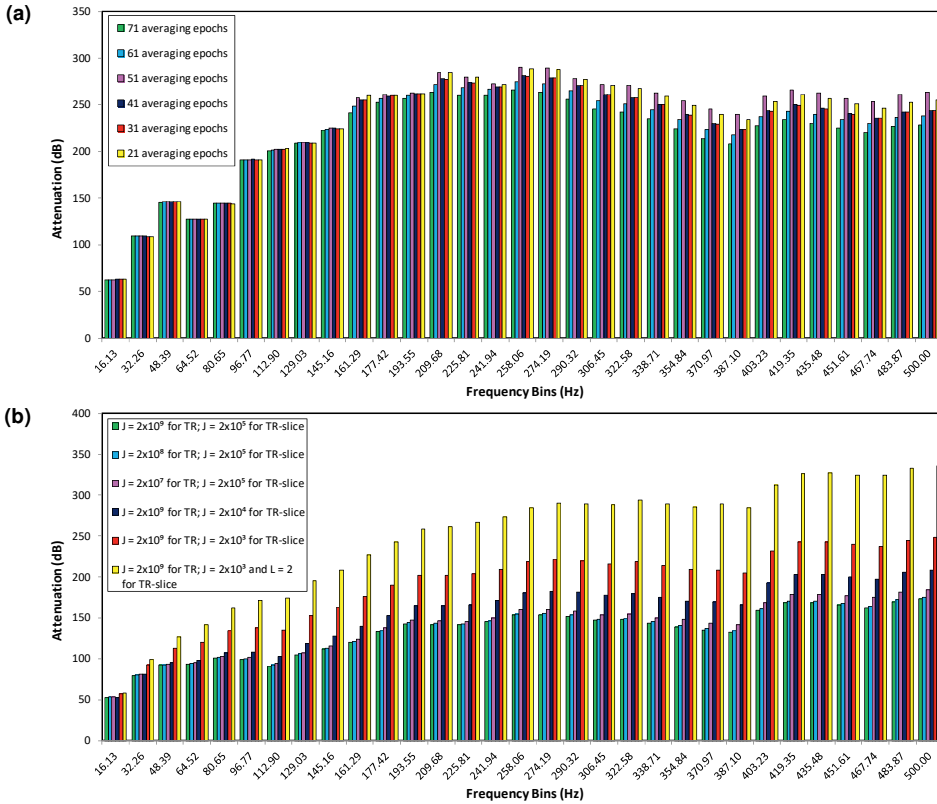


Figure 6.7: Attenuation in the frequency bins by application of (a) FASTR and (b) our methodology for an EEG excerpt picked up from the EEG electrode O2, taking into account different number of AAS averaging epochs and values of J and L (L equals 1 where not indicated) for OMA. Variation of the number of AAS averaging epochs is shown to have no significant influence on the degree of attenuation by the FASTR method within a certain frequency bin. Rather, variation of the parameters J and L used within the OMA approach are shown to significantly influence on the attenuation by our methodology within a certain frequency bin, especially at higher frequencies.

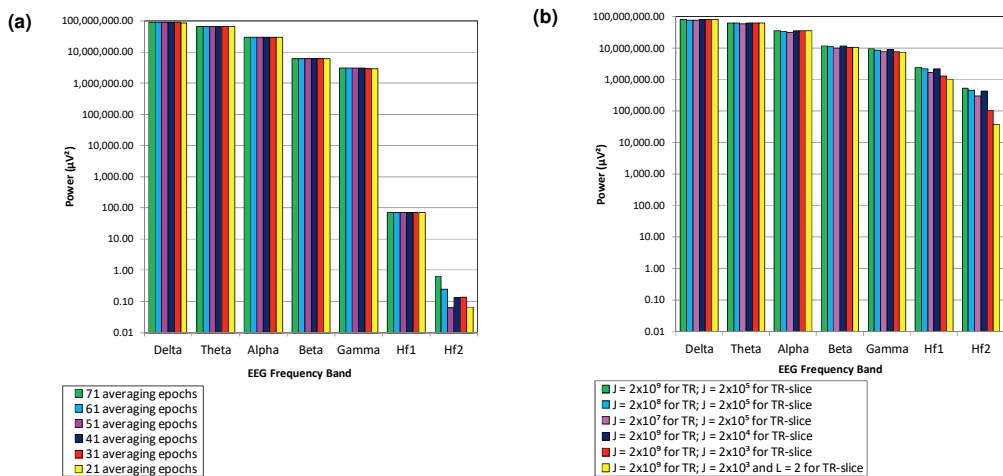


Figure 6.8: Spectral power within the frequency bands of the corrected EEG by (a) FASTR and (b) our methodology for an EEG excerpt picked up from the channel O2 (corresponding to Fig. 6.7), taking into account different number of AAS averaging epochs and values of J and L (L equals 1 where not indicated) for OMA. High-frequency spectral power has been better preserved in the corrected EEG by using our methodology.

As shown in Table 6.1, the attenuation in the artefact frequency bins by the combination AAS+OBS was higher than that by AAS alone, as expected. As depicted in Fig. 6.4, however, OMA alone might be used to achieve higher attenuation than AAS alone and AAS+OBS. The highest attenuation in the frequency bins was achieved by the usage of FASTR. However, as observed in Table 6.2, FASTR did not yield greater preservation of spectral power in higher-frequency bands of the corrected EEG, rather than the usage of OMA+HSN+OEA. Therefore, even though FASTR can achieve higher attenuation of the artefact around the frequency bins, it produces larger washing out of higher-frequency components in the corrected EEG. In parallel, it can be noticed that FASTR produces enlargement of spectral energy in the delta and theta frequency bands in comparison with the EEG signal corrected by AAS alone and AAS+OBS. This appears to be a result of a slight signal distortion that might have been introduced in the corrected EEG after application of ANC and LP filtering. Such an effect has not been observed in the corrected EEG by OMA+HSN+OEA in comparison with the EEG corrected by OMA alone.

In Figs. 6.7 and 6.8, the attenuation in the frequency bins associated with TR-slice as well as the spectral power quantification is shown, respectively, for an exemplary EEG electrode, O2. For these figures, some number of averaging epochs for the AAS method as well as some values of J and L (L equals 1 where not indicated) for the OMA method were taken into

account. It can be observed in Fig. 6.7 that the use of proper values of J and L enlarges the attenuation in a certain frequency bin, mainly at higher frequencies. Rather, variation of the number of AAS averaging epochs appears not to produce significant variation of the attenuation produced by FASTR in a certain frequency bin. A similar behaviour can be noticed for the spectral power of the corrected EEG (Fig. 6.8), where variation of the number of averaging epochs does not significantly change the power in a certain EEG bandwidth, rather than our methodology. In parallel, better preservation of the EEG signal especially at higher frequencies can also be achieved by using our methodology than FASTR. In case of FASTR, slightly better preservation of the spectral power might be observed only in the delta and theta frequency bands, as also indicated in Table 6.2. Thus, Tables 6.1 and 6.2 and Figs. 6.7 and 6.8 suggest that a better balance for the trade-off artefact attenuation versus preservation of the corrected EEG can be achieved by our methodology than FASTR, especially at higher frequencies.

6.5.2 Identification of epileptiform activity and clinical evaluation

Identification and annotation of epileptic spike occurrences in the time course corrected EEG by the proposed methodology as well as by the FASTR (AAS+OBS+ANC+LP filtering 70 Hz) were requested to the EEG expert. According to the visual inspection carried out by the EEG expert, it has been possible to successfully identify the occurrence of epileptiform activity in the corrected EEG provided by both methodologies, as depicted in Fig. 6.9 for EEG excerpts picked up from some exemplary EEG electrodes. Therefore, our methodology has shown to achieve identification of epileptiform activity in the corrected EEG data comparable to that obtained by the application of the FASTR method.

Under the occurrence of abrupt head movements, some spike-waves appeared to be affected by the movement influence which caused some degree of distortion of such waves. In some cases, the movement influence seemed to reinforce or weaken signal regions with suspicious epileptiform activity which might partially compromise its correct identification. Rather than in the signal corrected by FASTR, this effect was observed in a shorter length of the signal corrected by our methodology, in which the movement influence could be noticed. Thus, it might represent an important characteristic associated with the use of our methodology in this scenario since the occurrence of abrupt head movements cannot be prevented in epileptic patients.

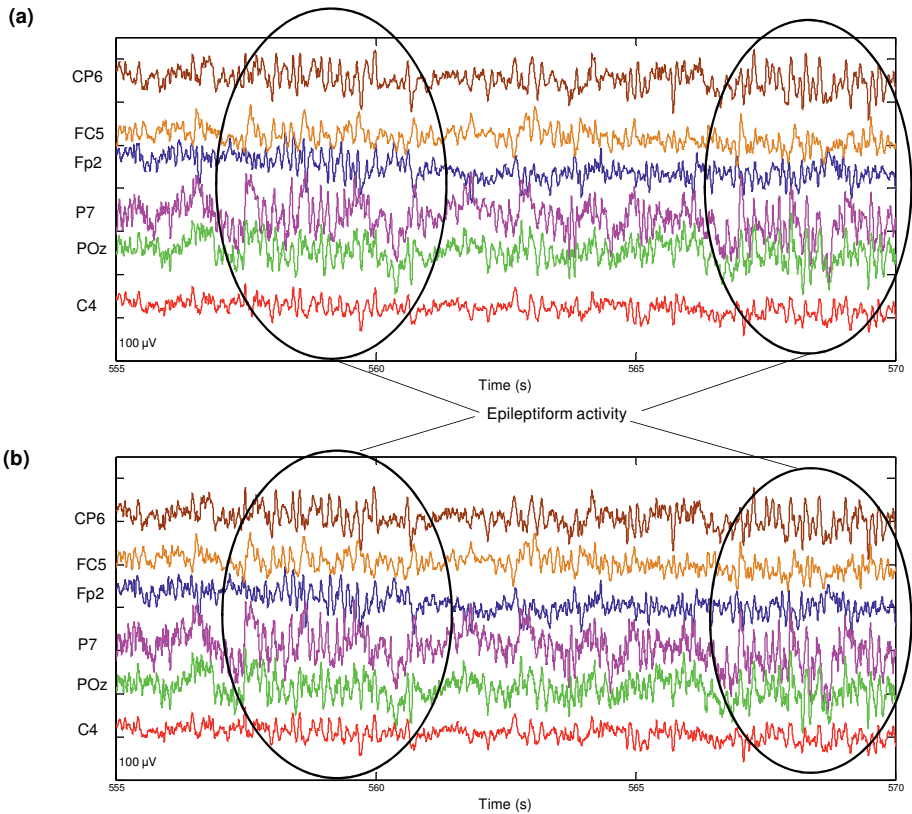


Figure 6.9: EEG excerpts containing epileptiform activity picked up from some exemplary EEG electrodes corrected by (a) FASTR and (b) our methodology.

Moreover, inasmuch as the occurrence of epileptiform activity as well as the movement artefact influence can be strengthened in higher fields of the MRI scanner, the use of a gradient artefact correction method more robust to abrupt head movements might represent an additional advantage in order to produce epileptiform activity more distinguishable in the corrected EEG signal (Eichele et al., 2010; Spencer, 2015; Bénar et al., 2003; Gotman and Pittau, 2011; Hauf et al., 2012).

6.6 Discussion

As observed in Figs. 6.3, 6.4, and 6.5, the comb-filtering provided by the template subtraction by AAS might not be able to effectively attenuate the gradient artefact, in such a way that a large amount of residual artefacts were left behind in the corrected EEG. In addition to being

affected by jitter problems (Braun, 1975; Mandelkowitz et al., 2006), the performance of AAS has strong dependency upon movements of the subject head, so that broadening of the gradient artefact spectral lines caused by micro-moments (Eq. (6.2)) may compromise the effectiveness of such a gradient artefact correction method. Thus, it is necessary to use additional processing approaches like principal component analysis, adaptive noise cancelling (ANC), independent component analysis, spatial filtering, and low-pass (LP) filtering in order to achieve the suppression of such residuals (Niazy et al., 2005; Allen et al., 2000; Eichele et al., 2010; Becker et al., 2005). These approaches, however, may also provoke unwanted removal of components of interest in the EEG signal, as can be noticed in Fig. 6.5 and Table 6.2. As for the use of the optimal basis set (OBS) based upon principal component analysis (Niazy et al., 2005), it may not produce effective suppression of the residual artefacts after AAS, as observed in Figs. 6.3 – 6.6 and Table 6.1.

In turn, the comb-filtering provided by the optimised moving-average (OMA) method is shown to be capable of providing a gradient artefact correction with higher attenuation within the artefact frequency bins than AAS alone or AAS+OBS (Table 6.1), thus provoking a smaller occurrence of residuals (Figs. 6.3, 6.4, and 6.5). Thereby, OMA is able to better address the broadening of the gradient artefact spectral lines around the frequency bins (as indicated in Eq. (6.2)), outperforming AAS and AAS+OBS in attenuating the artefact activity associated with TR-slice. In this way, the use of proper values of J and L in Eqs. (6.3) and (6.5) permits to increase the attenuation in higher-frequency artefact bins, but with less degradation of the EEG signal when compared with FASTR (Tables 6.1 and 6.2 and Figs. 6.7 and 6.8).

As also shown in Figs. 6.7 and 6.8, variation of the values of J and L is more effective in enlarging the attenuation provided by our methodology, rather than the variation the number of AAS averaging epochs for the FASTR method, but producing better preservation along the EEG frequency bandwidth, especially at higher frequencies. FASTR appears to slightly provide better preservation of the spectral power in the corrected EEG only in the delta and theta frequency bands, as indicated in Table 6.2 and Fig. 6.8. However, the spectral power in these EEG frequency bins is shown to be enlarged in comparison with the EEG corrected by AAS and AAS+OBS, which also appears to be associated with some distortion caused by ANC and LP filtering. OMA is also less prone to be affected by jitter problems because it is implemented to perform the artefact correction sample-by-sample, instead of estimation and subtraction of an average artefact template (Allen et al., 2000; Becker et al., 2005; Spencer,

2015; Ferreira et al., 2016). Those characteristics, thereby, indicate that our methodology could be used to achieve a better balance than AAS, AAS+OBS, and FASTR for the trade-off amount of artefact attenuation versus preservation of the corrected EEG, especially at higher frequencies.

When the dynamic stabilisation in the MRI scanner cannot be switched off, which has been the scenario under study in this work, TR-slice may no longer be an integer of the EEG sampling interval. Thereby, the construction of the average artefact template by AAS should be performed by using either a template with length TR or irregular epochs of length TR-slice (Allen et al., 2000; Spencer, 2015). However, the quality of the corrected EEG may be compromised in this scenario (Fig. 6.3a), thus being less effective than the template subtraction using regular epochs with TR-slice length (Mandelkow et al., 2010). Moreover, according to Mandelkow et al. (2010), subsequent application of the template subtraction for both TR and TR-slice is not able to solve this problem because the use of two averaging steps also degrades the quality of the corrected EEG which is dominated by the noise contribution from the averaged EEG signal. Rather, OMA could be applied in two steps without compromising the quality of the corrected EEG, as indicated by the results presented in Figs. 6.3 – 6.6 and Tables 6.1 and 6.2. Thereby, the application of OMA for TR-slice (jointly with the application for TR) could be used to obtain additional attenuation of the artefact activity associated with TR-slice, as indicated in Figs. 6.4 and 6.7 and Table 6.1.

As for the residual artefacts associated with broadening of spectral lines in the corrected EEG after OMA depicted in Fig. 6.4d, the highly selective notch (HSN) filtering and the optimised exponential average (OEA) are shown to effectively attenuate such residuals. As depicted in Figs. 6.1 and 6.5c, HSN and OEA can be used to provide more selective attenuation for residual artefacts in the gamma band (30 – 100 Hz) and in higher-frequency EEG bands than the usage of ANC and LP filtering. The balance for the trade-off between amount of artefact suppression and EEG signal preservation is a challenge during gradient artefact correction because suppression of the artefact can also provoke removal of components of the neuronal EEG (Ritter et al., 2007). Thus, the usage of more selective filtering approaches like HSN and OEA can lead to a better balance for such a trade-off. In case of conventional LP filtering, it is not effective in attenuating residual artefacts below the filter cut-off frequency on one hand. On the other hand, higher-frequency components of the neuronal EEG above the cut-off frequency may be undesirably removed (Fig. 6.5b and Table 6.2). The use of OEA can help to overcome this problem because this approach is able to produce residual artefact attenuation

more effectively in the gamma band and at higher frequencies than ANC and LP filtering (Fig. 6.5c and Tables 6.1 and 6.2).

In turn, when the power spectrum of the signal corrected by OMA+HSN is compared with the power spectrum of the signal corrected by OMA alone (Fig. 6.5c), it can be noticed that HSN filtering does not cause any attenuation of signal frequencies other than those above the set threshold assumed to be associated with artefact residuals. Regarding ANC, it may provoke large attenuation of residual artefacts in the gamma band, but at the expense of removal of EEG activity as well (Fig. 6.5b and Tables 6.1 and 6.2). All those characteristics help to explain the better preservation of EEG frequencies in the signal corrected by OMA+HSN+OEA in comparison with AAS+OBS+ANC+LP filtering (FASTR). Furthermore, OMA, HSN, and OEA have simple and data-driven implementation, not requiring any accurate information about triggers and other MRI events, as may be the case for data originally acquired for clinical (rather than research) purposes. In addition, our methodology shows to be much less computationally demanding than FASTR, requiring less time to process the gradient artefact correction and residual artefacts attenuation. Such a characteristic could be ascribed to the computational efficiency of Eqs. (4.2), (5.12), and (6.12) upon which the implementation of OMA, HSN, and OEA is based (Ferreira et al., 2018).

As depicted in Fig. 6.6, alterations of the artefact waveform due to head movements are also more prone to affect the performance of AAS or AAS+OBS than OMA. Because of those alterations, an average artefact template cannot characterise individual occurrences of the artefact waveform. The use of a sliding average window implementation whereby the probability of movement influence within a particular averaging window may be decreased has been proposed to minimise this problem (Allen et al., 2000; Becker et al., 2005; Niazy et al., 2005; Freyer et al., 2009). However, the correct choice of the number of averaging epochs poses difficulties to implementation of this approach since few windows can result in removal of neuronal EEG components of interest, whereas the use of many windows can lead to a substantial amount of residual artefacts in the corrected EEG after AAS. As a result, the influence of head movements may appear in the corrected EEG by AAS, requiring the use of OBS to minimise it, as observed in the corrected signals of Figs. 6.6a and 6.6b. Rather, OMA alone has been capable of attenuating such an influence.

As depicted in Fig. 6.6c, in case of the occurrence of transients due to abrupt head movements, it has profoundly affected the template estimate, so that the movement influence propagated

and appears along the corrected EEG in the regions corresponding to all epochs used for template averaging within the framework where the movement occurred. In this scenario, the use of AAS together with OBS, ANC, and LP filtering cannot account for the movement influence either (Sun and Hinrichs, 2009; Moosmann et al., 2009; Spencer, 2015). In case of OMA, we observed that the influence of abrupt movements over the gradient artefact correction provided by OMA has locally lain around the region in which the movement occurred. Thereby, in this scenario OMA is also shown to outperform the use of the sliding average window because it is capable of limiting the movement influence within a shorter region of the time course corrected EEG more effectively. Therefore, our method appears to possess improved robustness than AAS and FASTR in a scenario of occurrence of abrupt movements of the subject head. This characteristic could be used to facilitate the application of co-registered EEG-fMRI in studies that involve epileptic patients as well as children and during sleep, in which the occurrence of abrupt movements cannot be prevented (Sun and Hinrichs, 2009; Eichele et al., 2010; Spencer, 2015). Even though the information provided by using a camera tracking system within an algorithm that makes use of AAS and FASTR has been recently demonstrated to be useful to infer the amount of movement of the subject head and suppress the movement artefact (Maziero et al., 2016), this method is not directly designed to gradient artefact correction, rather than the methodology proposed here. In addition, this approach is not yet widely available for clinicians and investigators, nor is data-driven.

6.6.1 Limitations and future work

We observed that both AAS by sliding averaging window and OMA may suffer from ringing. A way we found to minimise the occurrence of ringing with OMA was its application in scalp potential excerpts with length equal to $M \times n / f_s$, where M corresponds to TR, n is a real integer, and f_s is the EEG sampling frequency. In case of the sliding averaging window by AAS, the ringing effect is supposed to always occur because the calculation of the average template for epochs in the ends of the excerpt may be compromised by an insufficient number of averaging epochs.

From a signal processing perspective, the occurrence of abrupt movements over a certain order of amplitude is likened to the linear superposition of an impulse signal in the scalp potential signal. In this way, the comb-filtering provided by the gradient artefact correction would succeed in attenuating the gradient artefact under the occurrence of abrupt head

movements case such a comb-filter had an impulse response with decreased settling time and shorter duration of decaying peaks (Ferreira et al., 2018). Thereby, the propagation of the movement influence along the corrected EEG might be minimised. In future work, this fact should be better investigated and might be used to bring further improvements in the gradient artefact correction under the occurrence of abrupt head movements. This is further discussed in Chapter 8. Also in future work, the results presented here should be generalised for EEG data recorded in more subjects and MRI scanners from different vendors in order to obtain a broader evaluation of the proposed methodology.

A characteristic of our methodology that still requires further investigation is the possibility of identifying high-frequency oscillations (HFOs) associated with the onset of epileptic activity. Fast HFOs ripples in the onset region of epileptic seizures are mostly present in the frequency range of 100 – 500 Hz (Gotman, 2010). As indicated in Table 6.2, such a bandwidth has been shown to be better preserved in the EEG corrected by our methodology than FASTR. Thereby, even though the presence of HFOs has not been confirmed by the expert in the EEG data under analysis in this work, they might be observed in other corrected data according to our methodology. Rather, those HFOs are prone to be suppressed in the signal corrected by FASTR because it does not allow access of EEG frequencies above the LP filtering cut-off frequency. Currently, HFOs have received increased attention but still requires the use of customised MRI sequences that are generally not available to all clinicians and investigators either (Freyer et al., 2009; Anami et al., 2003). Hence, our methodology might be exploited as a simpler alternative to access HFOs. Besides, our methodology should be applied and evaluated in other clinical studies, such as in those involving event related potentials (ERPs) and evoked potentials (EPs).

6.7 Conclusions

In this chapter, we have evaluated and demonstrated the relative efficacy of using the iterative application of moving-average and exponential average filters for attenuation of the gradient artefact and related residuals in the EEG signal recorded during co-registered EEG-fMRI. In this fashion, the results obtained by our methodology were compared with those obtained after application of the AAS and FASTR method. According to the outcomes presented in this chapter, the comb-filtering provided by the optimised moving-average (OMA) could be used

to effectively account for the periodic nature of the artefact associated with both MRI parameters TR and TR-slice. In addition, OMA has been shown to better address the broadening of the gradient artefact spectral lines associated with the slice-time (TR-slice) than the average artefact subtraction (AAS) method as well as AAS combined with the optimal basis set (OBS). Moreover, OMA is shown to be less affected by alterations in the gradient artefact waveform over time caused by subject head movements. This contributes to locally limiting the influence of abrupt head movements within a shorter region of the time course corrected EEG than using a sliding average window according to the AAS implementation. In turn, the highly selective notch (HSN) filtering and the optimised exponential average (OEA) are demonstrated to be capable of attenuating residual artefacts more selectively along the power spectrum of the corrected EEG than using ANC and conventional LP filtering. Thereby, HSN and OEA could contribute to increase the residual artefacts attenuation in the EEG gamma band and above, and simultaneously to provide better preservation of the EEG, especially at higher frequencies. Therefore, all those characteristics could enable the proposed methodology to provide better preservation of clinically relevant high-frequency EEG features than the often-used AAS and the FASTR correction method. Last, the clinical visual inspection performed here indicated that the proposed methodology could be used in studies involving identification of epileptiform activity in the time course EEG corrected for the gradient artefact.

CHAPTER 7

A Study of Attenuation of Residual Artefacts after Gradient Artefact Correction using a Non-Linear Filter based upon Differentiation between Consecutive Samples*

7.1 Abstract

This chapter presents a study about the residual artefacts resulting from the application of the gradient artefact correction methods. Those residual artefacts arise in the corrected EEG due to some factors, especially because of the broadening of the artefact spectral lines caused by tiny head movements, and may occupy a large bandwidth in the power spectrum of the corrected EEG. To investigate the extent of this bandwidth, we made use of the uncertainties related to the average template calculated by AAS to mathematically describe the residual artefacts in function of such uncertainties. In parallel, the larger signal slopes associated with the gradient artefact and residual artefacts were used as a parameter of a non-linear filtering approach termed signal slope adaption (SSD) to detect and attenuate the residual artefact activity. SSD is shown to perform a selective low-pass filtering of residual artefact samples, in such a way that it might be used to provide an indication of the usable bandwidth that is associated with the neuronal EEG. As such, this approach has been used to confirm the correctness of application of the optimised exponential average filtering presented in Chapter 6. In addition, we show that SSD could also be employed in other signal processing applications, such as the QRS detection in the ECG signal.

* This chapter was partly based on the papers:

Ferreira, J.L., Cluitmans, P.J.M., and Aarts, R.M. (2012). Gradient artefact correction in the EEG signal recorded within the fMRI scanner. Proc. BIOSIGNALS 2012 Conf.: 110-117.

Ferreira, J.L., Cluitmans, P.J.M., and Aarts, R.M. (2013a). Non-linear filter for gradient artefact correction during simultaneous EEG-fMRI. Signal Processing Research 2: 55-63.

7.2 Introduction

Co-registered EEG-fMRI has been considered a powerful tool to solve numerous questions in neuroscientific studies because of its promising capability to provide new insights into brain function. Albeit such a technique was firstly applied in the field of epilepsy (Warach et al., 1996; Seeck et al., 1998), the use of co-registered EEG-fMRI in several other studies has been reported in the literature over the past years (Villringer et al., 2010; Laufs et al., 2008). However, enhancements of the quality of EEG signal recorded during EEG-fMRI are still required in some applications, especially regarding the occurrence and suppression of artefacts induced in the EEG data by the varying magnetic fields of the MRI scanner. This is referred to as the gradient or imaging acquisition artefact (Allen et al., 2000; Mulert and Hegerl, 2009; Ritter et al., 2010).

As described in Section 2.4.1, the gradient artefact is induced in the potential recorded in the human scalp (scalp potential) by the rapid varying magnetic field gradients used for spatial encoding of the magnetic resonance signal, and radiofrequency pulses (RF) utilised for spin excitation. This artefact can be visualised in the recorded scalp potential as a repetitive waveform approximately stationary with period corresponding to repetition time (TR) or the time between the acquisition of two subsequent slices (TR-slice) in the MRI sequence (Anami et al., 2003; Ritter et al., 2010). The amplitudes of the gradient artefact can be several orders higher than that of the neuronal EEG signal. In addition, the repetitive feature of the gradient artefact can be observed as discrete harmonic artefact frequency intervals, or “frequency bins”, whose fundamental frequency occurs at multiples of the inverse of the artefact waveform period (Allen et al., 2000; Anami et al., 2003).

To minimise the induction effects, a number of solutions have been proposed to attenuate the gradient artefact at the source (Mullinger et al., 2011; Mullinger et al., 2014; Chowdhury et al., 2014). Nonetheless, as these techniques do not achieve effective suppression of the artefact, dedicated post-processing correction methods have to be applied to obtain an adequate correction of the gradient artefact. To this end, frequency-domain as well as time-domain techniques has been proposed, such as filtering in frequency-domain, average template-based approaches in frequency-domain, and average template-based approaches in the time-domain (for more details, see Table 3.2).

As discussed in Chapter 3, the average artefact subtraction (AAS) methodology has been deemed the most established post-processing computational methodology for gradient artefact correction. It consists of an average template-based approach in the time-domain that relies on the assumption of stationarity of the gradient artefact waveform as well as on the assumption of the gradient artefact and the EEG signal to be not correlated. According to the AAS implementation, an average artefact waveform template is calculated and then subtracted from the recorded scalp potential, allowing estimation of the corrected EEG (Allen et al., 2000). Although substantial attenuation of artefact activity is achieved by AAS, imprecise artefact template estimation due to variations of the artefact waveform morphology over time leads to remaining residual artefacts in the corrected EEG. Thus, additional correction techniques should be employed in order to suppress the residual artefacts and obtain a good quality for the corrected EEG, such as adaptive noise cancelling (ANC) and low-pass (LP) filtering with a cut-off frequency around 50 – 80 Hz. The use of such techniques, however, may also lead to suppression of frequency components of interest of the neuronal EEG around and over 80 Hz (Mullinger et al., 2014; Mandelkow et al., 2010; Allen et al., 2000; Spencer, 2015).

Statistical variations in the artefact waveform morphology have been mainly ascribed to the following reasons: the occurrence of subject head movements; and jitter problems related to inaccurate sampling of the artefact waveform. Albeit the effects of head motions can be usually attenuated by immobilising the subject within the MRI scanner, an average artefact template cannot characterise individual occurrences of the artefact waveform because of small drifts inserted in artefact waveform by head movements (Spencer, 2015; Yan et al., 2009). In attempt to minimise this problem, Allen et al. (2000) and Becker et al. (2005) proposed the use of a sliding average window implementation whereby the artefact template may be individually calculated for a particular occurrence of the artefact waveform. However, the correct choice of the number of averaging epochs poses difficulties to implementation of this approach since a low number of windows can result in removal of the neuronal EEG, whereas the use of many windows can lead to remaining residual artefacts after AAS. Moreover, as remarked by Spencer (2015), small head micro-movements cannot be cancelled out when using head vacuum cushions even with the most cooperative subjects. Those tiny movements provoke random variations in the amplitude of the gradient artefact components, which conceptually are likened to a random amplitude modulation. As a consequence, spectral components of the gradient artefact are broadened, especially in higher-frequency spectral bins, as described in Section 2.4.3.

In turn, to obtain a more precise sampling of the artefact waveform thus minimising jitter problems, synchronisation between the EEG sampling rate and MRI clock acquisition has been proposed by Anami et al. (2003) and Mandelkowitz et al. (2006). As demonstrated by these authors, this procedure can lead to substantial attenuation of residual artefacts and increase the usable bandwidth of the corrected EEG up to around 150 Hz. In parallel, some works have proposed to carry out post-processing correction of the timing error associated with the jitter problems (Negishi et al., 2004; Gonçalves et al., 2007; Huang et al., 2012; de Munck et al., 2013). However, it is generally difficult to access a bandwidth of the neuronal EEG over 80 Hz, so that estimation of an optimal artefact template is still object of study (Spencer, 2015). Approaches like principal component analysis (Niazy et al., 2005), independent component analysis (Mantini et al., 2007), and spatial filtering (Brookes et al., 2008) have proven to be quite useful to account for the statistical uncertainty associated with average templates as well. Nevertheless, undesirable suppression of components of interest of the neuronal EEG cannot be fully avoided by application of such approaches, especially regarding higher-frequencies in the EEG gamma band (30 – 100 Hz) and above.

In the previous chapters of this thesis, we have described the optimised moving-average (OMA) filtering as a novel gradient artefact correction approach that is capable of better attenuating the gradient artefact than AAS and simultaneously achieves better preservation of the EEG signal. Like AAS, nonetheless, OMA also relies on the assumption of stationary nature of the artefact waveform, so that some residual artefacts associated with broadening of artefact spectral lines caused by tiny subject head movements may still remain in the corrected EEG after OMA application (see Chapter 6). In the current chapter, we present a study we have undertaken to investigate the statistical variations of the gradient artefact waveform and their implications in the occurrence of residual artefacts along the power spectrum of the corrected EEG. To this end, we have made use of mathematical models to describe the residual artefacts after application of the AAS method as well as the information of variability contained in larger signal slopes that characterise the gradient artefact activity. As a result, a non-linear filter approach named signal slope adaption (SSD) was designed to investigate and attenuate the residual artefact activity, as described in Section 3.3. The use of such an approach is shown to perform a selective low-pass filtering in residual artefact samples which possesses higher signal slopes than those of the EEG signal. SSD is also shown to enable the identification of the usable bandwidth in the corrected EEG related to the neuronal EEG, as shown and discussed in Sections 7.4 and 7.5.

7.3 Methods

7.3.1 EEG and fMRI data

To implement and evaluate the proposed approach, we used three different types of EEG data sets recorded simultaneously with fMRI data. The reason to use these data sets was to assess and have a broader idea about to what extent the results obtained by using the proposed approach could be validated and applicable for different data sets and scanners from different vendors. Both MRI experimental setup and scanners provided by different vendors can change the morphology (shape and amplitude) of the gradient artefact waveform. In parallel, the MRI parameters TR and TR-slice that are fundamental for application of gradient artefact correction approaches like the AAS method vary according to type of scanner, and can influence on jitter problems and on the reproducibility of the gradient artefact waveform in consequence. Thus, it is important that performance measures are evaluated for individual data sets (Ritter et al., 2007). EEG data sets 1, 2, and 3 were recorded in MRI scanners provided by two different vendors, and different setups for the MRI parameters were utilised:

i) EEG data set 1: data set 1 was acquired by using a 3 T Discovery MR750 Scanner (GE, Waukesha, USA). A volunteer was scanned using a functional echo-planar imaging sequence (EPI) with 28 transversal slices and volume repetition time (TR) equal to 2000 ms. fMRI data acquisition was continuously performed, and TR was approximately adjusted as a multiple of the slice-time (TR-slice). The MRI clock and the EEG sampling frequency have been synchronised for a period corresponding to seven times the slice-time (TR-slice), equal to 500 ms. Thereby, TR-slice did not match a multiple of the sampling-frequency.

ii) EEG data set 2: acquisition of the EEG data set 2 was carried out using a 3 T Achieva Scanner (Philips, Best, The Netherlands). A second volunteer was scanned using a functional echo-planar imaging sequence (EPI) with 40 transversal slices and volume repetition time (TR) equal to 2000 ms. fMRI data acquisition was continuously performed, and TR was adjusted as a multiple of the slice-time (TR-slice). The MRI clock and the EEG sampling frequency have been synchronised, so that the slice-time (TR-slice equal to 50 ms) was set as a multiple of the EEG sampling frequency.

EEG data sets 1 and 2 were recorded using a 64 channels MRI-compatible BrainAmp MR plus amplifiers (Brain Products GmbH, Gilching, Germany). The volunteers wore an MRI-compatible EEG cap (BrainCap MR from EASYCAP GmbH). The cap was mounted with

sintered Ag-AgCl electrodes arranged according to the standard 10-5 system, and included one additional electrode placed on the subject back to record the ECG signal. The sampling rate of the EEG system was 5000 Hz.

iii) EEG data set 3: the scalp potential recordings corresponding to the data set 3 were collected simultaneously with the fMRI data for a research focused on epilepsy and post-traumatic stress disorder (PTSD) (van Liempt et al., 2011). The data were recorded using a 3 T Achieva Scanner (Philips, Best, The Netherlands) from one subject. fMRI was continuously performed using a functional echo-planar imaging sequence with 33 transversal slices (thickness 3 mm, TE 30 ms, TR 2500 ms). An MRI-compatible 64 channel polysomnograph (MRI 64, MicroMed, Treviso, Italy) was used to collect one ECG channel, two EOG channels, one EMG channel, and 60 EEG channels. A cap containing 64 Ag-AgCl electrodes was positioned in accordance with the standard 10-20 system. The sampling rate of the EEG system was 2048 Hz. The MRI clock and the EEG sampling frequency have been synchronised for the volume repetition time (TR). TR was not adjusted as a multiple of TR-slice. Thereby, TR-slice did not match a multiple of the sampling frequency.

All the recordings were conducted in accordance with the Declaration of Helsinki, and made with the approval of the local ethics committee and informed consent by the subjects.

7.3.2 Implementation of the average artefact subtraction methodology in this chapter

As mentioned in Sections 3.3 and 4.2, the basic idea behind the implementation of the average artefact subtraction (AAS) method consists of a coherent detection process whereby an average template of the gradient artefact waveform is subtracted from the scalp potential recordings in order to produce the corrected EEG (Allen et al., 2000):

$$\hat{e}_n = s_n - \frac{1}{N} \sum_{i=0}^{N-1} s_{n-iM}, \quad (7.1)$$

where \hat{e}_n and s_n are, respectively, the corrected EEG after template subtraction and the scalp potential signal; and the average artefact template, \hat{g}_n , matches the second term of the right hand side of Eq. (7.1) – corresponding to Eq. (4.7). Thereby, to construct the average artefact template \hat{g}_n , the scalp potential \mathbf{s} must be divided into N epochs of length M corresponding to the gradient artefact waveform period, thus matching the MRI repetition time (TR) or the slice-time (TR-slice). To identify the beginning of the MRI scan period, a marker is usually

employed either by using recording information provided by the scanner or by using a gradient identification method. In most of recording setups utilised nowadays, a phase-locking synchronisation hardware system assures the EEG system sampling frequency and the MRI scanner acquisition clock are exactly synchronised. Hence, TR (or TR-slice) is set as a multiple of the EEG system sampling interval in the recorded s_n , before estimating and subtracting \hat{g}_n (see Fig. 3.6). In case of misalignment between the EEG sampling rate and the MRI clock, however, interpolation and extrapolation within the average epochs should be performed before application of AAS (Allen et al., 2000, Ritter et al., 2007).

In this chapter, the AAS method has been performed using a home-built implementation in accordance with described above, and applied to estimate and subtract the artefact template associated with TR-slice, $M = \text{TR-slice}$. For estimation of TR-slice according to the time basis of the EEG sampling system, we firstly made use of a peak detection method whereby the onset of each slice could be identified. Accordingly, TR-slice was estimated by evaluation of the time interval between two subsequent peaks observed in s_n . Next, s_n was divided into epochs of length equal to TR-slice or $\text{TR-slice} \pm \Delta t$, where Δt corresponds to the sample variation because of the timing jitter. To perform the template averaging, epochs containing a $\text{TR-slice} \pm \Delta t$ number of samples were extrapolated or interpolated to compensate the time-misalignment. The number of segments considered for average was $N = 32$ epochs.

To calculate the samples of \hat{g}_n , their respective variances, and the corrected EEG, \hat{e}_n , we have used a mathematical approach adapted from Bishop (2006), Kay (1993), and Press et al. (1992). Its implementation was based upon the idea of minimum-variance unbiased estimation (Kay, 1993), in such a way that the mean of a random variable can be estimated by making use of its minimum variance. Thus, by minimizing the variance of a random variable with respect with an initial estimate of the mean, it allows to finding the best estimate for the mean. By making use of this idea, samples from different epochs into which the scalp potential was divided and had the same corresponding position p within the averaging epoch could be related to an initial choice for the template averaged sample, μ_p ($= \hat{g}_p$), by the following cost function:

$$\Psi_p(\mu_p) = \sum_{k=0}^{N-1} (s_{n-kN} - \mu_p)^2, \quad (7.2)$$

where n runs over the samples of \mathbf{s} ; N is the number of averaging epochs. Rewriting Eq. (7.2) into a matrix format:

$$\Psi_p(\mu_p) = \mathbf{K}^T \cdot \mathbf{K}. \quad (7.3)$$

\mathbf{K} is a vector with $N \times 1$ components, $K_p = s_{n-kN} - \mu_p$. Minimisation of Eq. (7.3) for every position p allows estimating the variance associated with each sample \hat{g}_p . Finally, the samples of $\hat{\mathbf{e}}$ result from the matrix \mathbf{Z} :

$$\mathbf{Z} = \mathbf{K} \cdot \mathbf{K}^T, \quad (7.4)$$

whose main diagonal elements correspond to the square of each sample \hat{e}_n .

7.3.3 Estimation of the residual artefacts

Taking into account Eq. (7.1), it can be rewritten according to the averaging epochs considered for template calculation (Mandelkow et al., 2010):

$$\begin{aligned} \hat{e}_i &= e_i + g_i - \frac{1}{N} \sum_{k=0}^{N-1} (e_k + g_k) \\ &= e_i + g_i - \frac{1}{N} \sum_{k=0}^{N-1} e_k - \frac{1}{N} \sum_{k=0}^{N-1} g_k, \end{aligned} \quad (7.5)$$

where \hat{e}_i is the estimate of the actual EEG in epoch i ; e_i and g_i are the actual EEG and the gradient artefact in epoch i ; and e_k and g_k are the actual EEG and the gradient artefact in the averaging epoch s_k . The amplitude of averaged EEG epochs in the third term of the right side of Eq. (7.5) equals $1/\sqrt{N}$ times the EEG RMS, in such a way that it is cancelled out by averaging (Braun, 1975; Gonçalves et al., 2007). Thus, the estimate of the average gradient artefact \hat{g}_i in epoch i corresponds to:

$$\hat{g}_i = \frac{1}{N} \sum_{k=0}^{N-1} (g_k). \quad (7.6)$$

In an optimal scenario in which the gradient artefact waveform is perfectly reproducible in each epoch, the estimate \hat{g}_i equals to g_i ($= g_k$), and thus \hat{e}_i matches the actual EEG, e_i . However, under realistic scanning conditions, changes in EEG recording geometry by subject

motion together with inconsistent scalp potential sampling due to systematic shift (jitter) between EEG system sampling and the MRI clock results in alterations in the artefact waveform. This generates a component of uncertainty, u_i , in the estimate \hat{g}_i that must be inserted in Eq. (7.6):

$$\hat{g}_i = \frac{1}{N} \sum_{k=0}^{N-1} (g_k + u_k) = \frac{1}{N} \sum_{k=0}^{N-1} g_k + \frac{1}{N} \sum_{k=0}^{N-1} u_k = g_i + u_i. \quad (7.7)$$

According to Eq. (7.7), the residual artefacts after AAS are contained in the uncertainty u_i . As mentioned by Mandelkow et al. (2010), Taylor expansion can be used to describe g_k . Thus, u_i can be estimated as:

$$\Rightarrow u_i = \frac{1}{N} \sum_{k=0}^{N-1} \left(g'_i(k\Delta t) + \frac{g''_i(k\Delta t)^2}{2!} + \frac{g'''_i(k\Delta t)^3}{3!} + \dots \right). \quad (7.8)$$

Therefore, the uncertainty u_i depends on the first and higher derivatives of the gradient artefact, the jitter (Δt), and the k number of epochs considered for averaging. As such, the analysis of those contributions to the artefact template uncertainty as indicated in Eq. (7.8) can help to understand the occurrence of residual artefacts in \hat{e}_i after subtraction of \hat{g}_i from s_i , and be used to minimise or attenuate them. In this respect, the effect of k in reducing the residual artefacts has been addressed by proposing a sliding-weighted moving-average window approach whose optimal implementation could be, in principle, experimentally performed by comparing the effects of different values of k (Becker et al., 2005; Freyer et al., 2009; Mandelkow et al., 2010). On the other hand, reduction of the impact of Δt in the uncertainty u_i could be achieved by using synchronisation of EEG system sampling frequency and the fMRI acquisition clock (Anami et al., 2003; Mandelkow et al., 2006), as well as timing error correction (Negishi et al., 2004; Gonçalves et al., 2007). In turn, to address the influence of the signal derivative on reduction of the residual artefacts, we have devised and exploited the signal slope adaption approach, described as follows.

7.3.4 Signal slope adaption (SSD) approach implementation

The analysis of the signal slope represented by the difference in amplitude between consecutive samples can be employed to detect undesirable frequency components and artefacts in digital signals (Scherg, 1982; Barlow, 1983; Cluitmans et al., 1993; van de Velde

et al., 1998). In this respect, the signal slope associated with steep signal magnitudes has been shown to be useful for detection of the muscle and other artefacts in the EEG signal (van de Velde et al., 1998). Accordingly, the larger slopes associated with the steep activity of the gradient artefact have been used to identify whether or not the EEG samples are artefact-free. To perform such identification, a slope threshold (*thrs*) must be estimated so that if the signal slope associated with a certain sample exceeds *thrs*, it is then identified containing artefact interference. The value of *thrs* is set by an evaluation of the range of the slope of control signals without serious artefact contamination, and can be estimated considering the probability distribution of the slope parameter (Cluitmans et al, 1993; van de Velde et al., 1998). Likewise, observation of the EEG recorded within the MRI scanner reveals that steep slopes and transient signal magnitudes in the order of millivolts per millisecond can be ascribed to the gradient artefact and its residuals (Eichele et al., 2010; Koskinen and Vartiainen, 2009; Niazy et al., 2005). Initially, we have investigated probability distributions of the slope parameter associated with the actual EEG and scalp potential excerpts \mathbf{s} , picked up from the same EEG electrode of one specific subject (Ferreira et al., 2012).

As actual EEG we used excerpts recorded inside the MRI scanner during non-scan periods (the reference EEG, \mathbf{e}_{ref}). In addition, we have analysed probability distributions of the slope parameter of the respective corrected EEG excerpts $\hat{\mathbf{e}}$, after AAS. Agreeing with Cluitmans et al. (1993), we observed that the signal slope parameter – first derivative: $D(\mathbf{x}) = (x_2 - x_1, x_3 - x_2, \dots, x_n - x_{n-1})$, associated with \mathbf{s} and $\hat{\mathbf{e}}$ possesses significant changes in the statistical distribution of the slope parameter in comparison with \mathbf{e}_{ref} (control signal), as can be observed in Fig. 7.1. Moreover, the statistical distribution of values of the signal slope of $\hat{\mathbf{e}}$ ($D(\hat{\mathbf{e}})$) and \mathbf{s} ($D(\mathbf{s})$) lie above the threshold calculated for \mathbf{e}_{ref} :

$$thrs = \mu_{D(\mathbf{e}_{\text{ref}})} + 3\sigma_{D(\mathbf{e}_{\text{ref}})}. \quad (7.9)$$

On the other hand, the probability distribution of the slope parameter $D(\mathbf{e}_{\text{ref}})$ estimated for \mathbf{e}_{ref} closely resembles Gaussian distributions (Fig. 7.1). Thus, the confidence interval associated with $\mu_{D(\mathbf{e}_{\text{ref}})} + 3\sigma_{D(\mathbf{e}_{\text{ref}})}$ encompasses approximately 99.5% of the distribution (Papoulis and Pillai, 2002; Cluitmans et al., 1993). By observing these distributions, it could be assumed that the signal slope corresponding to the corrected EEG should have a

distribution closer to the normal distribution as well, in accordance with the signal slope distribution observed for \mathbf{e}_{ref} .

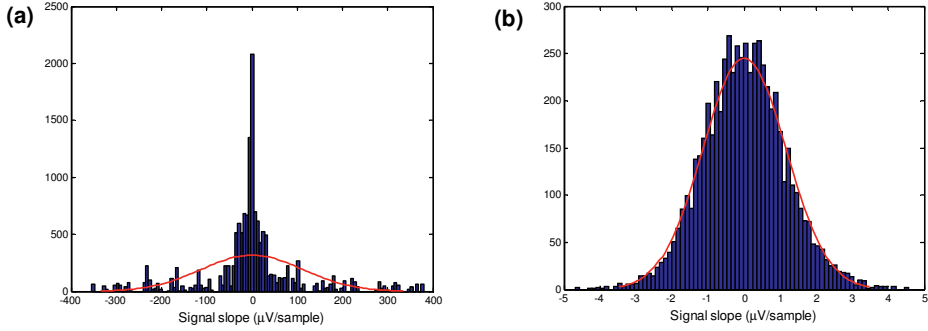


Figure 7.1: (a) Histogram of the signal slope $D(\mathbf{s})$ for a representative 3.0 s-length scalp potential excerpt, \mathbf{s} , electrode Oz, and corresponding fitted Gaussian distribution; (b) histogram of the signal slope $D(\mathbf{e}_{\text{ref}})$ for a 3.0 s-length reference EEG excerpt, \mathbf{e}_{ref} , picked up from the same EEG electrode (Oz), and corresponding fitted Gaussian distribution. Those excerpts were picked up from the recordings of one subject of the EEG data set 3.

Based on this assumption, we have devised an adaptive method whereby it could be possible to approximate $\hat{\mathbf{e}}$ to \mathbf{e} by making use of a signal slope parameter. According to our approach, a sample \hat{e}_n of the corrected EEG was mathematically modelled by the sum of the actual EEG plus the uncertainty u_i associated with each artefact template sample \hat{g}_i weighted by a certain filter parameter \hat{a}_n , as follows:

$$\hat{e}_n = s_n - (\hat{g}_i + |\hat{a}_n - a_n| u_i) = e_n + g_n - (\hat{g}_i + |\hat{a}_n - a_n| u_i) \approx e_n + |\hat{a}_n - a_n| u_i. \quad (7.10)$$

As indicated in Eq. (7.10), once the parameter \hat{a}_n is adjusted as closely as to the real value of the adaptive filter a_n , the uncertainty u_i would be attenuated, and the value of \hat{e}_n would tend to approximate to that of the actual EEG, e_n :

$$\lim_{\hat{a}_n \rightarrow a_n} \hat{e}_n \approx e_n. \quad (7.11)$$

As described in Eq. (7.8), the value of the uncertainty u_i is proportional to the first and higher derivatives associated with the gradient artefact. Thus, as parameter \hat{a}_n in Eq. (7.10), we

proposed to investigate the signal slope characterised by the maximum absolute value, d_n , of the difference between consecutive samples of the signal $\hat{\mathbf{e}}$, $D(\hat{\mathbf{e}})$:

$$d_n = \max |D(\hat{\mathbf{e}})|, \quad (7.12)$$

where n matches the subscript of the maximum slope within $D(\hat{\mathbf{e}})$. Using this equation, the two consecutive samples \hat{e}_n and \hat{e}_{n+1} associated with d_n were adapted as follows:

$$\begin{aligned} \hat{e}_{\text{adapt},n} &= \hat{e}_n - L_n, \\ \hat{e}_{\text{adapt},n+1} &= \hat{e}_{n+1} + L_n, \end{aligned} \quad (7.13)$$

where

$$L_n = \lambda \times d_n. \quad (7.14)$$

λ is the adaption factor ($0 < \lambda < 1$) to be applied to the parameter d_n . In Eq. (7.13), the sign of L_n was set positive when $\hat{e}_n > \hat{e}_{n+1}$, and vice-versa. The signal $\hat{\mathbf{e}}$ in Eq. (7.12) was then replaced by the modified signal $\hat{\mathbf{e}}_{\text{adapt}}$ which contains the adapted samples $\hat{e}_{\text{adapt},n}$ and $\hat{e}_{\text{adapt},n+1}$. Equations (7.12), (7.13), and (7.14) were iteratively recalculated until $d_n \leq \text{thrs}$. The decreasing value of d_n calculated at each iteration assured the convergence of Eq. (7.13) (see Fig. 7.16). Figure 7.2 depicts the flowchart-scheme of the procedure described in Eqs. (7.12)–(7.14), herein called signal slope adaption (SSD). As shown in this figure, the samples of $\hat{\mathbf{e}}$ are not adapted case the value of d_n in the first iteration is smaller than thrs .

In parallel, it can be experimentally shown that the decreasing values of d_n imply on decreasing of the first derivative as well as the higher derivatives in Eq. (7.8), and their impact over the uncertainty u_i in consequence. This effect can be, thereby, used to provoke the attenuation of the uncertainty \mathbf{u} in $\hat{\mathbf{e}}$, agreeing with Eq. (7.8). To make an assessment of preservation of the EEG signal after application of SSD, we used a procedure similar to that described in the scheme of Fig. 3.11. To this end, in place of the gradient artefact correction indicated in the scheme of Fig. 3.11, we used the SSD approach; and in place of \mathbf{s} , we used $\hat{\mathbf{e}}_{\text{adapt}}$. Next, the values of SNR and MSE were calculated, respectively, by using Eqs. (3.13) and (3.14).

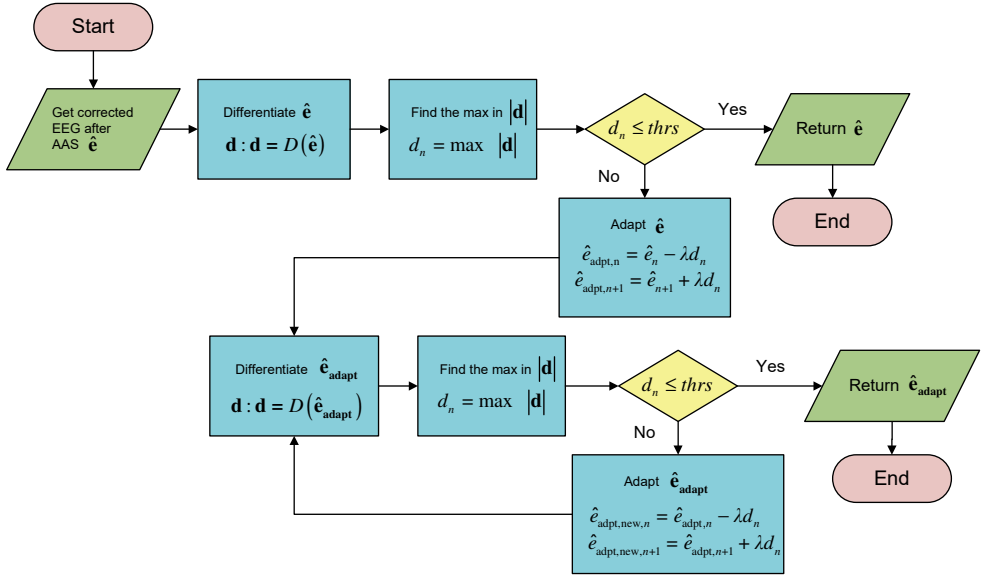


Figure 7.2: Flowchart-scheme of the signal slope adaption (SSD) algorithm described in Eqs. (7.12) – (7.14).

It is noteworthy that by the sum and subtraction of L_n as indicated in Eq. (7.16), the SSD approach does not change the expected value of \hat{e} :

$$\begin{aligned}
 E(\hat{e}_{\text{adapt}}) &= E\left(\frac{1}{I} \sum_0^n (\hat{e}_n - L_n)\right) + E\left(\frac{1}{I} \sum_n^{I-1} (\hat{e}_{n+1} + L_n)\right) \\
 \Rightarrow E(\hat{e}_{\text{adapt}}) &= E\left(\frac{1}{I} \sum_0^n \hat{e}_n\right) + L_n + E\left(\frac{1}{I} \sum_{n+1}^{I-1} \hat{e}_n\right) - L_n = E\left(\frac{1}{I} \sum_0^{I-1} \hat{e}_n\right) = E(\hat{e}). \quad (7.16)
 \end{aligned}$$

7.4 Results

The methodology described above has been implemented in MATLAB (The MathWorks Inc., Natick, USA) environment. Representative scalp potential excerpts picked up from the EEG data sets 1, 2, and 3, and the respective \hat{e} and \hat{g} resulting from the average template subtraction by the AAS ($N = 32$ averaging epochs) implementation indicated in Eqs. (7.2) – (7.4) are respectively depicted in Figs. 7.3, 7.4, and 7.5. As observed in Figs. 7.3b and 7.5b, large residual artefacts arose in the corrected EEG after subtraction of the artefact template.

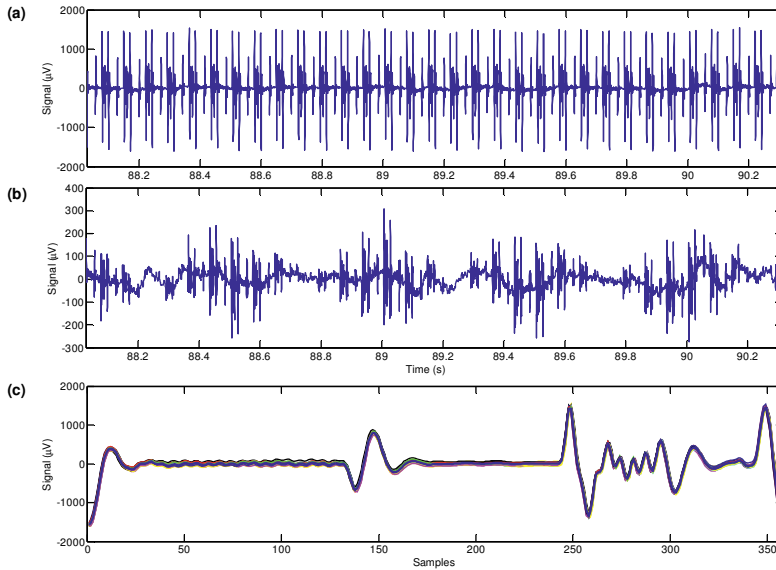


Figure 7.3: (a) Representative scalp potential, \mathbf{s} , recorded during fMRI acquisition, EEG data set 1, electrode position Fp1; (b) corrected EEG, $\hat{\mathbf{e}}$, after application of AAS; (c) set of 32 epochs (thinner traces) into which \mathbf{s} was divided (TR-slice = 357 samples), used for calculation of the artefact template (thicker blue trace). Residual artefacts after AAS can be noticed in $\hat{\mathbf{e}}$.

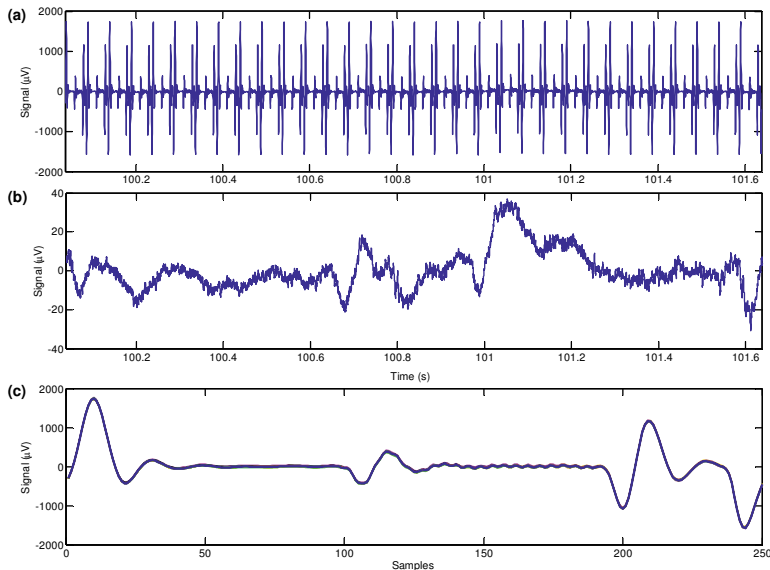


Figure 7.4: (a) Representative scalp potential, \mathbf{s} , recorded during fMRI acquisition, EEG data set 2, electrode position Fz; (b) corrected EEG, $\hat{\mathbf{e}}$, after application of AAS; (c) set of 32 epochs (thinner traces) into which \mathbf{s} was divided (TR-slice = 250 samples), used for calculation of the artefact template (thicker blue trace). Because of the high reproducibility of the artefact waveform (averaging epochs), the residual artefacts were strongly attenuated in $\hat{\mathbf{e}}$.

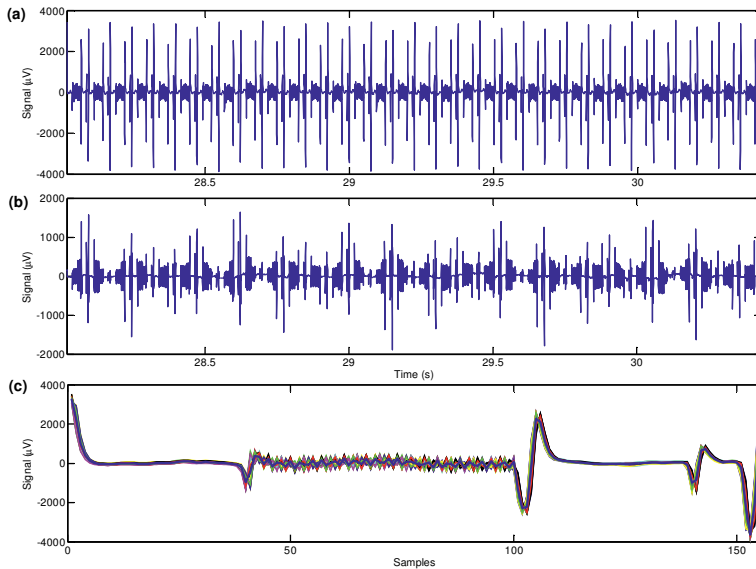


Figure 7.5: (a) Representative scalp potential, \mathbf{S} , recorded during fMRI acquisition, EEG data set 3, electrode position F6; (b) corrected EEG, $\hat{\mathbf{e}}$, after application of AAS; (c) set of 32 epochs (thinner traces) into which \mathbf{S} was divided (TR-slice = 155 samples), used for calculation of the artefact template (thicker blue trace). A substantial amount of residual artefacts arose in $\hat{\mathbf{e}}$ because of the lower reproducibility of the artefact waveform.

Like the signal slope distribution associated with the scalp potential contaminated with the gradient artefact (Fig. 7.1a), the occurrence of such residuals causes significant changes in the statistical distribution of the slope parameter in comparison with \mathbf{e}_{ref} , as can be observed in the histograms of Figs. 7.6a and 7.6c. Those residuals also occurred in Fig. 7.4b, but they have been strongly attenuated because of the high reproducibility of the averaging epochs (Fig. 7.4b). Thus, the statistical distribution of the slope parameter of the signal of Fig. 7.4b is shown to be approximated to a Gaussian distribution (Fig. 7.6b), as noticed for \mathbf{e}_{ref} in Fig. 7.1b.

The characteristics of the signal slope distributions observed in Fig. 7.6 are in accordance with the spectral analysis depicted in Fig. 7.7. The power spectrum of the signal of Fig. 7.4b lies closer to the power spectrum of the reference (baseline) EEG, in comparison with the power spectral of the signals of Figs. 7.3b and 7.5b. The worst case scenario is of the signal of Fig. 7.5 because of the lowest reproducibility of the artefact waveform.

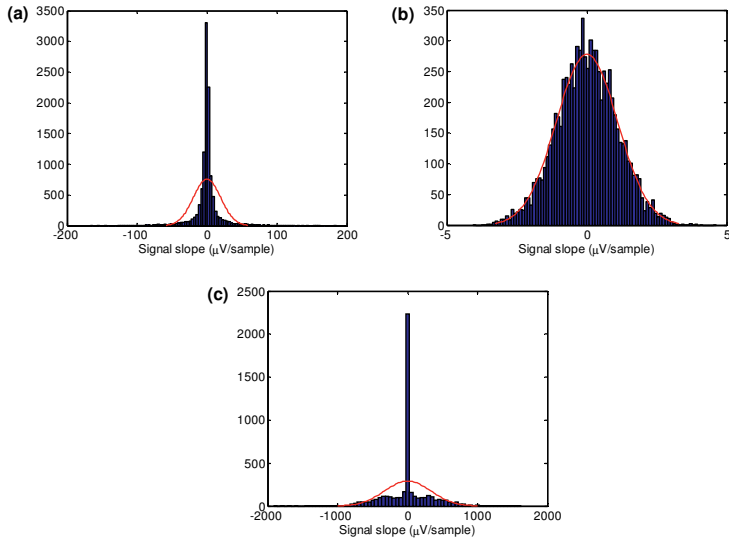


Figure 7.6: (a), (b), (c) Histogram of the signal slope for the signals of Figs. 7.3b, 7.4b, and 7.5b, and the respective fitted Gaussian distributions.

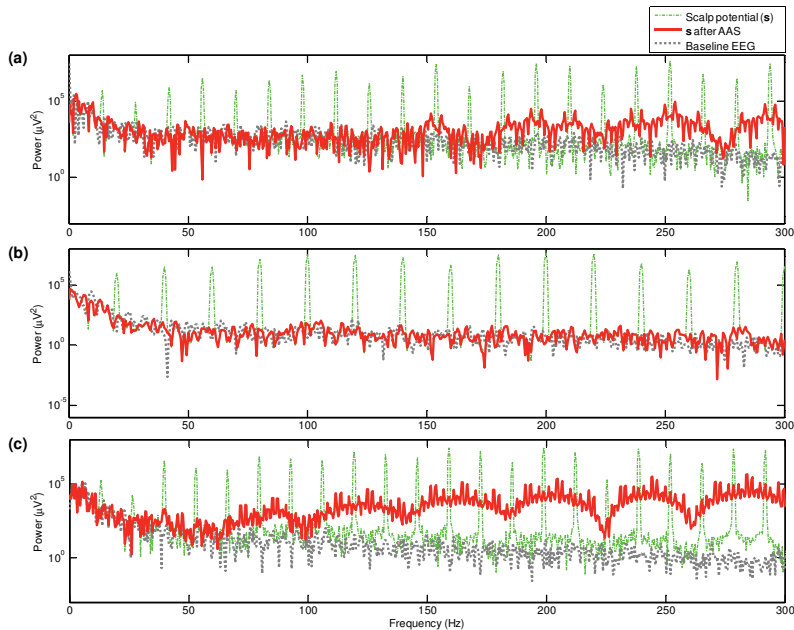


Figure 7.7: (a), (b), (c) Comparison of the power spectra of the signals of Figs. 7.3b, 7.4b, and 7.5b with the respective baseline (reference) EEG.

As usually performed in the literature, to attenuate the residual artefacts in the signals of Figs. 7.3b and 7.5b using low-pass (LP) filtering, the filter should be set up to suppress high-

frequency activity associated with the residual artefacts, and simultaneously preserve the neuronal EEG frequency activity of interest at most. In case of the occurrence of residual artefact activity in a lower bandwidth, lower filter cut-off frequencies should be used, but at the expense of suppression of EEG signal frequencies. This trade-off is illustrated in Figs. 7.8a and 7.8b which show the use of LP filtering to attenuate the residual artefacts in the signal of Fig. 7.3b. The filter was set as a 55-coefficient FIR, and the cut-off frequency is indicated in the figure.

When the cut-off frequency is equal to 250 Hz, the filter was not able to suppress the residual artefact that remains below the cut-off frequency. A LP filter with cut-off frequency of 100 Hz achieved suppression of the residuals, but in this case, high-frequency activity associated with the EEG signal has been removed as well. Figure 7.8c demonstrates how the signal slope adaption (SSD) approach depicted in Fig. 7.2 might be used to obtain a better balance for such a trade-off. This figure illustrates the SSD approach set for $\lambda = 0.9$ (Eq. (7.14)). SSD was applied in the signal of Fig. 7.3b before LP filtering, cut-off frequency 250 Hz. Clearly, high-frequency artefact activity has been better preserved in the signal of this figure, in comparison with the signal of Fig. 7.8b, but with more effective artefact attenuation than shown in Fig. 7.8a. Those characteristics are also observed in Figs. 7.9 and 7.10.

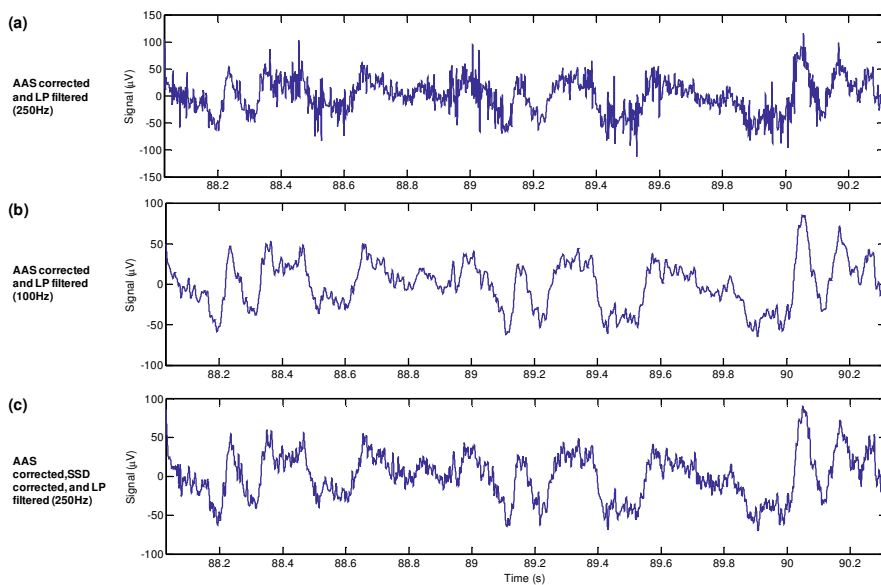


Figure 7.8: Top to bottom: scalp potential of Fig. 7.3a corrected by: (a) AAS with LP filtering, cut-off frequency 250 Hz; (b) AAS with LP filtering, cut-off frequency 100 Hz; (c) AAS with SSD and LP filtering, cut-off frequency 250 Hz.

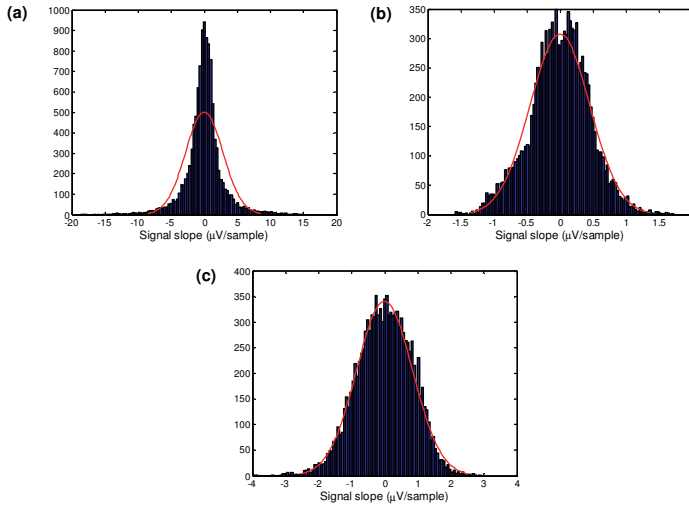


Figure 7.9: (a), (b), (c) Histogram of the signal slope for the signals of Figs. 7.8a, 7.8b, and 7.8c, and the respective fitted Gaussian distributions.

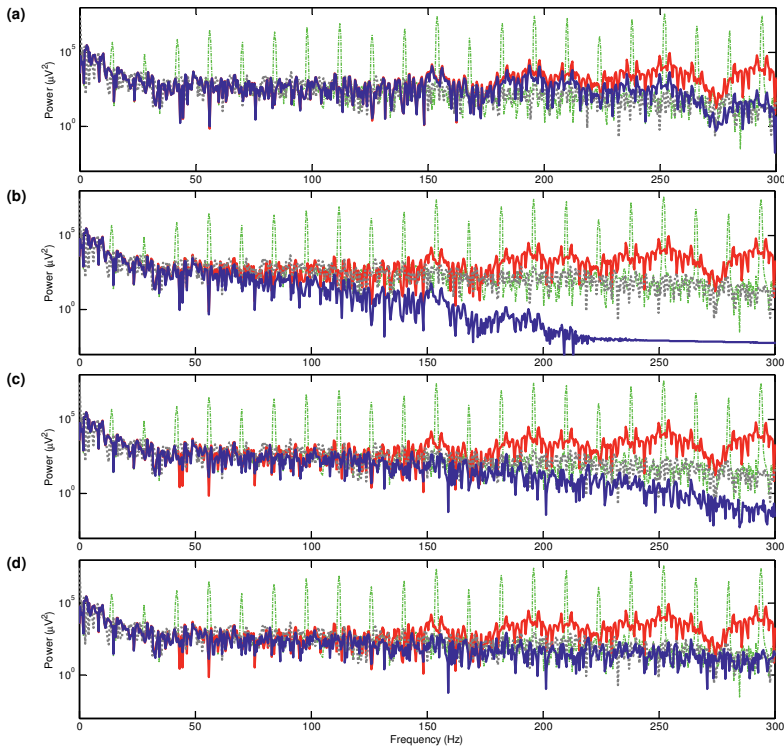


Figure 7.10: (a), (b), (c) Comparison of the power spectra of the signals of Figs. 7.8a, 7.8b, and 7.8c (thick blue traces) with the power spectra depicted in Fig. 7.7a; (d) comparison between the power spectrum of the signal of Fig. 7.3b after SSD (thick blue trace) with the power spectra depicted in Fig. 7.7a.

Application of the SSD approach before the filter has achieved the attenuation of the residual artefacts according to its slope characteristics. In this way, this approach selectively adapts and attenuates the samples associated with the residual artefacts which have higher values of signal slope. Thus, it is shown to preserve high-frequency activity of the EEG signal that have signal slope lower than $thrs$, allowing the use of higher cut-off frequencies for the LP filter. The use of SSD combined with the LP filter also makes the statistical distribution of the signal slope closely approximate to the Gaussian curve, as shown in Fig. 7.9c. This effect is roughly achieved by using LP filtering alone (Fig. 7.9c). In addition, by using SSD, the power spectrum of the signal after AAS is approximated to the baseline EEG as well (Fig. 7.10d). Those characteristics can also be observed when the LP filter and SSD are applied to the Fig. 7.5b, as depicted in Figs. 7.11, 7.12, and 7.13 ($\lambda = 0.9$). Whereas in the signal of Fig. 7.11b, the LP filtering alone with cut-off frequency 100 Hz was unable to effectively suppress the residuals artefacts. In the signal of Fig. 7.11c such residuals are shown to have been strongly attenuated. Therefore, it demonstrates that SSD may help to attenuate the residual artefacts after application of the AAS method and allow the enlargement of the usable bandwidth of the corrected EEG.

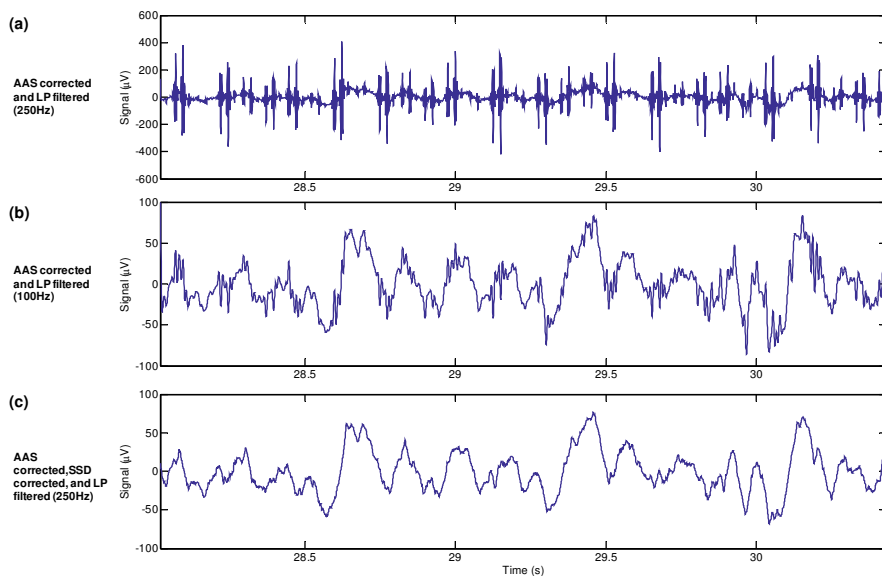


Figure 7.11: Top to bottom: scalp potential of Fig. 7.3c corrected by: (a) AAS with LP filtering, cut-off frequency 250 Hz; (b) AAS with LP filtering, cut-off frequency 100 Hz; (c) AAS with SSD and LP filtering, cut-off frequency 250 Hz.

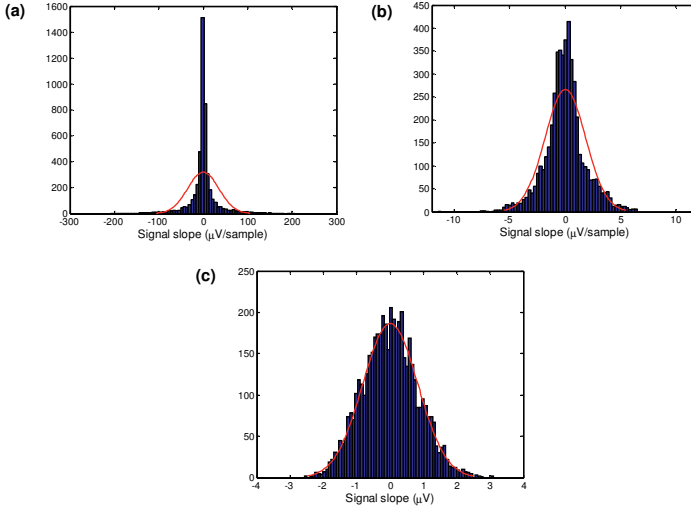


Figure 7.12: (a), (b), (c) Histogram of the signal slope for the signals of Figs. 7.11a, 7.11b, and 7.11c, and the respective fitted Gaussian distributions.

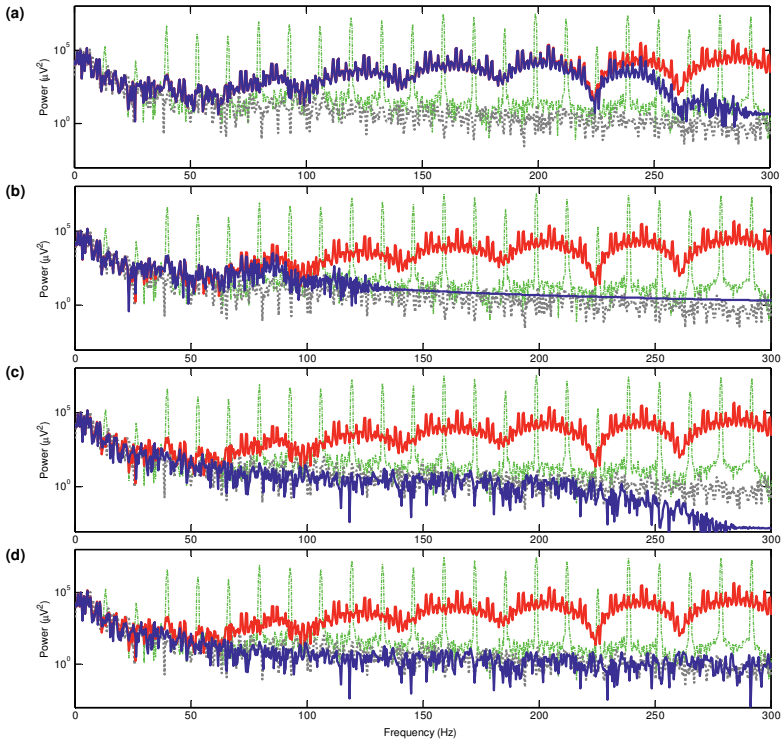


Figure 7.13: (a), (b), (c) Comparison of the power spectra of the signals of Figs. 7.11a, 7.11b, and 7.11c (thick blue traces) with the power spectra depicted in Fig. 7.7c; (d) comparison between the power spectrum of the signal of Fig. 7.5b after SSD (thick blue trace) with the power spectra depicted in Fig. 7.7c.

7.4.1 Evaluation of the EEG signal preservation after SSD

The assessment of EEG preservation is indicated in Figs. 7.14 and 7.15 and Tables 7.1 and 7.2. To perform this assessment, EEG excerpts of some electrode positions corresponding to the EEG data sets 1 and 3 were used, as indicated in Tables 7.1 and 7.2, with respective lengths around 2.3 and 2.4 s.

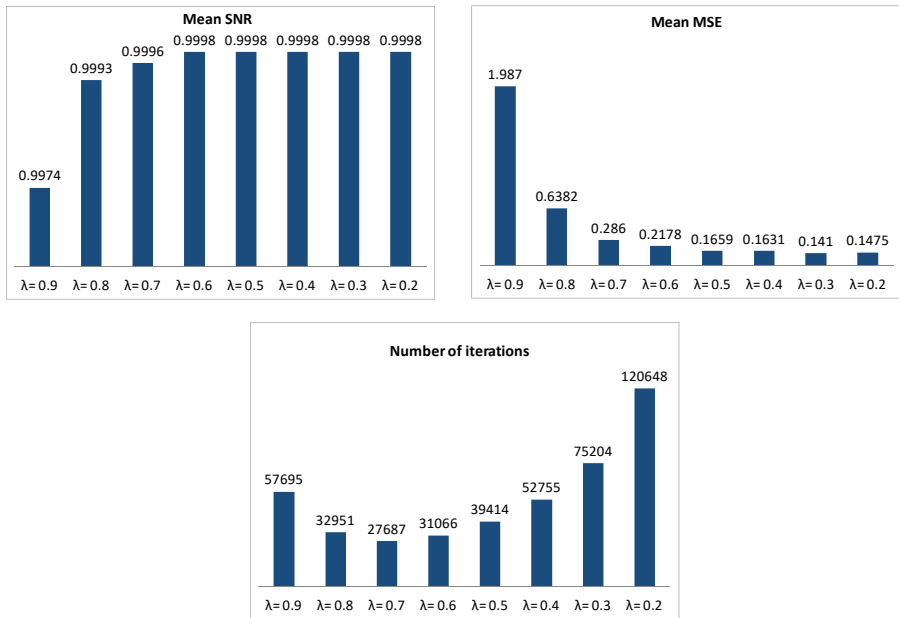


Figure 7.14: Median SNR, MSE, and number of iterations according to some values of λ (EEG data set 1).

Table 7.1: SNR and MSE for some EEG electrodes, taking into consideration the application of low-pass filtering in $e_{ref,n}$ and $\hat{e}_{ref,n}$ after SSD, and $\lambda = 0.5$ (EEG data set 1).

Measure	EEG Electrode	Filter cut-off frequency					
		No LP	250 Hz	150 Hz	120 Hz	100 Hz	70 Hz
SNR	Fp1	0.9980	0.9994	0.9999	0.9999	1.0000	1.0000
	F3	0.9888	0.9961	0.9993	0.9997	0.9998	0.9999
	Oz	0.9984	0.9997	0.9999	1.0000	1.0000	1.0000
	CPz	0.9904	0.9969	0.9992	0.9995	0.9996	0.9997
	Fz	0.9955	0.9988	0.9998	0.9999	0.9999	1.0000
	FC5	0.9956	0.9992	0.9999	0.9999	1.0000	1.0000
	AF3	0.9975	0.9992	0.9998	0.9999	0.9999	0.9999
MSE (μV^2)	Fp1	11.0545	3.5832	0.7017	0.3735	0.2577	0.1709
	F3	6.6989	2.2926	0.3640	0.1823	0.1211	0.0762
	Oz	1.6737	0.3093	0.0595	0.0399	0.0340	0.0307
	CPz	1.3486	0.4279	0.1010	0.0626	0.0484	0.0373
	Fz	0.7047	0.1830	0.0273	0.0137	0.0092	0.0059
	FC5	6.6988	1.2643	0.1609	0.0747	0.0469	0.0271
	AF3	3.8609	1.2757	0.2480	0.1437	0.1084	0.0830

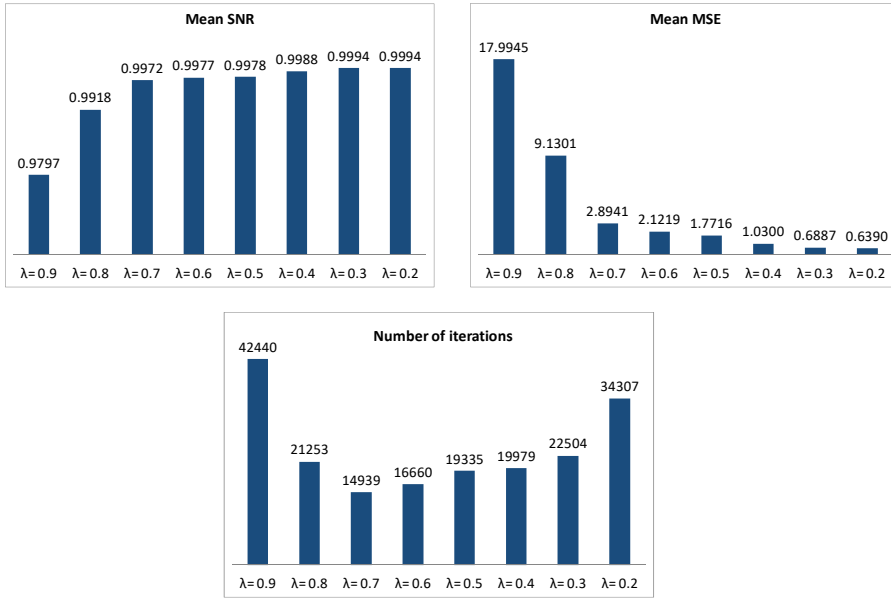


Figure 7.15: Median SNR, MSE, and number of iterations according to some values of λ (EEG data set 3).

Table 7.2: SNR and MSE for some EEG electrodes, taking into consideration the application of low-pass filtering in $e_{ref,n}$ and $\hat{e}_{ref,n}$ after SSD, and $\lambda = 0.5$ (EEG data set 3).

Measure	EEG Electrode	Filter cut-off frequency					
		No LP	250 Hz	150 Hz	120 Hz	100 Hz	70 Hz
SNR	Fp1	0.9915	0.9940	0.9963	0.9976	0.9985	0.9993
	F3	0.9849	0.9890	0.9925	0.9957	0.9976	0.9991
	T6	0.9977	0.9986	0.9991	0.9994	0.9996	0.9998
	Oz	0.9937	0.9959	0.9973	0.9982	0.9988	0.9995
	Cp2	0.9950	0.9978	0.9990	0.9994	0.9997	0.9999
	F6	0.9960	0.9971	0.9980	0.9986	0.9991	0.9996
	POz	0.9914	0.9947	0.9964	0.9976	0.9984	0.9994
MSE (μV^2)	Fp1	9.6593	6.7739	4.2229	2.6916	1.7754	0.7699
	F3	6.8529	4.9827	3.4416	1.9406	1.0986	0.4208
	T6	6.2173	3.8127	2.3200	1.5332	1.0967	0.5522
	Oz	5.8297	3.8185	2.4959	1.6798	1.1532	0.4959
	Cp2	1.7420	0.7609	0.3353	0.1951	0.1148	0.0350
	F6	7.5816	5.4745	3.7200	2.6265	1.7677	0.6680
	POz	3.3693	2.0671	1.4166	0.9554	0.6334	0.2568

As can be observed in Figs. 7.14 and 7.15, the SNR (Eq. (3.13)) and MSE (Eq. (3.14)) for the EEG data set 1 are, respectively, closer to unity and zero than those values estimated for the EEG data set 3. This appear to be associated with the higher sampling frequency of the EEG excerpts belonging to the EEG data set 1 as well as with the lower values of the signal slope parameter, d_n . In parallel, for the data sets 1 and 2 the lower the value of λ , the closer the

values of SNR and MSE are, respectively, to unity and zero as well (Figs. 7.14 and 7.15 and Tables 7.1 and 7.2). Therefore, this indicates that the EEG after application of SSD is shown to be better preserved for the EEG data set 1, especially by using lower values of λ . In addition, for both data sets, it can be noticed that the EEG signal is better preserved at lower-frequencies (lower LP filter cut-off frequencies), as indicated in Tables 7.1 and 7.2. The values of SNR and MSE in Figs. 7.14 and 7.15 and Tables 7.1 and 7.2 can also be used as an indication of how the reference EEG used during this evaluation and its estimate are converging or diverging from each other. In this way, SNR closer to unity and MSE closer to zero evidence higher convergence of the reference EEG and its estimate after application of SSD.

Regarding the number of iterations observed during the application of SSD, for either EEG data sets this number is lower when $\lambda = 0.7$, on one hand. On the other hand, the higher number of iterations occurs when λ is close to 1 or 0. Figure 7.16 illustrates the variation of the signal slope parameter d_n , according to the number of iterations of SSD ($\lambda = 0.3$). Even though the initial value of d_n in Fig. 7.16a (EEG data set 1) is lower than in Fig. 7.16b (EEG data set 3), a higher number of iterations is observed in Fig. 7.16a. This could be explained by the higher sampling frequency used for acquisition of the EEG data set 1 alike. Figure 7.16 also illustrates how d_n decreases at each iteration, which assures the convergence of Eq. (7.13).

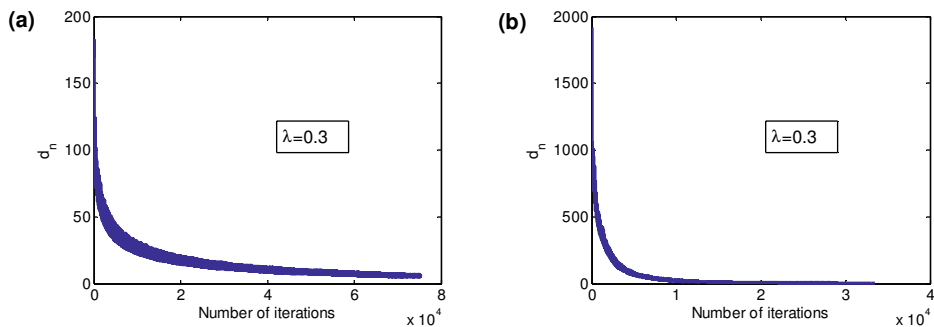


Figure 7.16: (a) Illustrative variation of the signal slope parameter d_n , according to the number of iterations, taking into account $\lambda = 0.3$ and the electrode position Fp1, EEG data set 1; (b) illustrative variation of the signal slope parameter, d_n , according to the number of iterations, taking into account $\lambda = 0.3$ and the electrode position Fp1, EEG data set 3.

7.5 Discussion

As mentioned in Chapters 3 and 4, the average template subtraction by AAS can be likened to a comb-filtering approach whose performance has high dependency on alterations that occur in the morphology of the gradient artefact waveform over time. In this way, the occurrence of residual artefacts after application of the AAS method is greatly dependent on the degree of reproducibility of the gradient artefact waveforms used for construction of the average artefact template. As can be observed in Figs. 7.4 and 7.7b, the more reproducible the artefact waveform, the less is the occurrence of the residual artefacts. In this case scenario, the histogram of the signal slope of the corrected signal is shown to be approximated to a Gaussian distribution (Fig. 7.6b), as with the histogram of signal slope of the reference (baseline) EEG (Fig. 7.1). This outcome agrees with the results of van de Velde et al. (1998) who used signal slope distributions to indicate the presence of muscle artefacts in the EEG signal. In parallel, in this scenario the power spectrum of the corrected EEG lies close to that of the reference EEG as well, as shown in Fig. 7.7b. On the other hand, a low reproducibility of the gradient artefact waveform may be encountered in EEG-fMRI experiments, which generally leads to a large amount of residual artefacts in the time course corrected EEG and in its spectrum above 80 Hz (Spencer, 2015), as can be observed in Figs. 7.3, 7.5, 7.7a, and 7.7c. This, thereby, makes the histogram of the signal slope of the corrected EEG not resemble a Gaussian distribution, as shown in Figs. 7.6a and 7.6c.

As remarked by Spencer (2015), it is generally difficult to access neuronal EEG frequencies above 80 Hz in the corrected EEG by AAS, because of the occurrence of the residual artefacts. To attenuate such residuals, the use of conventional FIR low-pass (LP) filtering with cut-off around 80 Hz is the usual practice suggested in the literature (Allen et al., 2000, Niazy et al, 2005; Spencer, 2015). However, this is carried out at the expense of the removal of spectral power above the filter cut-off, as depicted in Figs 7.10 and 7.13. Even though for the corrected EEG signal of Fig. 7.8b, the use of a filter cut-off around 100 Hz has been shown to substantially attenuate the residual artefacts, this is not the case for the corrected EEG signal of Fig. 7.11b. This is due to some residual artefacts that remain around and below the filter cut-off, thus distorting the corrected EEG. Hence, the filter cut-off should be reduced in order to improve the artefact attenuation.

The occurrence of residual artefacts after AAS can be related to the contributions of the inherent uncertainty associated with the averaging of artefact epochs, as indicated in Eq. (7.8).

Thus, the average artefact template uncertainty is influenced by the timing error Δt between the EEG sampling frequency and the clock of MRI acquisition and the number k of epochs used to calculate the average artefact. The influence of Δt and k over the performance of AAS has been addressed in a number of publications that demonstrated the importance of taking into account these parameters in order to reduce the occurrence of residual artefacts (Becker et al., 2005; Mandelkow et al., 2006; Freyer et al., 2009; Allen et al., 2000; Gonçalves et al., 2007; Huang et al., 2012; de Munck et al., 2013).

In addition, the uncertainty associated with the averaging epochs is also a function of the first and higher derivatives associated with the gradient artefact (Eq. (7.8)). Because of the steep signal slopes of the gradient artefact in the order of $10^4 \mu\text{V}/\text{ms}$, an imprecise sampling of $s_i(t)$ may result in strong variability of the artefact waveform across averaging epochs (Mullinger et al., 2008b; Eichele et al., 2010), as depicted in Figs. 7.3 and 7.5. Thus, by devising the SSD approach, described in Eqs. (7.12) – (7.14) and depicted in the flowchart-scheme of Fig. 7.2, we propose to exploit the contribution to the artefact template uncertainty associated with the higher derivatives of the gradient artefact and related residuals after AAS. Accordingly, SSD has been implemented based upon the first derivative characterised as the difference between consecutive samples of the digital signal, and modelled as the non-linear filter indicated in Eq. (7.10), whereby the estimation of the true EEG could be approximated to its true value by *manipulation* or *adaptation* of the signal slope defined as the parameter d_n (Eq. (7.12)) (Ferreira et al., 2012; Ferreira et al., 2013a).

The use of SSD after AAS application and its combination with LP filtering is shown to be capable of substantially attenuating the residual artefacts together with better preservation of high-frequency activity in the corrected EEG in comparison with LP filtering alone after AAS (Figs. 7.8, 7.10, 7.11, and 7.13). This fact could be explained by SSD to selectively adapt the samples associated with the artefact residuals which have higher signal slopes than the threshold, $thrs$, set for the reference EEG (Eq. (7.9)). According to SSD implementation, higher signal slopes have been assumed to be related to the artefact activity which, therefore, is demonstrated to be selectively attenuated in samples whose value of d_n is higher than $thrs$. As a result, high-frequency activity in the corrected EEG signal is well preserved in samples whose signal slope was lower than $thrs$. Thus, it permits the use of higher LP cut-off frequencies for the LP filter, and preservation of higher frequency activity in the corrected EEG in consequence (Figs. 7.14 and 7.15 and Tables 7.1 and 7.2).

Therefore, these results indicate that the SSD approach might contribute to obtain a better balance for the trade-off between artefact attenuation and EEG signal preservation, especially at high-frequencies. The use of SSD together with LP filtering is also shown to make the signal slope distribution of the corrected EEG closely resemble the Gaussian curve, as observed for the reference EEG (Figs. 7.1, 7.9, and 7.12). As such, these characteristics demonstrate the feasibility of using the signal slope parameter to investigate the attenuation of residual artefacts in the gradient artefact-corrected EEG, in accordance with the model for the uncertainty component associated with the artefact template described in Eq. (7.8).

An important remark regarding the power spectrum of the neuronal (baseline) EEG is that it typically decays proportionally to the inverse of the frequency ($1/f$), as observed in Figs. 7.7, 7.10, and 7.13 (Gutberlet, 2010). As can be noticed in Figs. 7.10a and 7.13a, the occurrence of residual artefacts over the baseline EEG power spectrum distorts the power spectrum of the corrected EEG after AAS, so that it may not show $1/f$ decay. As mentioned in Chapter 6, this fact can be ascribed to the residual artefacts which are associated with broadening of the artefact spectral lines caused by micro-movements of the subject head. The use of the SSD approach is shown to be capable of making the power spectrum of the corrected EEG approximate the baseline EEG power spectrum (Figs. 7.10d and 7.13d), thus enabling the identification of the usable bandwidth in the corrected EEG related to the neuronal EEG. This fact also evidences the correctness and importance of using a kind of filter like the optimised exponential average (OEA) to attenuate eventual residual artefact energy that remains over the baseline EEG, and are associated with the broadening of spectral lines caused by tiny head movements of the subject (Eq. (6.2)). As shown in Chapter 6, this effect may not be accounted for by the comb-filtering provided by AAS or OMA alone which rely on the assumption of stationary nature of the gradient artefact waveform.

Last, we did verify that the SSD approach indicated in Eqs. (7.12) – (7.14) could be extended to other signal processing applications, such as the detection of steep wave activity in other biological signals. In Ferreira et al. (2013d), we show a case study where SSD is employed for ECG peak identification. In this fashion, the idea behind this QRS detector was to employ SSD for selectively identification of the larger signal slopes associated with the samples of the QRS complexes. As an additional suggestion for future work, SSD might be applied and evaluated for detection and attenuation of other types of artefact in biological signals, such as the muscle artefact in the EEG (van de Velde et al., 1998).

7.5.1 Limitations and future work

A limitation observed during the use of the SSD approach is that Eqs. (7.12) – (7.14) represent a statistical detection and estimation approach, in such a way that the uncertainty associated with the average value estimated by Eq. (7.14) may lead to deviations in the estimation of the values of the adapted EEG, $\hat{\mathbf{e}}_{\text{adapt}}$, especially when large values of residual artefacts occurs in $\hat{\mathbf{e}}$. In this scenario, large deviations in $\hat{\mathbf{e}}_{\text{adapt}}$ were observed mainly when larger values of d_n occurred as well as lower EEG sampling frequencies were used (Fig. 7.16). In some preliminary studies we have undertaken (Ferreira et al., 2013b; Ferreira et al., 2013c; Ferreira et al., 2014b), investigation has been performed regarding the use of SSD to reduce the effect of broadening of artefact spectral lines before performing the attenuation of the harmonic components of the gradient artefact. However, these outcomes should be deeper addressed and assessed in future work.

Although the assumption of the presence of artefactual activity in EEG samples with larger values of d_n has been attested by van de Velde et al. (1998) and Cluitmans et al. (1993), and is clearly confirmed by Figs. 7.6, 7.9, and 7.12, some artefactual activity might be associated with EEG samples with smaller values of d_n as well. In this scenario, therefore, the SSD approach would not be able to attenuate the artefact activity associated with these samples. Thereby, the presence of artefactual activity in samples with d_n smaller than the threshold (*thrs*), as well as to what extent it impacts on the SSD performance should be better assessed in future work as well.

Another limitation of SSD is concerned with its number of iterations and processing time. Large values of d_n and large sampling frequencies can imply in a large number of iterations which may lead SSD to take a few minutes to process. In addition, the methodology proposed in this chapter has been evaluated for short length EEG excerpts with around 11000 samples at the most. For longer EEG excerpts, therefore, the processing time of our methodology could further be increased. Thus, some kind of optimisation procedure should also be implemented in future work in order to reduce the number of iterations and processing time of the SSD approach.

7.6 Conclusions

In this chapter, we have exploited the influence of the signal derivative as a contribution to the uncertainty associated with the average artefact template, and investigated how it could be used to describe the residual artefacts that arise in the gradient artefact-corrected EEG. To this end, we have designed the SSD approach which makes use of the signal slope as a non-linear filter parameter to detect and attenuate the residual artefact activity. According to our results, the SSD approach is shown to selectively attenuate the artefactual activity in samples containing residual artefacts after template subtraction by AAS. In parallel, the proposed approach is demonstrated to attenuate spectral energy associated with residual artefacts that lay above the baseline EEG power spectrum, so that it has permitted the use of higher LP filter cut-off frequencies. As SSD is also shown to be capable of approximating the power spectrum of the corrected EEG to the power spectrum of the baseline EEG, which decays proportionally to the inverse of the frequency, this evidences the importance of using the OEA filter presented in Chapter 6 for attenuation of residual artefacts owing to broadening of artefact spectral lines caused by subject head motions. Last, the results shown in this chapter confirm the feasibility of using the slope parameter characterised as the difference between consecutive samples of the digital signal to describe and detect artefacts and steep wave activity in biological signals.

CHAPTER 8

Gradient Artefact Suppression under the Occurrence of Abrupt Subject Head Movements*

8.1 Abstract

In this chapter, we present some considerations that might be useful to improve the EEG gradient artefact correction under the occurrence of abrupt movements of the subject head in the MRI scanner. In this scenario, the morphology of the gradient artefact can be profoundly altered over time, so that it may make it difficult to obtain a good EEG quality by using gradient artefact correction methods that rely on the stationary nature of the artefact waveform. Initially, we present a study in which we have investigated the use of cubic splines to model transients continuously inserted in the recorded scalp potential by abrupt head movements. By utilising cubic splines to model those transients and their subsequent subtraction from the recorded scalp potential, a more homogeneous artefact waveform can be obtained in the modified scalp potential and the gradient artefact correction is improved, as a consequence. Secondly, we suggest some filtering strategies that might help to improve the quality of the artefact-corrected EEG under the occurrence of abrupt head movements. Such procedures are shown to be useful for reducing the occurrence of residual artefacts after application of the gradient artefact correction, and thereby might be employed to obtain a better quality for the EEG signal in clinically realistic situations.

* This chapter was partly based on the papers:

Ferreira, J.L., Cluitmans, P.J.M., and Aarts, R.M. (2014b). Removal of gradient artefacts during transient head movements for continuous EEG-fMRI. Proc. BIOSIGNALS 2014b Conf.: 213-220.

Ferreira, J.L., Wu, Y., Besseling, R.M.H., Lamerichs, R., and Aarts, R.M (2016). Gradient artefact correction and evaluation of the EEG recorded simultaneously with fMRI data using optimised moving-average. J. Med. Eng. 2016: article ID 9614323, 1-17.

8.2 Introduction

Albeit combination of EEG-fMRI constitutes a promising tool for mapping of the brain activity as well as for cognitive studies and research, the occurrence of artefacts in the EEG signal still represents a challenge to be overcome in order to consolidate and broaden the range of applications of this technique. This is the case for the gradient or imaging acquisition artefact which is induced in the electroencephalogram by the rapidly varying magnetic field gradients and RF pulses of the MRI equipment (Ritter et al., 2010). The gradient artefact has amplitudes that can be much larger than those of the neuronal EEG. It possesses a characteristic waveform which is approximately the differential waveform of the magnetic fields that originate the artefact (Allen et al., 2000; Anami et al., 2003; Ritter et al., 2010; de Munck et al., 2013).

As described in Chapter 3, several correction methods have been proposed in the literature to attenuate the gradient artefact, such as the often-used average artefact subtraction (AAS) methodology proposed by Allen et al. (2000). However, improvements and the proposal of novel correction methodologies have been required, mainly to improve the access of higher-frequencies of the neuronal EEG in the gamma band and above (Spencer, 2015), as highlighted in the previous chapters. Another scenario that requires the enhancement of the gradient artefact correction is when large motions of the subject head occur within the MRI scanner. As remarked by Yan et al. (2009), the movement artefact induced in the recorded scalp potential by large head motions may compromise the effectiveness of the gradient artefact correction methods that rely on the stationary nature of the gradient artefact waveform due to the alterations and transients that affects the artefact morphology over time. In this scenario, the averaging template process by AAS may result in an inaccurate estimation of the artefact template, so that a large amount of residual artefacts owing to the movement influence may be left behind in the corrected EEG. In some cases of occurrence of large motions of the subject head, the corrected EEG signal may be corrupted beyond recovery (Spencer, 2015; Sun and Hinrichs, 2009; Mullinger et al., 2011; Eichele et al., 2010).

The use of a sliding average window has been proposed as an AAS variant in attempt to mitigate this problem, decreasing the probability of movement within a particular window (Allen et al., 2000; Becker et al., 2005; Freyer et al., 2009). Nevertheless, in addition to increasing the risk of subtraction of a clinical event of interest from the EEG signal, the windows which coincide with the movement continue locally altered by using this approach

(Yan et al., 2009). To circumvent this problem, Moosmann et al. (2009) propose a correction procedure that uses information related to head movement parameters obtained from an fMRI realignment algorithm to improve the accuracy of the artefact template. Likewise, Sun and Hinrichs (2009) described a method whereby the epochs used for template averaging are selected by weighting factors that account for the influence of the head position and movement on the artefact shape.

However, the performance of those approaches is compromised when multiple movements occur close together, in such a way that an insufficient number of averaging waveforms can be used to create the average artefact template. In addition, under the occurrence of signal transients slowly and continuously caused by abrupt head movements, application of those approaches might not result in a good quality for the artefact-corrected EEG either (Spencer, 2015). Thus, improvement of the existing correction methods as well as the proposal of novel correction approaches that take the occurrence of abrupt head motions into account is highly required, especially in studies in which those movements cannot be prevented, such as those involving children, epileptic patients, and during sleep (Moosmann et al., 2009; Spencer, 2015).

Instead of using an artefact average template, we have proposed in this thesis the usage of a novel methodology to correct the gradient artefact by using the optimised moving-average method described in Chapters 4, 5, and 6. As mentioned in Chapter 5, the OMA filtering is performed sample-by-sample rather than estimation of an average artefact template that is carried out using averaging epochs. In parallel, OMA could be used to further limit the region of influence of signal transients continuously inserted by abrupt head movements when compared with the use of a sliding average window, as reported in Chapter 6. In the current chapter, we present some considerations about those characteristics of the OMA approach, and demonstrate how some related filtering strategies might be useful to enhance the quality of the corrected EEG signal under the occurrence of abrupt head movements, as discussed in Section 8.4. In parallel, we propose a novel procedure to improve the correction of the gradient artefact affected by the occurrence of signal transients continuously inserted by abrupt head movements. To this end, we have made use of cubic splines curves to model such signal transients. Those cubic splines have been then used to modify and approximate the shape of the scalp potential to homogeneous data. According to our results, this approach can be used to reduce the signal transients influence over the gradient artefact correction, thus improving the quality of the restored EEG signal, as reported in the following section.

8.3 A study of gradient artefact correction under the occurrence of signal transients continuously inserted by abrupt head movements

8.3.1 EEG and fMRI data

The scalp potential recordings were collected simultaneously with the fMRI data for a research focused on epilepsy and post-traumatic stress disorder (PTSD) (van Liempt et al., 2011). The data were recorded using a 3 T Achieva Scanner (Philips, Best, The Netherlands) from one subject. fMRI was continuously performed using a functional echo-planar imaging sequence with 33 transversal slices (thickness 3 mm, TE 30 ms, TR 2500 ms). An MRI-compatible 64 channel polysomnograph (MRI 64, MicroMed, Treviso, Italy) was used to collect one ECG channel, two EOG channels, one EMG channel, and 60 EEG channels. A cap containing 64 Ag-AgCl electrodes was positioned in accordance with the standard 10-20 system. The sampling rate of the EEG system was 2048 Hz. The MRI clock and the EEG sampling interval have been synchronised for the volume repetition time (TR), so that $TR = 5120$ samples. The dynamic stabilisation in the MRI equipment has not been switched off, in such a way that TR was not adjusted as a multiple of the slice-time (TR-slice) and, thereby, TR-slice did not match a multiple of the sampling interval. The recordings were conducted in accordance with the Declaration of Helsinki, and made with the approval of the local ethics committee and informed consent by the subject.

8.3.2 Approach implementation

As mentioned in Section 2.4.3, the occurrence of large changes in the head position may result in a component or variant of the movement artefact that can be characterised as signal transients that are continuously and slowly added in the recorded scalp potential, s_n :

$$s_n = e_n + g_n + m_{u,n}, \quad (8.1)$$

where e_n and g_n are the actual EEG and the gradient artefact, respectively; and $m_{u,n}$ represents the signal transients inserted by the abrupt head movements. Larger changes of the head position over a certain amplitude may even result in faster signal transients, so that $m_{u,n}$ can be likened to the linear superposition of an impulse signal, $\delta_{u,n}$, in the recorded scalp potential:

$$s_n = e_n + g_n + \delta_{tr,n}. \quad (8.2)$$

Those signal transients may compromise the performance of gradient artefact methods that rely on the stationary nature of the artefact waveform, as mentioned earlier. To enhance the gradient artefact correction in excerpts of s_n containing the component $m_{tr,n}$ and/or $\delta_{tr,n}$, we proposed the algorithm indicated in the scheme of Fig. 8.1:

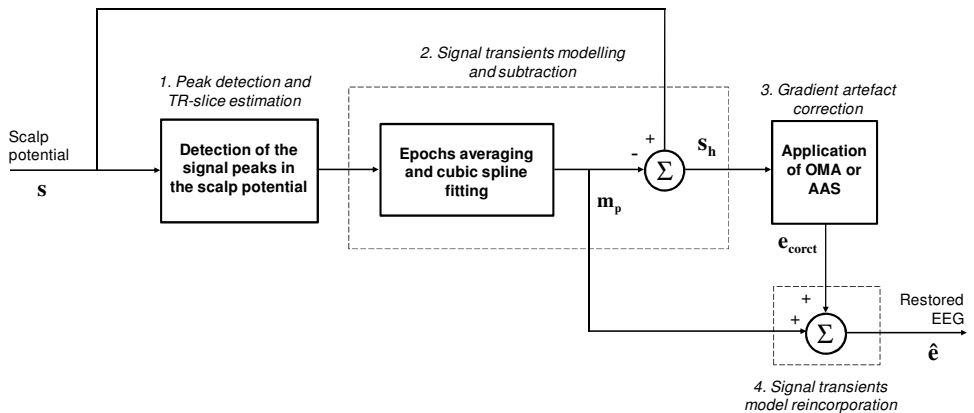


Figure 8.1: Scheme of the proposed methodology for gradient artefact correction under the occurrence of signal transients continuously caused by abrupt head movements.

Each step of the methodology indicated in the scheme above was implemented and applied in the EEG data in MATLAB (The MathWorks Inc., Natick, USA) environment.

8.3.3.1 Peak detection and TR-slice estimation

Implementation of the algorithm illustrated in Fig. 8.1 required the initial detection of the typical gradient artefact peaks that are observed in the recorded scalp potential. Such detection was necessary for implementation of the signal transients modelling (step 2 of Fig. 8.1). Localisation of those peaks was also important for estimation of the slice-time (TR-slice). Because the EEG excerpts under analysis were contaminated with transients, making it difficult the correct localisation of the peaks, we have used the ECG signal recorded simultaneously with the EEG channels to perform the peak detection. For the data under analysis, the value of TR-slice was estimated at 155 ± 1 samples (first 32 slices) and $178 + 1$ samples (last slice). The length of the scalp potential excerpt to be processed was set as 60×5120 samples, corresponding to 60 times the volume repetition time TR.

8.3.3.2 Signal transients modelling and subtraction

To model the signal transients, the scalp potential excerpt was divided into epochs of length equal to the time between the gradient artefacts peaks corresponding to the onset of each TR-slice observed in the scalp potential excerpt. Next, we have taken into account to average all samples of each epoch separately. Making the assumption that the gradient artefact waveform over TR-slice was stationary (i.e. it has been considered a slowly varying process from epoch to epoch) and had zero mean, that average only would run over values associated with the actual EEG signal and the signal transients. Hence, the resulting average points associated with each epoch would correspond to the mean variation of the signal transients and low-frequency components related to the actual EEG signal, from epoch to epoch. Figure 8.2a illustrates the implementation of such a procedure. The exemplary scalp potential excerpt shown in this figure was picked up from the electrode position F8.

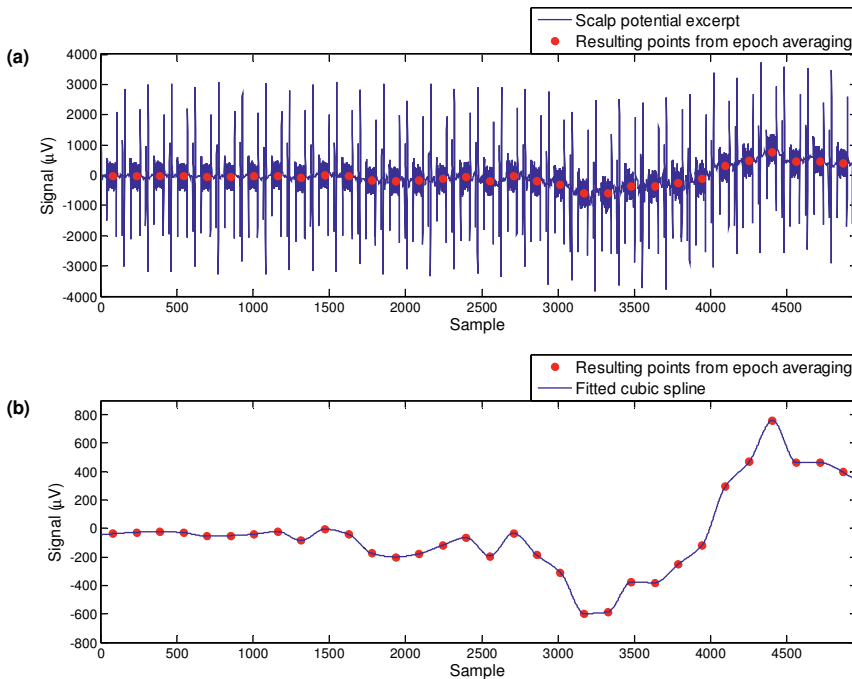


Figure 8.2: (a) Illustrative Scalp potential excerpt (blue trace) and resulting values from epoch averaging (red points); (b) resulting values from epoch averaging (red points) fitted by a cubic spline curve (blue trace).

The average values were plotted in the middle of each epoch (red points). Such points were plotted in Fig. 8.2b as well, together with a cubic spline curve which was used to fit those

points in a time continuous sense. Cubic splines have shown to be very useful to fit a smooth continuous curve to discrete data as well as especially attractive because they make use of piecewise polynomials with low-order to interpolate the data (Wolberg and Alf, 1999). Moreover, the data can be modelled by respecting constraints of smoothness and monotonicity. Thereby, the use of cubic spline fitting has been often proposed in a number of signal processing algorithms reported in the literature. For instance, empirical mode decomposition (Huang et al., 1998) makes use of cubic spline curves to estimate the upper and lower envelope before estimating the intrinsic mode functions. Koskinen and Vartiainen (2009) have also devised a cubic spline-based approach to improve the artefact template estimation during application of the AAS method.

According to the procedure shown in Fig. 8.2, because the cubic spline curve was fitted to the mean point of each epoch average, it also corresponds to the mean variation of the signal transients and low-frequency components associated with the actual EEG signal from epoch to epoch. Thus, the frequency activity associated with the gradient artefact and the neuronal EEG high-frequency components are contained in the signal resulting from the subtraction of the spline from the scalp potential. Such characteristics can be observed in the power spectra depicted in Fig. 8.3.

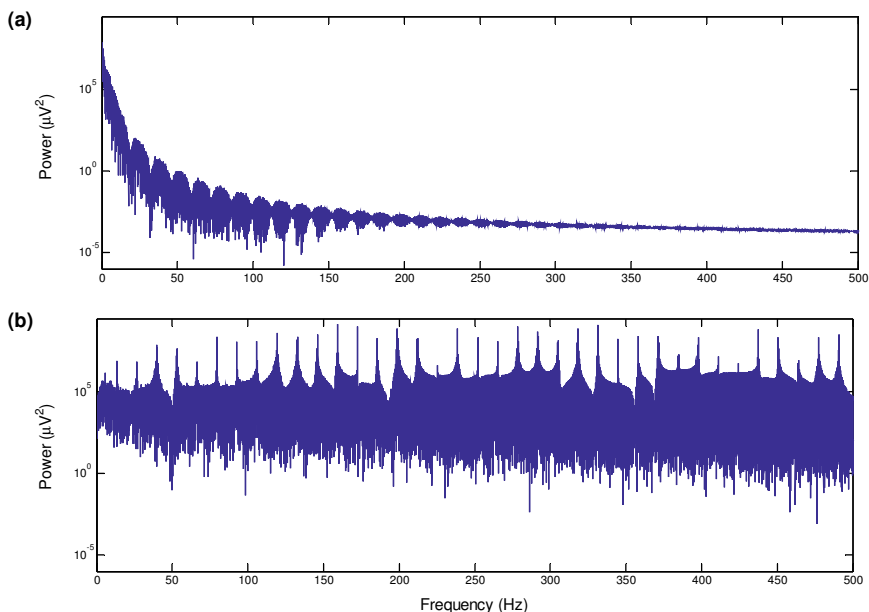


Figure 8.3: (a) Power spectrum of the fitted spline curve; (b) power spectrum of the signal resulting from the subtraction of the spline curve from the scalp potential. The gradient artefact frequencies are contained in (b).

Thereby, although transients continuously inserted in the scalp potential caused by abrupt head movements may possess high-frequency components, they can be characterised as low-frequency activity in comparison with the gradient artefact frequency components. Hence, the models of Eqs. (8.1) and (8.2) were changed to Eq. (8.3):

$$\mathbf{s} = \mathbf{m}_p + \mathbf{s}_h, \quad (8.3)$$

where \mathbf{m}_p is the fitted spline which corresponds to the sum of the signal transients \mathbf{m}_{tr} (or δ_{tr}) and the low-frequency components of \mathbf{e} ; and \mathbf{s}_h corresponds to the sum of the gradient artefact \mathbf{g} and the high-frequency components of \mathbf{e} . Therefore, according to Fig. 8.3 and Eq. (8.3), the gradient artefact correction should be applied solely in the signal \mathbf{s}_h which is the component of the recorded scalp potential that, in fact, contains the artefact activity. Thus, there is no need to apply the gradient artefact correction in the component \mathbf{m}_p , so that the inaccuracies introduced by the signal transients caused by the subject head movements during the application of the gradient artefact approach could be minimised.

To fit the cubic spline curve shown in Fig. 8.2, we have used the piecewise cubic Hermite interpolation method (Kreyszig, 2011; Fritsch and Carlson, 1980). According to the Hermite interpolation setup, given two points (x_i, y_i) and (x_{i+1}, y_{i+1}) , they are linked by the cubic interpolating polynomial $H_i(x)$ with the following constraints:

$$\begin{aligned} H_i(x_i) &= y_i, \\ H_i(x_{i+1}) &= y_{i+1}, \\ H'_i(x_i) &= y'_i, \\ H'_i(x_{i+1}) &= y'_{i+1}. \end{aligned}$$

$H_i(x)$ is described as $(x_i \leq x \leq x_{i+1})$:

$$\begin{aligned} H_i(x) &= a_i + b_i(x - x_i) + c_i(x - x_i)^2 \\ &+ d_i(x - x_i)^2(x - x_{i+1}), \end{aligned} \quad (8.4)$$

where the coefficients a_i , b_i , c_i , and d_i are calculated by taking into account the values of x_i , x_{i+1} , y_i , y_{i+1} , and certain slopes y'_i and y'_{i+1} at the two segment endpoints. These slopes are chosen in such a way that the shape and monotonicity within the data are respected. Finally, the piecewise interpolant is found by joining the I local cubic interpolants:

$$H(x) = \sum_{i=1}^I H_i(x). \quad (8.5)$$

In MATLAB, we have implemented the cubic Hermite interpolation method using the routine ‘pchip’.

8.3.3.3 Gradient artefact correction

As gradient artefact correction methodologies, we used the OMA approach ($M = 5120$, $p = 6$, $J = 60000$, and $L = 1$ for TR; $M = 155 \pm 1$, $J = 20000$, and $L = 1$ for TR-slice) described in Section 6.3.3, as well as our home-built AAS implementation described in Section 7.3.2, in order to perform a comparative evaluation of the obtained results. The AAS methodology was set using $N = 60$ and $M = 5120$, combined with LP filter cut-off 70 Hz. Both gradient artefact correction methodologies were applied in the component \mathbf{s}_h of Eq. (8.3), resulting in the artefact-corrected EEG, $\mathbf{e}_{\text{corect}}$.

8.3.3.4 Signal transients model reincorporation

Because the fitted spline model contains low-frequency components associated with the neuronal EEG signal, the signal \mathbf{m}_p could not be left out of the estimation of the restored EEG, $\hat{\mathbf{e}}$, but it has been reincorporated, as follows:

$$\hat{\mathbf{e}} = \mathbf{e}_{\text{corect}} + \mathbf{m}_p. \quad (8.6)$$

Therefore, the methodology is specifically proposed to improve the gradient artefact correction in the scalp potential, \mathbf{s} . Thus, the baseline associated with the signal transients still remains in the restored EEG, $\hat{\mathbf{e}}$.

8.3.3 Results

Figure 8.4 illustrates the application of the step 2 of the proposed methodology in the scalp potential excerpt of Fig. 8.2. In this excerpt (reproduced in Fig. 8.4a), the beginning of the signal transient occurred around 188.5 s. Figure 8.4b shows the signal component \mathbf{s}_h indicated in Eq. (8.3), resulting from the subtraction of the fitted spline from the scalp potential excerpt. It can be noticed that \mathbf{s}_h possesses a more homogeneous shape (i.e. data without large transients caused by abrupt head movements) in comparison with the signal of

Fig. 8.4a. Thus, this procedure can facilitate the reduction of the influence of the signal transients over the gradient artefact correction, as shown in the next example.

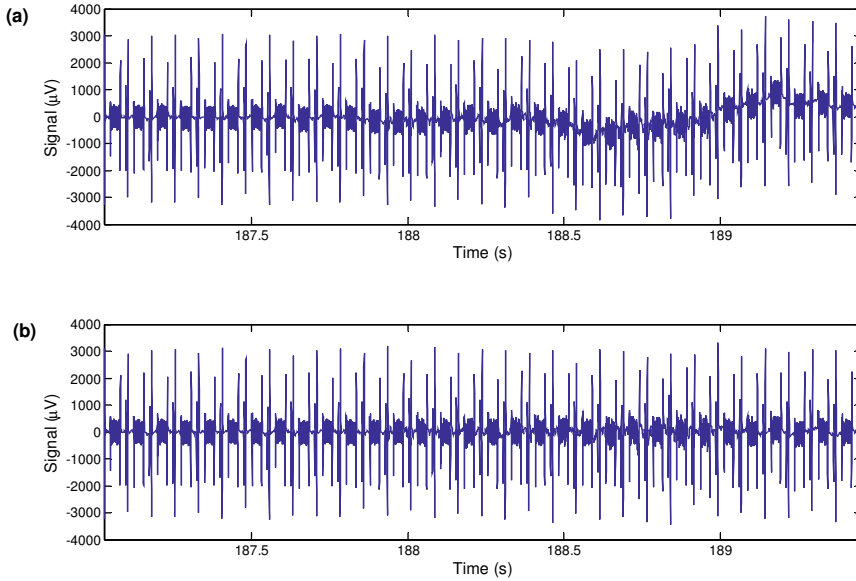


Figure 8.4: (a) Scalp potential excerpt of Fig. 8.2a; (b) signal component s_h (Eq. (8.3)), resulting from the subtraction of the fitted spline curve depicted in Fig. 8.2b from the scalp potential excerpt of (a). The signal s_h possesses an approximated homogeneous data shape in comparison with the scalp potential excerpt.

In Fig. 8.5a, a larger scalp potential excerpt 60×5120 samples (about 150 s) containing the excerpt of Fig. 8.4a is shown. A stronger signal transient due to some abrupt head movement of the subject head is also noticed about the time 165 s. The corresponding fitted spline, m_p , is shown in Fig. 8.5b. In turn, Fig. 8.5c shows the signal s_h resulting from the subtraction between the signals of Figs 8.5a and 8.5b. Like observed in Fig. 8.4b, the signal of Fig. 8.5c has a more homogeneous shape in comparison with the original scalp potential excerpt depicted in the signal of Fig. 8.5a.

Figure 8.6 depicts the restored EEG, \hat{e} , resulting from the application of the proposed methodology in the signal s_h of 8.5c. For comparison purposes, OMA and AAS were directly applied in the scalp potential excerpt of Fig. 8.5a as well. As observed in Figs. 8.6a and 8.6c, without using the proposed methodology, the quality of the corrected EEG is afflicted by the

movement influence, which can be noticed at time intervals regularly spaced around TR (= 2.5 s).

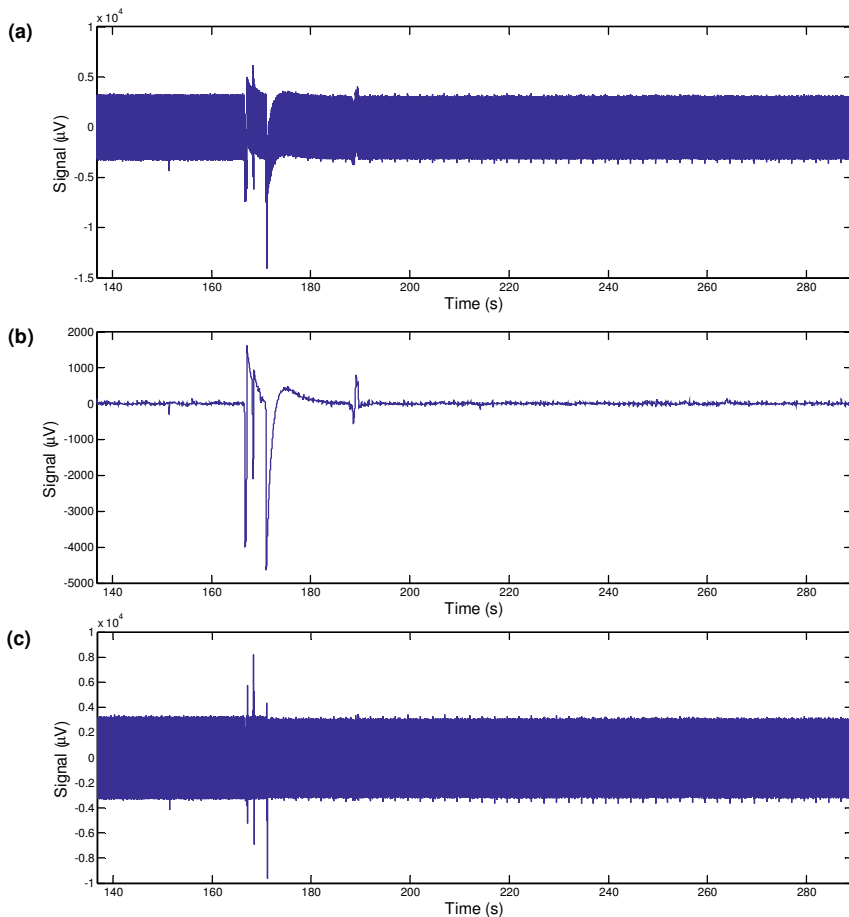


Figure 8.5: (a) Scalp potential excerpt containing transients due to abrupt head movements starting at around 165 s (electrode position F8); (b) fitted spline curve, \mathbf{m}_p ; (c) signal component \mathbf{S}_h resulting from subtraction between (a) and (b).

Whereas AAS is shown to produce smaller ripple (Fig. 8.6c) associated with the movement influence around the site of movement occurrence than OMA, the region of movement influence over the correction produced by OMA is narrower (Fig. 8.6a) than that observed for the AAS correction. In the latter case, the region of movement influence is shown to be spread out along all averaging epochs used to estimate the artefact template. A similar behaviour has been observed for the scalp potential excerpt of Fig. 6.8d (see Section 6.5 and 6.6).

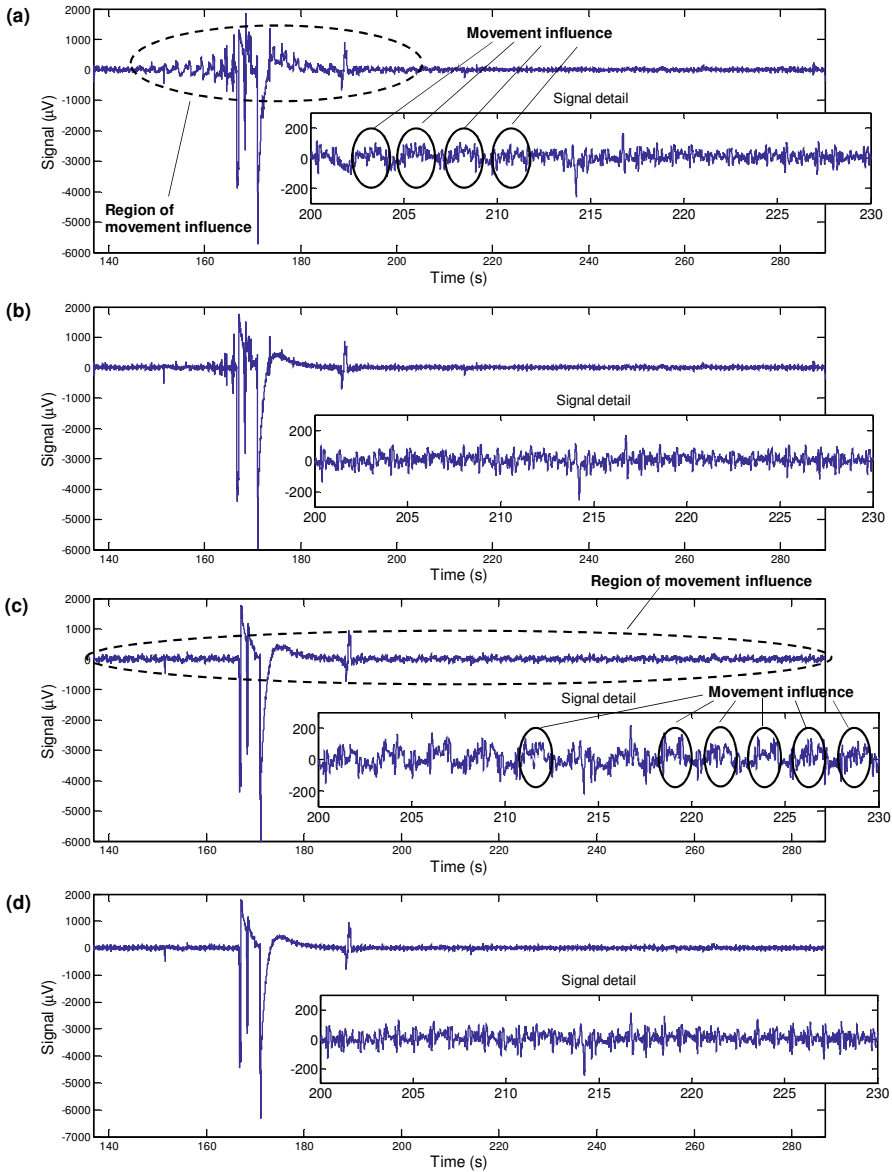


Figure 8.6: (a) OMA directly applied in the signal of Fig. 8.5a; (b) OMA applied in the signal of Fig. 8.5a according to the methodology proposed in Fig. 8.1; (c) AAS+LP filter directly applied in the signal of Fig. 8.5a; (d) AAS+LP filter applied in the signal of Fig. 8.5a according to the methodology proposed in Fig. 8.1. The movement influence noticed in (a) and (c) has been drastically reduced in (b) and (d) by using the proposed methodology.

Rather, by using our methodology depicted in Fig. 8.1, the region of movement influence has been drastically narrowed in the restored EEG by the gradient artefact correction provided by either OMA or AAS, as can be noticed in Figs. 8.6b and 8.6d. Therefore, this indicates that

the proposed methodology could be used to reduce the influence of the signal transients caused by abrupt movements of the subject head over the gradient artefact correction performance, thus improving the quality of the restored EEG in this scenario.

8.3.4 Discussion

A number of approaches have been suggested in the literature for suppression of the gradient artefact from the EEG data recorded within the MRI scanner during the occurrence of subject head movements (Moosmann et al., 2009; Sun and Hinrichs, 2009; Spencer, 2015). Nevertheless, improvement of such approaches and development of further correction techniques are still required to enhance the quality of the EEG restoration in this scenario, especially in case of signal transients continuously caused by the abrupt head motions, as described in Eqs. (8.1) and (8.2). In this fashion, we have proposed the methodology depicted in Fig. 8.1, whereby a cubic spline is used to model those signal transients, as illustrated in Fig. 8.2.

To estimate the interpolants of the cubic spline (Eqs. (8.4) and (8.5)), we have used the average point of epochs with length corresponding to TR-slice (Fig. 8.2). This procedure also represents a moving-average filtering process over a number of samples equal to TR-slice which suppresses high-frequency components from the scalp potential, including those related to the gradient artefact activity. Hence, the fitted cubic spline is shown to contain low-frequency components associated with the EEG signal and the signal transients itself, as depicted in Fig. 8.3. This effect is quite similar to that used during implementation of the optimised moving-average for gradient artefact correction (see Section 5.3.4) (Ferreira et al., 2014a). As depicted in Fig. 8.4, the subtraction of the cubic splines model enables the modified scalp potential excerpt to obtain a more homogeneous shape. This characteristic improves the performance of the gradient artefact correction method by its application in the signal s_h , instead of in the scalp potential (Fig. 8.6). Thus, the application of the proposed methodology of Fig. 8.1 reduces the influence of those signal transients on the gradient artefact correction, which permits to obtain a better quality for the restored EEG produced by either OMA or AAS, as demonstrated in Figs. 8.6b and 8.6d. Therefore, the subtraction and reincorporation of the spline model from the scalp potential data, according to the scheme of Fig. 8.1, act as an artifice to preserve the signal transients and EEG low-frequency signal components from an unnecessary processing by the gradient artefact correction method. Thus, introduction of inaccuracies and alterations in the artefact waveform by the signal transients

can be reduced because the gradient artefact correction can be solely applied in the component s_h .

The use of cubic spline fitting takes advantage of its flexibility of implementation, so that eventual outliers which might be obscured in the epoch averaging process (step 2 of Fig. 8.1) could be inserted in the fitting curve as well, depending on the need, to obtain a better representation of the signal transients. This characteristic shall be better evaluated in future work. It is also worthy of note that instead of using cubic splines, application of a high-pass filter in the scalp potential excerpt was shown not to be adequate during implementation of the proposed methodology. When using a high-pass filtering, the higher the cut-off frequency of the filter, the more is the amount of gradient artefact frequency activity which might remain in the signal m_p . As such, the gradient correction method should be applied in m_p as well. On the other hand, a low filter cut-off frequency might provoke insertion of high-frequency components associated with the transients in the signal s_h , in such a way that those inaccuracies owing to alterations in the artefact morphology could continue compromising the performance of the gradient artefact correction and the quality of the restored EEG (Yan et al., 2009; Spencer, 2015).

Another advantage observed within application of the methodology described in Fig. 8.1 is that it is data-driven, not requiring additional information associated with head movements quantified by using sensors, cameras, or derived from the subsequent (f)MRI scans (Moosmann et al., 2009; Sun and Hinrichs, 2009; Maziero et al., 2016). Recently, Maziero et al. have proposed the use of a camera tracking system in order to infer the amount of movement produced by the subject head, and thus utilise this information within an algorithm to suppress the movement artefact. Although this approach has shown to be quite promising, it is not yet available for all investigators, in addition to not being data-driven. Besides, this method is not directly designed to gradient artefact correction, but to correct the movement artefact. Rather, according to the approach proposed in this chapter, the head movement-related information has been directly inferred from the scalp potential data, as well as has been designed to improve the gradient artefact correction during the occurrence of large signal transients continuously inserted in the scalp potential data by abrupt head movements. Therefore, all these characteristics indicate that the cubic spline modelling as proposed in Fig. 8.1 could be employed to improve the quality of the restored EEG in this scenario.

8.3.5 Conclusions

In Section 8.3, we have proposed a novel method to improve the gradient artefact correction under the occurrence of signal transients continuously inserted in the scalp potential by abrupt subject head movements during co-registered EEG-fMRI. The proposed approach makes use of a cubic spline to model such signal transients which are then subtracted from the scalp potential before performing the application of the gradient artefact correction. This procedure is shown to change the shape of the scalp potential, in such a way that the gradient artefact waveforms along the modified scalp potential excerpt become more homogeneous. Thus, the influence of the signal transients over the gradient artefact correction could be minimised, especially when the stationary nature of the artefact waveform is assumed by the gradient artefact correction method, such as OMA and AAS. Therefore, our methodology is shown to be a promising tool to obtain an improved quality for the restored EEG within the scenario of alterations of the gradient artefact morphology produced by signal transients continuously inserted in the scalp potential recordings by abrupt head movements.

8.4 Other filtering strategies that might help to improve the gradient artefact correction under the occurrence of abrupt head movements

8.4.1 Linear superposition of an impulse signal

As discussed in Section 6.6, when the occurrence of the movement artefact is likened to the linear addition of an impulse signal $\delta_{tr,n}$ in the scalp potential excerpt (Eq. (8.2)), the comb-filtering provided by gradient artefact correction should possess an impulse response with decreased settling time and shorter duration of decaying peaks, otherwise residual artefacts due to $\delta_{tr,n}$ influence may be left behind in the artefact-corrected EEG. This characteristic can be observed in the impulse responses of H_{TDA} and H_c (Ferreira et al., 2018). A larger settling time is noticed for H_{TDA} than for H_c which correspond to the template subtraction by AAS and the optimised moving-average (OMA) filtering, respectively. As a consequence, the movement influence is shown to spread out in a larger length of the corrected EEG by AAS than corrected by OMA (see Figs. 6.8c, 8.6a, and 8.6c). On the other hand, H_c shows larger

decaying peaks around the time of the occurrence of the impulse. Thus, a stronger movement influence is observed in the region of movement influence (see Fig. 8.6a).

The impulse response, thereby, could be used to indicate how the comb-filtering related to the gradient artefact correction is about to cause more or less ripple, or to be more or less effective in limiting the region of movement influence in time course corrected EEG. As suggested in Section 6.6, the design of comb-filtering with impulse response with decreased settling time and shorter duration of decaying peaks might result in minimisation of the propagation of the movement influence along the corrected EEG (Vaseghi, 2000; Proakis and Manolakis, 1996). This fact should be better exploited and investigated in future work, and might be used to bring further improvements in the gradient artefact correction under the occurrence of abrupt head movements. This strategy might even be combined with the cubic splines fitting and subtraction proposed in Section 8.3 in attempt to further improve the gradient artefact correction in this scenario.

8.4.2 Sliding average window vs. optimised moving-average

Subtraction of a mean artefact template calculated over $2m+1$ sliding averaging window epochs could be described according to Eq. (8.7):

$$\begin{aligned}\hat{e}_i &= s_i - \frac{1}{2m+1} \sum_{k=-m}^m s_k = e_i + g_i - \frac{1}{2m+1} \sum_{k=-m}^m (e_k + g_k). \\ &= e_{\text{true},i} + g_i - \frac{1}{2m+1} \sum_{k=-m}^m e_{\text{true},k} - \frac{1}{2m+1} \sum_{k=-m}^m g_k,\end{aligned}\quad (8.7)$$

where \hat{e}_i is the estimate of the actual (neuronal) EEG in the epoch s_i ; s_k represents the epochs of the scalp potential considered for averaging; e_i and g_i are the actual EEG and the gradient artefact in the epoch s_i ; and e_k and g_k are the actual EEG and the gradient artefact in the epoch s_k . When the neuronal EEG signal and the gradient artefact are assumed to be uncorrelated, the amplitude of the averaged EEG epochs in the third term of the right hand side of Eq. (8.7) equals $1/\sqrt{2m+1}$ times the EEG RMS, in such a way that it is cancelled out by averaging. And the estimate of the average gradient artefact \hat{g}_i in epoch i corresponds to:

$$\hat{g}_i = \frac{1}{2m+1} \sum_{k=-m}^m g_k. \quad (8.8)$$

In an optimal scenario in which the gradient artefact waveform is perfectly reproducible in each epoch, the estimate \hat{g}_i equals to g_i ($= g_k$), and thus \hat{e}_i matches the actual EEG, e_i . However, under realistic scanning conditions, changes in the scalp potential recordings geometry by subject motion together with inconsistent scalp potential sampling due to systematic jitter between EEG system sampling frequency and the MRI clock results in alterations in the artefact waveform. This generates a component of uncertainty in the estimate \hat{g}_i that must be inserted in Eq. (8.8):

$$\Rightarrow \hat{g}_i = \frac{1}{2m+1} \sum_{k=-m}^m (g_m + u_k) = g_i + \frac{1}{2m+1} \sum_{k=-m}^m u_k. \quad (8.9)$$

Thus, \hat{e}_i in Eq. (8.7) could be expressed as the sum of the actual EEG, e_i , with the uncertainty u_i :

$$\hat{e}_i = e_i + \frac{1}{2m+1} \sum_{k=-m}^m u_m = e_i + u_i. \quad (8.10)$$

Therefore, the residual artefact that remains in the corrected EEG after AAS is associated with a component of uncertainty that represents the average of the particular uncertainties of samples belonging to the $2m+1$ averaging epochs taken into account for calculation of the artefact template. Hence, the influence of small drifts and subject head movements that occurs in scalp potential samples of $2m+1$ epochs (ranging from s_{n-mM} to s_{n+mM}) has an impact over the uncertainty u_i (Yan et al., 2009).

On the other hand, as described in Eq. (5.2), the artefact is estimated sample-by-sample through the moving-averaging filter when the optimised moving-average (OMA) is applied:

$$\begin{aligned} \frac{1}{M} \sum_{k=0}^{M-1} s_{n-k} &= \frac{1}{M} \sum_{k=0}^{M-1} (e_{n-k} + g_{n-k}). \\ &= \frac{1}{M} \sum_{k=0}^{M-1} e_{n-k} + \frac{1}{M} \sum_{k=0}^{M-1} g_{n-k} = \bar{e}_n + \frac{1}{M} \sum_{k=0}^{M-1} g_{n-k}. \end{aligned} \quad (8.11)$$

If an optimal scenario is assumed, the gradient artefact waveform is exactly stationary, and the term corresponding to the artefact in Eq. (8.11) can be cancelled out by integration, as indicated in Eq. (5.3). Under realistic conditions, however, the influence of subject head motions and jitter generates a component of uncertainty in Eq. (8.11):

$$\begin{aligned} \frac{1}{M} \sum_{k=0}^{M-1} s_{n-k} &= \bar{\hat{e}}_n + \frac{1}{M} \sum_{k=0}^{M-1} (g_{n-k} + u_{n-k}) \\ \frac{1}{M} \sum_{k=0}^{M-1} s_{n-k} &= \bar{\hat{e}}_n + \frac{1}{M} \sum_{k=0}^{M-1} g_{n-k} + \frac{1}{M} \sum_{k=0}^{M-1} u_{n-k} . \end{aligned} \quad (8.12)$$

Thereby, since the uncertainty component has been taken into consideration in Eq. (8.12), the term corresponding to the gradient artefact can precisely be cancelled out by integration. Backward application of the moving-average in Eq. (8.12) results in Eq. (8.13):

$$\begin{aligned} \frac{1}{M} \sum_{k=0}^{M-1} \left[\frac{1}{M} \sum_{k=0}^{M-1} s_{n-k} \right]_{n+k} &= \frac{1}{M} \sum_{k=0}^{M-1} \left[\bar{\hat{e}} + \frac{1}{M} \sum_{k=0}^{M-1} u_{n-k} \right]_{n+k} \\ &= e_{\text{comp},1,n} + \frac{1}{(M)^2} \sum_{k=-M+1}^{M-1} (M - |k|) u_{n+k} = e_{\text{comp},1,n} + u_{\text{comp},j,n} . \end{aligned} \quad (8.13)$$

And, thus, the uncertainty $u_{\text{comp},j,n}$ corresponds to:

$$\begin{aligned} u_{\text{comp},j,n} &= \frac{1}{(M)^2} \left[u_{n-M+1} + 2u_{n-M+2} + \dots + (M-1)u_{n-1} + (M)u_n + (M-1)u_{n+1} \dots \right. \\ &\quad \left. \dots + (M-1)u_{n+1} + 2u_{n+M-2} + u_{n+M-1} \right] . \end{aligned} \quad (8.14)$$

Therefore, in case of the OMA filter (Eq. (5.12)), the uncertainty is influenced by jitter and subject head movements that occur in the samples of the scalp potential ranging from s_{n-M+1} to s_{n+M-1} . This characteristic allows reducing the impact of small drifts and head movements by using OMA in comparison with AAS because the uncertainty associated with the corrected EEG by OMA is influenced by samples located in a shorter length of signal than the EEG corrected by the AAS sliding average window (see Sections 5.5, 5.6, 6.5, and 6.6).

8.4.3 Change in shape and amplitude of the gradient artefact

As mentioned in Section 2.4.3, when the subject makes a small change in position during acquisition of a certain volume N_1 , the gradient artefact morphology changes over time (Spencer, 2015):

$$s_n = \begin{cases} e_n + g_{2,n}, & \text{if } n < n_1 \\ e_n + g_{1,n}, & \text{if } n > n_1 \end{cases}, \quad (8.15)$$

where e_n corresponds to the EEG component in the scalp potential, s_n ; and $g_{1,n}$ and $g_{2,n}$ correspond, respectively, to the gradient artefact before and after the position change of the subject head at the time sample n_1 within the volume N_1 .

Spencer (2015) used the model of Eq. (8.16) to characterise the effect of those changes in shape and amplitude of the gradient artefact over the average artefact construction:

$$\hat{g}_n = \frac{1}{N} \left[\sum_{k=0}^{N_1-1} g_{1,k} + \sum_{k=N_1}^{N-1} g_{2,k} \right], \quad (8.16)$$

which can be rewritten as:

$$\hat{g}_n = g_{1,k} + \left(1 - \frac{N_1}{N} \right) \Delta g_n, \quad (8.17)$$

where Δg_n constitutes the difference between $g_{2,k}$ and $g_{1,k}$ caused by the small change in the head position. According to Eq. (8.17), \hat{g}_n depends on the size of the movement and its temporal incidence, and does not solely reflect the gradient artefact before and after the occurrence of the movement. The residual artefacts due to the movement influence in the corrected EEG are thus proportional to Δg_n (Spencer, 2015), and is about to be propagated to all epochs used for template construction.

In case of the optimised moving-average filtering, the change in the position of the subject head at the time sample n_1 within the volume N_1 is not reflected in all N epochs used for template averaging, but locally around the region of the change Δg_n . This characteristic can be explained by the OMA filtering being not implemented by construction of an average

template, but sample-by-sample instead. Thus, the movement influence caused by the change Δg_n in $g_{1,k}$ after the sample n_1 (resulting in $g_{2,k}$) might also be limited in a narrower region in the corrected EEG by OMA than by AAS. However, we observed that AAS can produce smaller ripple associated with the movement influence than OMA around the region of change Δg_n as well, like observed for larger signal transients continuously inserted in the scalp potential (see Section 8.4.1).

Moosmann et al. (2009) have demonstrated the effectiveness of using the information related to head movement parameters obtained from an fMRI realignment algorithm to minimise the influence of abrupt head movements due to a small position change of the subject, as described in Eq. (8.17). As remarked by Spencer (2015), however, this approach may not be effective when multiple movements occur close together in the recorded scalp potential as well as when signal transients are slowly and continuously caused by abrupt head movements. To simulate the influence due to a small change in position of the subject, Spencer (2015) proposed to generate a basis set of models to characterise the variations in the gradient artefact waveform in this scenario. Such models are then fitted and subtracted from the artefact-corrected EEG by AAS. This approach, however, has not yet been systematically evaluated, in such a way that the degree of preservation of the EEG signal together with the evaluation of artefact reduction remains unknown. In future work, we intend to apply such approaches in our data in order to obtain a better comparison with the filtering strategies discussed here.

8.5 Final discussion and concluding remarks

The occurrence of abrupt head movements in the scalp potential recordings during co-registered EEG-fMRI may profoundly compromise the performance of the gradient artefact correction. Especially in children, epilepsy patients, and sleeping subjects, the occurrence of such movements might not be prevented, thus affecting the quality of the corrected EEG due to the artefact residuals associated with the change of the subject head position. In this chapter, we have presented some strategies that might be useful for improving the quality of the corrected EEG in this scenario. As reported in Section 8.3, the use of cubic splines to model the transients continuously inserted in the scalp potential by abrupt subject head motions is shown to be effective and quite promising for minimising the impact of such

transients over the quality of the restored EEG. By using cubic splines, the modified scalp potential could be approximated to homogeneous data shape, in such a way as to reduce alterations of the artefact waveform morphology, thus improving the performance of either OMA or AAS.

As for the filtering strategies discussed in Section 8.4, they might be particularly useful for reducing the impact of the movement influence on the gradient artefact-corrected EEG as well as for limiting the region of the movement influence. In this fashion, when small movements of the subject head occur, the OMA filtering is shown to outperform the AAS sliding averaging window implementation because our approach is more effective in attenuating the impact of the movement influence in the corrected EEG. Likewise, when the movement artefact is likened to the superposition of an impulse signal in the scalp potential, OMA outperforms the AAS sliding average window by limiting the region of movement influence in the corrected EEG, although AAS is shown to produce smaller ripple in the corrected EEG due to the movement influence. As head movement-related information obtained from the MRI equipment or provided by camera tracking systems have not been available in the current work, approaches that make use of this kind of information have not been applied with our data analysis. In future work, we intend to perform this application in order to improve the comparative analysis between such approaches and the filtering strategies proposed in this chapter.

CHAPTER 9

Discussion and Conclusions

In this work, we proposed the optimised moving-average (OMA) filtering to suppress the gradient artefact from EEG recorded during co-registration of EEG and fMRI. OMA is a comb-filtering approach that allows shaping a magnitude response other than that provided by the often-used average artefact subtraction (AAS) method. In addition, OMA can be combined with other iterative filtering-based approaches that allow attenuation of the residual artefacts in the artefact-corrected EEG signal. In Section 9.1, we discuss the efficacy of our proposed methodology by using OMA in comparison with AAS and the FMRI artefact slice template removal (FASTR) methods, based on the results obtained and presented in previous chapters of this thesis. For this, we take into account the evaluation metrics used for artefact attenuation, preservation of the EEG signal, and the quality of EEG signal clinically indicated by visual inspection of the EEG expert. Section 9.2 provides a discussion of the measure proposed here to evaluate the quality of the gradient artefact-corrected EEG. Limitations and future perspectives of this work are described in Sections 9.3 and the overall conclusions are presented in Section 9.4.

9.1 Performance and relative efficacy of the gradient artefact correction methods

Since the advent of co-registered EEG-fMRI a couple of decades ago, the suppression of the gradient artefact and the improvement of the quality of the EEG signal recording during co-registered EEG-fMRI have been substantial challenges. Different solutions have been proposed in the literature, ranging from methods that aim to attenuate the artefact as it appears to post-processing methods that correct the artefact in the scalp potential after the recording.

Among the post-processing methods, the AAS solution is the most established and often-used approach. As such, it has formed the basis for most of the other correction methodologies making use of subtraction in time-domain, as described in Chapter 3. From a signal

processing and filter theory perspective, the AAS implementation corresponds to the time-domain averaging filter (H_{TDA}) described in Chapter 4, which itself consists of a comb-filtering approach based on a coherent detection process (Braun, 1975). Thereby, it is possible to construct and subtract an estimate of the gradient artefact, $\hat{g}(t)$, which can be characterised as an approximately repetitive waveform in the time course, from the scalp potential, $s(t)$.

As can be observed examining the magnitude response of the comb-filtering representative of AAS shown in Chapter 4, the width of the comb-filter stop-bands integrated within AAS is larger when a small number of averages, N , is used, and is narrowed for a larger number of averages. This characteristic affects the performance of AAS because few averages can result in removal of the neuronal EEG after template subtraction, whereas a larger number of averages can lead to remaining residual artefacts after AAS. It is also particularly important when broadening of the gradient artefact spectral lines due to tiny movements of the subject head is observed in the scalp potential spectrum around the artefact frequency bins associated with TR-slice. The current implementation of the AAS approach only provides the same width for all comb-filtering stop-bands. Thus, it cannot account for by the broadening of the artefact spectral lines around the higher-frequency artefact bins without simultaneously causing unnecessary attenuation in the lower-frequency artefact bins (Spencer, 2015).

An AAS implementation using a sliding averaging window as well as the construction of an optimal basis set (OBS) using principal component analysis has been proposed to account for the occurrence of movement artefacts caused by small changes in head position of the subject, and its impact on gradient artefact suppression (Allen et al., 2000; Niazy et al., 2005; Freyer et al., 2009). The sliding averaging window has been widely used and is commercially available in the AAS implemented in the software Brain Vision Analyzer 2. In turn, the OBS algorithm together with the sliding averaging window has been implemented in the often-used MATLAB-based plug-in FASTR. Both Brain Vision Analyzer 2 and FASTR have been used in Chapters 5 and 6 for the comparative analysis.

As demonstrated in Chapters 5 and 6, the artefact-corrected EEG using a sliding averaging window and OBS may be not effective in attenuating residual artefacts associated with head movements either. The AAS by sliding averaging window is shown to be susceptible to imprecise artefact template estimation due to variations of the artefact waveform morphology over time caused by small changes in the position of the subject's head. Even when a small number of averages epochs are used, the sliding averaging window may be not effective. By

using OBS jointly to AAS by sliding averaging window, the artefact template imprecision caused by small changes in the head position can be corrected. However, residual artefacts associated with head motions are still observed in the time course and power spectrum of the corrected EEG. Therefore, residual artefacts associated with broadened spectral lines caused by the tiny endogenous movements of the subject head may not be accounted for by the AAS sliding average window nor by the combination AAS and OBS (Spencer, 2015). It is therefore necessary to make use of a conventional low-pass (LP) filtering with cut-off at 70 Hz and adaptive noise cancelling (ANC) in order to suppress such residuals; in turn, frequencies above the filter cut-off frequency are inadvertently removed from the EEG signals, as mentioned in Chapters 1 – 3 and shown in Chapter 6.

The OMA filtering strategy as proposed in Chapter 4 entails a comb-filtering approach (H_C and H_L) that allows larger attenuation in higher-frequency stop-bands rather than the evenly broadened stop-bands provided by AAS. This characteristic explains why the OMA approach is more effective in accounting for the broadening of spectral lines associated with the slice repetition time (TR-slice) than AAS or the combination AAS+OBS. This could be observed in Chapters 5 and 6, where the residual artefacts are shown to be least apparent in the power spectra and the corresponding time course of the EEG signal corrected by OMA. In addition, OMA was shown to better attenuate the harmonic artefact activity associated with TR-slice than the AAS approach, while best preserving EEG signal components. As such, the OMA approach exhibits the most favourable trade-off between artefact suppression and preservation of the neuronal EEG and, in particular, clinically relevant high-frequency EEG features can potentially be better preserved.

In a scenario where the dynamic stabilisation cannot be switched off, and thus TR cannot be set as a multiple of TR-slice, OMA is also shown to be effective in attenuating the gradient artefact. Therefore, as shown in Chapter 6, our approach could be applied in two subsequent steps without compromising the quality of the corrected EEG. This is an important feature, because OMA can be used to individually address the artefact activity associated with TR and TR-slice and further attenuate the gradient artefact around their higher-frequency bins. In contrast, application of two AAS averaging steps, one for TR and another for TR-slice, has been proven to degrade the quality of the corrected EEG. In addition, the construction of the AAS template should be performed by using either a template with length TR or irregular

epochs of length TR-slice which has been demonstrated to be less effective than using regular epochs with TR-slice length (Mandelkow et al., 2010).

Another advantage of using OMA is its performance regarding the use of data without accurate information about MRI triggers and other events, as may be the case for data originally acquired for clinical rather than research purposes. In this respect, the use of volume-start and slice-start markers in the EEG data has not been necessary for implementation of OMA. Furthermore, even though reduction of jitter by using hardware synchronisation solutions has become increasingly available, OMA shows to be more robust within a scenario of misalignment between EEG sampling interval and TR-slice, as demonstrated in Chapter 5.

Still, some residual artefacts associated with broadening of the artefact spectral lines around the artefact bins related to TR-slice may not be suppressed after applying OMA. We have demonstrated that the use of the additional filters highly selective notch filtering (HSN) and optimised exponential average (OEA) yields a better EEG signal preservation performance compared to the use of LP filtering and ANC, especially at higher frequencies of the corrected EEG. As shown in Chapter 6, HSN and OEA achieve more selective attenuation for residual artefacts in the gamma band (30 – 100 Hz) and in higher-frequency EEG bands than ANC and LP. The power spectrum of the neuronal (baseline) EEG typically decays proportionally to the inverse of the frequency ($1/f$). The occurrence of spectral power activity above the baseline EEG power spectrum, therefore, is an indication of corruption by residual artefacts after AAS and OMA, suggesting that the expected power spectrum decay of $1/f$ is not present (Gutberlet, 2010; Mandelkow et al., 2006). This has been further confirmed in Chapter 7 by the use of the signal slope adaption (SSD) approach which was shown to attenuate the residual artefact activity and yield a corrected EEG power spectrum that obeyed $1/f$ -rule. This evidences the importance of applying filters like OEA in the corrected EEG to attenuate remaining residuals above the baseline EEG.

As mentioned above, OMA is also shown to be more effective in reducing the impact of small head movements on the quality of the corrected EEG compared to AAS alone. As discussed in Chapter 8, the comb-filtering integrated in OMA is performed sample-by-sample, rather than by template subtraction as performed in AAS. Therefore, the impact of the movement is spread along all the N epochs used for averaging and construction of the artefact template; the larger the number of epochs used for averaging, the larger is the region of the corrected EEG

affected by the movement influence. Rather, OMA is capable of limiting the influence of movements to a shorter region, which results in better preservation of the EEG in case of small head movements, as indicated by the values of SNR and MSE calculated in Chapter 5. These results could be extended to a scenario concerned with a movement artefact variant $m_{u,n}$, corresponding to the signal transients inserted in the scalp potential, $s_i(t)$, by abrupt head movements in general, as described in Chapter 8.

The impact of abrupt motion artefacts characterised by signal transients that are slowly and continuously inserted in the scalp potential, which can be likened to the superposition of an impulse signal $\delta_{u,n}$ in $s_i(t)$, can exceed a larger region in the corrected EEG that depends on the impulse response of the comb-filtering integrated to OMA and AAS (Ferreira et al., 2018). Here, we noticed that the comb-filtering approach which provides an impulse response with smaller settling time as well as smaller decaying peaks would yield a better EEG quality. As observed and discussed in Chapters 6 and 8, the region of movement influence for AAS is much larger than for OMA. This fact can therefore be ascribed to the impulse response of the comb-filtering integrated to OMA and AAS.

Attenuation of the movement artefact in the EEG data where $m_{u,n}$ and $\delta_{u,n}$ occur, has been studied by Maziero et al. (2016). They proposed the use of the information provided by a camera tracking system in combination with AAS and FASTR to suppress the movement artefact. Although this approach has shown to be quite promising, it is not yet available for all investigators and does not have a specific strategy for gradient artefact correction. Some researchers have also proposed an improved AAS correction under influence of small changes in shape and amplitude of the gradient artefact by using either head movement-related parameters or weighting factors for the AAS averaging epochs (Moosmann et al., 2009; Sun and Hinrichs, 2009). Most recently, Spencer (2015) proposed a novel method to account for the influence of the movement artefact over the gradient artefact correction in a scenario of small changes in position of the subject' head. According to this method, a basis set of models is produced to characterise the variations in the gradient artefact waveform, which is then used to attenuate residual artefacts from the artefact-corrected EEG by AAS. The performance of this method, however, has not yet been systematically evaluated and, therefore, the degree of preservation of the EEG signal associated with the level of artefact reduction remains unknown. In future work, we intend to compare performance of these approaches to the strategies to minimise the impact of the movement artefact on the gradient artefact correction,

as described and discussed in Chapter 8. The gradient artefact correction evaluation as proposed in this thesis could be used in this scenario as well (see Section 9.2).

Concerning the computational effort, our methodology is shown to be less computationally demanding than FASTR, requiring less time to process the gradient artefact correction and residual artefacts attenuation. This can be explained by our methodology being based upon iterative filtering methods that make use of the finite impulse response (FIR) filter, and thus takes advantage of the computational efficiency of this equation. Hence, the time required to compute the proposed approaches has shown to be quite low and comparable with the processing time of the AAS sliding averaging window performed by the Brain Vision Analyzer software which is also based upon the FIR moving-average filter.

The clinical evaluation performed by visual inspection of the EEG expert, as reported in Chapter 6, provided a preliminary clinical indication of the quality of the corrected EEG signals. According to the EEG expert, the occurrence of epileptiform activity has been successfully identified in the corrected EEG signals by both our methodology and the FASTR method. As our proposed methodology has been shown to be more robust to alterations of the artefact waveform over time, it would therefore be the most promising tool for gradient artefact correction in scenarios in which abrupt head movements cannot be prevented like in studies involving epileptic patients and children.

As shown in Chapters 4 and 6, iterative filtering can be used to design the comb-filtering approach integrated within the OMA approach as well as the HSN and OEA filters. Moreover, according to some preliminary investigations undertaken in this work as well, iterative filtering could also be used to design other types of filter such as high-pass and band-pass filters approximated to the ideal case. In addition, mathematical functions other than the FIR moving-average and the exponential average filters could also be used within such a filtering design approach.

In conclusion, the methodology proposed in this thesis is robust, accurate, fast, and has the additional advantage that it is fully data-driven. Hence, it does not require information provided by sensors, cameras, or derived from the subsequent (f)MRI scans, nor accurate information about MRI triggers and events, as mentioned above. OMA is therefore a useful tool in case of processing data originally acquired for clinical purposes rather than research purposes.

9.2 Gradient artefact correction evaluation

As described in Chapter 3, one of the big challenges for the consistent and systematic gradient artefact correction evaluation is posed by the stochastic nature of the EEG signal. Therefore, systematic and consistent evaluation of the gradient artefact performance is seldom encountered in the literature (Ritter et al., 2007; Ritter et al., 2010; Freyer et al., 2009).

The analysis of single events in the corrected EEG has shown to be effective for evaluation of the gradient artefact correction by identification of epileptic spikes, ERPs and EPs, and EEG rhythms present in the corrected EEG (Bénar et al., 2003; Niazy et al., 2005; Becker et al., 2005). However, these characteristics cannot be used when the focus is the spontaneous EEG. Caution should also be taken when quantifying the EEG power spectrum in certain spectral bands to evaluate the correction procedure because the spectrum represents an average measure of the frequencies contained in the time-domain signal. Residual artefacts and other events such as epileptic spikes might therefore be masked in the power spectrum of the corrected EEG, requiring the clinical assessment by an EEG expert to sufficiently assess the quality of the corrected EEG as well as the correct identification of the epileptiform activity (see Chapter 6). Likewise, the application of the gradient artefact correction in the reference EEG, as it is usually implemented (Freyer et al., 2009; Ritter et al., 2007), has the disadvantage of not accounting for the influence of the gradient artefact and other sources of interference during co-registration of EEG and fMRI data. A similar problem is encountered for the reference EEG recorded in phantoms or replaced by simulated data (Grouiller et al., 2007; Mandelkow et al., 2010; Spencer, 2015). Furthermore, the stochastic nature and lack of knowledge of the neuronal EEG make the comparison of the power spectrum of the artefact-corrected EEG with the spectrum of the reference EEG recorded inside and outside the scanner imprecise. The use of such procedures might hence make it difficult to obtain a good accuracy for the assessment of EEG preservation.

The assessment of EEG preservation as proposed in Chapter 3 effectively accounts for all the characteristics described above. For instance, when the focus is the spontaneous EEG, entire EEG excerpt lengths should be analysed as the characteristic of interest in order to obtain a more precise evaluation of the EEG preservation. Our proposed assessment approach works for larger EEG excerpts, allowing comparison in terms of the SNR and MSE and minimising the imprecision effects associated with the stochastic nature of the EEG signal. The SNR as calculated in Chapter 5 also permits the evaluation of frequency characteristics. As it is

implemented in the time-domain, this approach readily facilitates the comparison of frequency characteristics between reference EEG and corrected EEG excerpts, alleviating the need for quantification of the spectral power. In addition, the analysis of single events in the corrected EEG can also be effectively accounted for by our proposed approach.

Another contribution of the gradient artefact correction evaluation procedure adopted in this work is that it could form the basis for a systematic methodology evaluation. In this way, after choosing the component of interest to be assessed in the corrected EEG as well as the reference signal to be used during the assessment procedure, our approach for EEG preservation assessment proposed in Chapter 3 (or its combination with the visual inspection of an EEG expert) would be utilised to perform the assessment of EEG preservation. Then this analysis should be combined with the evaluation of the amount of artefact reduction, as performed in Chapter 5.

A disadvantage associated with the procedure above is that a representative reference EEG should always be available. Moreover, the measurement of the RMS and amplitude of the artefact voltage over time can be compromised when large amplitude transients caused by abrupt head movements are inserted in $s_i(t)$. Despite these limitations, our approach is suitable for a large majority of most clinical co-registered EEG-fMRI recordings performed nowadays.

9.3 Limitations, considerations, and directions for future work

One of the limitations we observed during application of the OMA methodology relates to the assumption of stationarity of the gradient artefact waveform. Like for the AAS method, violations of this assumption might degrade the quality of the EEG signal, especially in case of abrupt head motions. However, as discussed in Chapters 6 and 8, OMA could outperform the AAS sliding window approach as well as the OBS approach by severely limiting the time interval of the corrected EEG signal impacted by the artefact. Moreover, even though the filtering strategies mentioned in Chapter 8 could be used to reduce the movement influence and its impact on the gradient artefact-corrected EEG, further development and investigation of additional methodologies to eliminate the movement influence are encouraged in future work.

Also like AAS, OMA has been shown to achieve better results when a phase-lock synchronisation procedure between the EEG sampling frequency and the MRI acquisition frequency is used. Moreover, both gradient artefact correction methods may suffer from ringing. We aimed to minimise the occurrence of ringing with OMA by its application in scalp potential excerpts with length equal to $M \times n / f_s$, where M corresponds to TR, and n is a real integer. In case of the using AAS in a sliding averaging window implementation, the ringing effect cannot be prevented as the calculation of the average template for epochs in the ends of the excerpt may be compromised by an insufficient number of averaging epochs. The choice of the frequency bin width during evaluation of the power spectrum artefact reduction is another aspect that should be more elaborately investigated. Although the value of ± 1 Hz used in Chapters 5 and 6 as well as in Niazy et al. (2005) could be used to perform the assessment of artefact reduction around the frequency bins associated with TR-slice, it may not represent a realistic bandwidth as the broadening of the spectral lines around these bins might be much larger than that value, especially at higher frequencies.

Since better preservation of high-frequency activity in the corrected EEG in comparison to the AAS and OBS method can be achieved using our methodology, we envisage that it can be potentially exploited as a simpler alternative to access HFOs during co-registered EEG-fMRI (Freyer et al., 2009; Anami et al., 2003). This, however, still requires further investigation, as discussed in Chapter 6. Clinical application of our methodology in studies involving EPs and ERPs is also awaited. As a further suggestion for future work, we would like to apply our methodology in EEG data of a larger number of subjects recorded in a wider range of MRI scanners to assess its generalisability. Also, the performance of our methodology in correction of other types of periodic artefacts such as the artefact that affects the scalp potential during electrical impedance tomography (Fabrizi et al., 2010) should be assessed.

Lastly, our EEG preservation assessment approach could also be used to evaluate the impact of any other signal processing procedure. To this end, the blocks labelled with **Gradient artefact correction** in Fig. 3.11 should be replaced by the signal processing procedure under investigation, and the reference EEG replaced by the reference signal according to degree of preservation of the characteristics of interest evaluated in the output signal, as has been performed for the SSD approach in Chapter 7.

9.4 Overall conclusions

To improve the performance of gradient artefact correction and maximise the quality of the corrected EEG signal recorded during co-registered EEG-fMRI, this thesis reports on the development of novel filtering techniques and the comparison of their performance with the established AAS and the also often-used FASTR method.

We concluded that our filtering techniques achieve a superior artefact removal from the co-registered EEG signal, especially in a higher-frequency EEG bandwidth. This is a direct result of the better attenuation provided by the OMA approach in higher-frequency artefact bins than the average artefact template subtraction employed by AAS and the combination AAS+OBS method. In parallel, the HSN and OEA filtering are shown to be more effective than the usage of ANC and conventional LP filtering in simultaneously suppressing remaining residual artefacts and preserving the EEG. Moreover, in addition to its lower computational demand compared to FASTR and alleviation of the need for accurate information on MRI trigger events, our methodology for gradient artefact correction is less sensitive to the influence of abrupt movements of the subject's head. This is an important characteristic in studies in which these types of movement cannot be prevented like those involving epileptic patients. We have shown that in a clinical setting, where an EEG expert performed visual inspection of the corrected EEG signals, the epileptiform activity could be successfully identified.

In addition, our strategy for the evaluation of EEG preservation after gradient artefact correction is proven to be simple and effective in accounting for the stochastic nature of the EEG signal. The evaluation of the gradient artefact correction methods, as proposed in this work, could also be used as an outline for a systematic evaluation of any gradient artefact correction method as well as artefact correction in general.

Last but not least, the novel filtering techniques presented in this work could eventually be used in other signal processing applications as well. The iterative methodology of FIR-moving average-based methods was demonstrated to be useful for comb, notch, and low-pass filtering design, with substantial flexibility. For instance, these types of filter are recurring and ubiquitous in signal processing applications like harmonic analysis. In parallel, in addition to its use to detect and attenuate residual artefacts after AAS, the SSD approach could be used for detection of other kinds of artefact and steep wave activity, such as QRS complex

detection in the ECG signal. Therefore, aside their ability to improve the quality of the EEG data in studies that make use of neurophysiologic and cognitive mapping of the brain by co-registered EEG-fMRI, the filtering tools designed and proposed in thesis are potentially useful in a wide variety of biomedical and other signal processing applications.

References

- Abreu, R., Leite, M., Jorge, J., Grouiller, F., van der Zwaag, W., Leal, A., and Figueiredo, P. (2016). Ballistocardiogram artifact correction taking into account physiological signal preservation in simultaneous EEG-fMRI. **Neuroimage**, 135, pp. 45-63.
- Abreu, R., Leal, A., and Figueiredo, P. (2018). EEG-Informed fMRI: A review of data analysis methods. **Front. Hum. Neurosci.**, 12, article 29, pp. 1-23.
- Allen, P.J. (2010). EEG instrumentation and safety. In: C. Mulert and L. Lemieux (eds.), **EEG-fMRI: Physiological basis, technique, and applications**. Springer-Verlag: Berlin, Heidelberg, pp. 115-133.
- Allen, P.J., Polizzi, G., Krakow, K., Fish, D.R., and Lemieux, L. (1998). Identification of EEG events in the MR scanner: the problem of pulse artifact and a method for its subtraction. **Neuroimage**, 8(3), pp. 229-239.
- Allen, P.J., Josephs, O., and Turner, R. (2000). A method for removing imaging artifact from continuous EEG recorded during functional MRI. **Neuroimage**, 12(2), pp. 230-239.
- Altman, N.R. and Bernal, B. (2006). Pediatric applications of fMRI. In: S.H. Faro and F.B. Mohamed (eds.), **Functional MRI: Basic principles and clinical applications**. Springer: New York, pp. 394-428.
- Anami, K., Saitoh, O., Yumoto, M., Tanaka, F., Kawagoe, Y., Ohnishi, T., and Matsuda, H. (2002). Reduction of ballistocardiogram with a vacuum head-fixating system during simultaneous fmri and multi-channel monopolar EEG recording. **Int. Congr. Ser.**, 1232, pp. 427-431.
- Anami, K., Mori, T., Tanaka, F., Kawagoe, Y., Okamoto, J., Yarita, M., Ohnishi, T., Yumoto, M., Matsuda, H., and Saitoh, O. (2003). Stepping stone sampling for retrieving artifact-free electroencephalogram during functional magnetic resonance imaging. **Neuroimage**, 19(2), pp. 281-295.

- EC57, A.A. (1998). **Testing and reporting performance results of cardiac rhythm and ST segment measurement algorithms** (AAMI Recommended Practice/ American National Standard). Association for the Advancement of Medical Instrumentation.
- Anwar, M.N., Bonzano, L., Sebastiano, D.R., Roccatagliata, L., Gualniera, G., Vitali, P., Ogliaastro, C., Spadavecchia, L., Rodriguez, G., Sanguineti, V., Morasso, P., and Bandini, F. (2009). Real-time artifact filtering in continuous VEPs/fMRI recording. **J. Neurosci. Methods**, 184(2), pp. 213-223.
- Arzeno, N.M., Deng, Z.-D., and Poon, C.-S. (2008). Analysis of first-derivative based QRS detection algorithms. **IEEE Trans. Biomed. Eng.**, 55(2), pp. 478-484.
- Bagshaw, A.P. and Bénar, C.-G. (2010). Scanning strategies for simultaneous EEG-fMRI recordings. In: M. Ullsperger and S. Debener (eds.), **Simultaneous EEG and fMRI: Recording, analysis, and applications**. Oxford University Press: New York, pp. 85-93.
- Bandettini, P.A. (2009). Functional MRI limitations and aspirations. In: E. Kraft, G. Gulyás, and E. Pöppel (eds.), **Neural correlates of thinking**. Springer-Verlag: Berlin, Heidelberg, pp. 15-38.
- Barlow, J.S. (1983). Muscle spike artifact minimisation in EEGs by time-domain filtering. **Electroencephalogr. Clin. Neurophysiol.**, 55(4), pp. 487-491.
- Becker, R., Ritter, P., Moosmann, M., and Villringer, A. (2005). Visual evoked potentials recovered from fMRI scan periods. **Hum. Brain Mapp.**, 26(3), pp. 221-230.
- Belliveau, J.W., Kennedy, D.N., McKinstry, R.C., Buchbinder, B.R., Weisskoff, R.M., Cohen, M.S., Vevea, J.M., Brady, T.J., and Rosen, B.R. (1991). Functional mapping of the human visual-cortex by magnetic resonance imaging. **Science**, 254(5032), pp. 716-719.
- Bénar, C.-G., Aghakhani, Y., Wang, Y., Izenberg, A., Al-Asmi, A., Dubeau, F., and Gotman, J. (2003). Quality of EEG in simultaneous EEG-fMRI for epilepsy. **Clin. Neurophysiol.**, 114(3), pp. 569-580.
- Benitez, D.S., Gaydecki, P.A., Zaidi, A., and Fitzpatrick, A.P. (2000). A new QRS detection algorithm based on the Hilbert transform. **Comput. Cardiol.**, 27, pp. 379-382.

- Bergmann, T.O., Mölle, M., Diedrichs, J., Born, J., and Siebner, H.R. (2012). Sleep spindle-related reactivation of category-specific cortical regions after learning face-scene associations. **Neuroimage**, 59(3), pp. 2733-2742.
- Berne, R.M., Levy, M.N., Koeppen, B.M., and Stanton, B.A. (2003). **Physiology**. 5th edition. Mosby-Elsevier: St. Louis.
- Bishop, C.M. (2006). **Pattern recognition and machine learning**. Springer: New York.
- Bondi, M.W., Houston, W.S., Eyster, L.T., and Brown, G.G. (2005). fMRI evidence of compensatory mechanisms in older adults at genetic risk for Alzheimer disease. **Neurology**, 64(3), pp. 501-508.
- Bonmassar, G., Purdon, P.L., Jääskeläinen, I.P., Chiappa, K., Solo, V., Brown, E.N., and Belliveau, J.W. (2002). Motion and ballistocardiogram artefact removal for interleaved recording of EEG and EPs during MRI. **Neuroimage**, 16(4), pp. 1127-1141.
- Braun, S. (1975). The extraction of periodic waveforms by time domain averaging. **Acustica**, 32(2), pp. 69-77.
- Braun, S. (2011). The synchronous (time domain) average revisited. **Mech. Syst. Signal Pr.**, 25(4), pp. 1087-1102.
- Brookes, M.J., Mullinger, K.J., Stevenson, C.M., Morris, P.G., and Bowtell, R. (2008). Simultaneous EEG source localisation and artefact rejection during concurrent fMRI by means of spatial filtering. **Neuroimage**, 40(3), pp. 1090-1104.
- Brown, M.A. and Semelka, R.C. (2003). **MRI: Basic principles and applications**. 3rd edition. Wiley-Liss: New York.
- Carmichael, D.W., Hamandi, K., Laufs, H., Duncan, J.S., Thomas, D.L., and Lemieux, L. (2008). An investigation of the relationship between BOLD and perfusion signal changes during epileptic generalised spike wave activity. **Magn. Reson. Imaging**, 26(7), pp. 870-873.
- Carmichael, D. (2010). Image quality issues. In: C. Mulert and L. Lemieux (eds.), **EEG-fMRI: Physiological basis, technique, and applications**. Springer-Verlag: Berlin, Heidelberg, pp. 173-199.

- Centeno, M., Tierney, T.M., Perani, S., Shamshiri, E.A., StPier, K., Wilkinson, C., Konn, D., Banks, T., Vulliemoz, S., Lemieux, L., and Pressler, R.M. (2016). Optimising EEG-fMRI for localisation of focal epilepsy in children. **PLoS One**, 11(2), p. e0149048.
- Chowdhury, M.E.H., Mullinger, K.J., Glover, P., and Bowtell, R. (2014). Reference layer artefact subtraction (RLAS): a novel method of minimizing EEG artefacts during simultaneous fMRI. **Neuroimage**, 84, pp. 307-319.
- Chowdhury, M.E.H., Mullinger, and Bowtell, R. (2015). Simultaneous EEG-fMRI: evaluating the effect of the cabling configuration on the gradient artefact. **Phys. Med. Biol.**, 60, pp. N241-N250.
- Christmann, C., Koepp, C., Braus, D.F., Ruf, M., and Flor, H. (2007). A simultaneous EEG-fMRI study of painful electric stimulation. **Neuroimage**, 34(4), pp. 1428-1437.
- Clark Jr., J.W. (2010). The origin of biopotentials. In: J.G. Webster (ed.), **Medical instrumentation: Application and design**. 4th edition. Wiley: Hoboken, pp. 126-188.
- Clifford, G.D. (2006). ECG statistics, noise, artifacts, and missing data. In: G.D. Clifford, F. Azuaje, and P. McSharry (eds.), **Advanced methods and tools for ECG data analysis**. Artech House: Boston, London, pp. 55-99.
- Cluitmans, P.J.M. (1990). **Neurophysiological monitoring of anesthetic depth**. Ph.D. Thesis. Eindhoven University of Technology: Eindhoven, The Netherlands.
- Cluitmans, P.J.M. (2010). **Neuromonitoring – lecture notes**. Eindhoven University of Technology: Eindhoven, The Netherlands.
- Cluitmans, P.J.M., Jansen, J.W., and Beneken, J.E.W. (1993). Artifact detection and removal during auditory evoked potential monitoring. **J. Clin. Monit.**, 9(2), pp. 112-120.
- Daniel, A.J., Smith, J.A., Spencer, G.S., Jorge, J., Bowtell, R., and Mullinger, K.J. (2019). Exploring the relative efficacy of motion artefact correction techniques for EEG data acquired during simultaneous fMRI. **Hum. Brain Mapp.**, 40(2), pp. 578-596.
- Davis, K.D. (2006). fMRI of clinical pain. In: S.H. Faro and F.B. Mohamed (eds.), **Functional MRI: Basic principles and clinical applications**. Springer: New York, pp. 429-443.

- Debener, S., Strobel, A., Sorger, B., Peters, J., Kranczioch, C., Engel, A.K., and Goebel, R. (2007). Improved quality of auditory event-related potentials recorded simultaneously with 3-T fMRI: removal of the ballistocardiogram artefact. **Neuroimage**, 34(2), pp. 587-597.
- Debener, S., Kranczioch, C., and Gutberlet, I. (2010). EEG quality: origin and reduction of the EEG cardiac-related artefact. In: C. Mulert and L. Lemieux (eds.), **EEG-fMRI: Physiological basis, technique, and applications**. Springer-Verlag: Berlin, Heidelberg, pp. 135-151.
- Deichmann, R., Nöth, U., and Weiskopf, N. (2010). The basics of functional magnetic resonance imaging. In: C. Mulert and L. Lemieux (eds.), **EEG-fMRI: Physiological basis, technique, and applications**. Springer-Verlag: Berlin, Heidelberg, pp. 39-62.
- Delorme, A. and Makeig, S. (2004). EEGLAB: an open source toolbox for analysis of single-trial EEG dynamics including independent component analysis. **J. Neurosci. Methods**, 134(1), pp. 9-21.
- de Munck, J.C., Goncalves, S.I., Huijboom, L., Kuijer, J.P.A., Pouwels, P.J.W., Heethaar, R.M., and da Silva, F.L. (2007). The hemodynamic response of the alpha rhythm: an EEG/fMRI study. **Neuroimage**, 35(3), pp. 1142-1151.
- de Munck, J.C., van Houdt, P.J., Gonçalves, S.I., van Wegen, E., and Ossenblok, P.P.W. (2013). Novel artefact removal algorithms for co-registered EEG/fMRI based on selective averaging and subtraction. **Neuroimage**, 64, pp. 407-415.
- de Souza, A.C.S., Yehia, H.C., Sato, M.A., and Callan, D. (2013). Brain activity underlying auditory perceptual learning during short period training: simultaneous fMRI and EEG recording. **BMC Neurosci.**, 14(1), p. 8.
- D'Esposito, M. (2006). Cognitive neuroscience applications. In: S.H. Faro and F.B. Mohamed (eds.), **Functional MRI: Basic principles and clinical applications**. Springer: New York, pp. 468-495.
- Dresler, M., Wehrle, R., Spoormaker, V.I., Koch, S.P., Holsboer, F., Steiger, A., Obrig, H., Sämann, P.G., and Czisch, M. (2012). Neural correlates of dream lucidity obtained from contrasting lucid versus non-lucid REM sleep: a combined EEG/fMRI case study. **Sleep**, 35(7), pp. 1017-1020.

- Detre, J.A. (2004). fMRI: applications in epilepsy. **Epilepsia**, 45, pp. 26-31.
- Eichele, T., Moosmann, M., Wu, L., Gutberlet, I., and Debener, S. (2010). Removal of MRI artifacts from EEG recordings. In: M. Ullsperger and S. Debener (eds.), **Simultaneous EEG and fMRI: Recording, analysis, and applications**. Oxford University Press: New York, pp. 95-106.
- El-Tatar, A. and Fokapu, O. (2011). Modeling MR induced artifacts contaminating electrophysiological signals recorded during MRI. In: **Proceedings of 33rd Annual International Conference of the IEEE EMBS (EMBC '2011)**, IEEE, Boston, USA, August 30 – September 3, 2011, pp. 7135-7138.
- Fabrizi, L., Yerworth, R., McEwan, A., Gilad, O., Bayford, R., and Holder, D.S. (2010). A method for removing artefacts from continuous EEG recordings during functional electrical impedance tomography for the detection of epileptic seizures. **Physiol. Meas.**, 31(8), pp. S57-S72.
- Ferreira, J.L., Cluitmans, P.J.M, and Aarts, R.M. (2012). Gradient artefact correction in the EEG signal recorded within the fMRI scanner. In: **Proceedings of the 5th International Conference on Bio-inspired Systems and Signal Processing (BIOSIGNALS '2012)**, INSTICC, Vilamoura, Portugal, February 1 – 4, 2012, pp. 110-117.
- Ferreira, J.L., Cluitmans, P.J.M., and Aarts, R.M. (2013a). Non-linear filter for gradient artefact correction during simultaneous EEG-fMRI. **Signal Processing Research**, 2(3), pp. 55-63.
- Ferreira, J.L., Cluitmans, P.J.M, and Aarts, R.M. (2013b). Gradient artefact modelling using a set of sinusoidal waveforms for EEG correction during continuous fMRI. **Signal Processing Research**, 2(2), pp. 39-48.
- Ferreira, J.L., Aarts, R.M., and Cluitmans, P.J.M. (2013c). Effective extraction and filtering of frequency components in physiological signals using sum-of-sinusoids modelling. **Signal Processing Research**, 2(4), pp. 73-80.
- Ferreira, J.L., Cluitmans, P.J.M., and Aarts, R.M. (2013d). Detection of sharp wave activity in biological signals using differentiation between consecutive samples. In: **Proceedings of the**

6th International Conference on Bio-inspired Systems and Signal Processing (BIOSIGNALS '2013), INSTICC, Barcelona, Spain, February 11 – 14, 2013, pp. 327-332.

Ferreira, J.L., Aarts, R.M., and Cluitmans, P.J.M. (2014a). Optimized moving-average filtering for gradient artefact correction during simultaneous EEG-fMRI. In: **Proceedings of the 5th ISSNIP-IEEE Biosignals and Biorobotics Conference: Biosignals and Robotics for Better and Safer Living (BRC '2014)**, IEEE, Salvador, Brazil, May 26 – 28, 2014, pp. 1-6.

Ferreira, J.L., Aarts, R.M., and Cluitmans, P.J.M. (2014b). Removal of gradient artefacts during transient head movements for continuous EEG-fMRI. In: **Proceedings of the 7th International Conference on Bio-inspired Systems and Signal Processing (BIOSIGNALS '2014)**, INSTICC, Angers, France, March 3 – 6, 2014, pp. 213-220.

Ferreira, J.L., Wu, Y., Besseling, R.M.H., Lamerichs, R., and Aarts, R.M. (2016). Gradient artefact correction and evaluation of the EEG recorded simultaneously with fMRI data using optimised moving-average. **J. Med. Eng.**, vol. 2016, article ID 9614323, pp. 1-17.

Ferreira, J.L., Wu, Y., R., and Aarts, R.M. (2018). Enhancement of the comb-filtering selectivity using iterative moving-average for periodic waveform and harmonic elimination. **J. Healthc. Eng.**, vol. 2018, article ID 7901502, pp. 1-14.

Ferreira, J.L., Besseling, R.M.H., Wu, Y., Arends, J., and Carrette, E. (2018). Evaluating the relative efficacy and clinical usefulness of the gradient artefact correction using iterative filtering. To be submitted.

Foucher, J.R., Otzenberger, H., and Gounot, D. (2003). The BOLD response and the gamma oscillations respond differently than evoked potentials: an interleaved EEG-fMRI study. **BMC Neurosci.**, 4(1), p. 22.

Foucher, J.R., Otzenberger, H., and Gounot, D. (2004). Where arousal meets attention: a simultaneous fMRI and EEG recording study. **Neuroimage**, 22(2), pp. 688-697.

Fox, M.D. and Raichle, M.E. (2007). Spontaneous fluctuations in brain activity observed with functional magnetic resonance imaging. **Nat. Rev. Neurosci.**, 8(9), pp. 700-711.

- Frank, M.J., Gagne, C., Nyhus, E., Masters, S., Wiecki, T.V., Cavanagh, J.F., and Badre, D., (2015). fMRI and EEG predictors of dynamic decision parameters during human reinforcement learning. **J. Neurosci.**, 35(2), pp. 485-494.
- Freyer, F., Becker, R., Anami, K., Curio, G., Villringer, A., and Ritter, P. (2009). Ultrahigh-frequency EEG during fMRI: pushing the limits of imaging-artifact correction. **Neuroimage**, 48(1), pp. 94-108.
- Fritsch, F.N. and Carlson, R.E. (1980). Monotone piecewise cubic interpolation. **SIAM. J. Numer. Anal.**, 17(2), pp. 238-246.
- Galvin, J.E., Price, J.L., Yan, Z., Morris, J.C., and Sheline, Y.I. (2011). Resting bold fMRI differentiates dementia with Lewy bodies vs Alzheimer disease. **Neurology**, 76(21), pp. 1797-1803.
- Garreffa, G., Carnì, M., Gualniera, G., Ricci, G.B., Bozzao, L., De Carli, D., Morasso, P., Pantano, P., Colonnese, C., Roma, V., and Maraviglia, B. (2003). Real-time MR artifacts filtering during continuous EEG/fMRI acquisition. **Magn. Res. Imaging.**, 21(10), pp. 1175-1189.
- Gazzaniga, M.S., Ivry, R.B., and Mangun, G.R. (2013). Cognitive neuroscience: **The biology of the mind**. 4th edition. W.W. Norton: New York.
- Gebhardt, H., Blecker, C.R., Bischoff, M., Morgen, K., Oschmann, P., Vaitl, D., and Sammer, G. (2008). Synchronised measurement of simultaneous EEG-fMRI: a simulation study. **Clin. Neurophysiol.**, 119(12), pp. 2703-2711.
- Gibson, A.P., Hebden, J.C., and Arridge, S.R. (2005). Recent advances in diffuse optical imaging. **Phys. Med. Biol.**, 50(4), pp. R1-R43.
- Goebel, R. (2007). Localization of brain activity using functional magnetic resonance imaging. In: C. Stippich (ed.), **Clinical functional MRI: Presurgical functional neuroimaging**. Springer-Verlag: Berlin, Heidelberg, pp. 9-51.
- Goebel, R. and Esposito, F. (2010). The added value of EEG-fMRI in imaging neuroscience. In: C. Mulert and L. Lemieux (eds.), **EEG-fMRI: Physiological basis, technique, and applications**. Springer-Verlag: Berlin, Heidelberg, pp. 97-112.

- Goldman, R.I., Stern, J.M., Engel Jr., J., and Cohen, M.S. (2000). Acquiring simultaneous EEG and functional MRI. **Clin. Neurophysiol.**, 111(11), pp. 1974-1980.
- Gonçalves, S.I., Pouwels, P.J.W., Kuijter, J.P.A., Heethaar, R.M., and de Munck, J.C. (2007). Artefact removal in co-registered EEG/fMRI by selective average subtraction. **Clin. Neurophysiol.**, 118(11), pp. 2437-2450.
- Gotman, J. (2010). High frequency oscillations: The new EEG frontier? **Epilepsia**, 51(s1), pp. 63-65.
- Gotman, J. and Pittau, F. (2011). Combining EEG and fMRI in the study of epileptic discharges. **Epilepsia**, 52(s4), pp. 38-42.
- Grouiller, F., Vercueil, L., Krainik, A., Segebarth, C., Kahane, P., and David, O. (2007). A comparative study of different artefact removal algorithms for EEG signals acquired during functional MRI. **Neuroimage**, 38(1), pp. 124-137.
- Gutberlet, I. (2010). Recording EEG Signals Inside the MRI. In: M. Ullsperger and S. Debener (eds.), **Simultaneous EEG and fMRI: Recording, analysis, and applications**. Oxford University Press: New York, pp. 69-83.
- Haas, L.F. (2003). Hans Berger (1873-1941), Richard Caton (1842-1926), and electroencephalography. **J. Neurol. Neurosurg. Psychiatry**, 74(1), pp. 9.
- Hamilton, P.S. and Tompkins, W.J. (1986). Quantitative investigation of QRS detection rules using the MIT/BIH Arrhythmia Database. **IEEE Trans. Biomed. Eng.**, BME-33(12), pp. 1157-1165.
- Hanslmayr, S., Volberg, G., Wimber, M., Raabe, M., Greenlee, M.W., and Bäuml, K.H.T. (2011). The relationship between brain oscillations and BOLD signal during memory formation: a combined EEG-fMRI study. **J. Neurosci.**, 31(44), pp. 15674-15680.
- Hauf, M., Scheidegger, O., Rummel, C., Rahman, A., and Wiest, R. (2012). Recent developments of simultaneous EEG/fMRI in epilepsy: towards clinical application? **Epileptologie**, 29, pp. 90-98.

- Hirsch, J. (2006). Brain mapping for neurosurgery and cognitive neuroscience. In: S.H. Faro and F.B. Mohamed (eds.), **Functional MRI: Basic principles and clinical applications**. Springer: New York, pp.139-182.
- Hoffmann, A., Jäger, L., Werhahn, K.J., Jaschke, M., Noachtar, S., and Reiser, M. (2000). Electroencephalography during functional echo-planar imaging: detection of epileptic spikes using post-processing methods. **Magn. Res. Med.**, 44(5), pp. 791-798.
- Horovitz, S.G., Fukunaga, M., de Zwart, J.A., van Gelderen, P., Fulton, S.C., Balkin, T.J., and Duyn, J.H. (2008). Low frequency BOLD fluctuations during resting wakefulness and light sleep: A simultaneous EEG - fMRI study. **Hum. Brain Mapp.**, 29(6), pp. 671-682.
- Hornak, J.P. (2010). **The basics of MRI**. Rochester Institute of Technology: New York. Available at: <<http://www.cis.rit.edu/htbooks/mri/>>. Access in 6 Dec. 2010.
- Huang, C.-H., Ju, M.-S., and Lin, C.-C. (2012). A robust algorithm for removing artifacts in EEG recorded during FMRI/EEG study. **Comput. Biol. Med.**, 42(4), pp. 458-467.
- Huang, N.E., Shen, Z., Long, S.R., Wu, M.C., Shih, H.H., Zheng, Q., Yen, N.-C., Tung, C.C., Liu, H.H. (1998). The empirical mode decomposition and the Hilbert spectrum for nonlinear and non-stationary time series analysis. **Proc. R. Soc. Lond. A**, 454(1971), pp. 903-995.
- Iannetti, G.D. and Mouraux, A. (2010). Combining EEG and fMRI in pain research. In: C. Mulert and L. Lemieux (eds.), **EEG-fMRI: Physiological basis, technique, and applications**. Springer-Verlag: Berlin, Heidelberg, pp. 365-384.
- Jorge, J., van der Zwaag, W., and Figueiredo, P. (2014). EEG-fMRI integration for the study of human brain function. **Neuroimage**, 102, pp. 24-34.
- Kassebaum, N.J., Arora, M., Barber, R.M., Bhutta, Z.A., Brown, J., Carter, A., Casey, D.C., Charlson, F.J., Coates, M.M., Coggeshall, M., and Cornaby, L. (2016). Global, regional, and national disability-adjusted life-years (DALYs) for 315 diseases and injuries and healthy life expectancy (HALE), 1990–2015: a systematic analysis for the Global Burden of Disease Study 2015. **The Lancet**, 388(10053), pp. 1603-1658.
- Kay, S.M. (1993). **Fundamentals of statistical signal processing: Estimation theory**. Prentice Hall: Upper Saddle River.

- Kesavadas, C., Thomas, B., Sujesh, S., Ashalata, R., Abraham, M., Gupta, A.K., and Radhakrishnan, K. (2007). Real-time functional MR imaging (fMRI) for presurgical evaluation of paediatric epilepsy. **Pediatr. Radiol.**, 37(10), pp. 964-974.
- Kim, S.-G. and Bandettini, P.A. (2006). Principles of functional MRI. In: S.H. Faro and F.B. Mohamed (eds.), **Functional MRI: Basic principles and clinical applications**. Springer: New York, pp. 3-23.
- Klein, C., Hänggi, J., Luechinger, R., and Jäncke, L. (2015). MRI with and without a high-density EEG cap – what makes the difference?. **Neuroimage**, 106, pp. 189-197.
- Köhler, B.U., Hennig, C., and Orglmeister, R. (2002). The principles of software QRS detection. **IEEE Eng. Med. Biol. Mag.**, 21(1), pp. 42-57.
- Koskinen, M. and Vartiainen, N. (2009). Removal of imaging artifacts in EEG during simultaneous EEG/fMRI recording: reconstruction of a high-precision artifact template. **Neuroimage**, 46(1), pp. 160-167.
- Krakow, K. (2006). fMRI of epilepsy. In: S.H. Faro and F.B. Mohamed (eds.), **Functional MRI: Basic principles and clinical applications**. Springer: New York, pp. 315-341.
- Kreyszig, E. (2011). **Advanced engineering mathematics**. 10th edition. Wiley: Hoboken.
- Larcombe, S.J., Kennard, C., and Bridge, H. (2018). Increase in MST activity correlates with visual motion learning: a functional MRI study of perceptual learning. **Hum. Brain Mapp.**, 39(1), pp. 145-156.
- Laufs, H., Daunizeau, J., Carmichael, D.W., and Kleinschmidt, A. (2008). Recent advances in recording electrophysiological data simultaneously with magnetic resonance imaging. **Neuroimage**, 40(2), pp. 515-528.
- LeVan, P., Zhang, S., Knowles, B., Zaitsev, M., and Hennig, J. (2016). EEG-fMRI Gradient Artifact Correction by Multiple Motion-Related Templates. **IEEE Trans. Biomed. Eng.**, BME-63(12), pp. 2647-2653.
- Li, J., Chen, Y., Taya, F., Lim, J., Wong, K., Sun, Y., Bezerianos, A. (2017). A unified canonical correlation analysis-based framework for removing gradient artifact in concurrent

EEG/fMRI recording and motion artifact in walking recording from EEG signal. **Med. Biol. Eng. Comput.**, 55(9), pp. 1669-1681.

Lin, L., Wang, Y., and Zhou, H. (2009). Iterative filtering as an alternative algorithm for empirical mode decomposition. **Adv. Adapt. Data Anal.**, 1(04), pp. 543-560.

Liu, Z., de Zwart, J.A., van Gelderen, P., Kuo, L.-W., and Duyn, J.H. (2012). Statistical feature extraction for artifact removal from concurrent fMRI-EEG recordings. **Neuroimage**, 59(3), pp. 2073-2087.

Lloyd-Fox, S., Blasi, A., and Elwell, C.E. (2010). Illuminating the developing brain: the past, present and future of functional near infrared spectroscopy. **Neurosci. Biobehav. Rev.**, 34(3), pp. 269-284.

Lopes da Silva, F. (2010). EEG: origin and measurement. In: C. Mulert and L. Lemieux (eds.), **EEG-fMRI: Physiological basis, technique, and applications**. Springer-Verlag: Berlin, Heidelberg, pp. 19-38.

Lopes da Silva, F. and van Rotterdam, A. (1999). Biophysical aspects of EEG and magnetoencephalogram generation. In: E. Niedermeyer and F. Lopes da Silva (eds.), **Electroencephalography: Basic principles, clinical applications, and related fields**. 4th edition. Williams & Wilkins: Baltimore, pp. 93-109.

Luo, Q. and Glover, G. H. (2012). Influence of dense-array EEG cap on fMRI signal. *Magnetic resonance in medicine*, 68(3), pp. 807-815.

Mahadevan, A., Acharya, S., Sheffer, D.B., and Mugler, D.H. (2008) Ballistocardiogram artifact removal in EEG-fMRI signals using discrete hermite transforms. **IEEE J. Sel. Topics Signal Process.**, 2(6), pp. 839-853.

Mandelkow, H., Halder, P., Boesiger, P., and Brandeis, D. (2006). Synchronisation facilitates removal of MRI artefacts from concurrent EEG recordings and increases usable bandwidth. **Neuroimage**, 32(3), pp. 1120-1126.

Mandelkow, H., Brandeis, D. and Boesiger, P. (2010). Good practices in EEG-MRI: the utility of retrospective synchronisation and PCA for the removal of MRI gradient artefacts. **Neuroimage**, 49(3), pp. 2287-2303.

- Mantini, D., Perrucci, M.G., Cugini, S., Ferretti, A., Romani, G.L., and del Gratta, C. (2007). Complete artifact removal for EEG recorded during continuous fMRI using independent component analysis. **Neuroimage**, 34(2), pp. 598-607.
- Masterton, R.A.J., Abbott, D.F., Fleming, S.W., and Jackson, G.D. (2007). Measurement and reduction of motion and ballistocardiogram artefacts from simultaneous EEG and fMRI recordings. **Neuroimage**, 37(1), pp. 202-211.
- Matsuda, T., Matsuura, M., Ohkubo, T., Ohkubo, H., Atsumi, Y., Tamaki, M., Takahashi, K., Matsushima, E., and Kojima, T. (2002). Influence of arousal level for functional magnetic resonance imaging (fMRI) study: simultaneous recording of fMRI and electroencephalogram. **Psychiatry Clin. Neurosci.**, 56(3), pp. 289-290.
- Maziero, D., Velasco, T.R., Hunt, N., Payne, E., Lemieux, L., Salmon, C.E.G., and Carmichael, D.W. (2016). Towards motion insensitive EEG-fMRI: correcting motion-induced voltages and gradient artefact instability in EEG using an fMRI prospective motion correction (PMC) system. **Neuroimage**, 138, pp. 13-27.
- McFadden, P.D. (1987). A revised model for the extraction of periodic waveforms by time-domain averaging. **Mech. Syst. Signal Pr.**, 1(1), pp. 83-95.
- Meher, J., Meher, P., and Dash, G. (2011). Improved comb filter based approach for effective prediction of protein coding regions in DNA sequences. **JSIP**, 2(02), pp. 88-99.
- Meltzer, J.A., Negishi, M., Mayes, L.C., and Constable, R.T. (2007). Individual differences in EEG theta and alpha dynamics during working memory correlate with fMRI responses across subjects. **Clin. Neurophysiol.**, 118(11), pp. 2419-2436.
- Michel, C.M. and Brandeis, D. (2010). The sources and temporal dynamics of scalp electric fields. In: M. Ullsperger and S. Debener (eds.), **Simultaneous EEG and fMRI: Recording, analysis, and applications**. Oxford University Press: New York, pp. 3-19.
- Michels, L., Bucher, K., Lüchinger, R., Klaver, P., Martin, E., Jeanmonod, D., and Brandeis, D. (2010). Simultaneous EEG-fMRI during a working memory task: modulations in low and high frequency bands. **PLoS One**, 5(4), p. e10298.

MIT-BIH (1998). **Database Distribution**. Massachusetts Institute of Technology, Cambridge. Available at: <<http://ecg.mit.edu/>>.

Moosmann, M., Schönfelder, V.H., Specht, K., Scheeringa, R., Nordby, H., and Hugdahl, K. (2009). Realignment parameter-informed artefact correction for simultaneous EEG-fMRI recordings. **Neuroimage**, 45(4), pp. 1144-1150.

Mulert, C. and Hegerl, U. (2009). Integration of EEG and fMRI. In: E. Kraft, G. Gulyás, and E. Pöppel (eds.), **Neural correlates of thinking**. Springer-Verlag: Berlin, Heidelberg, pp. 95-106.

Mulert, C., Jäger, L., Schmitt, R., Bussfeld, P., Pogarell, O., Möller, H.-J., Juckel, G., and Hegerl, U. (2004). Integration of fMRI and simultaneous EEG: towards a comprehensive understanding of localization and time-course of brain activity in target detection. **Neuroimage**, 22(1), 83-94.

Mullinger, K., Debener, S., Coxon, R., and Bowtell, R. (2008). Effects of simultaneous EEG recording on MRI data quality at 1.5, 3 and 7 tesla. **Int. J. Psychophysiol.**, 67 (3), pp. 178–188.

Mullinger, K.J., Morgan, P.S., and Bowtell, R. (2008b). Improved artifact correction for combined electroencephalography/functional MRI by means of synchronisation and use of vectorcardiogram recordings. **J. Magn. Reson. Imaging.**, 27(3), pp. 607-616.

Mullinger, K. Brookes, M. Geirsdottir, G. and Bowtell, R. (2008c). Average gradient artefact subtraction: the effect on neuronal signals. **Presented at the 14th Annual Meeting of the Organization for Human Brain Mapping (OHBM 2008)**, Elsevier, Melbourne, Australia, Jun 15–19, 2008.

Mullinger, K.J. and Bowtell, R. (2010). Influence of EEG equipment on MR image quality. In: M. Ullsperger and S. Debener (eds.), **Silmultaneous EEG and fMRI: Recording, analysis, and applications**. Oxford University Press: New York, pp. 107-117.

Mullinger, K.J., Yan, W.X., and Bowtell, R. (2011). Reducing the gradient artefact in simultaneous EEG-fMRI by adjusting the subject's axial position. **Neuroimage**, 54(3), pp. 1942-1950.

- Mullinger, K.J., Chowdhury, M.E.H., and Bowtell, R. (2014). Investigating the effect of modifying the EEG cap lead configuration on the gradient artifact in simultaneous EEG-fMRI. **Front. Neurosci.**, 8, article 226, pp. 1-10.
- Murta, T., Leite, M., Carmichael, D.W., Figueiredo, P., and Lemieux, L. (2015). Electrophysiological correlates of the BOLD signal for EEG-informed fMRI. **Hum. Brain Mapp.**, 36(1), pp. 391-414.
- Negishi, M., Abildgaard, M., Nixon, T., and Constable, R.T. (2004). Removal of time-varying gradient artifacts from EEG data acquired during continuous fMRI. **Clin. Neurophysiol.**, 115(9), pp. 2181-2192.
- Niazy, R.K., Beckmann, C.F., Iannetti, G.D., Brady, J.M., and Smith, S.M. (2005). Removal of FMRI environment artifacts from EEG data using optimal basis sets. **Neuroimage**, 28(3), pp. 720-737.
- Niedermeyer, E. (1999). Historical aspects. In: E. Niedermeyer and F. Lopes da Silva (eds.), **Electroencephalography: Basic principles, clinical applications, and related fields**. 4th edition. Williams & Wilkins: Baltimore, pp. 1-14.
- Ogawa, S., Lee, T., Kay, A., and Tank, D. (1990). Brain magnetic resonance imaging with contrast dependent on blood oxygenation. **Proc. Natl. Acad. Sci. USA.**, 87(24), pp. 9868-9872.
- Oh, S.S., Han, Y., Lee, J., Yun, S.D., Kang, J.K., Lee, E.M., Yoon, H.W., and Chung, J.-Y., Park, H. (2014). A pulse artifact removal method considering artifact variations in the simultaneous recording of EEG and fMRI. **Neurosci. Res.**, 81-82, pp. 42-50.
- Olson, W.H. (2010). Basic concepts of medical instrumentation. In: J.G. Webster (ed.), **Medical instrumentation: Application and design**. 4th edition. Wiley: Hoboken, pp. 1-44.
- Oppenheim, A.V. and Schafer, R.W. (1999). **Discrete-time signal processing**. 2nd edition. Prentice-Hall: Upper Saddle River.
- Oostenveld, R. and Praamstra, P. (2001). The five percent electrode system for high-resolution EEG and ERP measurements. **Clin. Neurophysiol.**, 112(4), pp. 713-719.

- Pan, H., Epstein, J., Silbersweig, D. A., and Stern, E. (2011). New and emerging imaging techniques for mapping brain circuitry. *Brain Res Rev.*, 67(1-2), pp. 226-251.
- Pan, J. and Tompkins, W.J. (1985). A real-time QRS detection algorithm. **IEEE Trans. Biomed. Eng.**, BME-32(3), pp. 230-236.
- Papoulis, A. and Pillai, S.U. (2002). **Probability, random variables, and stochastic processes**. 4th edition. McGraw-Hill: New York.
- Papoutsis, M., Weiskopf, N., Langbehn, D., Reilmann, R., Rees, G., and Tabrizi, S.J. (2018). Stimulating neural plasticity with real-time fMRI neurofeedback in Huntington's disease: a proof of concept study. **Hum. Brain Mapp.**, 39(3), pp. 1339-1353.
- Pascual-Marqui, R.D. (1999). Review of methods for solving the EEG inverse problem. **Int. J. Bioelectromagn.**, 1(1), pp. 75-86.
- Pisauro, M.A., Fouragnan, E., Retzler, C., and Philiastides, M.G. (2017). Neural correlates of evidence accumulation during value-based decisions revealed via simultaneous EEG-fMRI. **Nat. Commun.**, 8(15808), pp. 1-9.
- Pittau, F., Dubeau, F., and Gotman, J. (2012). Contribution of EEG/fMRI to the definition of the epileptic focus. **Neurology**, 78(19), pp. 1479-1487.
- Portas, C.M., Krakow, K., Allen, P., Josephs, O., Armony, J.L., and Frith, C.D. (2000). Auditory processing across the sleep-wake cycle: simultaneous EEG and fMRI monitoring in humans. **Neuron**, 28(3), pp. 991-999.
- Press, W.H., Teukolsky, S.A., Vetterling, W.T., and Flannery, B.P. (1992). **Numerical recipes in C: The art of scientific computing**. 2nd edition. Cambridge University Press: Cambridge.
- Proakis, J.G. and Manolakis, D.G. (1996). **Digital signal processing: Principles, algorithms, and applications**. 3rd edition. Prentice-Hall: Upper Saddle River.
- Prodić, A., Chen, J., Maksimović, D., and Erickson, R.W. (2003). Self-Tuning digitally controlled low-harmonic rectifier having fast dynamic response. **IEEE Trans. Power Electron.**, 18(1), pp. 420-428.

- Raichle, M.E. (2009). A brief history of human brain mapping. **Trends Neurosci.**, 32(2), pp. 118-126.
- Rangayyan, R.M. (2002). **Biomedical signal analysis: A case-study approach**. Wiley: New York.
- Razavi, N., Jann, K., Koenig, T., Kottlow, M., Hauf, M., Strik, W., and Dierks, T. (2013). Shifted coupling of EEG driving frequencies and fMRI resting state networks in schizophrenia spectrum disorders. **PLoS One**, 8(10), p. e76604.
- Rezk, S., Join, C., and El Asmi, S. (2011). An algebraic derivative-based method for R wave detection. In: **Proceedings of the 19th European Signal Processing Conference (EUSIPCO '2011)**, IEEE, Barcelona, Spain, August 29 – September 2, 2011, pp. 1578-1582.
- Rinck P.A. (2017). **Magnetic Resonance in Medicine: A Critical Introduction**. 11th edition. EMRF/TRTF: Norderstedt. Available at: <<https://www.magnetic-resonance.org/contents.html>>. Access in 5 Apr. 2019.
- Ritter, P. and Villringer, A. (2006). Simultaneous EEG-fMRI. **Neurosci. Biobehav. Rev.**, 30(6), pp. 823-838.
- Ritter, P., Moosmann, M., and Villringer, A. (2009). Rolandic alpha and beta EEG rhythms' strengths are inversely related to fMRI-BOLD signal in primary somatosensory and motor cortex. **Hum. Brain Mapp.**, 30(4), pp. 1168-1187.
- Ritter, P., Becker, R., Freyer, F., and Villringer, A. (2010). EEG quality: the image acquisition artefact. In: C. Mulert and L. Lemieux (eds.), **EEG-fMRI: Physiological basis, technique, and applications**. Springer-Verlag: Berlin, Heidelberg, pp. 153-171.
- Ritter, P., Becker, R., Graefe, C., and Villringer, A. (2007). Evaluating gradient artifact correction of EEG data acquired simultaneously with fMRI. **Magn. Reson. Imaging**, 25(6), pp. 923-932.
- Roberts, K., Papadaki, A., Gonçalves, C., Tighe, M., Atherton, D., Shenoy, R., McRobbie, D., and Anand, P. (2008). Contact heat evoked potentials using simultaneous EEG and fMRI and their correlation with evoked pain. **BMC Anesthesiol.**, 8(1), p. 8.

- Rousselet, G.A. (2012). Does filtering preclude us from studying ERP time-courses?. **Front. Psychol.**, 3, p. 131.
- Ryali, S., Glover, G.H., Chang, C., and Menon, V. (2009). Development, validation, and comparison of ICA-based gradient artifact reduction algorithms for simultaneous EEG-spiral in/out and echo-planar fMRI recordings. **Neuroimage**, 48(2), pp. 348-361.
- Salmeron, B.J. and Stein, E.A. (2006). Pharmacological applications of fMRI. In: S.H. Faro and F.B. Mohamed (eds.), **Functional MRI: Basic principles and clinical applications**. Springer: New York, pp. 444-467.
- Sanei, S. and Chambers, J.A. (2007). **EEG signal processing**. Wiley: Hoboken.
- Savoy, R.L. (2001). History and future directions of human brain mapping and functional neuroimaging. **Acta Psychol.**, 107(1-3), pp. 9-42.
- Saykin, A.J. and Wishart, H.A. (2006). fMRI of memory in aging and dementia. In: S.H. Faro and F.B. Mohamed (eds.), **Functional MRI: Basic principles and clinical applications**. Springer: New York, pp. 221-244.
- Scherg, M. (1982). Simultaneous recording and separation of early and middle latency auditory evoked potentials. **Electroencephalogr. Clin. Neurophysiol.**, 54(3), pp. 339-341.
- Seeck, M., Lazeyras, F., Michel, C.M., Blanke, O., Gericke, C.A., Ives, J., Delavelle, J., Golay, X., Haenggeli, C.A., de Tribolet, N., and Landis, T. (1998). Non-invasive epileptic focus localization using EEG-triggered functional MRI and electromagnetic tomography. **Electroencephalogr. Clin. Neurophysiol.**, 106(6), pp. 508-512.
- Shipley, J.T. (2001). **The origin of English words: A discursive dictionary of Indo-European roots**. Johns Hopkins University Press: Baltimore.
- Siedband, M.P. (2010). Medical imaging systems. In: J.G. Webster (ed.), **Medical instrumentation: Application and design**. 4th edition. Wiley: Hoboken, pp. 528-589.
- Sijbers, J., Michiels, I., Verhoye, M., van Audekerke, J., van der Linden, A., and van Dyck, D. (1999). Restoration of MR-induced artifacts in simultaneously recorded MR/EEG data. **Magn. Reson. Imaging**, 17(9), pp. 1383-1391,

- Sijbers, J., van Audekerke, J., Verhoye, M., van der Linden, A., and van Dyck, D. (2000). Reduction of ECG and gradient related artifacts in simultaneously recorded human EEG/fMRI data. **Magn. Reson. Imaging.**, 18(7), pp. 881-886.
- Sladky, R., Friston, K.J., Tröstl, J., Cunnington, R., Moser, E., and Windischberger, C. (2011). Slice-timing effects and their correction in functional MRI. **Neuroimage**, 58(2), pp. 588-594.
- Smith, S.W. (1999). **The scientist and engineer's guide to digital signal processing.** 2nd edition. California Technical Publishing: San Diego.
- Snyder, A.Z. and Raichle, M.E. (2010). Studies of the human brain combining functional neuroimaging and electrophysiological methods. In: M. Ullsperger and S. Debener (eds.), **Silmultaneous EEG and fMRI: Recording, analysis, and applications.** Oxford University Press: New York, pp. 47-65.
- Solana, A.B., Hernández-Tamames, J.A., Manzanedo, E., García-Álvarez, R., Zelaya, F.O., and del Pozo, F. (2014). Gradient induced artifacts in simultaneous EEG-fMRI: effect of synchronisation on spiral and EPI k-space trajectories. **Magn. Res. Imaging.**, 32(6), pp. 684-692.
- Sörnmo, L. and Laguna, P. (2005). **Bioelectrical signal processing in cardiac and neurological applications.** Elsevier-Academic Press: New York.
- Spencer, G.S. (2015). **EEG-fMRI: novel methods for gradient artefact correction.** Ph.D. Thesis. University of Nottingham: Nottingham, United Kingdom.
- Stippich, C. (2007). Introduction to presurgical functional MRI. In: C. Stippich (ed.), **Clinical functional MRI: Presurgical functional neuroimaging.** Springer-Verlag: Berlin, Heidelberg, pp. 1-7.
- Sun, L. and Hinrichs, H. (2009). Simultaneously recorded EEG-fMRI: removal of gradient artifacts by subtraction of head movement related average artifact waveforms. **Hum. Brain Mapp.**, 30(10), pp. 3361-3377.
- Tahir, M. and Mazumder, S.K. (2014). Improving dynamic response of active harmonic compensator using digital comb filter. **IEEE Trans. Emerg. Sel. Topics Power Electron.**, 2(4), pp. 994-1002.

- Thakor, N.V., Webster, J.G., and Tompkins, W.J. (1984). Estimation of QRS complex power spectra for design of a QRS filter. **IEEE Trans. Biomed. Eng.**, BME-31(11), pp. 702-706.
- Turesky, T.K., Olulade, O.A., Luetje, M.M., and Eden, G.F. (2018). An fMRI study of finger tapping in children and adults. **Hum. Brain Mapp.**, 39(8), pp. 3203-3215.
- Turner, R. and Jones, T. (2003). Techniques for imaging neuroscience. **Br. Med. Bull.**, 65(1), pp. 3-20.
- Uludağ, K. and Roebroeck, A. (2014). General overview on the merits of multimodal neuroimaging data fusion. **Neuroimage**, 102, pp. 3-10.
- van de Velde, M., van Erp, G., and Cluitmans, P.J.M. (1998). Detection of muscle artefact in the normal human awake EEG. **Electroencephalogr. Clin. Neurophysiol.**, 107(2), pp. 149-158.
- van Liempt, S., Vermetten, E., Lentjes, E., Arends, J., and Westenberg, H. (2011). Decreased nocturnal growth hormone secretion and sleep fragmentation in combat-related posttraumatic stress disorder; potential predictors of impaired memory consolidation. **Psychoneuroendocrinology**, 36(9), pp. 1361-1369.
- Vaseghi, S.V. (2000). **Advanced digital signal processing and noise reduction**. 2nd edition. New Wiley: Chichester.
- Villringer, A., Mulert, C., and Lemieux, L. (2010). Principles of multimodal functional imaging and data integration. In: C. Mulert and L. Lemieux (eds.), **EEG-fMRI: Physiological basis, technique, and applications**. Springer-Verlag: Berlin, Heidelberg, pp. 3-17.
- Vincent, J.L., Larson-Prior, L.J., Zempel, J.M., and Snyder, A.Z. (2007). Moving GLM ballistocardiogram artefact reduction for EEG acquired simultaneously with fMRI. **Clin. Neurophysiol.**, 118(5), pp. 981-998.
- Vlček, M. and Zahradník, P. (2004). Fast analytical design algorithms for FIR notch filters. **IEEE Trans. Circuits Syst. I, Reg. Papers**, 51(3), pp. 608-623.

- Wan, X., Iwata, K., Riera, J., Ozaki T., Kitamura, M., and Kawashima, R. (2006). Artefact reduction for EEG/fMRI recording: nonlinear reduction of ballistocardiogram artefacts. **Clin. Neurophysiol.**, 117(3), pp. 668-680.
- Wang, Y., Wei, G.-W., and Yang, S. (2012). Iterative filtering decomposition based on local spectral evolution kernel. **J. Sci. Comput.**, 50(3), pp. 629-664.
- Warach, S., Ives, J.R., Schlaug, G., Patel, M.R., Darby, D.G., Thangaraj, V., Edelman, R.R., and Schomer, D.L. (1996). EEG-triggered echo-planar functional MRI in epilepsy. **Neurology**, 47(1), pp. 89-93.
- World Health Organization (2006). **Neurological disorders: Public health challenges**. WHO: Geneva. Available at: <https://www.who.int/mental_health/neurology/neurodiso/en/>. Access in 7 Apr. 2019.
- World Health Organization (2017a). **Atlas: Country resources for neurological disorders**. 2nd edition. WHO: Geneva. Available at: <https://www.who.int/mental_health/neurology/atlas_second_edition/en/>. Access in 7 Apr. 2019.
- World Health Organization (2017b). **Global atlas of medical devices**. WHO: Geneva. Available at: <https://www.who.int/medical_devices/publications/global_atlas_meddev2017/en/>. Access in 7 Apr. 2019.
- Widmann, A., Schröger, E., and Maess, B. (2015). Digital filter design for electrophysiological data—a practical approach. **J. Neurosci. Methods**, 250, pp. 34-46.
- Wiest, R., Abela, E., and Rummel, C. (2015). Simultaneous EEG-fMRI in epilepsy. In: C. Stippich (ed.), **Clinical functional MRI: Presurgical functional neuroimaging**. 2nd edition. Springer-Verlag: Berlin, Heidelberg, pp. 159-177.
- Wolberg, G. and Alfy, I. (1999). Monotonic cubic spline interpolation. In: **Proceedings of the Computer Graphics International Conference (CGI '1999)**, IEEE, Canmore, Canada, June 7 – 11, 1999, pp. 188-195.

Yan, W.X., Mullinger, K.J., Brookes, M.J., and Bowtell, R. (2009). Understanding gradient artefacts in simultaneous EEG/fMRI. **Neuroimage**, 46(2), pp. 459-471.

Yan, W.X., Mullinger, K.J., Geirsdottir, G.B., and Bowtell, R. (2010). Physical Modeling of Pulse Artefact Sources in Simultaneous EEG/fMRI. **Hum. Brain Mapp.**, 31, pp. 604-620.

Yurgelun-Todd, D.A., Renshaw, P.F., and Femia, L.A. (2006). Applications of fMRI to psychiatry. In: S.H. Faro and F.B. Mohamed (eds.), **Functional MRI: Basic principles and clinical applications**. Springer: New York, pp. 183-220.

Zeng, Z., Xie, Y., Wang, Y., Guan, Y., Li, L., and Zhang, X. (2017). An improved harmonic current detection method based on parallel active power filter. In: **Proceedings of the 2nd Asia Conference on Power and Electrical Engineering (ACPEE '2017)**, IOP Publishing, Shanghai, China, March 24 – 26, 2017, 199 (1), 012143, pp. 1-6.

Zijlmans, M., Huiskamp, G., Hersevoort, M., Seppenwoolde, J.H., van Huffelen, A.C., and Leijten, F.S. (2007). EEG-fMRI in the preoperative work-up for epilepsy surgery. **Brain**, 130(9), pp. 2343-2353.

Zotev, V., Yuan, H., Misaki, M., Phillips, R., Young, K. D., Feldner, M. T., and Bodurka, J. (2016). Correlation between amygdala BOLD activity and frontal EEG asymmetry during real-time fMRI neurofeedback training in patients with depression. **Neuroimage Clin.**, 11, pp. 224-238.

Zotev, V., Phillips, R., Misaki, M., Wong, C.K., Wurfel, B.E., Krueger, F., Feldner, M., and Bodurka, J. (2018). Real-time fMRI neurofeedback training of the amygdala activity with simultaneous EEG in veterans with combat-related PTSD. **Neuroimage Clin.**, 19, pp.106-121.

List of the author's publications

Journal and conference articles (in thesis)

1. Ferreira, J.L., Wu, Y., Besseling, R.M.H., Lamerichs, R., and Aarts, R.M. (2016). Gradient artefact correction and evaluation of the EEG recorded simultaneously with fMRI data using optimised moving-average. **J. Med. Eng.**, vol. 2016, article ID 9614323, pp. 1-17.
2. Ferreira, J.L., Wu, Y., R., and Aarts, R.M (2018). Enhancement of the comb-filtering selectivity using iterative moving-average for periodic waveform and harmonic elimination. **J. Healthc. Eng.**, vol. 2018, article ID 7901502, pp. 1-14.
3. Ferreira, J.L., Besseling, R.M.H., Wu, Y., Arends, J., and Carrette, E. (2018). Evaluating the relative efficacy and clinical usefulness of the gradient artefact correction using iterative filtering. To be submitted.
4. Ferreira, J.L., Cluitmans, P.J.M., and Aarts, R.M. (2013a). Non-linear filter for gradient artefact correction during simultaneous EEG-fMRI. **Signal Processing Research**, 2(3), pp. 55-63.
5. Ferreira, J.L., Cluitmans, P.J.M, and Aarts, R.M. (2013b). Gradient artefact modelling using a set of sinusoidal waveforms for EEG correction during continuous fMRI. **Signal Processing Research**, 2(2), pp. 39-48.
6. Ferreira, J.L., Aarts, R.M., and Cluitmans, P.J.M. (2013c). Effective extraction and filtering of frequency components in physiological signals using sum-of-sinusoids modelling. **Signal Processing Research**, 2(4), pp. 73-80.
7. Ferreira, J.L., Cluitmans, P.J.M, and Aarts, R.M. (2012). Gradient artefact correction in the EEG signal recorded within the fMRI scanner. In: **Proceedings of the 5th International Conference on Bio-inspired Systems and Signal Processing (BIOSIGNALS '2012)**, INSTICC, Vilamoura, Portugal, February 1 – 4, 2012, pp. 110-117.

8. Ferreira, J.L., Cluitmans, P.J.M., and Aarts, R.M. (2013d). Detection of sharp wave activity in biological signals using differentiation between consecutive samples. In: **Proceedings of the 6th International Conference on Bio-inspired Systems and Signal Processing (BIOSIGNALS '2013)**, INSTICC, Barcelona, Spain, February 11 – 14, 2013, pp. 327-332.
9. Ferreira, J.L., Aarts, R.M., and Cluitmans, P.J.M. (2014a). Optimized moving-average filtering for gradient artefact correction during simultaneous EEG-fMRI. In: **Proceedings of the 5th ISSNIP-IEEE Biosignals and Biorobotics Conference: Biosignals and Robotics for Better and Safer Living (BRC '2014)**, IEEE, Salvador, Brazil, May 26 – 28, 2014, pp. 1-6.
10. Ferreira, J.L., Aarts, R.M., and Cluitmans, P.J.M. (2014b). Removal of gradient artefacts during transient head movements for continuous EEG-fMRI. In: **Proceedings of the 7th International Conference on Bio-inspired Systems and Signal Processing (BIOSIGNALS '2014)**, INSTICC, Angers, France, March 3 – 6, 2014, pp. 213-220.

Journal and conference articles and book chapter (not in thesis)

1. Ferreira, J.L., Pereira, N.C., Oliveira Júnior, M., Vasconcelos, F.H., Parreira, V.F., and Tierra-Criollo, C.J. (2010). Maximum respiratory pressure measuring system: calibration and evaluation of uncertainty. **SBA Controle & Automação**, 21(6), 588-597.
2. Ferreira, J.L., Pereira, N.C., Oliveira Júnior, M., Silva, J.L., Britto, R., Parreira, V.F., Vasconcelos, F.H., and Tierra-Criollo, C.J. (2008). Application of weighted least squares to calibrate a digital system for measuring the respiratory pressures. In: **Proceedings of the 1st International Conference on Biomedical Electronics and Devices (BIODEVICES'2008)**, INSTICC, Funchal, Portugal, January 28 – 31, 2008, pp. 220-223.
3. Ferreira, J.L., Pereira, N.C., Oliveira Júnior, M., Silva, J.L., Britto, R., Parreira, V.F., Vasconcelos, F.H., and Tierra-Criollo, C.J. (2008). Análise da calibração para um medidor digital de pressões respiratórias. In: **Proceedings of 21^o Congresso Brasileiro de Engenharia Biomédica**, SBEB, Salvador, Brazil, November 16 – 20, 2008, pp. 741-744.

4. Ferreira, J.L., Pereira, N.C., Oliveira Júnior, M., Silva, J.L., Britto, R., Parreira, V.F., Vasconcelos, F.H., and Tierra-Criollo, C.J. (2007). Calibração e cálculo da incerteza para um medidor digital de pressões respiratórias. In: **Proceedings of the 7th International Seminar on Electrical Metrology**, Belo Horizonte, Brazil, September 12 – 14, 2007.
5. Ferreira, J.L., Vasconcelos, F.H., and Tierra-Criollo, C.J. (2011). A case study of applying weighted least squares to calibrate a digital maximum respiratory pressures measuring system. In: A. McEwan and G.D. Gargiulo (eds.), **Applied biomedical engineering**. InTech: Croatia, pp. 419-432.

Acknowledgments

First of all, I am grateful to God, source of all wisdom, science, knowledge, light, and inspiration. He who strengthened and conducted my steps along my PhD road.

Secondly, to my parents, Manoel and Leonor, for their unconditional love, support, and help; may God always bless you, *que Deus mesmo possa abençoá-los sempre*.

My sincere gratitude to my supervisor, Prof. Ronald Aarts, who did his best to guide me within my PhD project, and helped me to improve and conclude this work. To Yan Wu and René Besseling, who also guided me and gave me precious technical information and valuable inputs within my PhD project. To Prof. Johan Arends for his valuable contributions in regards to clinical evaluation of the EEG signals. To Rolf Lamerichs and Evelien Carrette, who also provided me precious technical and clinical information regarding the EEG-fMRI data.

To Dr. Robert Stoermer of Brain Products for kindly providing some of the data presented in this work as well as the Vision Analyzer software. To Rogier Wildeboer for kindly reviewing this work and giving some useful tips to improve it. To Prof. Pierre Cluitmans, who was my technical supervisor in my first PhD years and helped me to become an independent researcher. To professors, staff, and students of the Signal Processing Systems Group (SPS), Department of Electrical Engineering, and TU/e in general, who shared with me valuable experiences, stories, fellowship, and helped me during my stay at TU/e, especially Prof. Rui Castro for his important advices along my PhD road.

To the TU/e student associations, to say some of them: Thor, Intermate, and SVTN J.D. van der Waals; for sure, you do make student' life lighter, funnier, and joyful. To the Student Sport Center Eindhoven (SSC), especially the volleyball association ESVV Hajraa; without the sporting activities and friendship you offered me, my PhD life at TU/e would be much harder. To all my friends I made during my PhD life and stay in Eindhoven. To all my friends I made during my PhD life and stay in the Netherlands, in especial those of the Community Our Lady Aparecida in Handel as well as those of the Paterskerk in Eindhoven.

A special acknowledgment to Prof. Carlos Julio Tierra-Criollo of UFRJ/UFMG, who supervised me during my master study in Brazil and whose help was crucial to obtain the scholarships that supported me during my stay at TU/e. To the Erasmus Mundus – EBW II project and CNPq – Science without Borders program which granted the scholarships to financially support my PhD project at TU/e, with special thanks to Ana Reis of the University of Porto and Anneroo Dijkhuis of TU/e. To Otniel Ribeiro for kindly helping with the cover design.

Finally, to all who contributed one way or another to the conclusion of this work. May God bless you all too: “*Health and Peace*”, as Eustachius van Lieshout used to say, a Dutch missionary who lived in Brazil in the first decades of the last century.

About the author

José Leonardo Ferreira was born on the 24th April 1975 in Diamantina, Brazil. In 2000, he received his Bachelor's degree in Electrical Engineering at Federal University of Minas Gerais (UFMG) in Belo Horizonte, Brazil. In 2008, he obtained his M.Sc. in Electrical Engineering with focus on biomedical engineering/ signal processing at Federal University of Minas Gerais (UFMG) in Belo Horizonte, Brazil. From 2010 he started a PhD project in the Signal Processing Systems Group of the Eindhoven University of Technology (TU/e), the Netherlands, granted by Erasmus Mundus – EBW II project and by CNPq – Science without Borders program. The results of his PhD research are presented in this thesis. He was employed at CEPEL/ELETRONBRAS System (2000) in Rio de Janeiro and at FHEMIG (2003) in Belo Horizonte, Brazil, where he worked as an electrical engineer. In 2018, he was employed at Federal University of Jequitinhonha and Mucuri's Valley (UFVJM) in Diamantina as a university professor for education and teaching of algorithms, programming languages, and basic computer science of engineering bachelor's students. His research interests include signal processing, biomedical signal processing, machine learning, and algorithms and computer science applied to engineering.

“My soul magnifies the Lord, and my spirit rejoices in God my Savior!...”

Luke, 1:46

“The future belongs to those who believe in their dreams”

Motivational phrase printed on a wall of the PSV football team’s dressing room

(PSV Stadium – June 2013)

